



**HAL**  
open science

# Hydrogenated polymorphous silicon: establishing the link between hydrogen microstructure and irreversible solar cell kinetics during light soaking

Ka-Hyun Kim

► **To cite this version:**

Ka-Hyun Kim. Hydrogenated polymorphous silicon: establishing the link between hydrogen microstructure and irreversible solar cell kinetics during light soaking. Materials Science [cond-mat.mtrl-sci]. Ecole Polytechnique X, 2012. English. NNT: . pastel-00747463

**HAL Id: pastel-00747463**

**<https://pastel.hal.science/pastel-00747463>**

Submitted on 31 Oct 2012

**HAL** is a multi-disciplinary open access archive for the deposit and dissemination of scientific research documents, whether they are published or not. The documents may come from teaching and research institutions in France or abroad, or from public or private research centers.

L'archive ouverte pluridisciplinaire **HAL**, est destinée au dépôt et à la diffusion de documents scientifiques de niveau recherche, publiés ou non, émanant des établissements d'enseignement et de recherche français ou étrangers, des laboratoires publics ou privés.

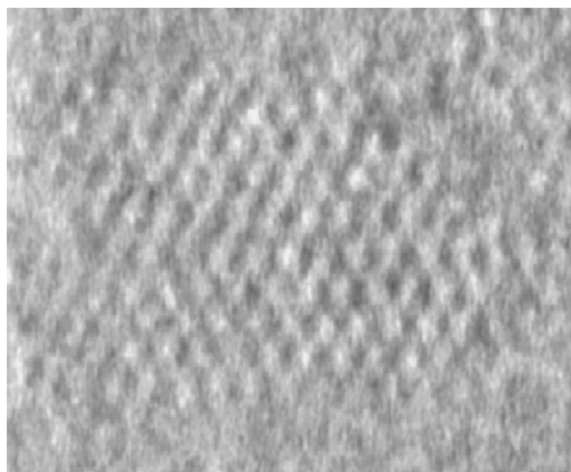


**TOTAL**



Doctoral thesis in Physics / Materials Science

**Hydrogenated polymorphous silicon:  
establishing the link between hydrogen  
microstructure and irreversible solar  
cell kinetics during light soaking**



**Ka-Hyun Kim**





## THÈSE

Présentée en vue d'obtenir le grade de

### **Docteur de l'École Polytechnique**

Spécialité : Physique / Science des Matériaux

par

**Ka-Hyun Kim**

### **Hydrogenated polymorphous silicon: establishing the link between hydrogen microstructure and irreversible solar cell kinetics during light soaking**

Thèse soutenue le 9 Octobre 2012 devant le jury compose de :

Prof.	Anna Fontcuberta i Morral	Rapporteur
Prof.	Laifa Boufendi	Rapporteur
Dr.	Friedhelm Finger	Examineur
Dr.	Edward A. G. Hamers	Examineur
Dr.	Lars Oberbeck	Examineur
Dr.	René A.C.M.M. van Swaij	Examineur
Prof.	Pere Roca i Cabarrocas	Directeur de thèse
Dr.	Erik V. Johnson	Co-directeur de thèse





## RAPPORT DE SOUTENANCE

### DOCTORAT DE L'ÉCOLE POLYTECHNIQUE

Nom : **KIM**  
Prénom : **Ka-Hyun**  
Spécialité : **Science des Matériaux**

Sujet : **Hydrogenated polymorphous silicon: establishing the link between hydrogen microstructure and irreversible solar cell kinetics during light soaking**

Date de soutenance :

Président du jury : - A. FONTCUBERTA I MORRAL  
Membres du jury : - FRIEDELH JINGER  
- ERIK JOHNSON  
- René van Swaaij  
- Edward Hamers  
- LARS OBERBECK  
- Laïfa BOUFENDI  
- Pere Roca i Cabarrocas

Signature :  
Signature :  
Signature :  
Signature :  
Signature :  
Signature :  
Signature :

Rapport (2) :

M. Ka-Hyun KIM made an extremely clear and concise presentation, focusing on the more important and original results of the impressive quantity of work he performed, and showing his complete mastery of the subject

DÉCISION DU JURY, MENTION ACCORDÉE :

~~Honorable~~

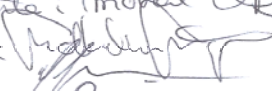
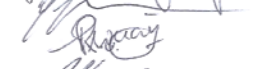
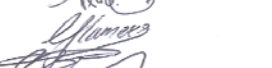
Très honorable

Le conseil de l'Ecole Doctorale a décidé qu'à compter du 1er avril 2007 la mention "très honorable avec félicitations" n'est plus attribuée pour les thèses de l'Ecole Polytechnique

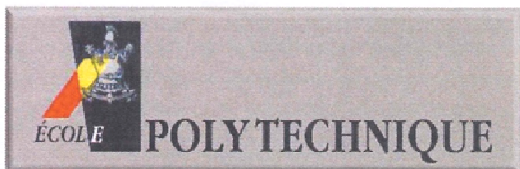
(2) Si nécessaire, utiliser le verso

Mr KIM was very prepared to answer all the questions which ranged over many different topics, from plasma physics to materials science and solar cell operation, a further proof of his maturity, depth and broad knowledge in the subject. The jury was further impressed by the number of experiments Mr. KIM performed, as well as his creativity in the analysis and interpretation. His independent thinking and honesty in his presentation and answers was also much appreciated.

For all these reasons the members of the jury delivered him the Doctorate Grade with "Tres Honorabile" distinction.

Anna Fontcaldevila i Mompal   
Friedrich Fricke   
Erik Johnson   
René van Swaaij   
Edward Hamers   
LARS OBERBECK 

Laiifa BOUFENDI   
Pae Noca Cabaneros 



## AVIS DU JURY SUR LA REPRODUCTION DE LA THÈSE

Nom, Prénom de l'auteur : KIM, Ka-Hyun

Titre de la thèse : Hydrogenated polymorphous silicon: establishing the link between microstructure and irreversible solar cell kinetics during light soaking.

Date de soutenance de thèse :

9 Oct. 2012

Composition du jury :

Président : Dr. Anna Fontcuberta i Morral

Rapporteurs : Anna Fontcuberta i Morral

Laila Boufendi

Membres : Friedhelm Finger

Edward A.G. Hamers

Lars Oberbeck

René ACM van Swaaij

Pere Roca i Cabarrocas

Erik V. Johson.

Reproduction de la thèse soutenue :

- Thèse pouvant être reproduite en l'état  
 Thèse pouvant être reproduite après corrections  
 Thèse ne pouvant pas être reproduite

Signature du Président du jury

Cet imprimé doit être retourné après signature avec le rapport de soutenance à la Direction de l'École Doctorale



## Acknowledgments

For the past three years, this thesis would not have been possible without the support of many people. I thank to Vincent Schachter, Marc Vermeersch, and Loïc Francke for welcoming me into TOTAL-LPICM joint research team and for supporting from industry side. I thank to Lars Oberbeck for accepting jury for my PhD defense and continuous supporting. I deeply appreciate all the members of juries, Prof. Anna Fontcuberta i Morral, Prof. Laifa Boufendi, Friedhelm Finger, Edward A. G. Hamers, and René A.C.M.M. van Swaaij.

The deepest gratitude is due to my director, Prof. Pere Roca i Cabarrocas for his invaluable support and guidance. I also express my gratitude to Prof. Jin Jang, Prof. Yvan Bonnassieux, Erik V. Johnson, Samir Kasouti, and Alexey Abramov. Since my master program, they have been my mentors and directors, and it is impossible to imagine my PhD thesis without their help, support and guidance.

I am proud of that I am one of the earliest members of TOTAL-LPICM joint research team, and I appreciate everyone in “les algecos”, Martin Labrune, Antoine Salomon, Patricia Prod'homme, Jérôme Damon-Lacoste, Coralie Charpentier, Jean-Francois Besnier, Ludovic Hudanski, Guillaume Courtois, Nada Habka, Jean-Christophe Dornstetter, Igor Sobkowicz, and Bastien Bruneau. I confess that les algecos have been the world's happiest and the funniest workplace thank to those colleagues.

I am grateful to Benedict O'Donnell, Romain Cariou, Alfonso Torres-Rios, Changseok Lee, Kihwan Kim, Jinyoun Cho, Mun-Ho Song, Taewoo Jeon, Chang-Hyun Kim, Jongwoo Jin, Youn-Ho Heo, Pavel Bulkin, Tatiana Novikova, Rosa Ruggeri, Sofia Gaiaschi, Rym Boukhicha, Parsathi Chatterjee, Dmitri Daineka, Bicher Haj Ibrahim, Sergey Abolmasov, Maher Oudwan, Mario Moreno, Sanjay Ram, Linwei Yu, and Junzhuan Wang, with whose great knowledge, literature and discussion, my PhD thesis could be completed.

Also special thanks to all laboratory members, Rosaria Antonelli, Laurent Baraton, Rachida Boubekri, Jean-Eric Bouree, Marc Chaigneau, Jerome Charliac, Frederic Farci, Enric Garcia-Caurel, Bernard Geffroy, Cyril

Jadaud, Laurent Kroely, Emmanuel Lefeuvre, Frederic Liege, Joaquim Nassar, Razvigor Ossikovski, Eric Paillassa, Jacqueline Samson, Denis Tondelier, Holger Vach, Jean-Charles Vanel, Omid Yaghmazadeh, Joonwon Lim, Yong-Bin Jeong, Myung-Jin Lim, Taeha Hwang, Kihwan Seok, Jinwoo Choi, Hojoong Kwon, Sungyeop Jung, and Heechul Woo.

At last, I wish to express my love and gratitude to my beloved family and *ma chérie*, Kyoungsoon.

# Contents

Acknowledgments.....	<b>ix</b>
Contents .....	<b>xi</b>
List of Figures.....	<b>xiii</b>
List of Tables .....	<b>xix</b>
List of Abbreviations and Symbols .....	<b>xxi</b>
Chapter 1 – Backgrounds.....	<b>23</b>
1.1 Introduction.....	24
1.2 Plasma enhanced chemical vapor deposition .....	24
1.3 Hydrogenated amorphous silicon.....	27
1.4 Staebler-Wronski effect .....	28
1.5 Hydrogenated polymorphous silicon.....	31
1.6 Material and device characterization .....	33
1.6.1 Spectroscopic Ellipsometry and Modelling .....	35
1.6.2 UV-VIS Transmission-Reflection .....	36
1.6.3 Sub-gap absorption measurements.....	38
1.6.4 Fourier transform infrared spectroscopy .....	39
1.6.5 Hydrogen exodiffusion .....	41
1.6.6 Dark conductivity.....	42
1.6.7 Atomic Force Microscopy and Scanning Electron Microscopy.....	44
1.6.8 Diode dark J(V) .....	46
1.6.9 Solar cell parameters .....	48
Chapter 2 – Hydrogenated Polymorphous Silicon – Material.....	<b>54</b>
2.1 Introduction.....	56
2.2 ARCAM reactor .....	56
2.3 a-Si:H and pm-Si:H deposition.....	59
2.4 Gas flow rate series.....	67
2.5 Pressure series .....	70
2.6 RF power series.....	74
2.7 Ts series.....	79
2.8 Powder formation and residence time .....	85

2.9 Summary .....	89
<b>Chapter 3 – Hydrogenated Polymorphous Silicon Solar Cells.....</b>	<b>97</b>
3.1 Introduction.....	98
3.2 Standard PIN solar cells.....	98
3.3 Effect of light-trapping .....	106
3.4 Intrinsic layer optimization.....	107
3.5 HR pm-Si:H PIN solar cells.....	113
3.6 Stability issues of PIN solar cells.....	119
3.7 Summary .....	123
<b>Chapter 4 – Light-Induced Degradation and Solar Cell Stability ...</b>	<b>125</b>
4.1 Introduction.....	126
4.2 PIN solar cell device stability – initial behavior .....	126
4.3 Light-induced structural changes .....	144
4.4 Light-induced hydrogen motion .....	160
4.5 Hypothesis on light-induced changes .....	171
4.6 Long-term stability and new device structure .....	174
4.7 Summary .....	181
<b>Chapter 5 – Prospective – Towards High Stabilized Efficiency.....</b>	<b>189</b>
5.1 Introduction.....	190
5.2 p-type $\mu\text{-SiO}_x$ .....	190
5.3 pm-Si:H NIP solar cells using p-type $\mu\text{-SiO}_x$ .....	200
5.4 Stable pm-Si:H NIP solar cells.....	210
5.5 Summary .....	212
<b>Conclusion and perspectives .....</b>	<b>215</b>
<b>Annex .....</b>	<b>221</b>
<b>List of publications .....</b>	<b>237</b>

# List of Figures

Figure 1.1 – (a) Schematic view of the potential distribution in a RF discharge where the RF voltage is applied to the RF electrode, with dielectric substrate, and (b) time-dependent sheath voltages .....	26
Figure 1.2 – Absorption coefficient ( $\alpha$ ) versus the photon energy measured by various measurement techniques, such as FTIR, PDS or CPM, UV-VIS TR and SE. ....	34
Figure 1.3 – Example of SE modeling. (a) The fitting result of a measured SE spectrum of pm-Si:H on glass and its model. (b) The model structure. The model consists of a bulk layer and surface roughness.....	36
Figure 1.4 – Example of the determination of $E_{Tauc}$ . (a) A UV-VIS-IR Transmission spectrum of pm-Si:H and (b) Tauc plot of a-Si:H and pm-Si:H on glass substrate.....	37
Figure 1.5 – Photothermal deflection spectroscopy (PDS) spectra of a-Si:H and pm-Si:H .....	39
Figure 1.6 – FTIR stretching modes peak of (a) a-Si:H and (b) pm-Si:H PIN layer stacks and the deconvolution. Note that stretching mode peak of pm-Si:H consists of a MSM at $2030\text{ cm}^{-1}$ .....	40
Figure 1.7 – Hydrogen exodiffusion spectra of a-Si:H and pm-Si:H PIN layer stacks deposited on glass substrate.....	42
Figure 1.8 – Arrhenius plot of the temperature dependent dark conductivity of intrinsic a-Si:H, pm-Si:H, and $\mu\text{c-Si:H}$ layers. $E_a$ and the conductivity at room temperature can be extracted from the extrapolation. ....	44
Figure 1.9 – (a) AFM and (b) SEM images of surface morphology of pm-Si:H PIN solar cell on textured Asahi. ....	46
Figure 1.10 – Dark $J(V)$ curves of good and bad pm-Si:H PIN diodes. Extrapolation from the linear region of the forward bias shows the different dark $J(V)$ parameters for different PIN diode quality. ....	48
Figure 1.11 – An equivalent circuit of a solar cell. An ideal solar cell consists of a current source connected in parallel with a rectifying diode, $R_s$ and $R_{SH}$ .....	48
Figure 1.12 – An example of solar cell $J(V)$ curve. $J_{sc}$ , $V_{oc}$ , $FF$ , $P_{max}$ are marked.....	50
Figure 2.1 – Photo of ARCAM reactor and inside of vessel. Three plasma chambers are seen.....	58
Figure 2.2 – Schematic view of one of the plasma boxes used in ARCAM. ....	59
Figure 2.3 – Electron-induced dissociative-excitation of $\text{SiH}_4$ molecules upon electron impact. All the species are produced spontaneously from electronic excited states via a one-electron-impact dissociation pathway .....	60
Figure 2.4 – Schematic of processes of a $\text{SiH}_3$ radical on growing a-Si:H surface .....	61
Figure 2.5 – Schematic of the process of powder formation in silane plasmas .....	64
Figure 2.6 – QMS scanned molecular mass distribution of (a) a-Si:H and (b) pm-Si:H deposition condition at plasma on/off condition. Note that in pm-Si:H deposition condition, higher-order silane species such as $\text{Si}_2\text{H}_x$ and $\text{Si}_3\text{H}_x$ are observed.....	66
Figure 2.7 – Representative results of gas flow series. (a) QMS analysis of signal intensity ratio of $\text{Si}_2\text{H}_x$ to $\text{SiH}_x$ and $\text{Si}_3\text{H}_x$ to $\text{SiH}_x$ as functions of gas flow ratio $R$ , and (b) $r_d$ and surface roughness as functions of $\text{SiH}_4$ flow .....	69
Figure 2.8 – $r_d$ , SE surface roughness, and AFM measured RMS roughness as functions of	

deposition pressure. Calculated residence time at each pressure is marked at top. Typical values for a-Si:H are also given as reference .....	71
Figure 2.9 – AFM images and its cross-section of (a) standard a-Si:H, (b) pm-Si:H deposited at 2 Torr, and (c) pm-Si:H deposited at 4 Torr. Note that at higher pressure, larger surface features and rougher surface is observed. Note that the size of the bumps cannot be attributed to individual nanoparticles (a few nanometers) .....	72
Figure 2.10 – Hydrogen exodiffusion spectra of a set of pm-Si:H films deposited under different pressure from 2 to 5 Torr .....	73
Figure 2.11 – $r_a$ , surface roughness and microstructure parameter R as functions of RF power. DC bias on the RF electrode is marked at top. Typical values for a-Si:H are also given as reference ...	75
Figure 2.12 – (a) FTIR stretching mode spectra of pm-Si:H under various RF power and (b) hydrogen content calculated from (a). Note that stretching mode peak shifts towards higher wavenumbers with higher RF power. Hydrogen content of a-Si:H is marked as cross. (c) FTIR stretching mode absorption spectra of a-Si:H films deposited by PECVD (solid) and magnetron sputtering (dashed lines). Spectra are shown in pairs to compare features for samples with hydrogen content of 7, 13, 20, and 24 at.% .....	77
Figure 2.13 – Demonstrations of stretching mode deconvolution of spectra shown in Figure. 2.12(a). In (a), (c), and (e), the spectra are deconvoluted into classical two modes. In this case, both LSM and HSM show peak shift. In (b), (d), and (f), the spectra are deconvoluted into three modes including MSM at 2030 $\text{cm}^{-1}$ . It is shown that the stretching mode peak shift can be attributed to the evolution of MSM mode .....	78
Figure 2.14 – $r_a$ , surface roughness and optical bandgap as functions of $T_s$ .....	81
Figure 2.15 – Effect of substrate temperature on hydrogen incorporation in pm-Si:H. (a) Hydrogen exodiffusion spectra of pm-Si:H deposited at different $T_s$ from 175 °C to 275 °C, and (b) hydrogen content in pm-Si:H and microstructure parameter R as functions of $T_s$ as deduced from FTIR study .....	82
Figure 2.16 – Evolution of normalized photoconductivity as a function of light-soaking time for pm-Si:H films deposited at different $T_s$ .....	83
Figure 2.17 – (a) FTIR transmission spectra in Si-O-Si stretching mode region of $T_s$ series and (b) Activation energy, room temperature conductivity of $T_s$ series .....	80
Figure 2.18 – SIMS profile of hydrogen and oxygen content of a RF power series of pm-Si:H deposited on FZ c-Si .....	86
Figure 2.19 – (a) SIMS profile of residence time series. Total pressure and gas flow ratio is fixed, while only gas flow is changed. (b) O and H content from (a) as functions of calculated residence time .....	87
Figure 2.20 – (a) Optical bandgap, $E_{opt}$ , versus $r_d$ of different pressure, RF series of pm-Si:H. (b) Tauc plot of one of the RF series in (a). (c) Hydrogen content, $C_H$ , versus $r_a$ .....	89
Figure 3.1 – SEM image of the cross-section of a pm-Si:H PIN solar cell deposited on textured $\text{SnO}_2$ substrate and its schematic drawing. In SEM image, silicon layers appear dark due to the low conductivity .....	99
Figure 3.2 – Initial dark J(V) characteristics of a-Si:H and pm-Si:H PIN solar cells. Ideality factor and $J_0$ can be extracted from the extrapolation of forward bias region. Note that intrinsic layer	

thickness was about 3000 Å.....	104
Figure 3.3 – Initial characteristics of a-Si:H and pm-Si:H PIN solar cells. (a) J(V) curve and (b) external quantum efficiency. Note that intrinsic layer thickness was about 3000 Å, and Al back-contact was used.....	105
Figure 3.4 – Initial characteristics of a pm-Si:H PIN solar cell with different back reflector of Al and ITO/Ag. (a) J(V) curve and (b) external quantum efficiency. Note that intrinsic layer thickness was about 3300 Å.....	108
Figure 3.5 – Initial characteristics of a pm-Si:H PIN solar cells deposited under various gas flow. Note that intrinsic layer thickness was about 3000 Å, Al back contact are used .....	110
Figure 3.6 – SIMS profile of hydrogen and oxygen content for different gas flow in intrinsic pm-Si:H deposition condition. Note that entire layer stack is deposited on FZ c-Si wafer, and a-Si:H was also deposited as a reference .....	111
Figure 3.7 – Initial characteristics of an optimized pm-Si:H PIN solar cell (a) J(V) curve and (b) external quantum efficiency. Intrinsic layer thickness was about 2500 Å, and ITO/Ag was used as back reflector .....	112
Figure 3.8 – EQE of various pm-Si:H PIN solar cells. pm-Si:H PIN solar cells deposited at 210 °C are indeed HR pm-Si:H solar cells with Ag back-reflector that shown in Table 3.7. pm-Si:H PIN solar cell deposited at 175 °C is one with ITO/Ag shown in Table 3.6.....	115
Figure 3.9 – Initial fill factor of pm-Si:H PIN solar cells versus optical bandgap ( $E_{opt}$ ) of various pm-Si:H PIN solar cells. Note that the $E_{opt}$ is also a consequence of $\tau_r$ , so $\tau_r$ is also marked on the plot. There is a general trend in $\tau_r$ - $E_{opt}$ - $FF$ , in which pm-Si:H having high $FF$ come from low $\tau_r$ . $FF$ - $E_{opt}$ relation of HR pm-Si:H shows a little shift from std pm-Si:H series probably due to high $T_s$ (210 °C) .....	116
Figure 3.10 – Initial characteristics of HR pm-Si:H PIN solar cells deposited at 10 Å/s and 20 Å/s. The PIN at 20 Å/s was annealed at 160 °C for two hours, while the PIN at 10 Å/s was annealed at 150 °C for 30 minutes in order to avoid Ag diffusion.....	119
Figure 3.11 – Evolution of solar cell parameters of PIN solar cells using different intrinsic layers, (a) $\eta$ , (b) $FF$ , (c) $V_{oc}$ , and (d) $J_{sc}$ during LS under an illumination of 1 sun. The PIN solar cells were light-soaked and measured the J(V) curve by non-filtered Oriel-Apex Xe lamp.....	121
Figure 4.1 – Evolution of a-Si:H and pm-Si:H PIN solar cell parameters. (a) $\eta$ , (b) $FF$ , (c) $V_{oc}$ , and (d) $J_{sc}$ during light-soaking under an illumination of 200 mW/cm <sup>2</sup> .....	128
Figure 4.2 – Evolution of a-Si:H and pm-Si:H PIN solar cell parameters: (a) $\eta$ , (b) $FF$ , (c) $V_{oc}$ , and (d) $J_{sc}$ during LS under an illumination of 1 sun. Note that every 10 hours LS was interrupted and the solar cells were annealed at 160 °C for 2 hours in order to check for the reversibility of the light-soaking effect. Note that the error bars indicate temperature dependent ( $\pm 7.5$ °C) variation of solar cell parameters .....	131
Figure 4.3 – EQE curves of both a-Si:H and pm-Si:H PIN solar cells in their as-deposited, light-soaked, and annealed states .....	134
Figure 4.4 – Normalized efficiency of a-Si:H and pm-Si:H PIN solar cells as functions of LS time and fit to the model .....	137
Figure 4.5 – Evolution of a-Si:H and pm-Si:H PIN solar cell parameters under yellow illumination: (a) $\eta$ , (b) $FF$ , (c) $V_{oc}$ , and (d) $J_{sc}$ during LS of band-pass filtered 570 nm illumination. Note that the	

LS intensity was about 40 mW/cm<sup>2</sup>, and J(V) curves are measured under white light of 100 mW/cm<sup>2</sup>. The intrinsic layer thickness of PIN solar cells is 3000 Å ..... 139

Figure 4.6 – Evolution of a-Si:H and pm-Si:H PIN solar cell parameters: (a)  $\eta$ , (b)  $FF$ , (c)  $V_{oc}$ , and (d)  $J_{sc}$  during LS under an illumination of 1 sun and healing. Note that after 90 minutes of LS, the PIN solar cells are left in the dark for another 90 mins. At last, the PIN solar cells were again light-soaked for another 90 minutes. The intrinsic layer thickness of PIN solar cells is 5000 Å... 141

Figure 4.7 – Evolution of Raman spectra during LS of (a) a-Si:H and (b) pm-Si:H PIN solar cells, and (c) Raman spectrum of as-deposited pm-Si:H PIN solar cell and its deconvolution ..... 146

Figure 4.8 – Evolution of TO peak position during light-soaking. Note that on some samples we have checked that these material properties did not change after turning off the light ..... 146

Figure 4.9 – AFM images of a-Si:H and pm-Si:H PIN layer stacks on Corning Eagle glass before (a, c) and after (b, d) LS, and (e) mean surface grain area evolution during LS, as extracted from AFM images. Note that no evolution is observed for the a-Si:H PIN layer stacks, and that the evolution for the pm-Si:H PIN layer stacks stops when the LS is turned off..... 148

Figure 4.10 – (a) Demonstration of zone selection for AFM images to follow changes in area of individual grains, and (b) average surface area evolution of selected grains during LS of pm-Si:H PIN layer stacks ..... 149

Figure 4.11 – SEM images of pm-Si:H PIN solar cell surface when deposited on flat ZnO:Al : (a) as-deposited, and (c) LS for 16 hours. (inset b, d) AFM image of surface shown in Figure..... 151

Figure 4.12 – An AFM image of a pm-Si:H PIN solar cell on textured Asahi substrate after 100 hours of LS and (b) cross-sectional profile measurement through center of hole showing a depth of film thickness ..... 151

Figure 4.13 – Optical images of a-Si:H and pm-Si:H PIN layer stacks at various stages of current-injection degradation (CID). CID condition was done for 200 mins under 300 mA/cm<sup>2</sup>, and it is equivalent to the LS of 500 hrs under 1 sun illumination ..... 154

Figure 4.14 – An AFM image of a pm-Si:H PIN solar cell on Cr/glass substrate after CID and (b) cross-sectional profile measurement through center of bubble shown in Figure 4.13. CID condition was done for 200 mins under 300 mA/cm<sup>2</sup>, and it is equivalent to the LS of 500 hrs under 1 sun illumination ..... 156

Figure 4.15 – Summary of SE modeling of pm-Si:H PIN layer stacks before and after LS of 500 hrs. (a) the structure of the optical model, (b) optical bandgap ( $E_{opt}$ ) and raw  $\epsilon_2$  spectra (inset), and (c) modeled refractive index before/after LS. The sample was light-soaked under Mercury lamp illumination and the intensity was about 0.7 sun ..... 156

Figure 4.16 – Absorption coefficient spectra of FTIR stretching modes of (a) a-Si:H and (c) pm-Si:H PIN layer stacks on intrinsic FZ wafer and their zoom-in to the peak (b, d). The spectra are extracted from infrared transmission at four light-soaking (LS) states: as-deposited (black), after one hour of LS (red), after 5 hours (blue) and after 20 hours (green)..... 161

Figure 4.17 – Hydrogen exodiffusion spectra of co-deposited (a) a-Si:H and (b) pm-Si:H PIN layer stacks for different light-soaking (LS) states. Note that the pm-Si:H PIN layer stack shows abrupt disappearance of the peak around 350 °C even after 1 hour of LS, while there is only small change in a-Si:H PIN layer stack ..... 164

Figure 4.18 – Schematic representation of proposed mechanism for structural defect formation

through localized delamination. In the as-deposited state (a), a weak film/substrate interface is due to the pm-Si:H deposition conditions. Light-soaking (b) introduces volume changes, stress relaxation, and nanovoids agglomerate into larger ones. Molecular hydrogen in the material becomes mobile and diffuses to the interface where it forms hydrogen cavities (c). The delamination continues to release built-in “compressive” stress, and the stress relaxation eventually results in the formation of macroscopic defects such as bubbles and holes (d), as well as the accumulation of hydrogen at the interface ..... 173

Figure 4.19 – Evolution of solar cell parameters of selected PIN and NIP solar cells summarized in Table 4.4: (a)  $\eta$ , (b)  $FF$ , (c)  $V_{oc}$ , and (d)  $J_{sc}$  during LS under an Hg lamp illumination. Note that multiple individual solar cells on  $2.5 \times 2.5$  cm<sup>2</sup> substrate are measured and the solar cell parameters are averaged. The maximum and minimum values are reflected in error bars. Al is used as back-reflector in PIN solar cells except the state-of-art reference sample, and ITO is used in NIP..... 176

Figure 4.20 – Optical images of pm-Si:H PIN and NIP solar cells as deposited (a, c) and light-soaked (b, d). There are large macroscopic changes in the pm-Si:H PIN solar cell, resulting in a loss of the actual solar cell area, while NIP solar cell shows no visible changes ..... 178

Figure 4.21 – The  $J_{sc}$  loss as a function of the area loss, in the PIN case represented in Figure 4.19 and 4.20. The loss of  $J_{sc}$  shows clear proportionality to the area loss..... 179

Figure 4.22 – Hydrogen exodiffusion results of pm-Si:H NIP solar cells for three states : as-deposited (black), after one hour of LS (red), and after 20 hours (blue). The NIP structure shows no significant change in exodiffusion signal as well as no delamination ..... 181

Figure 5.1 – Raman spectra of p-type  $\mu\text{-SiO}_x$  layers deposited with different CO<sub>2</sub> flow. A transition from crystalline ( $520\text{ cm}^{-1}$ ) to amorphous ( $480\text{ cm}^{-1}$ ) when varying CO<sub>2</sub> flow is notably seen..... 192

Figure 5.2 – SE spectra of various p-type layers. p-type  $\mu\text{-SiO}_x$  deposited with two different CO<sub>2</sub> flows, 2 and 3 sccm are also shown..... 193

Figure 5.3 – (a) Evolution of SiO<sub>2</sub>,  $\mu\text{-Si}$ , and a-Si volume fractions of p-type  $\mu\text{-SiO}_x$  as functions of CO<sub>2</sub> flow deduced from BEMA method, (b) structure of optical model, and (c) Raman crystalline fraction  $X_c$  and SE top layer crystalline fraction  $X_c$  versus thickness of fully crystallized bottom layer ..... 194

Figure 5.4 – Absorption coefficient of various p-type layers. p-type  $\mu\text{-SiO}_x$  deposited with two different CO<sub>2</sub> flow, 2 and 3 sccm are also shown.  $E_{04}$  can be extracted at the energy where  $\alpha=10^4$  ..... 197

Figure 5.5 –  $E_{04}$  from transmission measurement and SiO<sub>2</sub> fraction deduced from SE modeling as functions of CO<sub>2</sub> flow. Note that  $E_{04}$  and SiO<sub>2</sub> fraction show strong correlation..... 197

Figure 5.6 – Arrhenius plots of various p-type layers. p-type  $\mu\text{-SiO}_x$  deposited with two different CO<sub>2</sub> flows, 2 and 3 sccm are also shown. Activation energy ( $E_a$ ) can be extracted from the slopes of the plots ..... 199

Figure 5.7 –  $E_a$  and  $\sigma_{RT}$  from  $\sigma(T)$  measurement and  $\mu\text{-Si}$  fraction ( $X_c$ ) deduced from SE modeling as functions of CO<sub>2</sub> flow. Note that  $E_a$ ,  $\sigma_{RT}$  and  $\mu\text{-Si}$  fraction show strong correlation ..... 200

Figure 5.8 – Initial characteristics of a pm-Si:H NIP solar cell using p-type  $\mu\text{-SiO}_x$  (a)  $J(V)$  curve and (b) external quantum efficiency. The intrinsic layer thickness was about  $2500\text{ \AA}$ , and NIP solar cell is deposited on textured Asahi. Thickness of p  $\mu\text{-SiO}_x/\mu\text{-Si:H}$  bi-layer is  $280\text{ \AA}$  ..... 203

Figure 5.9 – Evolution of pm-Si:H NIP solar cell parameters as functions of intrinsic layer thickness: (a)  $\eta$ , (b)  $FF$ , (c)  $V_{oc}$ , and (d)  $J_{sc}$ . Note that initial and stabilized solar cell parameters are shown together. For the stabilization, the NIP solar cells are light-soaked under 1 sun of Hg lamp for 500 h, and J(V) curves are measured under 100 mW/cm<sup>2</sup> of simulated AM1.5 spectrum. Thickness of p  $\mu\text{-SiO}_x/\mu\text{-Si:H}$  bi-layer is 280 Å..... 205

Figure 5.10 – Evolution of pm-Si:H NIP solar cell parameters as functions of p-type  $\mu\text{-SiO}_x$  layer thickness: (a)  $\eta$ , (b)  $FF$ , (c)  $V_{oc}$ , and (d)  $J_{sc}$ . Note that initial and stabilized solar cell parameters are shown together. For the stabilization, the NIP solar cells are light-soaked under 1 sun of Hg lamp, and J(V) curves are measured under 100 mW/cm<sup>2</sup> of AM1.5 spectrum. Thickness of p  $\mu\text{-Si:H}$  layer is 100 Å ..... 207

Figure 5.11 – Evolution of EQE curves of pm-Si:H NIP solar cells with different p-type  $\mu\text{-SiO}_x$  layer thickness. Thickness of p  $\mu\text{-Si:H}$  layer is 100 Å. Interestingly,, the decrease of the p-type layer thickness enhances both short and long wavelength regions ..... 208

Figure 5.12 – Initial, stabilized and annealed (at 160 °C for 2 hrs) characteristics of an optimized pm-Si:H NIP solar cell (a) J(V) and (b) EQE curves. Intrinsic layer thickness was about 2500 Å 205

Figure 5.13 – Evolution of solar cell parameters of selected PIN and NIP solar cells (a)  $\eta$ , (b)  $FF$ , (c)  $V_{oc}$ , and (d)  $J_{sc}$  during LS under an Hg lamp illumination. Note that various individual solar cells (up to six) on the 2.5×2.5 cm<sup>2</sup> substrates were measured and the solar cell parameters are averaged. The maximum and minimum values are reflected in error bars. Al is used as back-reflector in PIN solar cells, and ITO is used in NIP. After the LS, the cells are annealed (at 160 °C for 2 hrs) and checked for reversibility of the light-induced degradation..... 211

# List of Tables

Table 1.1 – Typical SE modeling parameters of a-Si:H and pm-Si:H .....	36
Table 1.2 – Material parameters deduced from sub-gap absorption PDS spectra in Figure 1.5. $E_u$ , $N_D$ , and $E_{04}$ of a-Si:H and pm-Si:H .....	39
Table 1.3 – The deconvolution result of Figure 1.6.....	41
Table 2.1 – Fitting parameters of the FTIR stretching mode deconvolution in Figure. 2.13. Note that in three peaks deconvolution each peak positions are fixed.....	79
Table 2.2 – Controllable plasma parameters and their benefits, drawbacks and solutions. Note that most of the case, the drawbacks are powder formation, and solutions are indeed trade-off of each other cause-and-effects.....	91
Table 3.1 – Deposition condition and physical properties of the standard PIN solar cells components .....	102
Table 3.2 – Ideality factor $n$ and $J_0$ of a-Si:H and pm-Si:H PIN solar cells in Figure 3.2. Dark diode parameters are extracted from the extrapolation of forward bias region.....	104
Table 3.3 – Solar cell parameters of PIN solar cells shown in Figure 3.3 .....	105
Table 3.4 – Solar cell parameters of PIN solar cells shown in Figure 3.4 .....	108
Table 3.5 – Gas flow and SE modeling parameters from pm-Si:H PIN solar cells deposited in three different intrinsic layer conditions. Note that the three pm-Si:H PIN solar cells are having identical substrates (Textured SnO <sub>2</sub> :F and corning glass), both p and n-type layers, and Al back contacts. For the intrinsic layer deposition condition, only gas flow and total flow were varied while total pressure, RF power, and T <sub>s</sub> were fixed at 2 Torr, 5 W, and 175 °C, respectively.....	109
Table 3.6 – Solar cell parameters of PIN solar cells shown in Figure 3.5. Oxygen content deduced from Figure 3.6 is also marked. Note that multiple individual solar cells on 2.5×2.5 cm <sup>2</sup> substrate are measured and the solar cell parameters are averaged. Al back-contact was used .....	110
Table 3.7 – Gas flow and SE modeling parameters from HR pm-Si:H PIN solar cells deposited in five different intrinsic layer conditions. Note that the five HR pm-Si:H PIN solar cells are having identical substrates (Textured SnO <sub>2</sub> :F and corning glass), both p and n-type layers, and Ag back contacts. For the intrinsic layer deposition condition, only gas flow was varied while total pressure, RF power, and T <sub>s</sub> were fixed to 3 Torr, 30 W, and 210 °C, respectively .....	114
Table 3.8 – Solar cell parameters of HR pm-Si:H PIN solar cells shown in Figure 3.7. Note that multiple individual solar cells on 2.5×2.5 cm <sup>2</sup> substrate are measured and the solar cell parameters are averaged. Ag back-contacts are used .....	114
Table 3.9 – Process conditions of pm-Si:H PIN solar cells. From 10 to 20 Å/s condition, silane concentration ratio, RF power was increased. At the same time, pressure was lowered and T <sub>s</sub> was increased in order to suppress powder formation.....	118
Table 3.10 – Solar cell parameters of HR pm-Si:H PIN solar cells in Figure 3.10. Note that multiple individual solar cells on 2.5×2.5 cm <sup>2</sup> substrate are measured and the solar cell parameters are averaged. Ag back-contact is used in 10 Å/s PIN, and Al back-contact is used in 20 Å/s PIN.....	119
Table 3.11 – Solar cell parameters extracted from light-soaking test in Figure 3.11. Degradation, $\Delta\eta$ and intrinsic layer thickness, $d_i$ are also marked. Note that low light-induced degradation of HR	

pm-Si:H PIN solar cells compared to a-Si:H and 1.5 Å/s pm-Si:H PIN solar cells are indeed due to the low initial efficiency. The stabilized efficiency is a consequence of both initial efficiency and  $\Delta\eta$  ..... 122

Table 4.1 – Fitting parameters of modeling in Figure 4.4.  $y_0$  is estimated stabilized efficiency,  $A_I$  is magnitude of degradation,  $\tau$  decides an inflection point of the defect creation, and  $\beta$  is a broadening term, which characterize the “stretched” nature of the expression ..... 137

Table 4.2 – Fitting parameters of Tauc-Lorentz dispersion model of Figure 4.15.  $E_{opt}$  is the optical bandgap,  $E_0$  is peak-to-peak transition energy, whereas A and C are fitting parameters related to the film density and the disorder ..... 159

Table 4.3 – Peak positions and integrated areas extracted from exodiffusion results of Figure 4.17. Data are presented for co-deposited pm-Si:H cell layer stacks in the as-deposited state and after two light-soaking times ( 1 hour, and 20 hours) ..... 166

Table 4.4 – Process conditions of various PIN and NIP solar cells. The intrinsic layers of PIN solar cells were deposited at various RF power, and some PIN solar cells had same material properties with different intrinsic layer thickness ..... 174

Table 5.1 – Summary of the deposition conditions of p-type  $\mu\text{-SiO}_x$ ..... 191

Table 5.2 – Solar cell parameters of an optimized pm-Si:H NIP solar cell from Figure 5.12..... 209

## List of Abbreviations and Symbols

Acronym		Unit
AFM	Atomic force microscopy	
a-Si:H	Hydrogenated amorphous silicon	
a-SiC:H	Hydrogenated amorphous silicon carbon	
$C_H$	Hydrogen content	at. %
CVD	Chemical vapor deposition	
$d_i$	Intrinsic later thickness	Å or nm
$E_g$	Bandgap	eV
$E_{opt}$	Optical bandgap	eV
$E_{Tauc}$	Tauc optical bandgap	eV
$FF$	Fill factor	
FTIR	Fourier transform infrared spectroscopy	
HR	High deposition rate	
ITO	Indium tin oxide	
$J(V)$	Current density to voltage characteristics	
$J_o$	Diode reverse saturation current density	mA/cm <sup>2</sup>
$J_{sc}$	Short-circuit current density	mA/cm <sup>2</sup>
LS	Light-soaking	
$n$	Diode ideality factor	
nc-PSi	Nanocrystalline porous silicon	
$N_D$	Defect density	#cm <sup>-3</sup>
pc-Si:H	Hydrogenated protocrystalline silicon	
PECVD	Plasma enhanced chemical vapor deposition	
pm-Si:H	Hydrogenated polymorphous silicon	
PVD	Physical vapor deposition	
QMS	Quadrupole mass spectrometer	
$R_s$	Series resistance	Ωcm <sup>2</sup>
$R_{SH}$	Shunt resistance	Ωcm <sup>2</sup>
sccm	Standard cubic centimeter per minute	
SE	Spectroscopic ellipsometry	
SIMS	Secondary ion mass spectrometry	
SWE	Staebler-Wronski effect	
TCO	Transparent conducting oxide	
TR	Transmission-reflection	
$T_s$	Substrate temperature	°C
$r_d$	Deposition rate	
$V_{oc}$	Open-circuit voltage	V
$\tau_r$	Residence time	s
μc-Si:H	Hydrogenated microcrystalline silicon	
μc-SiO <sub>x</sub>	Microcrystalline silicon oxide	
$\mu_H$	Hydrogen chemical potential	



# Chapter 1

## Background

1.1 Introduction.....	24
1.2 Plasma enhanced chemical vapor deposition .....	24
1.3 Hydrogenated amorphous silicon.....	27
1.4 Staebler-Wronski effect .....	28
1.5 Hydrogenated polymorphous silicon .....	31
1.6 Material and device characterization .....	33
1.6.1 Spectroscopic Ellipsometry and Modelling.....	35
1.6.2 UV-VIS Transmission-Reflection.....	36
1.6.3 Sub-gap absorption measurements .....	38
1.6.4 Fourier transform infrared spectroscopy.....	39
1.6.5 Hydrogen exodiffusion .....	41
1.6.6 Dark conductivity.....	42
1.6.7 Atomic Force Microscopy and Scanning Electron Microscopy .....	44
1.6.8 Diode dark J(V) .....	46
1.6.9 Solar cell parameters .....	48

### 1.1 Introduction

This chapter introduces general background information for readers. Basic knowledge on plasma enhanced chemical vapor deposition, hydrogenated amorphous silicon and polymorphous silicon, Staebler-Wronski effect, material and device characterization such as spectroscopic ellipsometry and model, UV-VIS-IR transmission-reflection, sub-gap absorption measurements (PDS, CPM), Fourier transform infrared absorption, hydrogen exodiffusion, dark conductivity, atomic force microscope and scanning electron microscope, diode dark  $J(V)$ , solar cell parameters will be briefly presented, and reference textbooks with more detail will be cited.

### 1.2 Plasma enhanced chemical vapor deposition

Plasma enhanced chemical vapor deposition (PECVD) is a thin film fabrication method based on the dissociation of gas molecules by electron impact in an electrical discharge, instead of thermal dissociation (CVD). In PECVD, the dissociation of a precursor gas and the surface reactions of ionized species are controlled by the plasma. Since electron temperature of a low-pressure discharge is high enough ( $\sim 2\text{--}5\text{ V}$ ) for dissociation, the deposition can be carried out at substrate temperatures ( $T_s$ ) much lower than for pure CVD. Such low  $T_s$  allows large area electronic applications on cheap substrates. Process pressure is usually higher than that used in reactive-ion-etching because secondary reactions between radical species are often desired in PECVD. The process pressures used in this thesis covers the range from 45 to 5000 mTorr. Therefore, mean free paths of radical species are small, of order 0.003–0.3 mm. The plasma densities are in the range from  $10^9\text{--}10^{11}\text{ cm}^{-3}$ , and the

fractional ionizations are low, of order  $10^{-4}$ . Surface activation energies for PECVD are often small, occasionally negative. Hence deposition rates ( $r_d$ ) are usually not very sensitive to the  $T_s$ . However, physical properties and morphology of the films are generally strong functions of  $T_s$ .

The use of a RF discharge enables PECVD deposition on insulating substrates i.e. glass. The excitation frequency of power supply ranges from a few kHz to 200 MHz, but the usual frequency used for RF-PECVD is 13.56 MHz. This frequency was chosen by a standard for international telecommunications as an unoccupied frequency. Industry is interested more and more by higher process frequencies such as 27.13 MHz, 40.68 MHz (2<sup>nd</sup> and 3<sup>rd</sup> harmonics of 13.56 MHz), but this study only deals with the excitation frequency of 13.56 MHz. This is currently a standard frequency for which we can easily find commercial generators and matching box. A matching box is inserted between RF generator and the plasma in order to minimize the reflected power.

Capacitively coupled plasma (CCP) systems are one of the most common types of industrial plasma sources. They essentially consist of two metal electrodes separated by a small distance, placed in a reactor. An electrode is connected to the RF generator, through a matching box and DC current blocking capacitor ( $C_B$ ) while the other is grounded. Usually, the matching box circuit includes  $C_B$  inside. A plasma is ignited between the two electrodes, and at the interface between the plasma and the electrodes, the sheath arises. Because electrons are much lighter than ions, electrons will fly out of the plasma, leaving behind positive ions in the plasma, and thus leaving the bulk plasma charged positively relative to the electrodes. The electron-free region between the plasma and the walls is named the sheath, and the resulting

potential drop from the plasma to the sheath is called the plasma potential ( $V_p$ ).

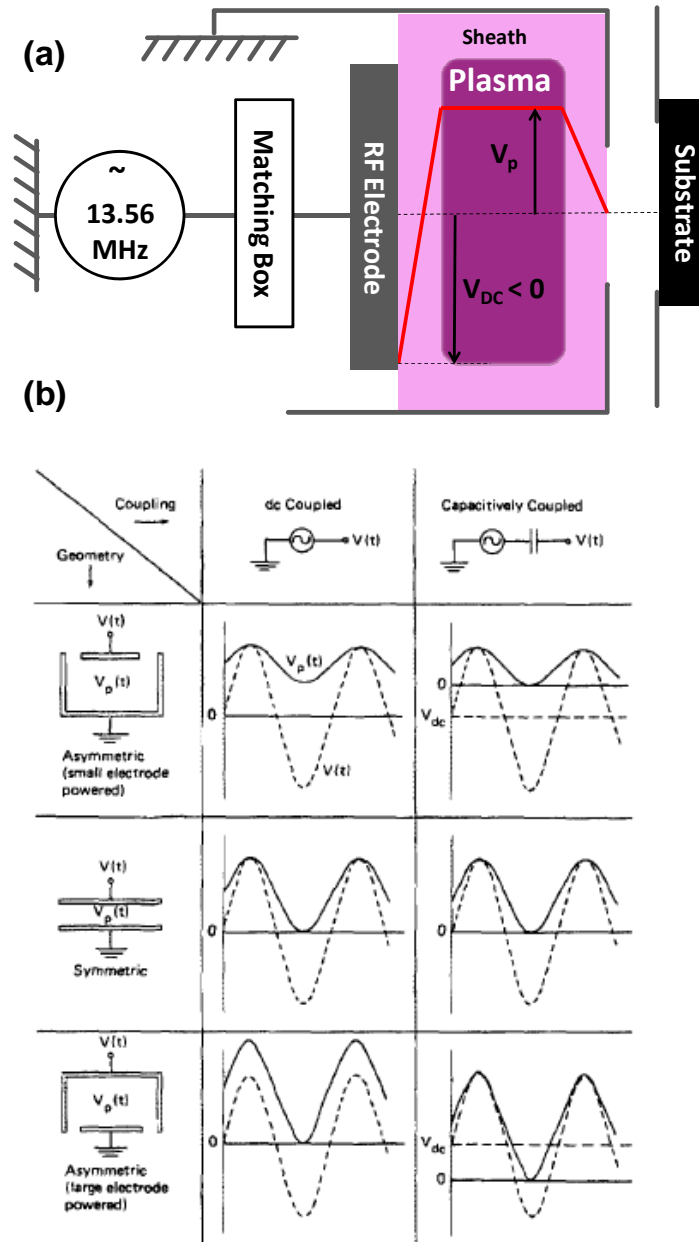


Figure 1.1 – (a) Schematic view of the potential distribution in a RF discharge where the RF voltage is applied to the RF electrode, with dielectric substrate, and (b) time-dependent sheath voltages. Figure 1.1(b) from Ref. [1.3]

The sheath shows rectifying characteristic. When the RF electrode is biased to a negative voltage, essentially all electrons (and any negative ions) are repulsed, but there is only small ion current, due

to low ion velocity. Otherwise, when the RF electrode is positively biased, there is a large electron current. Furthermore, if the net area of the grounded electrode is actually larger than that of the RF electrode, the discharge becomes asymmetric, and makes RF electrode negatively charged. Such behavior in the discharge is called self bias or DC bias ( $V_{DC}$ ), and it is related to the capacitive nature of the sheath. Under RF field,  $C_B$  is negatively charged through the rectifying characteristic of the sheath, compensating for the unequal current flow in each RF cycle. When using an insulating substrate e.g. glass, the plasma behaves as a variable load, and so the substrate is at floating potential and acts like a capacitor in series with  $C_B$ .

More details on plasma discharge process are found in the thesis of P. Roca i Cabarrocas [1.1] or the textbooks such as Ref. [1.2]. Figure 1.1 shows a schematic view of the potential distribution in a RF discharge and time-dependent sheath voltages and currents.

### **1.3 Hydrogenated amorphous silicon**

Hydrogenated amorphous silicon (a-Si:H) has been the most promising candidate for over two decades as an absorber layer for thin film solar cells. It is obvious that a-Si:H creates tremendous interest for two reasons. First, the material has several interesting properties that opened up many opportunities for semiconductor device applications. For example, due to the high absorption coefficient of a-Si:H in the visible range of the solar spectrum, a 1  $\mu\text{m}$  thick a-Si:H layer is sufficient to absorb 90% of the photon energy above its bandgap ( $\sim 1.7$  eV). Second, the glow discharge deposition technique, also referred to as PECVD, has enabled the production of a-Si:H films over large areas ( $2.1 \times 2.5$  m<sup>2</sup>) and at a

low substrate temperature (100 to 400 °C). The low process temperature allows the use of a wide range of low cost substrates such as glass, metal or polymer foils. Furthermore, a-Si:H can be simply doped and alloyed by adding the appropriate gases to a source gas, usually silane. These features have made a-Si:H a promising candidate for low cost thin film solar cells.

Since the first a-Si:H solar cell was reported by Carlson and Wronski [1.4] in 1976 with an efficiency of 2.4 %, great improvements have been made. Nowadays, a-Si:H single junction solar cells show stable efficiencies above 10 % [1.5], and a-Si:H based multijunction solar cells present initial efficiencies above 16 % [1.6], thus competing with polycrystalline silicon solar cells. More detail on a-Si:H can be found in the textbook of R. A. Street [1.7].

### **1.4 Staebler-Wronski effect**

Shortly after the development of the first a-Si:H solar cell in 1976, a light induced degradation effect was reported by Staebler and Wronski in 1977 [1.8, 1.9]. They reported that the dark conductivity and photoconductivity of a-Si:H are reduced significantly by prolonged illumination. This was correlated to the creation of metastable defects under illumination. Interestingly, metastable defects can be annealed out at temperatures above 150 °C. The reversible changes that occur between the annealed, initial, and the “light-soaked”, degraded states, introduces a shift of the Fermi level towards midgap, and have become one of the most investigated phenomena in a-Si:H based materials and solar cells. Since the first report, light induced metastable changes in the properties of hydrogenated amorphous silicon are referred to as the Staebler-Wronski effect (SWE).

The most common model has been the hydrogen bond switching model which proposes that photo-excited electrons and holes recombine at weak Si-Si bond locations. The accompanying non-radiative energy release is sufficient to break the weak bond, and that a back-bonded H atom prevents restoration of the broken bond by a bond switching event. Another model, known as the charge transfer model suggests that preexisting spinless centers (positively and negatively charged dangling bonds) are transformed to neutral dangling bonds by capture of excess carriers. The SWE is less significant in heavily doped materials [1.9].

Many reports suggest that the intrinsic and light induced defects are closely related to the microstructure of the sample, in particular to the hydrogen content ( $C_H$ ) and Si-H bonding configuration [1.10]. For example, material with lower  $C_H$  and films containing fluorine or chlorine show a less pronounced SWE [1.11]. In fact, the role of impurities is somewhat controversial. It is known that impurity incorporation, such as carbon, nitrogen, and oxygen, at concentrations in the film above  $10^{19} \text{ #cm}^{-3}$  lead to a more pronounced SWE [1.12-1.15]. However, it is not very clear if the alloying changes to the atomic network allow more defect creation [1.13], or if the impurities are directly associated with the light-induced degradation kinetics.

The creation of metastable defect states can be induced by pulsed and prolonged illumination [1.9], rapid quenching [1.16], current-injection, and double-injection currents [1.17, 1.18], as well as by keV electron bombardment [1.19]. In other words, defect creation requires an external excitation energy to cross the barrier between two states. Annealing can be considered as the reverse recovery process achieved by thermal excitation.

Stutzmann et al. showed that the defect density ( $N_D$ )

depends on the generation rate  $G$  and the time  $t$  as,

$$N_D(t) = C \cdot G^{\frac{2}{3}} t^{\frac{1}{3}}$$

where  $C$  is a constant depending on the tail-to-tail transitions [1.12]. The non-radiative recombination of electron-hole pairs at tail states release an energy of about 1.5 eV that possibly breaks weak bonds and thus creates dangling bonds. In order to prevent the recombination of the two broken bonds, a neighboring hydrogen atom moves to isolate the two dangling bonds. In the annealing process, the hydrogen atoms revert back to their original positions. Hydrogen is thus directly involved both in the defect creation and annealing.

Redfield and Bube provided a more practical model, explaining that illumination can cause the reverse process (light-induced annealing) of defect creation. When the illumination is kept on for a long time, the forward and reverse rates balances and a steady state is reached. The light-induced defect creation follows stretched exponential form

$$N_D = N_S - (N_S - N_0) \exp \left[ - \left( \frac{t}{\tau} \right)^\beta \right]$$

where  $N_D$  is the density of metastable defects,  $N_S$  is the saturated defect density, which is final state,  $N_0$  is the initial defect density.  $\tau$  decides an inflection point of the defect creation, and  $\beta$  is a broadening term, which characterizes the “stretched” nature [1.20]. The RB model, summarized above, shows good agreement with light-induced degradation behavior, and it is well explained by the fact that light-induced degradation and annealing balance out, and therefore the degradation saturates.

Based on experimental observation that over a wide range

of exposure times the cell efficiency degrades linearly with the logarithm of time, while the defect density follows a power law or stretched exponential form in time (as described in above), the following simplified relationship can be proposed

$$\eta \approx -A \log N_D$$

where  $\eta$  is the cell efficiency and  $A$  is a constant depending on the structure of the solar cell such as intrinsic layer thickness, respectively [1.21].

There are still new findings being discovered on the subject of the degradation of a-Si:H, in particular on the range of hydrogen motion involved [1.22], and large structural changes in the material such as light-induced volume changes [1.23], healing after light-induced degradation [1.24], coalescence and agglomeration of voids into larger macroscopic defects [1.25, 1.26], increase in Si-H absorption [1.27-1.29], and light-induced hydrogen effusion spectrum shift to lower temperatures [1.30].

### **1.5 Hydrogenated polymorphous silicon**

The first report on hydrogenated polymorphous silicon (pm-Si:H) was published in 1988 [1.31]. Roca i Cabarrocas et al. reported that the structure of silicon films can consist of nanometer-sized ( $\sim 2$  nm) ordered regions in a disordered matrix when prepared under particular RF glow discharge conditions. The glow discharge condition was indeed at the transition between hydrogenated amorphous silicon (a-Si:H) to hydrogenated microcrystalline silicon ( $\mu$ c-Si:H). The transition between the two discharge regimes was controlled by increasing the process pressure at a constant RF voltage, whereupon an abrupt increase in the dissociation in the plasma and a decrease in  $V_{DC}$  was observed, a phenomenon which

has been correlated to the onset of formation of powders in the discharge [1.32].

HRTEM reveals that a number of ordered domains ( $\sim$  few nm) are embedded in the a-Si:H matrix. The corresponding electron diffraction patterns verify that the ordered regions are nanocrystals. Silicon-hydrogen stretching mode infrared absorption in pm-Si:H is characterized by the distinguishing presence of a band at  $2030\text{ cm}^{-1}$ , showing that the microstructure in pm-Si:H has been greatly modified with respect to a-Si:H. The concentration of small crystallites is approximately less than 10% [1.33]. Spectroscopic ellipsometry measurements demonstrated that pm-Si:H films are more dense than a-Si:H, in spite of their high hydrogen content, in the range of 15~20 %. This peculiar structure of pm-Si:H results in a low defect density (down to order of  $10^{14}\text{ cm}^{-3}$  at Fermi level as measured by SCLC and modulated photocurrent) and higher resistance to light soaking than a-Si:H [1.34].

There is a controversial argument that pm-Si:H is often confused with hydrogenated protocrystalline silicon (pc-Si:H) [1.35, 1.36]. Indeed, both materials are grown from highly hydrogen diluted silane plasma, and they are both depicted as highly heterogeneous mixed-phase materials. Moreover, due to the mixed-phase nature of these materials, their optical band gap are wider than that of a-Si:H [1.31, 1.37], and both materials show the characteristic low temperature peak near  $400\text{ }^{\circ}\text{C}$  in the hydrogen exodiffusion spectrum [1.38, 1.39]. However, distinct differences still exist in the plasma physics during their deposition and their material nanostructures [1.40]. In particular, while the growth of pc-Si:H is assumed to rely on  $\text{SiH}_3$  radicals, pm-Si:H deposition relies on the presence of plasma synthesized nanocrystals [1.36, 1.40]. Due to the growth mechanism of pc-Si:H, its mixed-phase

nanostructure appears after an amorphous incubation layer. In other words, the heterogeneous nature of pc-Si:H only appears after some thickness. However, in pm-Si:H, the mixed-phase nature appears homogeneously through the film thickness because of the different deposition mechanism. It is an important point in practical solar cell application because the nanostructure and physical properties of pc-Si:H mainly depend on both hydrogen dilution and film thickness while those of pm-Si:H are independent of thickness.

The contribution of plasma generated nanocrystals to pm-Si:H deposition has been demonstrated by using a thermal gradient between the RF electrode and the substrate holder [1.36] as well as by controlling bias voltage applied to the substrate holder [1.41]. It is proposed that positively charged nanocrystals accelerate along the  $V_p$  of the plasma and introduce amorphization with the energetic ion bombardment. It has also been shown that the crystalline fraction of silicon thin films is significantly modified by controlling impact energy, and the conventional growth mechanism based on ionized radicals cannot explain the impact energy controlled crystalline fraction change [1.42]. One can conclude that the key point to understanding pm-Si:H is the plasma physics, in particular, the plasma generated nanoparticle formation.

### **1.6 Material and device characterization**

One of the most important physical properties in solar cell materials is absorption coefficient ( $\alpha$ ). Due to their disordered nature and complex composition, a-Si:H and pm-Si:H films react to photons of wide range of energy: the molecular vibration of Si-H bonds are detected by infrared absorption; inter-band electronic transitions are observed (by UV-VIS-IR spectrophotometry) with an

optical bandgap around 1.7 eV, and these materials also show a sub-gap absorption due to the particular density-of-states structure, attributed to the tail states and mid-gap defect states.

The optical properties listed above can all be accurately represented by  $\alpha$ , even though the measurement methods vary. Figure 1.2 shows absorption coefficient ( $\alpha$ ) versus the photon energy measured by various measurement techniques, such as Fourier transform infrared spectroscopy (FTIR), photothermal deflection spectroscopy (PDS), constant photocurrent method (CPM), ultraviolet-visible-infrared (UV-VIS-IR) transmission-reflection (TR) and spectroscopic ellipsometry (SE).

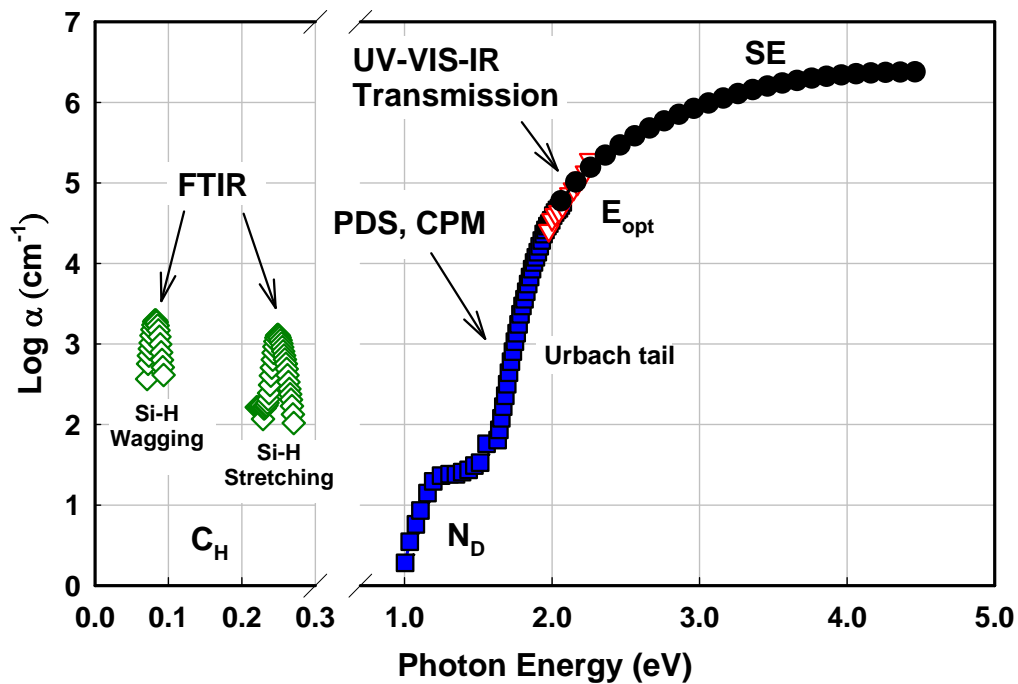


Figure 1.2 – Absorption coefficient ( $\alpha$ ) versus the photon energy measured by various measurement techniques, such as FTIR, PDS or CPM, UV-VIS TR and SE.

### 1.6.1 Spectroscopic Ellipsometry and Modelling

Various material parameters can be obtained from the measurement and modelling of Spectroscopic Ellipsometry (SE) spectra. Ellipsometry can be thought of as an optical impedance measurement, while TR can be viewed as power measurements. Impedance measurements give the amplitude and phase, whereas power measurements only give amplitudes. Exploiting the additional information gained through ellipsometry, the Tauc-Lorentz dispersion model is widely used in SE models. If only a single transition is considered [1.43], the imaginary part of the dielectric function is given by:

$$\varepsilon_i = 2nk = \begin{cases} \frac{A \cdot E_0 \cdot C \cdot (E - E_g)^2}{E \cdot (E^2 - E_0^2)^2 + C^2 \cdot E^2} & E > E_g \\ 0 & E \leq E_g \end{cases}$$

where  $E_0$  is the peak transition energy,  $E_g$  is the optical band gap,  $C$  is the broadening term, and  $A$  is proportional to the transition probability matrix element [1.43, 1.44]. In practice, the optical bandgap obtained from  $\varepsilon_i$  (obtained from a different equation) is also called the Cody gap ( $E_{\text{Cody}}$ ) [1.45, 1.46]. It is also known that  $A$  and  $C$  are related to the material density and the disorder, respectively [1.33].

The Tauc-Lorentz dispersion law assumes uniformity throughout the layer. However, the porosity of the layer, including any surface roughness, may introduce some fraction of void, and this phenomenon can be introduced by the Bruggeman effective medium approximation (BEMA) [1.47, 1.48].

Measurements of thickness and refractive index are another major application of ellipsometry. Careful interpretation of the ellipsometry-modeled thickness should be done because most of

the models assume uniform optical properties and a sharp and planar film-substrate interface. Generally, the measurements appear to give reasonable average thicknesses based on the macroscopic Maxwell's equations. Figure 1.3 shows an example of SE modeling including a fitting result of a measured SE spectrum of pm-Si:H on glass and its model. The model consists of a bulk layer and a surface roughness. Table 1.1 shows typical SE modeling parameters of a-Si:H and pm-Si:H.

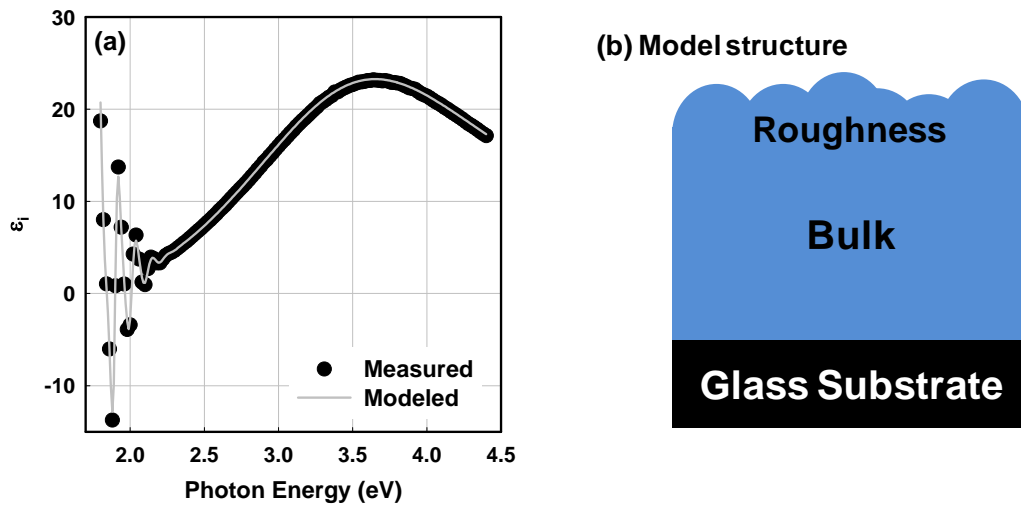


Figure 1.3 – Example of SE modeling. (a) The fitting result of a measured SE spectrum of pm-Si:H on glass and its model. (b) The model structure. The model consists of a bulk layer and surface roughness.

	$E_{opt}$	A	$E_0$	C	Roughness (Å)
a-Si:H	1.67	211.1	3.57	2.28	10.5
pm-Si:H	1.70	225.8	3.63	2.14	16.7

Table 1.1 – Typical SE modeling parameters of a-Si:H and pm-Si:H.

### 1.6.2 UV-VIS Transmission-Reflection

The optical bandgap of a material can be also determined by direct Transmission-Reflection (TR) method, as TR measurements are used to determine the optical absorption coefficient ( $\alpha$ ). During

transmission measurements, light is incident on the sample and the transmitted light is measured as a function of wavelength. The transmittance  $T$  of a sample under light incident normal to the sample surface is

$$T = \frac{(1-R)^2 e^{-\alpha d}}{1 + R^2 e^{-2\alpha d} - 2R e^{-\alpha d}}$$

and  $\alpha$  can be expressed as

$$\alpha = -\frac{1}{d} \ln \left( \frac{\sqrt{(1-R)^4 + 4T^2 R^2} - (1-R)^2}{2TR^2} \right)$$

The Tauc optical gap ( $E_{\text{Tauc}}$ ) is determined through an extrapolation of the linear trend in the expression below,

$$\sqrt{\alpha h\nu} = A(h\nu - E_{\text{Tauc}})$$

where  $E_{\text{Tauc}}$  is an optical gap [1.49], and  $A$  is a constant related to the width of tail states [1.50, 1.51].  $E_{\text{Tauc}}$  is generally accepted as an optical bandgap of a-Si:H related materials, although less variation in the determination is in  $E_{\text{Cody}}$  is observed than for the case of  $E_{\text{Tauc}}$  [1.52].

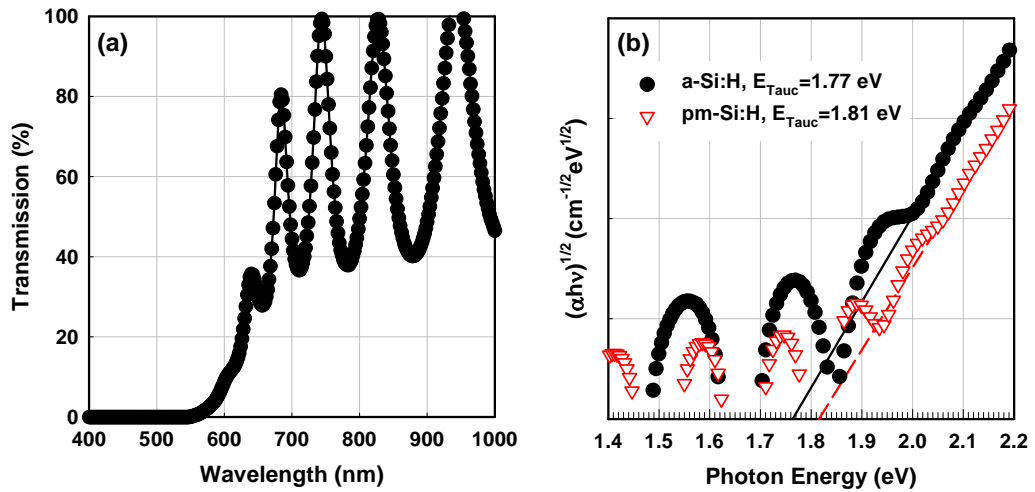


Figure 1.4 – Example of the determination of  $E_{\text{Tauc}}$ . (a) A UV-VIS-IR Transmission spectrum of pm-Si:H and (b) Tauc plot of a-Si:H and pm-Si:H on glass substrate.

### 1.6.3 Sub-gap absorption measurements

SE and TR measure the high energy, high absorption transitions. In the weak absorption regime near the band edge, the determination of  $\alpha$  by direct optical measurement is difficult because of the interference fringes and instrument sensitivity. The photothermal deflection spectroscopy (PDS) and the constant photocurrent method (CPM) allow one to detect weak signals in sub-gap absorption.

For PDS, a laser beam passing just above the surface is deflected by the thermal change in refractive index of the liquid in which the sample is immersed. The CPM uses a background illumination to ensure that the recombination lifetime does not depend on the photon energy and intensity of the illumination. In spite of the technical difficulty, the measurement of  $\alpha$  at low energy is particularly important because it provides information on the localized states such as band tails and midgap defect density.

Figure 1.5 shows PDS spectra of a-Si:H and pm-Si:H, and Table 1.2 shows the material parameters such as  $E_u$ ,  $N_D$ , and  $E_{04}$  deduced from Figure 1.5. For photon energies lower than  $E_g$ , the  $\alpha$  follows an exponential decay with photon energy  $h\nu$ :

$$\alpha(h\nu) = \alpha_0 \exp\left(\frac{h\nu}{E_u}\right)$$

where  $E_u$  is the Urbach energy, which is attributed to the width of band tail states [1.53]. The midgap defect density,  $N_D$ , is determined from the integration of the sub-gap absorption [1.54],

$$N_D = 7.9 \times 10^{15} \int_{\frac{E_g}{2}}^{\infty} \Delta\alpha \, dE$$

At last, another optical bandgap,  $E_{04}$  can be defined as the photon

energy where  $a$  equals to  $10^4 \text{ cm}^{-1}$ .

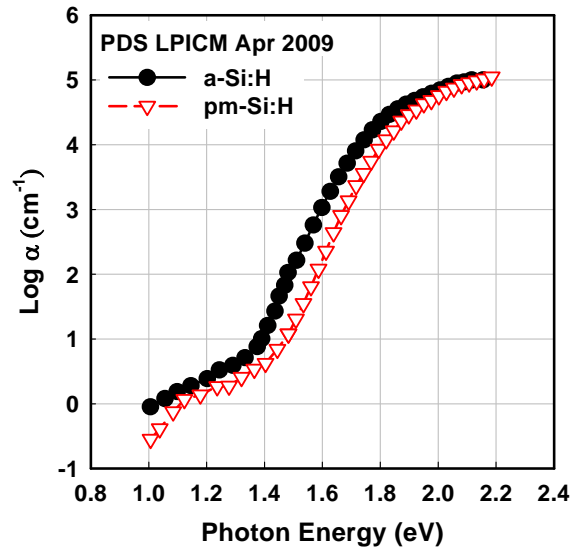


Figure 1.5 – Photothermal deflection spectroscopy spectra of a-Si:H and pm-Si:H.

	$E_u$ (meV)	$N_D$ ( $10^{16} \text{ #cm}^{-3}$ )	$E_{04}$ (eV)
a-Si:H	60.2	6.31	1.712
pm-Si:H	59.2	4.59	1.797

Table 1.2 – Material parameters deduced from sub-gap absorption PDS spectra in Figure 1.5.  $E_u$ ,  $N_D$ , and  $E_{04}$  of a-Si:H and pm-Si:H.

#### 1.6.4 Fourier transform infrared spectroscopy

Because hydrogen definitely plays an important role in material quality i.e. defect passivation, the detailed characterization of hydrogen is an interesting subject. Fourier transform infrared absorption spectroscopy (FTIR) detects the molecular vibration of Si-H bonds [1.55-1.57]. In particular, stretching absorption modes located at around  $2000 \text{ cm}^{-1}$  are important because they provide information on various mono-, di-, and multi-hydrides (e.g. Si-H, Si-H<sub>2</sub>) bonds. For the transmission measurement, samples should be deposited on a highly resistive, float-zone (FZ) c-Si wafer. There are two reasons: low carrier density of highly resistive c-Si prevents

free-carrier absorption in IR region, and the intrinsic c-Si provides the most similar refractive index to a-Si:H films.

Stretching mode absorption peaks consist of low stretching mode (LSM) and high stretching mode (HSM) peaks at around  $1990\text{ cm}^{-1}$  and  $2090\text{ cm}^{-1}$ , respectively. It is known that FTIR stretching mode of pm-Si:H can be deconvoluted into peaks including a medium stretching mode (MSM), band centered at  $2030\text{ cm}^{-1}$  [1.58], and the evolution of this MSM is interpreted as Si-H bonds at silicon nanocrystal surfaces [1.38], or platelets [1.59]. Figure 1.6 shows the FTIR stretching modes peaks of a-Si:H and pm-Si:H and an example of the deconvolution.

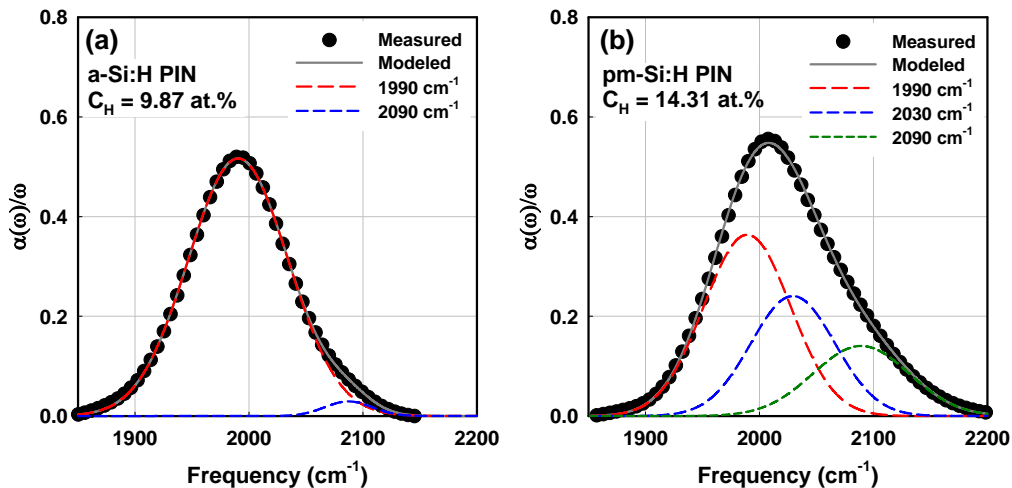


Figure 1.6 – FTIR stretching modes peak of (a) a-Si:H and (b) pm-Si:H PIN layer stacks and the deconvolution. Note that stretching mode peak of pm-Si:H consists of a MSM at  $2030\text{ cm}^{-1}$ .

<b>a-Si:H</b>	<b>1990</b>	<b>Area</b>	<b>48.66</b>
		<b>FWHM</b>	<b>103.0</b>
	<b>2090</b>	<b>Area</b>	<b>1.77</b>
		<b>FWHM</b>	<b>52.17</b>
	<b>Total Area</b>		<b>50.43</b>
<b>pm-Si:H</b>	<b>1990</b>	<b>Area</b>	<b>52.38</b>
		<b>FWHM</b>	<b>106.16</b>
	<b>2030</b>	<b>Area</b>	<b>14.31</b>
		<b>FWHM</b>	<b>80.91</b>
	<b>2090</b>	<b>Area</b>	<b>11.17</b>
		<b>FWHM</b>	<b>86.23</b>
	<b>Total Area</b>		<b>77.86</b>

Table 1.3 – The deconvolution result of Figure 1.6

### 1.6.5 Hydrogen exodiffusion

Since FTIR only detects hydrogen bound to silicon atoms, a complementary measurement technique is required to detect molecular hydrogen in the material. NMR experiments revealed that molecular hydrogen forms up to 40 % of the total hydrogen content in a-Si:H [1.60]. One of the common methods to measure the hydrogen evolution is from the rate of pressure increase of gas released into a known volume, for samples heated at constant rate. The experiment is often called hydrogen exodiffusion or thermal desorption. Hydrogen exodiffusion sensitively detects structural characteristics of the material such as interconnected voids, nanoparticle surfaces, amorphous matrices, and isolated voids [1.61].

In practice, the sample is placed inside a vacuum chamber, to which is attached a furnace. The overall system is kept at pressure of  $10^{-7}$  mbar during experiment through primary and turbo pumps. Hydrogen exodiffusion spectra are measured and monitored by Quadruple Mass Spectrometer (QMS), measuring the partial pressure (count) and are recorded in a continuous manner with increasing temperature. The H<sub>2</sub>O spectrum as a function of

temperature is also carefully recorded to see whether H<sub>2</sub> comes from the sample or from any water molecules present in the form of moisture. More detailed explanations and interpretations on the hydrogen exodiffusion results will be dealt with in following chapters. Figure 1.7 shows typical hydrogen exodiffusion spectra of a-Si:H and pm-Si:H PIN layer stacks deposited on glass substrate.

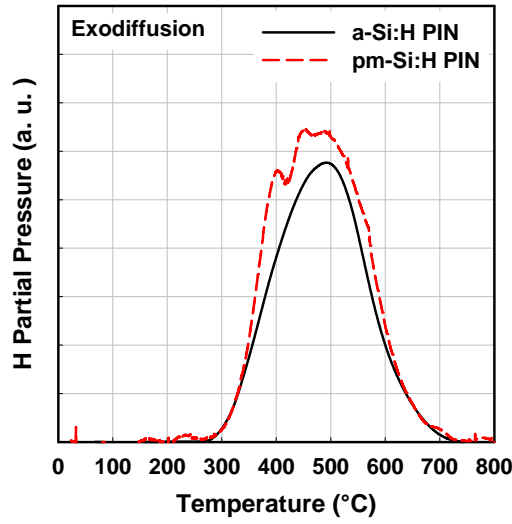


Figure 1.7 – Hydrogen exodiffusion spectra of a-Si:H and pm-Si:H PIN layer stacks deposited on glass substrate.

### 1.6.6 Dark conductivity

Conductivity ( $\sigma$ ) is an electrical property of the material. As a semiconductor, the  $\sigma$  of a-Si:H and pm-Si:H is thermally activated and depends on the carrier concentration ( $n$ ) as a function of temperature. The  $\sigma$  is the product of  $n$  and  $\mu$ ,

$$\sigma = nq\mu$$

By definition, in non-degenerate semiconductors, the Fermi-Dirac approaches and Boltzmann statistics express the carrier concentration  $n$  as:

$$n = N_C \exp\left(-\frac{E_C - E_F}{kT}\right)$$

where  $N_C$  is the effective density of states (in the conduction band),  $E_C$  and  $E_F$  are conduction band (or valence band, depends on the majority carrier) and Fermi energy level, respectively [1.62]. The  $\sigma$  also depends on the carrier mobility  $\mu$ , but the temperature dependence of  $\mu$  is far less significant than that of  $n$ . The temperature dependent conductivity  $\sigma(T)$  is therefore given by

$$\sigma(T) = \sigma_0 \exp\left(-\frac{E_C - E_F}{kT}\right) = \sigma_0 \exp\left(-\frac{E_a}{kT}\right)$$

where  $E_a$  is the activation energy of majority carriers. In practice,  $E_a$  is usually measured by placing the thin film sample on a heating stage and monitoring the change in the dark conductivity as a function of temperature. Optimal quality films exhibit a straight line over many orders of magnitude on  $\log(\sigma)$  versus  $1000/T$  Arrhenius plot and hence its slope is defined as,

$$\log(\sigma(T)) = \log \sigma_0 - \frac{1}{0.1982} \cdot E_a \cdot \frac{1000}{T}$$

$E_a$  is important in both intrinsic and doped materials because it gives information on the location of the Fermi level. In case of intrinsic layers,  $E_a$  is usually about half of the  $E_g$ . An example of Arrhenius plot of the temperature dependent dark conductivity of intrinsic a-Si:H, pm-Si:H, and  $\mu$ c-Si:H layers are displayed in Figure 1.8.

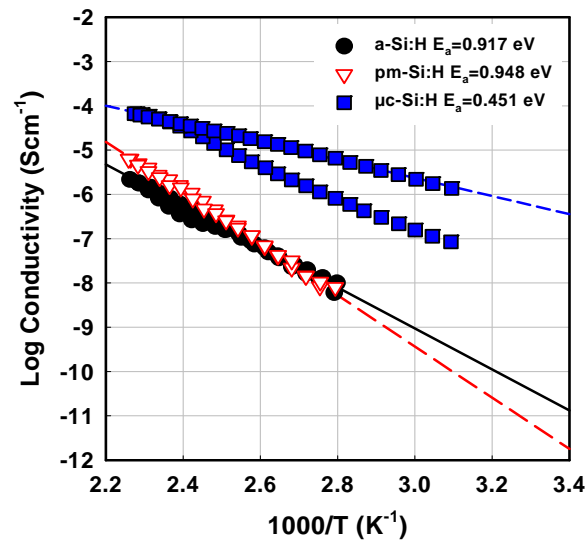


Figure 1.8 – Arrhenius plot of the temperature dependent dark conductivity of intrinsic a-Si:H, pm-Si:H, and  $\mu\text{c-Si:H}$  layers.  $E_a$  and the conductivity at room temperature can be extracted from the extrapolation.

### 1.6.7 Atomic Force Microscopy and Scanning Electron Microscopy

Atomic force microscope (AFM) and scanning electron microscope (SEM) are useful tools to observe nano-scale morphology. AFM is a high-resolution type of scanning probe microscope to observe surface morphology of the specimen. Since it does not rely on any optics, it provides a resolution of fractions of a nanometer, more than 1000 times better than the optical diffraction limit. The AFM consists of a microscale cantilever with a sharp tip at its end that is used to scan the sample surface. The cantilever is typically made of silicon or silicon nitride with a tip radius of curvature on the order of nanometers. When the tip is brought into proximity of a sample surface, forces between the tip and the sample lead to a deflection of the cantilever. The deflection is measured using a laser spot reflected from the top surface of the cantilever into an array of photodiodes. Tapping mode is usually preferred to prevent cantilever dragging across the surface and resulting surface

damage while expecting higher resolution than non-contact mode. The scanning rate, scanning area and the image resolution are important trade-off factors.

SEM is a type of electron microscope that images the sample surface by scanning it with a high-energy beam of electrons in a raster scan pattern. The electrons interact with the atoms that make up the sample producing signals that contain information about the sample's surface topography, composition and other properties such as electrical conductivity. The types of signals produced by an SEM include secondary electrons, back scattered electrons (BSE), characteristic x-rays, cathodoluminescence, specimen current, and transmitted electrons. In the most common or standard detection mode, secondary electron imaging, the SEM can produce very high-resolution images of a sample surface, revealing details about 1 to 5 nm in size. Due to the way these images are created, SEM micrographs have a very large depth of field yielding a characteristic three-dimensional appearance useful for understanding the surface structure of a sample. A wide range of magnifications is possible. The contrast in an SEM depends on a number of factors. For a flat, uniform sample the image shows no contrast. Contrast is also influenced by surface conditions, local electric fields, conductivities of the sample and by the surface tilt.

AFM and SEM are exemplary complementary measurements, for the contrast of SEM images often deceptively caused by the conductivity of the surface objects, while AFM can also suffer from various artifacts such as damaged tips or thermal drift. Figure 1.9 shows AFM and SEM images of the surface morphology of a pm-Si:H PIN solar cell on textured Asahi.

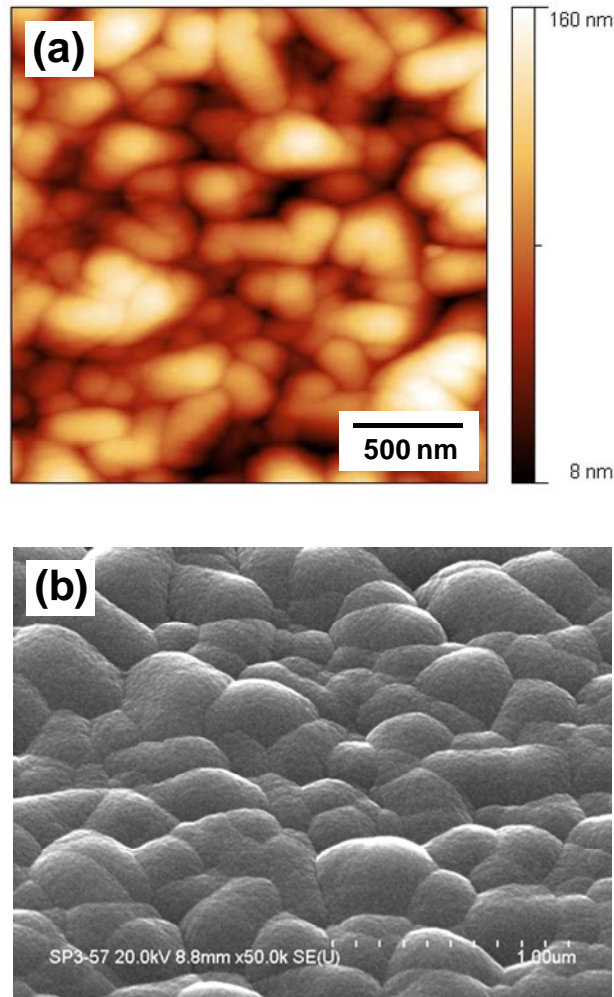


Figure 1.9 – (a) AFM and (b) SEM images of surface morphology of pm-Si:H PIN solar cell on textured Asahi.

### 1.6.8 Diode dark $J(V)$

As a semiconductor device, a solar cell is first and foremost a diode. The ideal diode has zero resistance under the forward bias, and infinite resistance (conducts zero current) under the reverse bias. In other words, the semiconductor diode acts as an electrical rectifier. The ideal diode equation is given by

$$J = J_0 \left[ \exp\left(\frac{qV}{nk_B T}\right) - 1 \right]$$

where  $k_B T$  is thermal energy ( $\sim 0.02586$  eV at  $27^\circ\text{C}$ ),  $J_0$  is reverse

saturation current, and  $n$  is diode ideality factor [1.63, 1.64]. Ideally, log current density versus voltage of the diode shows linear proportionality in the forward bias region. Extrapolating the linear region down to the y axis ( $V=0$ ) gives  $J_0$ , while the slope,  $m$ , is given by

$$m = \frac{d \log J}{dV}$$

The knowing the slope and sample temperature allows the ideality factor to be determined from the relationship

$$n = \frac{q}{2.3 \cdot k_B T \cdot m}$$

Typical a-Si:H and pm-Si:H solar cells are PIN diodes: a thick (~250 nm) intrinsic layer is sandwiched in between P and N layers. The intrinsic layer makes the PIN diode an inferior rectifier, but makes the device suitable for photovoltaic applications. More details on the device physics of the PN junction diode can be found in the textbooks such as Ref [1.63]. Figure 1.10 shows dark J(V) curves of a good and a bad pm-Si:H PIN diodes. Extrapolation from the linear region in the forward bias shows that good PIN diodes should have smaller  $n$  and  $J_0$ .

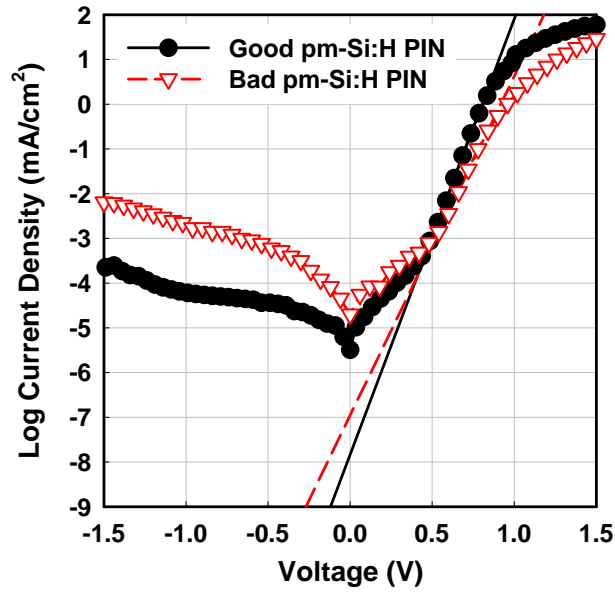


Figure 1.10 – Dark  $J(V)$  curves of good and bad pm-Si:H PIN diodes. Extrapolation from the linear region of the forward bias shows the different dark  $J(V)$  parameters for different PIN diode quality.

### 1.6.9 Solar cell parameters

An ideal solar cell can be represented by a current source connected in parallel with a rectifying diode, as shown in the equivalent circuit of Figure 1.11.

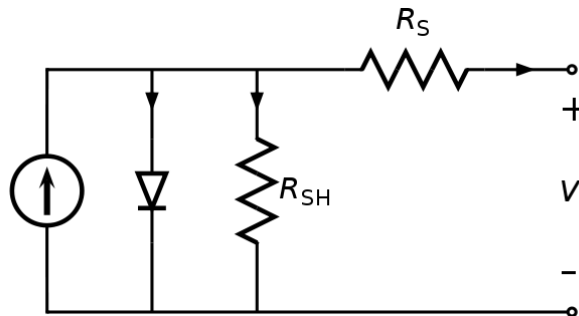


Figure 1.11 – An equivalent circuit of a solar cell. An ideal solar cell consists of a current source connected in parallel with a rectifying diode,  $R_S$  and  $R_{SH}$ .

The corresponding  $J(V)$  characteristic is described by the Shockley solar cell equation

$$J = J_{ph} - J_0 \left[ \exp\left(\frac{qV}{k_B T}\right) - 1 \right] \quad \Big|_{R_S \approx 0, R_{SH} \approx \infty}$$

where  $k_B T$  is thermal energy ( $\sim 0.02586$  eV at  $27^\circ\text{C}$ ),  $J_0$  is reverse saturation current. The photogenerated current density ( $J_{ph}$ ) is closely related to the photon flux incident on the cell and its dependence on the wavelength of light is frequently discussed in terms of the quantum efficiency or spectral response. In the ideal case, the short-circuit current density ( $J_{sc}$ ) is equal to the  $J_{ph}$  and the open circuit voltage ( $V_{oc}$ ) is given by

$$V_{oc} = \frac{k_B T}{q} \ln\left(1 + \frac{J_{ph}}{J_0}\right)$$

In the operation condition such as  $J_{sc} \sim 10$  mA/cm<sup>2</sup> and  $J_0 < 10^{-6}$  mA/cm<sup>2</sup>, the relationship can be simplified,

$$V_{oc} = \frac{k_B T}{q} \ln\left(\frac{J_{ph}}{J_0}\right)$$

Of particular interest is the point on the  $J(V)$  curve where the power produced is at a maximum. This is referred to as the maximum power point ( $P_{max}$ ), which defines the largest possible area rectangle for any point on the  $J(V)$  curve. The fill factor ( $FF$ ) is a measure of the squareness of the  $J(V)$  characteristic and is always less than one. It is the ratio of the areas of the two rectangles, between  $P_{max}$  and  $V_{oc}J_{sc}$ .

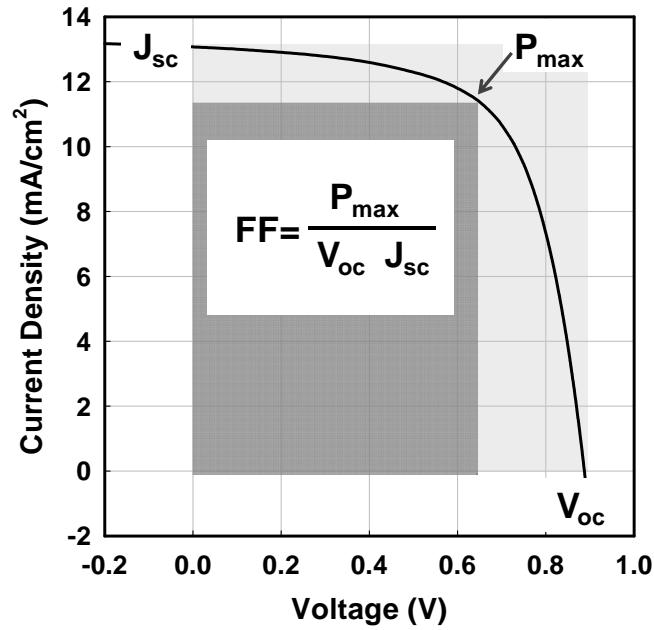


Figure 1.12 – An example of solar cell  $J(V)$  curve.  $J_{sc}$ ,  $V_{oc}$ ,  $FF$ ,  $P_{max}$  are marked.

Usually the  $FF$  of solar cells decreases with series resistance ( $R_s$ ) and shunt resistance ( $R_{SH}$ ). Interfaces between the layers and the sheet resistance of solar cell itself causes  $R_s$ , and surface leakage near the edge of the film, pinholes in the film, and back-diffusion of carriers increases  $R_{SH}$ . Finally, the most important figure of merit for a solar cell is its conversion efficiency,  $\eta$ , which is defined as

$$\eta = \frac{FF \cdot V_{oc} \cdot J_{sc}}{P_{in}}$$

The incident power,  $P_{in}$ , is determined by the properties of the light spectrum incident upon the solar cell. Figure 1.11 shows an example of solar cell  $J(V)$  curve. More details on solar cell  $J(V)$  curve interpretation can be found in Ref [1.65].

---

## References

- 1.1 P. Roca i Cabarrocas, Ph.D. Thesis, Université Paris VII (1988).
- 1.2 M. A. Lieberman and Alan J. Lichtenberg, Principles of Plasma Discharges and Materials Processing, 2nd Edition, Wiley-VCH, 2005. In particular the chapters 1, 11, and 16.
- 1.3 K. Köhler, J. W. Coburn, D. E. Horne, E. Kay, and J. H. Keller J. Appl. Phys. 57, 59 (1985).
- 1.4 D. E. Carlson and C. R. Wronski, Appl. Phys. Lett. 28, 671 (1976).
- 1.5 S. Benagli, D. Borrello, E. Vallat-Sauvain, J. Meier, U. Kroll, J. Hötzel, J. Bailat, J. Steinhauser, M. Marmelo, G. Monteduro, and L. Castens, Proc. 24th European PVSEC, Hamburg 2009, pp. 21-25.
- 1.6 B. Yan, G. Yue, L. Sivec, J. Yang, S. Guha, and C-S. Jiang, Appl. Phys. Lett. 99, 113512 (2011).
- 1.7 R. A. Street, Hydrogenated Amorphous silicon. Cambridge University Press; 1991.
- 1.8 D. L. Staebler and C. R. Wronski, Appl. Phys. Lett. 31, 292 (1977).
- 1.9 D. L. Staebler and C. R. Wronski, J. Appl. Phys. 51, 3262 (1980).
- 1.10 H. Fritzsche. Annu. Rev. Mater. Res. 31, 47 (2001).
- 1.11 P. K. John, B. Y. Tong, S. K. Wong, and K. P. Chik, Method of making highly stable modified amorphous silicon and germanium films, U.S. Patent No. 4402762 (1983).
- 1.12 M. Stutzmann, W. Jackson and C. Tsai, Phys. Rev. B 32, 23 (1985).
- 1.13 R. S. Crandall, D. E. Carlson, A. Catalano, and H. A. Weakliem, Appl. Phys. Lett. 44, 200 (1984).
- 1.14 J. Woerdenweber, T. Merdzhanova, A. Gordijn, H. Stiebig, W. Beyer, Sol. Energ. Mater. Sol. Cells 95, 2811 (2011).
- 1.15 T. Merdzhanova, J. Woerdenweber, W. Beyer, A. Gordijn, R. Schmitz, A. Mück, U. Zastrow, L. Niessen, J. Klomfaß, W. Reetz, H. Stiebig, and U. Rau, Proc. 24th European PVSEC, Hamburg 2009, pp. 2660-2664.
- 1.16 R. A. Street, J. Kakalios, and T. M. Hayes, Phys. Rev. B 34, 3030 (1986).
- 1.17 R. A. Street, Appl. Phys. Lett. 59, 1084 (1991).
- 1.18 A. Dasgupta, N. Palit, and S. Ray, Sol. Energ. Mater. Sol. Cells 55, 395 (1998).
- 1.19 U. Schneider, B. Schröder, and F. Finger, J. Non-Cryst. Solids

- 114, 633 (1989).
- 1.20 D. Redfield and R. H. Bube, *Appl. Phys. Lett.* 54, 1037 (1989).
- 1.21 L. Yang, L. Chen, and A. Catalano, *Appl. Phys. Lett.* 59, 840 (1991).
- 1.22 H. M. Branz, *Phys. Rev. B* 59, 5498 (1999).
- 1.23 P. Tzanetakis, *Sol. Energ. Mater. Solar Cells.* 78, 369 (2003).
- 1.24 J. M. Pearce, J. Deng, M. L. Albert, C. R. Wronski, R. W. Collins, Photovoltaic Specialists Conference, Conference Record of the 31st IEEE p.1536 (2005).
- 1.25 S. B. Zhang and H. M. Branz, *Phys. Rev. Lett.* 87, 105503 (2003).
- 1.26 A. H. M. Smets, MRS 2012 Spring Meeting, Oral Presentation A4.3 (San Francisco, 2012).
- 1.27 Z. Yiping, Z. Dianlin, K. Guanglin, P. Guangqin, and L. Xianbo *Phys. Rev. Lett.* 74, 558 (1995).
- 1.28 R. Darwich, P. Roca i Cabarrocas, S. Vallon, R. Ossikovski, P. Morin, and K. Zellamam, *Phil. Mag. B* 72, 363 (1995).
- 1.29 S. Sheng, G. Kong, and X. Liao, *Solid State Commun.* 116, 519 (2000).
- 1.30 R. Weil, A. Busso, and W. Beyer, *Appl. Phys. Lett.* 53, 2477 (1988).
- 1.31 P. Roca i Cabarrocas, S. Hamma, S. N. Sharma, G. Viera, E. Bertran, and J. Costa, *J. Non-Cryst. Solids* 227-230, 871 (1998).
- 1.32 C. Bohm and J. Perrin, *J. Phys. D: Appl. Phys.* 24, 865 (1991).
- 1.33 A. Fontcuberta i Morral, P. Roca i Cabarrocas, and C. Clerc, *Phys. Rev. B* 69, 125307 (2004).
- 1.34 M. Meaudre, R. Meaudre, R. Butte, S. Vignoli, C. Longeaud, J.P. Kleider, P. Roca i Cabarrocas, *J. Appl. Phys.* 86, 946 (1999).
- 1.35 R. W. Collins, A. S. Ferlauto, G. M. Ferreira, C. Chen, J. H. Koh, R. J. Koval, Y. H. Lee, J. M. Pearce, C. R. Wronski *Sol. Energ. Mater. Solar Cells* 78, 143 (2003).
- 1.36 A. Fontcuberta i Morral, P. Roca i Cabarrocas, *Thin Solid Films* 383, 161 (2001).
- 1.37 C. R. Wronski, B. Von Roedern, A. Koodziej, *Vacuum* 82, 1145 (2008).
- 1.38 P. Roca i Cabarrocas, A. Fontcuberta i Morral, Y. Poissant, *Thin Solid Films* 403–404, 39 (2002).
- 1.39 J. Yang and S. Guha, *Mat. Res. Soc. Symp. Proc.* 557, 239 (1999).

- 
- 1.40 P. Roca i Cabarrocas, *Phys. Stat. Sol. (c)* 1, 1115 (2004).
- 1.41 N. Chaâbane, V. Suendo, H. Vach and P. Roca i Cabarrocas, *Appl. Phys. Lett.* 88, 203111 (2006).
- 1.42 A. Matsuda, *Thin Solid Films* 337, 1 (1999).
- 1.43 G. E. Jellison, Jr. and F. A. Modine, *Appl. Phys. Lett.* 69, 371 (1996).
- 1.44 G. E. Jellison, Jr., F. A. Modine, P. Doshi, and A. Rohatgi, *Thin Solid Films* 313, 193 (1998).
- 1.45 G. D. Cody, *Mater. Res. Soc. Symp. Proc.* 862, A1.3.1 (2005).
- 1.46 G. D. Cody, B. G. Brooks, and B. Abeles, *Sol. Energ. Mater.* 8, 231 (1982).
- 1.47 D. A. G. Bruggeman, *Annalen der Physik*, 24, 637 (1935).
- 1.48 A. Abramov, Y. Djeridane, R. Vanderhaghen, and P. Roca i Cabarrocas, *J. Non-Cryst. Solids* 352, 964 (2006).
- 1.49 J. Tauc, R. Grigorovici, and A. Vancu, *Phys. Status Solidi* 15, 627 (1966).
- 1.50 T. Globus, G. Ganguly, and P. Roca i Cabarrocas, *J. Appl. Phys.* 88, 1907 (2000).
- 1.51 P. Roca i Cabarrocas, P. Morin, V. Chu, J. P. Conde, J. Z. Liu, H. R. Park, and S. Wagner, *J. Appl. Phys.* 69, 2942 (1991).
- 1.52 Tat M. Mok and Stephen K. O'Leary, *J. Appl. Phys.* 102, 113525 (2007).
- 1.53 F. Urbach, *Phys. Rev.* 92, 1324 (1953).
- 1.54 W. B. Jackson and N. Amer, *Phys. Rev. B* 25, 5559 (1982).
- 1.55 M. H. Brodsky, M. Cardona, and J. J. Cuomo, *Phys. Rev. B* 16, 3556 (1977).
- 1.56 G. Lucovsky, R. J. Nemanich, and J. C. Knights, *Phys. Rev. B* 19, 2064 (1979).
- 1.57 A. A. Langford, M. L. Fleet, B. P. Nelson, W. A. Lanford, and N. Maley, *Phys. Rev. B* 45, 13367 (1992).
- 1.58 S. Lebib and P. Roca i Cabarrocas, *Eur. Phys. J. Appl. Phys.* 26, 17 (2004).
- 1.59 A. H. M. Smets and M. C. M. van de Sanden, *Phys. Rev. B* 76, 073202 (2007).
- 1.60 P.A. Fedders, D.J. Leopold, P.H. Chan, R. Borzi, and R.E. Norberg, *Phys. Rev. Lett.* 85, 401 (2000).
- 1.61 W. Beyer, W. Hilgers, P. Prunici, D. Lennartz, *J. Non-Cryst.*

Solids , Article in Press,  
<http://dx.doi.org/10.1016/j.jnoncrysol.2011.09.030>

- 1.62 S. M. Sze, K. K. NG, Physics of semiconductor devices. Wiley; 3rd edition. 2007; citing pp. 17-20.
- 1.63 S. M. Sze, K. K. NG, Physics of semiconductor devices. Wiley; 3rd edition. 2007; citing chapter 2.
- 1.64 D. K. Schroder, Semiconductor material and device characterization. Wiley-IEEE Press; 3rd edition. 2006; citing pp.185-188.
- 1.65 T. Markvart and L. Castaner (Eds), Solar Cells: Materials, Manufacture and Operation. Elsevier Science; 2005; citing chapter IIa-1.

# Chapter **2**

## **Hydrogenated Polymorphous Silicon – Material**

2.1 Introduction.....	56
2.2 ARCAM reactor .....	56
2.3 a-Si:H and pm-Si:H deposition.....	59
2.4 Gas flow rate series.....	67
2.5 Pressure series .....	70
2.6 RF power series.....	74
2.7 Ts series.....	79
2.8 Powder formation and residence time .....	85
2.9 Summary .....	86

### 2.1 Introduction

This chapter mainly deals with the properties of pm-Si:H films produced under a wide range of deposition conditions, aiming for a high deposition rate ( $r_d$ ). From an industrial point of view, a high  $r_d$  over large areas while preserving a good material quality is sought after. Nowadays, cost reduction is one of the most important issues in photovoltaics. Even though a-Si:H based solar cell technology is already produced at low cost of \$ 0.5/W<sub>p</sub> [2.1], M. A. Green expects that further cost reduction is needed down to \$ 0.1/W<sub>p</sub> for a-Si:H based technology [2.2]. In this chapter, we have tested the effect of process parameters on pm-Si:H films deposition in order to increase the  $r_d$ . The causes of and consequences for the material properties of PECVD deposited pm-Si:H films at various  $r_d$  are studied. The aim of this work is to study the plasma process conditions and understand their effect on the  $r_d$  and the material properties. Readers should also note that the discussion on pm-Si:H is based on our current understanding of its growth mechanism (which includes plasma-synthesized silicon nanoparticles contributing to the deposition).

### 2.2 ARCAM reactor

Intrinsic pm-Si:H films were deposited in the ARCAM reactor [2.3]. ARCAM is a monochamber-multiplasma reactor, consisting of a single vacuum vessel containing three independent plasma chambers. Figure 2.1 shows the inside of the vessel. The vacuum vessel is a 400 mm diameter stainless steel cylinder. Its bottom face contains a pumping port, gas inlets, and the RF electrode terminals with plasma boxes. The cover can be opened for loading operations and is equipped with a water-cooled seal. The whole vacuum vessel can be heated up to 300 °C by an oven-like structure made of regulated thermo-coax wires. A

protecting thermal isolation surrounds the whole vacuum chamber minimizing the thermal losses. The top, the wall, and the cover parts of the reactor can be independently heated, but the temperature for the three parts is usually set at the same value. The reactor is always heated at the desired substrate temperature and kept at a base pressure of  $10^{-7}$  mbar.

A rotating plate handles six 100 mm diameter substrates allowing large sample productions without breaking vacuum. One of the substrate positions (typically #6) is usually reserved for the ignition of the silane plasma and to pre-coat the plasma chambers. Multichamber system and the rotating plate with multiple sample handling is a key feature in ARCAM reactor, in order to minimize cross-contamination. In PIN solar cells, controlling the interfaces is very important, in particular p/i interface that mainly determines the solar cell properties [2.4-2.6]. However, silane plasma is a reactive environment where deposition takes place at the same time as etching and sputtering of the material deposited on the walls of the reactor. These effects may produce a cross contamination between the different layers constituting a device when deposited in a monochamber system. In PIN solar cells, a boron tail from p-type layer may be incorporated in the intrinsic layer and deteriorate the p/i interface quality [2.6]. Multichamber systems provide sharp interfaces, a necessary condition for obtaining high efficiency of PIN solar cells.

Each plasma chamber consists of a RF electrode disk surrounded by a grounded cylinder (plasma box, diameter of 150 mm). The area of each plasma electrode is  $171.95 \text{ cm}^2$ . RF electrodes and plasma boxes can be very easily removed and modified to vary the plasma geometry, most importantly the inter-electrode distance, enabling one to control the symmetry of the discharge or the gas residence time. The gas flows from the inlet hole below the RF

electrode to the upper plasma chamber and to the pumping port through a 2 mm gap between the upper part of plasma chamber and the substrate holder. This annular flow restriction creates a positive differential pressure between plasma chamber and the vacuum vessel and thus also reduces chemical contamination during deposition. The gas pressure in the vacuum chamber is regulated by an electrically driven throttle valve. Therefore the gas pressure can be controlled by either gas flow rate or pumping rate. The pumping system of ARCAM consists of two lines, the base pressure of  $10^{-7}$  mbar is ensured by a turbo-molecular pump, backed by a rotary vane pump. The pumping during glow discharge process is ensured by a roots pump backed by a rotary vane pump. Figure 2.2 shows a schematic view of one of the plasma boxes used in ARCAM.



Figure 2.1 – Photo of ARCAM reactor and inside of vessel. Three plasma chambers are seen.

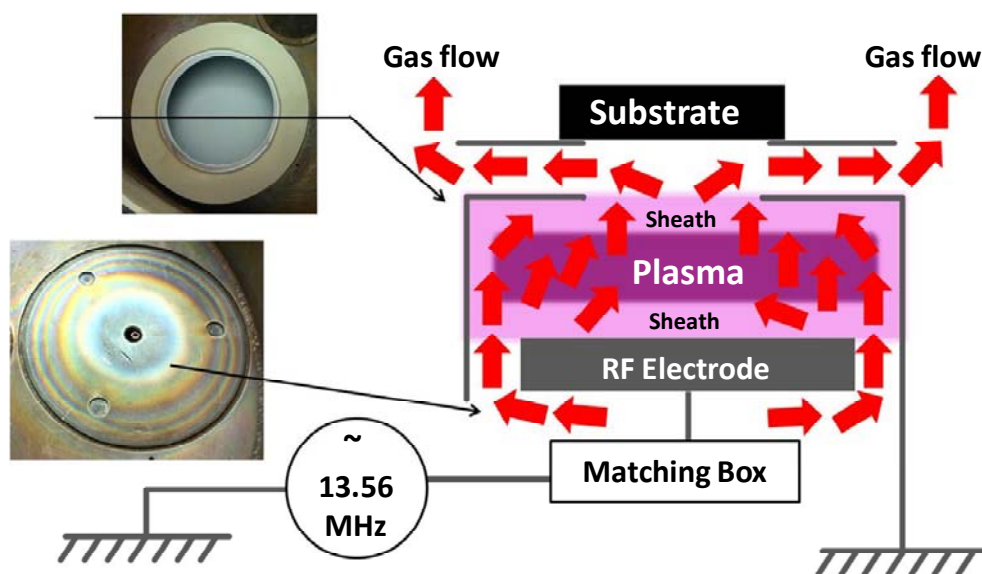


Figure 2.2 – Schematic view of one of the plasma boxes used in ARCAM.

### 2.3 a-Si:H and pm-Si:H deposition

PECVD deposition of a-Si:H is usually done by dissociation of silane ( $\text{SiH}_4$ ) or  $\text{SiH}_4\text{-H}_2$  gas mixtures. Gas-phase additions such as  $\text{B}_2\text{H}_6$  (or TMB,  $\text{BF}_3$ ) and  $\text{PH}_3$  are used to obtain p- or n-type material, respectively. The substrate temperatures ( $T_s$ ) are between 25–400 °C, depending on the application. In case of ARCAM, our optimum  $T_s$  is at around 175 °C.  $\text{SiH}_4$  is tetrahedral molecule, having a heat of formation of 34.3 kJ/mol and a Si–H bond distance of 1.5 Å. Gas discharge is usually done at a pressure of 0.1-10 Torr and RF power density of 10–100 mW/cm<sup>2</sup>, yielding a  $r_d$  of 1-10 Å/s.

Electron collisions with silane molecules are the primary excitation event in the plasma. Electrons having different energies in the plasma excite ground state electrons in the molecular orbit of silane molecules to their electronic excited states depending on the energy of the electrons, often up to 70 eV [2.7-2.10]. Electronic excited states of silane molecules are dissociative states meaning that spontaneous dissociation occurs from those electronic excited states to

a variety of radicals. Figure 2.3 represents some of the species that can be generated by glow discharge.

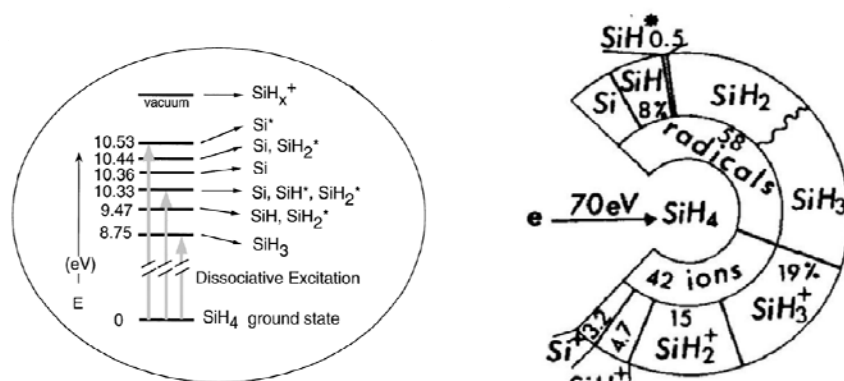


Figure 2.3 – Electron-induced dissociative-excitation of SiH<sub>4</sub> molecules upon electron impact. All the species are produced spontaneously from electronic excited states via a one-electron-impact dissociation pathway. Figure from Ref [2.8, 2.7].

Surface reactions during the film growth determine film properties. Addition of H<sub>2</sub> in the discharge greatly modifies surface reaction probability, introducing secondary reactions such as etching, chemical annealing, and surface diffusion [2.8-2.10]. The growth surface, shown in Fig. 2.5, consists of active sites, containing at least one dangling bond, and passive sites, containing either silicon or hydrogen atoms at all four bonds. At the usual deposition temperature of  $T_s < 400$  °C, growing film surface is covered by hydrogen [2.11]. The surface reaction probability  $\beta$  can be expressed as,

$$\beta = 1 - r = s + \gamma \quad 0 \leq \beta \leq 1$$

where  $r$  is the coefficient of reflection,  $s$  the sticking probability of the Si atom and  $\gamma$  the recombination probability as a volatile species. Low  $\beta$  values allow conformal coverage and dense material. The dangling bonds are created by processes such as ion bombardment and H abstraction. SiH<sub>2</sub> can insert itself into the matrix upon impact with the surface at either active or passive sites. Due to its low mobility, giving a sticking probability of near 1, incorporation of SiH<sub>2</sub> leads to film

growth in a manner similar to that of physical vapor deposition (PVD). Such films are generally of poor quality, having voids, undesired surface roughness, and other surface defects.  $\text{SiH}_3$  radicals are indeed more favorable due to higher surface mobility, so they react weakly with the a-Si:H surface.  $\text{SiH}_3$  has a small sticking coefficient. According to the modeling, it can diffuse up to 1  $\mu\text{m}$  before contributing on film deposition, probably through repeated desorption and physisorption events [2.11].  $\text{SiH}_3$  can diffuse along the surface but can stick only at active sites, filling in the surface roughness and contributing to growth of a smooth, high-quality film with conformal coverage associated with a chemical vapor deposition [2.12].

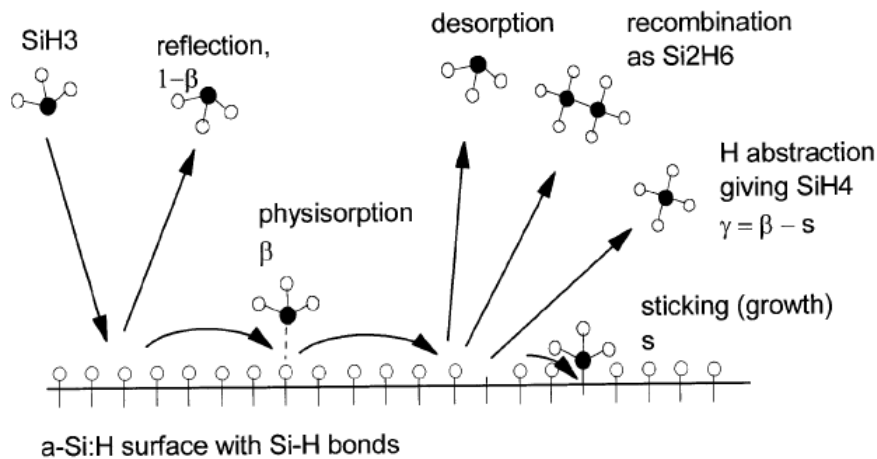


Figure 2.4 – Schematic of processes of a  $\text{SiH}_3$  radical on growing a-Si:H surface. From Ref [2.11].

Dissociation of  $\text{SiH}_4$  and  $\text{H}_2$  produces atomic hydrogen, and atomic hydrogen can move in and out of the surface during growth of films. This diffusion allows hydrogen to react with the silicon network in the subsurface region, after the silicon has attached to the surface. The hydrogen also terminates dangling bonds and removes weak bonds while excess hydrogen is evolved from the film. The free exchange of the hydrogen between the film and the plasma establishes (approximate) equilibrium between the plasma gas and the film. Thus

the concentration of hydrogen in the film and the reactions with the network depend on the chemical potential of the hydrogen in the plasma.

R. A. Street introduced the hydrogen chemical potential ( $\mu_{\text{H}}$ ) in the plasma as,

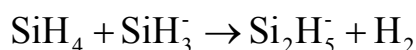
$$\mu_{\text{H}} = E_{\text{H}} + kT \ln \left( \frac{N_{\text{H}}}{N_{\text{H0}}} \right)$$

where  $E_{\text{H}}$  is the energy of atomic H in vacuum,  $N_{\text{H}}$  is the concentration in the plasma, and  $N_{\text{H0}}$  is the effective density of states ( $2.5 \cdot 10^{24} \text{ cm}^{-3}$  at 550 K) [2.13]. Novikova et al. have performed a numerical modeling of hydrogen plasma and have shown  $N_{\text{H}}$  is around  $10^{14} \text{ cm}^{-3}$  [2.14].  $\mu_{\text{H}}$  is an important growth parameter and is strongly related to the structure of a-Si:H. An increase in  $\mu_{\text{H}}$  breaks weak Si-Si bonds and passivates dangling bonds, which leads to a sharp valence band tail. Weak Si-Si bonds which lie below the  $\mu_{\text{H}}$  are broken while stronger bonds remain. Therefore, the structural order of the film material greatly depends on  $\mu_{\text{H}}$ . In a simple material, the concentration of hydrogen should increase as the chemical potential is raised at least in general terms, nevertheless actual deposition process and gas phase reactions are much more complicated. In extreme case, excess hydrogen in the plasma induces a transition to microcrystalline silicon ( $\mu\text{c-Si:H}$ ). A possible explanation is that  $\mu_{\text{H}}$  is increased by  $\text{H}_2$  dilution to a critical point that there is no amorphous structure available with degree of structural order determined  $\mu_{\text{H}}$ . The transition to crystalline growth is enhanced by high H concentration in the plasma, high RF power, and optimum  $T_{\text{s}}$ , since all three raise the chemical potential. More practical view on hydrogen role such as etching, chemical annealing, and surface diffusion can be found in references elsewhere [2.8-2.10].

It is thought that powder formation in the plasma is initiated by the nucleation and agglomeration of particles (less than 3 nm in diameter), and begins through polymerization of the species. In the explanation of the initiation of powder formation, there are two schools of thought. One school explains that powder formation starts from an insertion reaction of SiH<sub>2</sub> with SiH<sub>4</sub> forming Si<sub>2</sub>H<sub>6</sub> [2.15, 2.16], thus the reaction can be expressed as,



The other school [2.17, 2.18] suggests condensation reaction below,



Powder formation is indeed very pronounced under high pressure [2.19], and pm-Si:H is produced under plasma conditions close to the powder formation [2.19]. The most significant difference in plasma conditions of pm-Si:H in comparison to a-Si:H is high pressure and high RF power [2.20], which are related to the residence time and the electron density, respectively. The presence of primary radicals and longer residence time increases the probability of collisions between radicals. Primary negative ions can react, giving rise to a first nucleation, but additional polymerization reactions need a hydrogen loss from the surface. However, secondary negative ions can strongly polymerize in a chain reaction, be confined in the plasma and contribute to growth of the particles inside the plasma [2.21]. The increase in the total pressure results an increase in the density of growth precursors in the plasma, followed by onset of agglomeration with a sharp increase in the  $r_d$ . Such transition in silane plasma chemistry to the “dusty” regime is called the  $\alpha$ - $\gamma'$  transition [2.22], and there is a sharp edge between  $\alpha$ - $\gamma'$  transition, the deposition contributed by agglomerates of the primary particles [2.23].

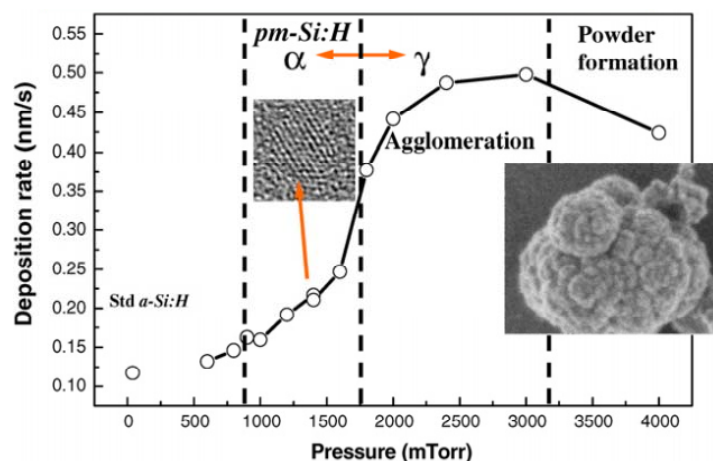


Figure 2.5 – Schematic of the process of powder formation in silane plasmas. Starting from silicon radicals, it leads to formation of nanometer size clusters and nanocrystals that can be considered as the primary nanoparticles. Their density increases with the total pressure until a critical concentration of  $10^{11} \text{ cm}^{-3}$ , above which they form agglomerates of 10 nm. This process can continue by the formation of larger agglomerates and end with the formation of larger powders. Depending on the plasma conditions, the whole process from the primary particles up to the powders can take a few seconds or it can be sustained under a steady state at some intermediate stage. In the case of pm-Si:H deposition the agglomeration phase is avoided by keeping the pressure at values for which the characteristic time for diffusion is smaller than the agglomeration time. Result from Ref [2.23].

Figure 2.6 shows QMS scanned molecular mass distribution of plasma species under conditions of pm-Si:H and a-Si:H deposition. In both a-Si:H and pm-Si:H deposition, there is a decrease in  $\text{SiH}_x$  signal (molecular mass  $\sim 30$ ) that is attributed to the fact that the silane is dissociated and consumed to the deposition. An increase in  $\text{SiH}_x$  species is undetectable because the QMS was installed at the gas exhaust line (right after the throttle valve). Unstable radicals are expected to recombine into  $\text{SiH}_4$ . An interesting point is that poly-silane species, such as  $\text{Si}_2\text{H}_x$  (molecular mass  $\sim 60$ ) and  $\text{Si}_3\text{H}_x$  (molecular mass  $\sim 90$ ), are significantly detected during pm-Si:H deposition. There is no higher order silane species signal in a-Si:H deposition condition. Detection of the higher order silane species is one of the most distinguished differences of pm-Si:H in comparing to a-Si:H, and the higher order silane species are believed to initiate the nanoparticle growth and contribute in the deposition of pm-Si:H. One can notice that the detection of poly-silane species by QMS could also

## 2.3 a-Si:H and pm-Si:H deposition

be indicative of the existence of larger poly-silane species (e.g.  $\text{Si}_x\text{H}_x$ ,  $x > 3$ ), and the signal detected by the QMS could be only the fragments of the larger poly-silane species.

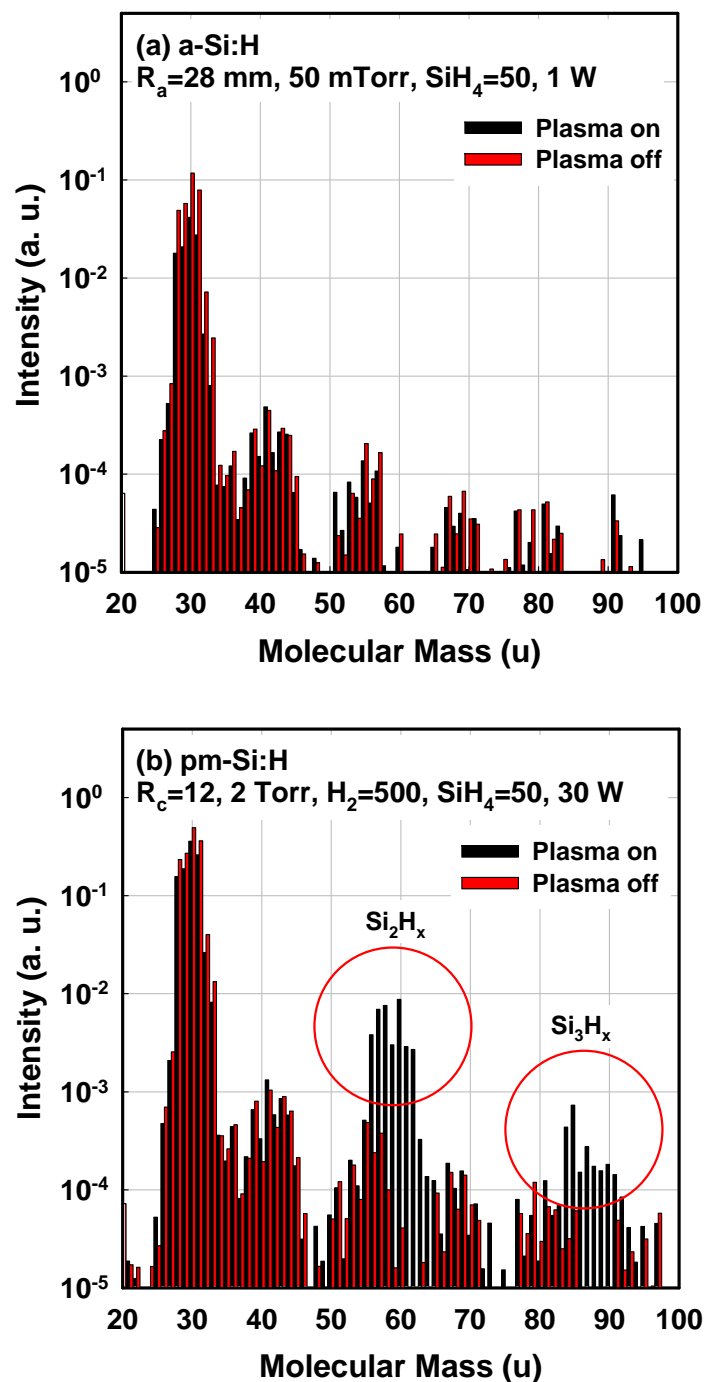


Figure 2.6 – QMS scanned molecular mass distribution of (a) a-Si:H and (b) pm-Si:H deposition condition at plasma on/off condition. Note that in pm-Si:H deposition condition, higher-order silane species such as  $\text{Si}_2\text{H}_x$  and  $\text{Si}_3\text{H}_x$  are observed.

Greater gas residence time is a key factor leading to nanoparticle formation. The growth of nanoparticles is partially determined by gas residence time,  $\tau_r$  [2.24]. The  $\tau_r$  can be defined as,

$$\tau_r \text{ (s)} = \frac{P \cdot Vol_r}{Q}$$

where  $P$  is pressure in Torr,  $Vol_r$  is volume of reactor in  $l$  (16  $l$  in ARCAM), and  $Q$  is total gas flow [2.26]. Unit of gas flow is usually in standard cubic centimeters per minute (sccm) and can be converted into  $\text{Torr} \cdot l \text{ (sec)}^{-1}$  using the conversion relation below,

$$1 \text{ (sccm)} = 0.0127 \left( \frac{\text{Torr} \cdot l}{s} \right)$$

In case of Figure 2.6,  $\tau_r$  of a-Si:H and pm-Si:H is found to be 1.13 and 4.58 s, respectively.

In practice, the plasma process condition of pm-Si:H is very different from that of a-Si:H. Even by observing the matching capacitance of the a-Si:H and pm-Si:H processes, one can see that the plasma impedance of those two deposition conditions are far apart. Nevertheless, the uniqueness of pm-Si:H from a-Si:H can be an endless debate because of the difficulty in the detection of structural uniqueness of pm-Si:H. Currently, the detection of nanocrystals is only possible by transmission electron microscopy (TEM). In spite of the difficulty in the detection of the plasma generated nanoparticle, their contribution is still considered the a feature of pm-Si:H deposition [2.25]. More work on the deposition mechanism and plasma process is needed, but the aim of this thesis is the fabrication of solar cells consisting of pm-Si:H and the study on their light-induced degradation. Therefore, readers should note that the discussion in this work on pm-Si:H is based on our current understanding of its growth mechanism (including a contribution to the deposition of plasma synthesized

silicon nanoparticles).

## 2.4 Gas flow rate series

Higher  $\text{SiH}_4$  partial pressure is one way to increase  $r_d$ , so the effect of different process gas flows was studied. The gas flow ratio of  $\text{SiH}_4$  and  $\text{H}_2$  was varied while the other process parameters were fixed e.g. pressure = 3.5 Torr,  $T_s = 210$  °C, RF = 30 W. Gas flow ratio R is defined as;

$$R = \frac{\text{SiH}_4}{\text{SiH}_4 + \text{H}_2}$$

where  $\text{SiH}_4$  and  $\text{H}_2$  are the gas flow rate of gas in sccm. The films are deposited on flat corning glass. SE measurement and modeling result are provided. Typical values for a-Si:H are also marked as  $\times$ . The goal of this chapter is to demonstrate the trend of the material properties during the parametric studies.

QMS analysis of signal intensity ratio  $\text{SiH}_x$  to  $\text{Si}_2\text{H}_x$  is shown in Figure 2.7(a). The result gives interesting view on the effects of gas flow on pm-Si:H deposition, as this signal ratio could represent a proportional measure of nanoparticle formation. Figure 2.7(a) shows  $\text{Si}_2\text{H}_x/\text{SiH}_x$  and  $\text{Si}_3\text{H}_x/\text{SiH}_x$  ratio as functions of gas flow ratio R. Total pressure and RF power were fixed at 2 Torr and 30 W, respectively. The total gas pressure was kept constant by adjusting the throttling valve. Increasing the  $\text{H}_2$  dilution reduces  $\text{Si}_2\text{H}_x$  and  $\text{Si}_3\text{H}_x$  concentration in the plasma. Ifuku et al. have studied the behavior of plasma generated nanoparticles under different  $\text{H}_2$  flow, and have shown that average particle size decreases when  $\text{SiH}_4$  was diluted by  $\text{H}_2$  [2.24]. For the formation of the nanoparticles in the plasma, polymerization of the species is needed. The nucleation and agglomeration of the species or particles are enhanced by larger

concentration of precursor ( $\text{SiH}_4$  partial pressure or total pressure). When the gas flow ratio  $R$  is smaller than 0.025, the film deposition is largely modified. For example, there is no deposition on glass substrate at the gas flow ratio  $R$  of 0.01, while the deposited material changes from  $\mu\text{c-Si:H}$  at 0.02 to  $\text{pm-Si:H}$  at 0.05. The signal intensity ratio for  $\text{a-Si:H}$  deposition (45 mTorr, 1 W, pure silane dissociation) is marked as  $\times$ . When the gas flow ratio  $R$  is lower than 0.025,  $\text{Si}_2\text{H}_x$  signal intensity ratio is small and goes down to  $10^{-3}$ . In other words, there is large difference in concentration of  $\text{Si}_2\text{H}_x$  and  $\text{SiH}_x$  species in plasma. Above a gas flow ratio  $R$  of 0.04, the  $\text{Si}_2\text{H}_x/\text{SiH}_x$  signal intensity ratio increases and saturates. Interestingly,  $\text{Si}_2\text{H}_x/\text{SiH}_x$  and  $\text{Si}_3\text{H}_x/\text{SiH}_x$  intensity ratio show different slopes upon the gas flow ratio  $R$ . It suggests that  $\text{Si}_2\text{H}_x$  and  $\text{Si}_3\text{H}_x$  have different physical origins. In other words,  $\text{Si}_2\text{H}_x$  and  $\text{Si}_3\text{H}_x$  are fragments of different types of higher order silane species. Figure 2.7(b) shows that the  $r_d$  increases under  $\text{SiH}_4$  flow rate, which is interesting, as the  $\text{Si}_2\text{H}_x$  concentration saturates. However, the surface roughness also increases at high  $r_d$ , so notably there is a change in the material.

A low  $\text{SiH}_4$  flow rate (highly diluted silane gas) leads to  $\mu\text{c-Si:H}$  deposition, which indicates that  $\mu_{\text{H}}$  is significantly high in this region. In this region, low  $\text{Si}_2\text{H}_x$  intensity can be attributed to the fact that atomic H dissociates higher order silane species. The atomic H can also prevent agglomeration of growth precursors, passivating the surface of nanoparticles.  $\text{SiH}_4$  can be also recycled by H in plasma from dissociation of higher order silane species. It is important to consider why  $\text{a-Si:H}$  deposition condition also shows low concentration of higher order silane species. Indeed,  $\text{a-Si:H}$  deposition conditions are completely different from  $\text{pm-Si:H}$  deposition condition; they consist of low pressure of 45 mTorr, dissociation of 50 sccm pure  $\text{SiH}_4$ , and low RF power of 1 W. In  $\text{a-Si:H}$  deposition condition, H induced gas phase reaction is much less significant in pure  $\text{SiH}_4$  dissociation, and

nanoparticle formation is suppressed under such low pressure. Silicon nanoparticle growth greatly depends on  $\text{SiH}_4$  partial pressure [2.27] and hydrogen dilution [2.24]. Therefore formation of higher order silane species is not expected in a-Si:H deposition condition. Auxiliary SE results obtained in this study can be found in annex 2.1.

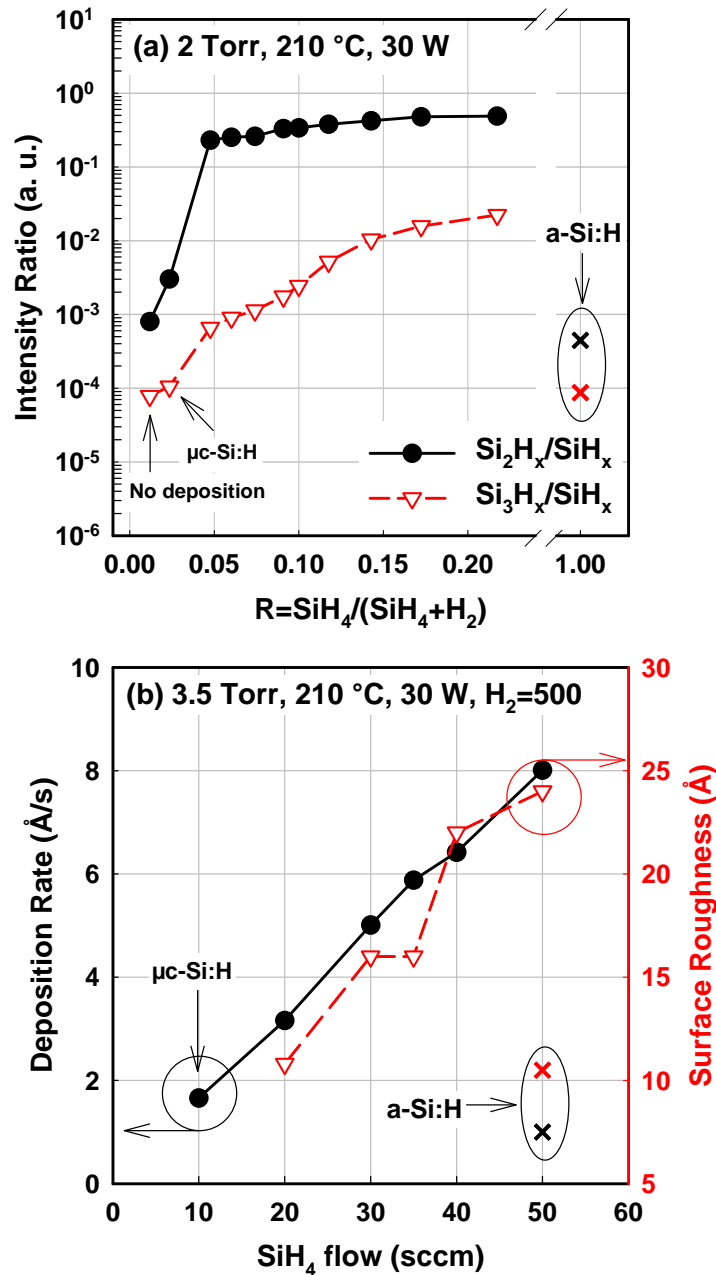


Figure 2.7 – Representative results of gas flow series. (a) QMS analysis of signal intensity ratio of  $\text{Si}_2\text{H}_x$  to  $\text{SiH}_x$  and  $\text{Si}_3\text{H}_x$  to  $\text{SiH}_x$  as functions of gas flow ratio  $R$ , and (b)  $r_a$  and surface roughness as functions of  $\text{SiH}_4$  flow.

### 2.5 Pressure series

High pressure deposition leads to a reduction of the ion energy [2.28, 2.29], denser material [2.30] as well as high  $r_d$  [2.31]. High energy of the positive ions causes ion bombardment on growing film surface [2.32], thus results high defect density material and poor device [2.28, 2.33]. On the other hand, high pressure deposition conditions risk powder formation [2.34] that are associated with a deterioration of the film quality due to the production of pinholes, roughness and porosity [2.35], and columnar growth [2.36]. Indeed, in the high  $r_d$  condition, the characteristics of plasma deposition process changes, which is characterized by the impinging species having a high sticking coefficient that each molecule remains where it first strikes at the growth surface. In that case the growth rate is determined by the flux of species striking the surface.

Figure 2.8 shows  $r_d$  and surface roughness as functions of deposition pressure. Deposition pressure was adjusted by controlling throttle valve opening, thus also changing the residence time of ionized gas species. A link between powder formation and residence time (dependence on gas flow and pressure) has been observed for deposition [2.24], and the generation of powder is highly facilitated by increasing residence time [2.37]. Therefore, a short residence time (high gas flow rate or low pressure) is required to suppress powder formation. In Figure 2.8, the total pressure was varied from 2 to 5.5 Torr, which for the ARCAM reactor, means that  $\tau_r$  was changed from 4.53 to 12.2 s. The surface roughness was estimated from two different methods, SE modeling and AFM measurement. In Figure 2.8,  $r_d$  and surface roughness increase when the deposition pressure increases. SE roughness and RMS roughness by AFM show similar trends.

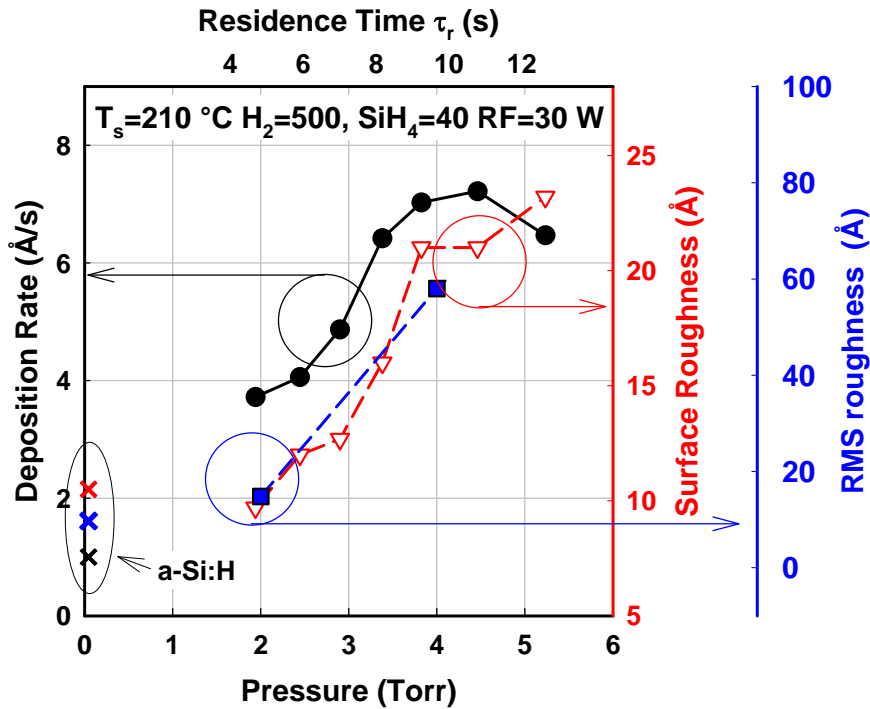
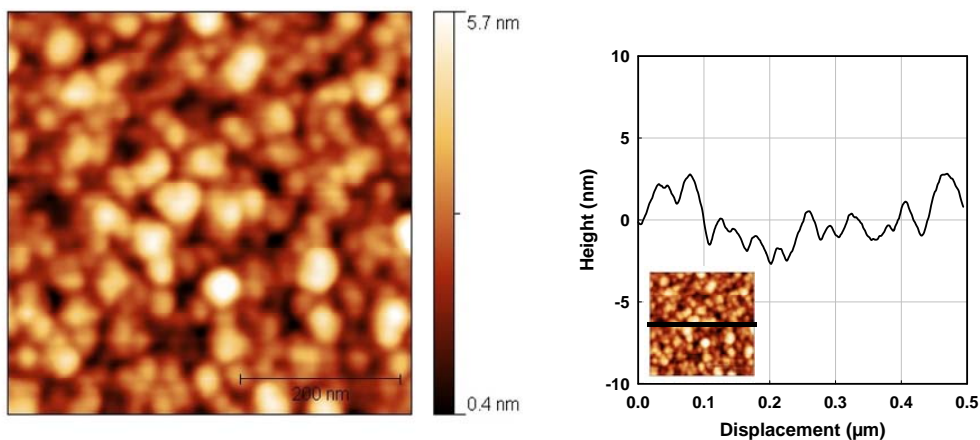


Figure 2.8 –  $r_d$ , SE surface roughness, and AFM measured RMS roughness as functions of deposition pressure. Calculated residence time at each pressure is marked at top. Typical values for a-Si:H are also given as reference.

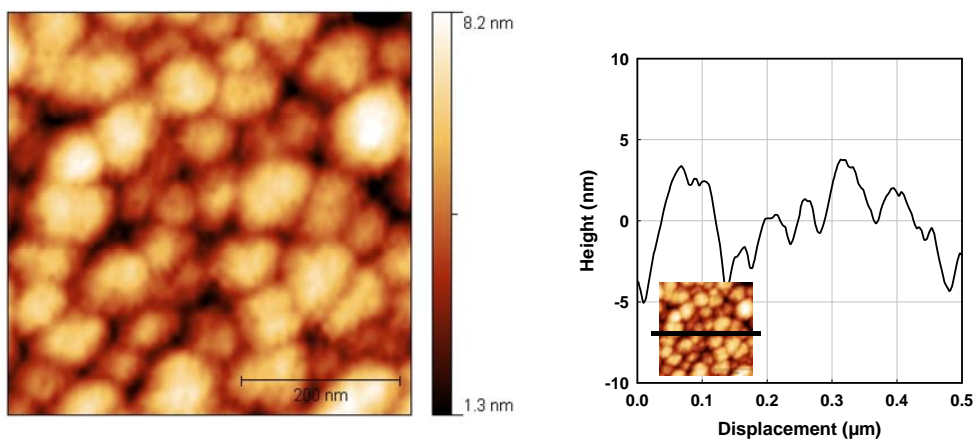
Regarding the correlation between powder formation and residence time [2.24, 2.37], we suggest that higher  $r_d$  at high pressure possibly comes from higher concentration of growth precursor generated in the plasma. At the same time, deposition at very high pressures ( $P > 3$  Torr) increases the surface roughness. One of the possible explanations on the surface roughness evolution is the contribution of the positively charged precursors. At high pressure, one can imagine the high concentration of ions leads to high concentration of positively charged growth precursors. The effect of the deposition condition on the surface morphology is reflected by a set of AFM images.

Figure 2.9 shows AFM images of standard a-Si:H, pm-Si:H deposited at 2 Torr and pm-Si:H deposited at 4 Torr. Increasing the pressure from 45 mTorr to 4 Torr leads to an increase in both RMS roughness and surface feature size. The surface feature in Figure 2.9(b)

**(a) a-Si:H at 45 mTorr**  
RMS ~ 0.97 nm



**(b) pm-Si:H at 2 Torr**  
RMS ~ 1.48 nm



**(c) pm-Si:H at 4 Torr**  
RMS ~ 5.8 nm

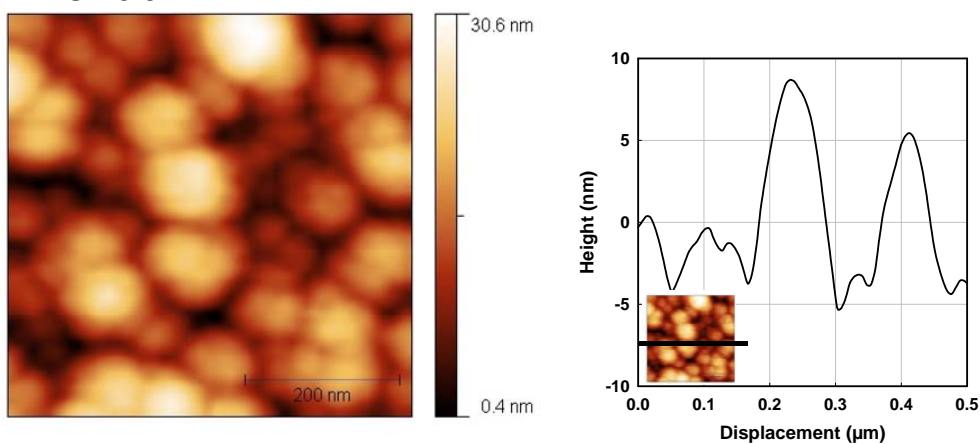


Figure 2.9 – AFM images and its cross-section of (a) standard a-Si:H, (b) pm-Si:H deposited at 2 Torr, and (c) pm-Si:H deposited at 4 Torr. Note that at higher pressure, larger surface features and rougher surface is observed. Note that the size of the bumps cannot be attributed to individual nanoparticles (a few nanometers).

and (c) could be interpreted as surface roughness introduced by high sticking coefficient. It should be noted that the height of the surface feature (several nanometers) is orders of magnitude smaller than the surface feature size of few hundred nanometers.

One can notice that the deposition at pressure above 3 Torr results in material with high roughness and high porosity. Hydrogen exodiffusion sensitively detects interconnected voids in the material; in particular a-Si:H materials demonstrate that a void related microstructure is a major source of defects [2.38, 2.39]. Figure 2.10 shows exodiffusion spectra of a set of pm-Si:H films deposited under different pressure values from 2 to 5 Torr.

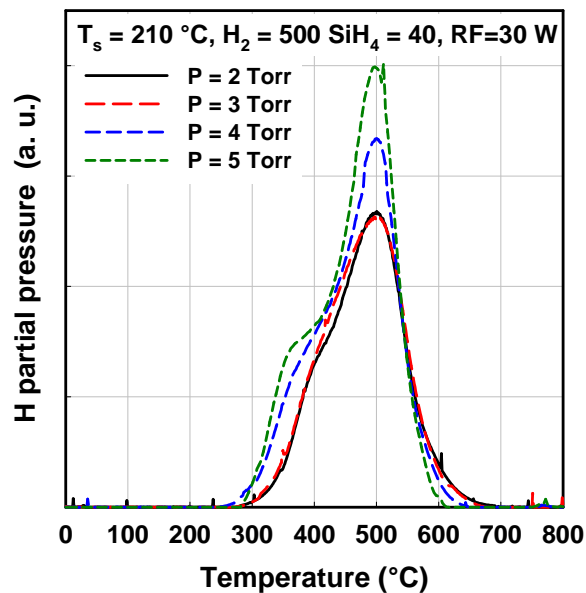


Figure 2.10 – Hydrogen exodiffusion spectra of a set of pm-Si:H films deposited under different pressure from 2 to 5 Torr.

Figure 2.10 shows that increasing deposition pressure increases hydrogen evolution at both 350 °C and 500 °C. In particular, hydrogen evolution at 350 °C is closely related to the porosity of the material. Material structure with a high degree of columnar morphology or extensive internal inhomogeneity evolves a large amount of hydrogen

between 300-400 °C with further evolution near 500-600 °C, while samples made under CVD growth conditions have only the higher temperature peak [2.40]. The evolution peak at 300-400 °C is also considered to be molecular hydrogen release from internal surface of interconnected voids [2.41] or from silicon nanoparticle surfaces [2.42]. Moreover, in case of silicon nanoparticles, the low temperature hydrogen effusion peak shifts to lower temperature when larger nanoparticles are incorporated [2.42]. Therefore, one can conclude that high pressure deposition results in higher porosity. Another interesting point is that the shoulder of exodiffusion spectra at 600 °C slightly decreases at higher deposition pressure. The exodiffusion shoulder at 600 °C indicates hydrogen evolution from isolated voids [2.6]. Therefore, increase in deposition pressure of pm-Si:H resulted in a decrease in the isolated void density and increase in interconnected void density. Such trend could also imply a larger area of internal surface, providing more space to hydrogen. A trade-off seems to exist between the interconnected voids (350 °C shoulder) and isolated voids (600 °C shoulder). The last point is that high pressure deposition also increases the hydrogen evolution signal at 500 °C, which is thought to be bound Si-H [2.40]. The existence of a low temperature exodiffusion peak can be also interpreted as incomplete structural re-construction [2.38]. Auxiliary results obtained for this pressure series can be found in annex 2.2.

### **2.6 RF power series**

Increasing the RF power is another way to increase the  $r_d$ . As a higher RF power results a higher electron density in the plasma, the dissociation rate increases [2.43, 2.44]. However, the rise in the electron density increases ionization and polymerization becomes more intense, which leads to uncontrolled growth of powder. As mentioned

in the pressure series section, an increase in  $r_d$  can lead to high surface roughness and deteriorate the material quality. Furthermore, high RF power causes high ion bombardment energy for the positive ions on growing film surface [2.32]. Controlling the voltage waveform of the plasma excitation source could be helpful solution controlling of the powder production through the primary parameters [2.45].

Figure 2.11 shows  $r_d$ , surface roughness and the microstructure parameter R (defined below) as functions of RF power.

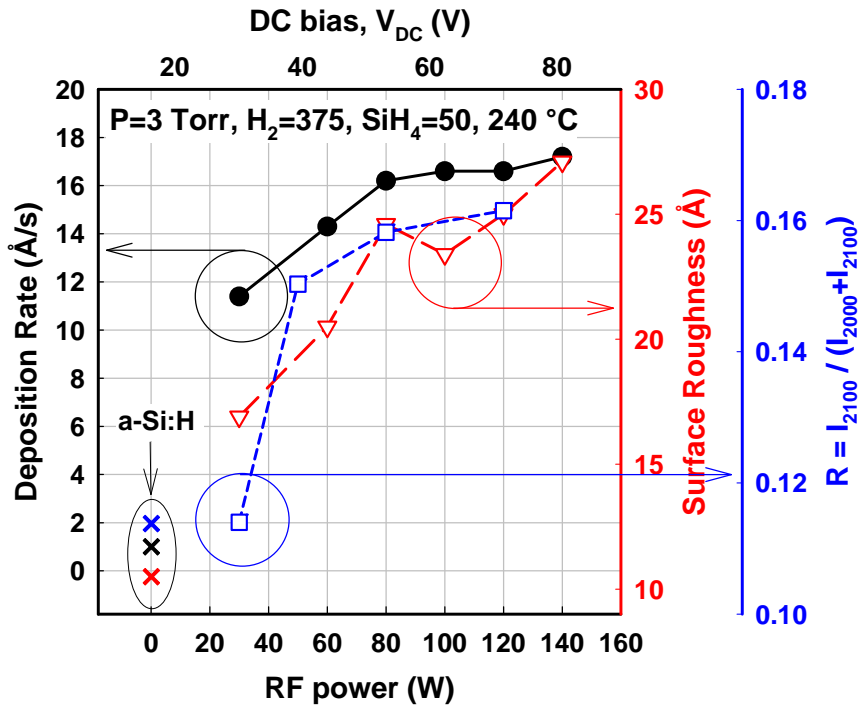


Figure 2.11 –  $r_d$ , surface roughness and microstructure parameter R as functions of RF power. DC bias on the RF electrode is marked at top. Typical values for a-Si:H are also given as reference.

The microstructure parameter R is defined as

$$R = \frac{I_{2100}}{I_{2100} + I_{2000}}$$

and the microstructure parameter R is typically described as a ratio of

dihydrides to monohydrides. Even though the a-Si:H microstructure has been the subject of a continuing debate, the microstructure parameter  $R$  is believed to indicate the concentration of nanovoids [2.46], and there is a correlation between microstructure and material properties in the sense that material and device stability deteriorates with increasing nanovoid density [2.46, 2.47]. Microstructure parameter  $R$  is related to the fraction of dihydrides, and it is also reported that a high amount of dihydrides in the film has the same result as a high nanovoid density [2.8]. In Figure 2.11,  $r_d$  and surface roughness increase with RF power. One might expect that high RF power creates higher concentration of growth precursors and further contributes to high  $r_d$ . One can also notice that the increasing surface roughness can be often associated to a signature of material deterioration, as discussed in the pressure series section.

Further information of hydrogen bonding is obtained from the evolution of FTIR stretching mode spectra with RF power. Figure 2.12 shows FTIR stretching mode spectra of pm-Si:H produced at varying RF power. With increasing RF power, hydrogen content ( $C_H$ ) of pm-Si:H film increase up to 22 at.%, but the evolution of FTIR stretching mode of pm-Si:H differs from that of a-Si:H as reported in the literature [2.48]. In such results for a-Si:H, at such high  $C_H$ , the fraction in the  $2100\text{ cm}^{-1}$  peak becomes very significant and even larger than at  $2000\text{ cm}^{-1}$ , but in pm-Si:H, the evolution of  $2100\text{ cm}^{-1}$  fraction is much less pronounced. Indeed, the evolution of the FTIR stretching mode of pm-Si:H resembles that of a-Si:H deposited by magnetron sputtering [2.49]. This modest evolution of the dihydrides peak in pm-Si:H could be explained by claiming that plasma generated nanoparticles are heavier than radical species, and therefore have a higher sticking coefficient. Moreover, increasing sheath potential at high RF power would accelerate any positively charged nanoparticles.

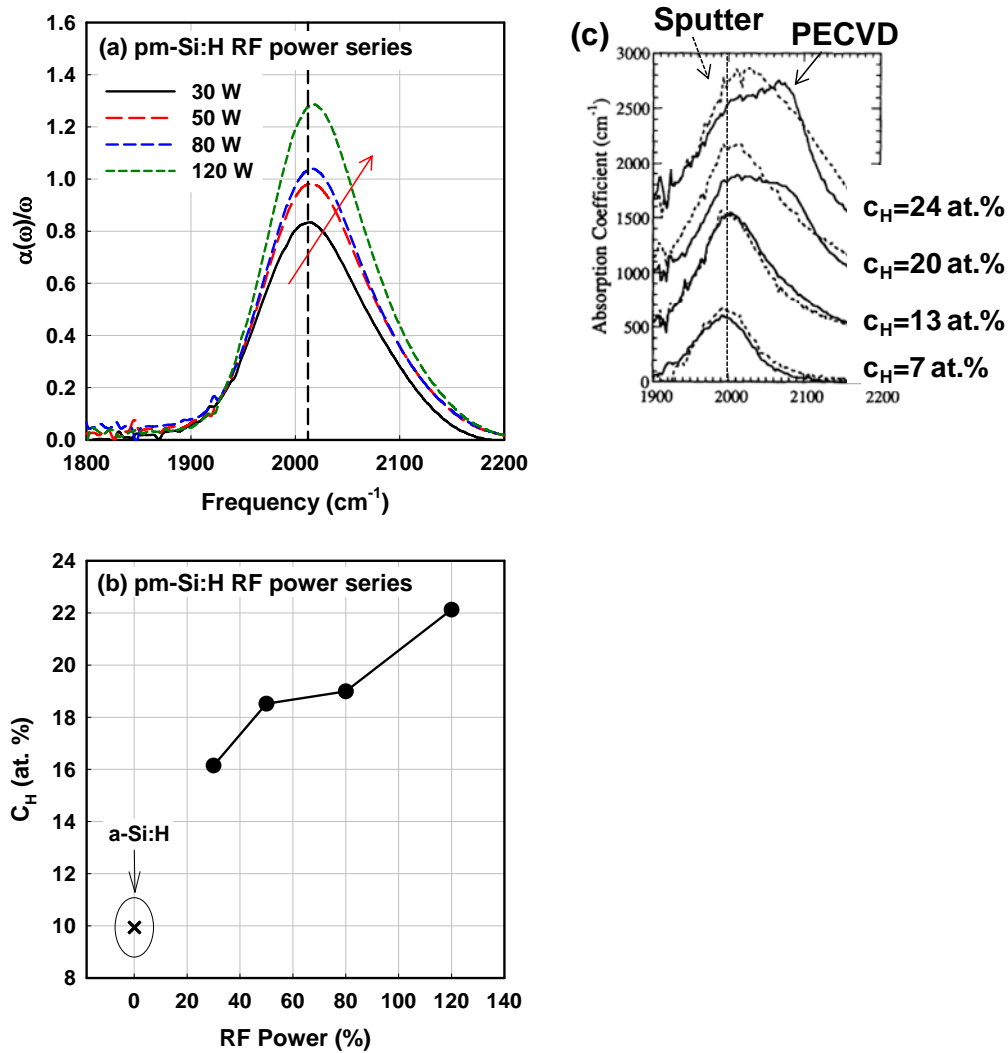


Figure 2.12 – (a) FTIR stretching mode spectra of pm-Si:H under various RF power and (b) hydrogen content calculated from (a). Note that stretching mode peak shifts towards higher wavenumbers with higher RF power. Hydrogen content of a-Si:H is marked as cross. (c) FTIR stretching mode absorption spectra of a-Si:H films deposited by PECVD (solid) and magnetron sputtering (dashed lines). Spectra are shown in pairs to compare features for samples with hydrogen content of 7, 13, 20, and 24 at.%. The result from Ref [2.49].

In Figure 2.12(a), the evolution of the FTIR stretching mode spectra of pm-Si:H with various RF powers showed the peak shift to a higher frequency region, and this shift is separated into a low stretching mode (LSM) and a high stretching mode (HSM) peaks in Figure 2.13 (a), (c), and (e), using the peak position of LSM and HSM bands at 1990 cm<sup>-1</sup> and 2090 cm<sup>-1</sup>, respectively. Using such a deconvolution for pm-Si:H, the medium stretching mode (MSM), band centered at 2030 cm<sup>-1</sup> [2.20] has been interpreted as Si-H bonds at

silicon nanocrystal surfaces [2.50], and as an increase in surface/volume ratio [2.42].

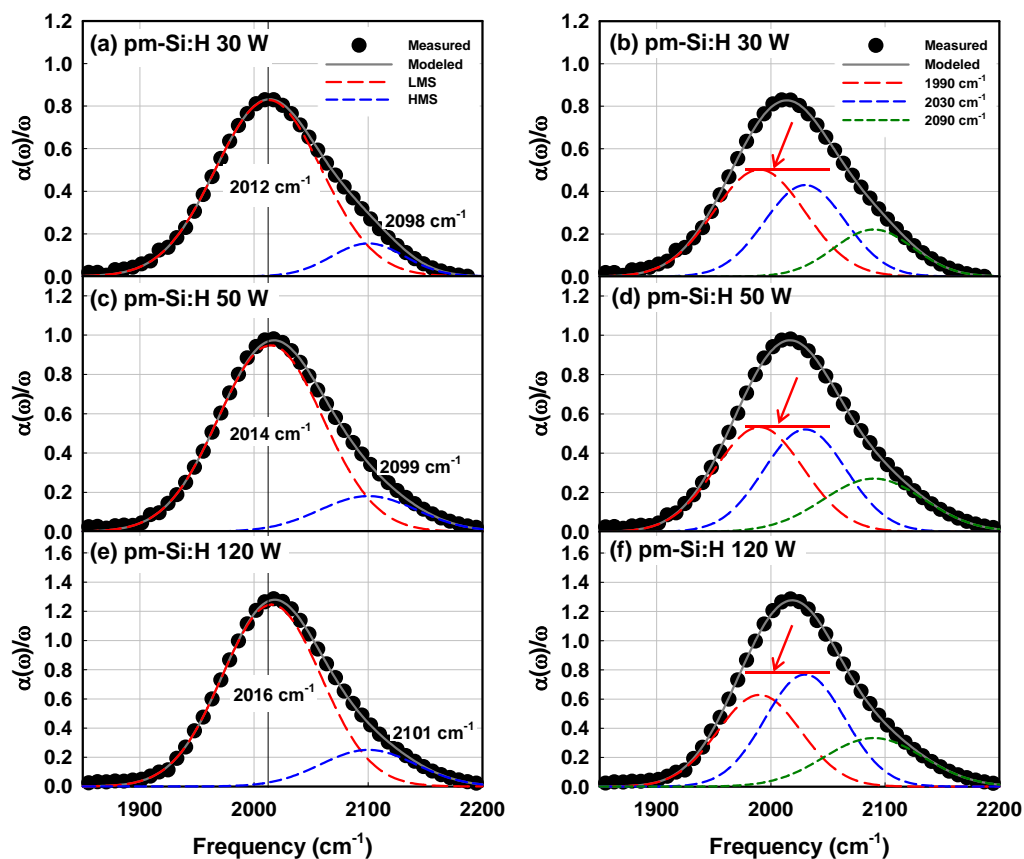


Figure 2.13 – Demonstrations of stretching mode deconvolution of spectra shown in Figure 2.12(a). In (a), (c), and (e), the spectra are deconvoluted into classical two modes. In this case, both LSM and HSM show peak shift. In (b), (d), and (f), the spectra are deconvoluted into three modes including MSM at 2030  $\text{cm}^{-1}$ . It is shown that the stretching mode peak shift can be attributed to the evolution of MSM mode.

In Figure 2.13, an alternative three peak deconvolution is demonstrated in (b), (d), and (f). In this three-band deconvolution, the peak position of the LSM, MSM, and HSM are fixed to 1990, 2030, and 2090  $\text{cm}^{-1}$ , respectively. It is seen that the evolution of MSM mode is remarkable, and therefore the stretching mode peak shift could be also attributed to the evolution of MSM band. In Ref [2.49], Langford et al. described the evolution of stretching mode as a “broadening”. However, at that time, the existence of 2030  $\text{cm}^{-1}$  band was not recognized.

Gradual stretching mode peak shift to higher frequency can be attributed to larger internal surface, under higher RF power. Table 2.1 summarizes the fitting parameters of the deconvolution in Figure 2.13. Auxiliary results obtained in RF power series can be found in annex 2.3.

		RF power (W)	30	50	120
2 peaks	LSM	Center	2012	2014	2016
		Area	67.1	81.12	97.1
		FWHM	109.6	108.4	108.0
	HSM	Center	2098	2099	2101
		Area	9.25	10.54	12.45
		FWHM	75.6	100.6	101.8
Total Area		76.35	91.66	109.55	
3 peaks	1990	Area	35.21	36.12	39.11
		FWHM	94.1	91.0	85.7
	2030	Area	26.6	34.04	46.25
		FWHM	83.1	85.1	86.5
	2090	Area	14.91	21	24.41
		FWHM	82.0	104.2	105.4
	Total Area		76.72	91.09	109.77

Table 2.1 – Fitting parameters of the FTIR stretching mode deconvolution in Figure. 2.13. Note that in three peaks deconvolution each peak positions are fixed.

## 2.7 $T_s$ series

At the deposition temperature of  $150 < T_s < 400$  °C, the growing surface is covered by hydrogen [2.51]. Surface hydrogen coverage is reduced at higher temperature, and the growth surface is no longer covered by hydrogen at  $T_s > 400$  °C [2.29]. One must recall that regarding the chemical potential  $\mu_H$ , the optimum growth temperature of  $150 < T_s < 300$  °C is explained by the balance between hydrogen diffusion and interactions. At  $T_s < 100$ , the diffusion coefficient of H is too low to allow structural equilibration. At higher temperatures, the H diffusion is fast enough to allow the film structure and H content to be determined by the  $\mu_H$ . The surface reactions first establish a

structural order determined by  $\mu_{\text{H}}$ , and then continue to remove hydrogen. At  $T_{\text{s}} < 400$ , temperature reduces  $\mu_{\text{H}}$ , thus induces disordered film at a lower hydrogen concentration. Optimum films are therefore grown at the lowest temperature at which the kinetic limitation can be avoided [2.13]. Increase in  $T_{\text{s}}$  decreases hydrogen content ( $C_{\text{H}}$ ) [2.11, 2.43]. Moreover, the material stability largely relies on the dihydride concentration [2.8], so an increase in  $T_{\text{s}}$  would make more stable material.

Figure 2.14 shows the  $r_{\text{d}}$ , surface roughness and optical bandgap ( $E_{\text{opt}}$ ) as functions of  $T_{\text{s}}$ . One can notice that the effect of  $T_{\text{s}}$  on the  $r_{\text{d}}$  is quite small compared to that of pressure or RF power. However, there is a moderate decrease in the  $r_{\text{d}}$  at the  $T_{\text{s}}$  higher than 210 °C, and it is attributed that high  $T_{\text{s}}$  suppresses initiation of nanoparticles [2.52-2.54]. At high temperature, thermal motion of particles is highly stimulated, thus the diffusion of (negatively charged) growth precursor is facilitated. Therefore, growth precursors have higher probability to escape the plasma, thus prevent powder formation. In addition, through a similar mechanism, narrow inter-electrode distance also prevents powder formation [2.55, 2.56], but the smallest inter-electrode distance (12 mm) is used in this study, so we are already taking benefit from the narrow inter-electrode distance. It is another interesting result that  $E_{\text{opt}}$  decreases as  $T_{\text{s}}$  increases. It suggests that there is structural change in pm-Si:H deposited at high  $T_{\text{s}}$ .

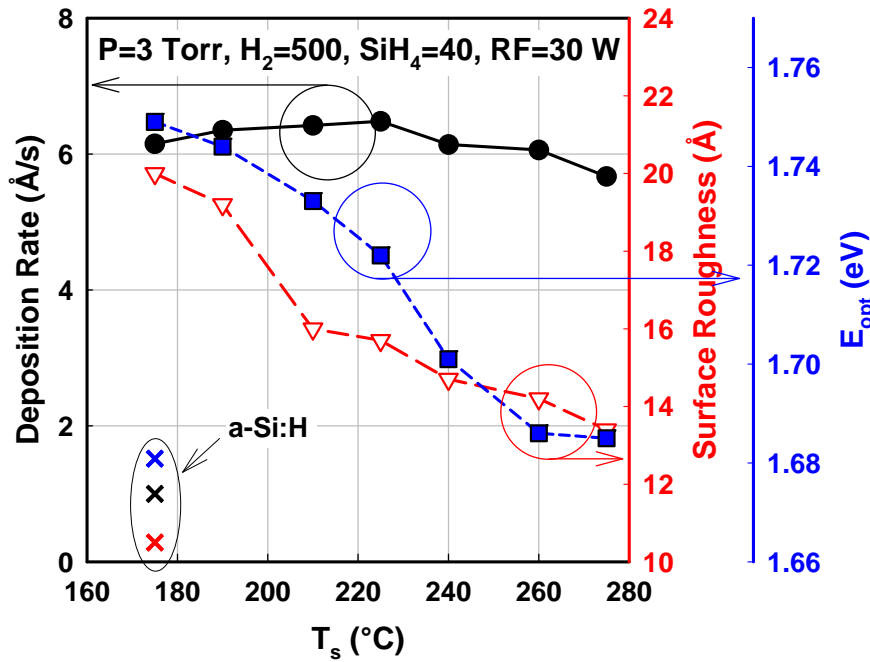


Figure 2.14 –  $r_d$ , surface roughness and optical bandgap as functions of  $T_s$ .

Figure 2.15(a) shows exodiffusion spectra of pm-Si:H deposited at different  $T_s$  from 175 °C to 275 °C. Figure 2.15(b) also shows  $C_H$  and microstructure parameter  $R$ . At higher  $T_s$ , hydrogen evolution at both 350 °C and 500 °C is reduced. Exodiffusion result is again coherent with decreased  $C_H$  and microstructure parameter  $R$  deduced from FTIR. Recalling that both exodiffusion peak at 350 °C and microstructure parameter  $R$  indicate material porosity, the deposition at higher  $T_s$  results in more compact material structure. Suppression of powder formation would be significant at high  $T_s$ , and it is attributed to the dissociation of growth precursors since  $\mu_H$  increase, thus increase in material density at high  $T_s$  can be attributed to the suppression of powder formation.

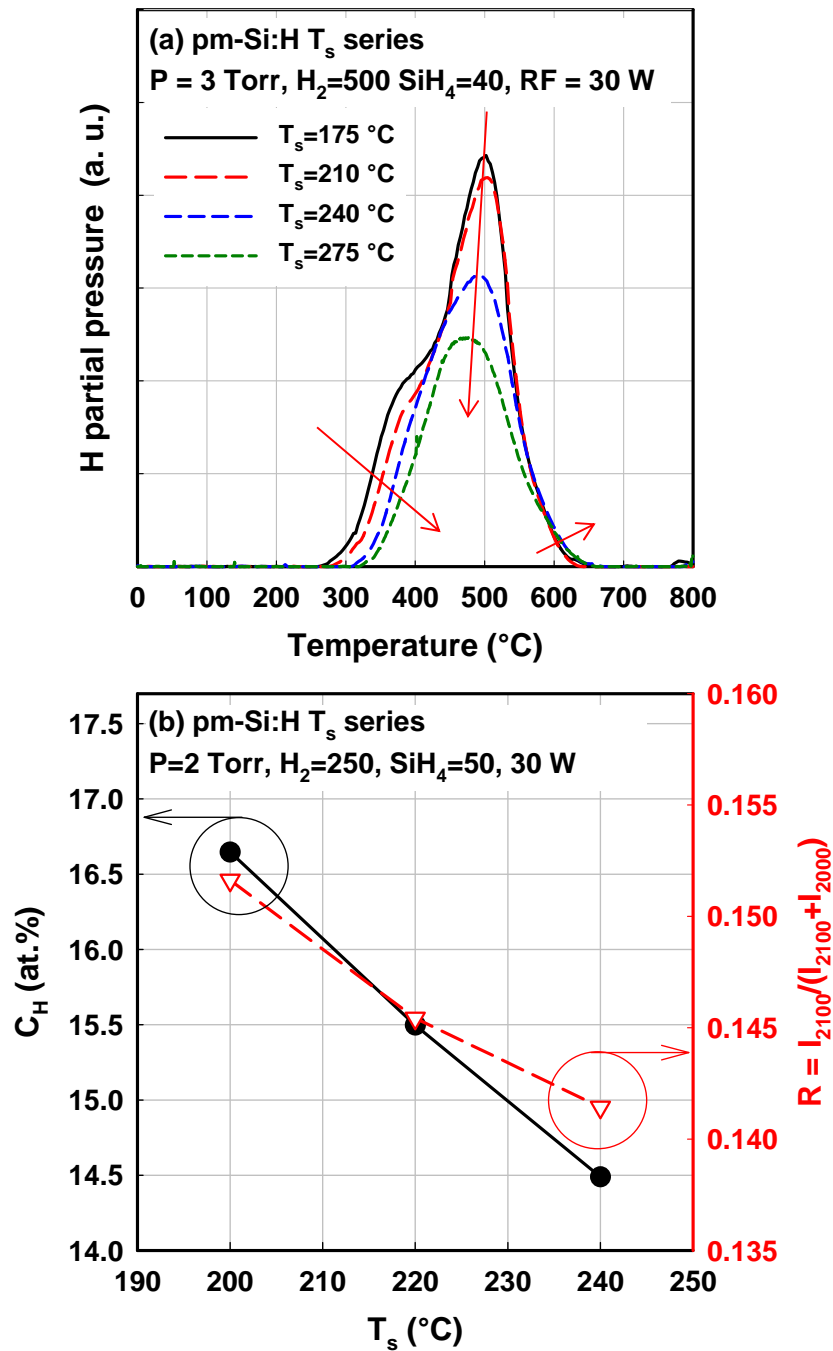


Figure 2.15 – Effect of substrate temperature on hydrogen incorporation in pm-Si:H. (a) Hydrogen exodiffusion spectra of pm-Si:H deposited at different  $T_s$  from 175 °C to 275 °C, and (b) hydrogen content in pm-Si:H and microstructure parameter  $R$  as functions of  $T_s$  as deduced from FTIR study.

Furthermore, the 600 °C shoulder of exodiffusion spectra shows a slight broadening at higher  $T_s$ . This 600 °C shoulder indicates the

density of isolated voids [2.6], and the trade-off between isolated voids and interconnected voids are related to the material porosity, as discussed in previous sections. It is interesting that at higher  $T_s$ , the high temperature exodiffusion peak shifts to lower temperature. A high temperature exodiffusion peak position is decided by material reconstruction during low temperature hydrogen effusion [2.57], so structural modification during deposition should have been more pronounced at high  $T_s$ , due to high  $\mu_H$ .

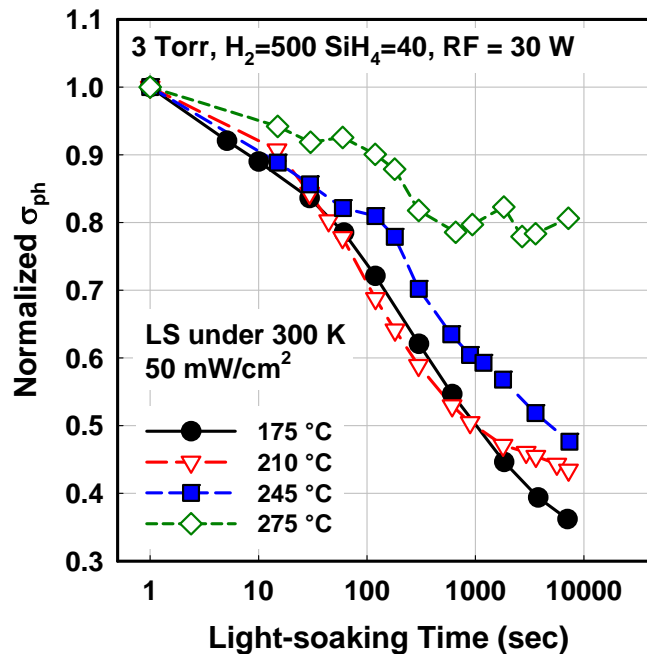


Figure 2.16 – Evolution of normalized photoconductivity as a function of light-soaking time for pm-Si:H films deposited at different  $T_s$ .

At higher  $T_s$ , both  $C_H$  and dihydrides fraction  $I_{2100}$  decreased. Therefore, high temperature deposition could make a stable material. Figure 2.16 shows evolution of normalized photoconductivity as a function of light-soaking time. A series of pm-Si:H deposited at different  $T_s$  from 175 °C to 275 °C are tested. Light-soaking was done at 300 K, under 40 mW/cm<sup>2</sup>. During the light-soaking for  $10^4$  seconds, pm-Si:H deposited at 275 °C showed the lowest light-induced

degradation. Moreover, result shows that magnitude of the light-induced degradation depends on the  $T_s$ , which is attributed to the  $C_H$ .

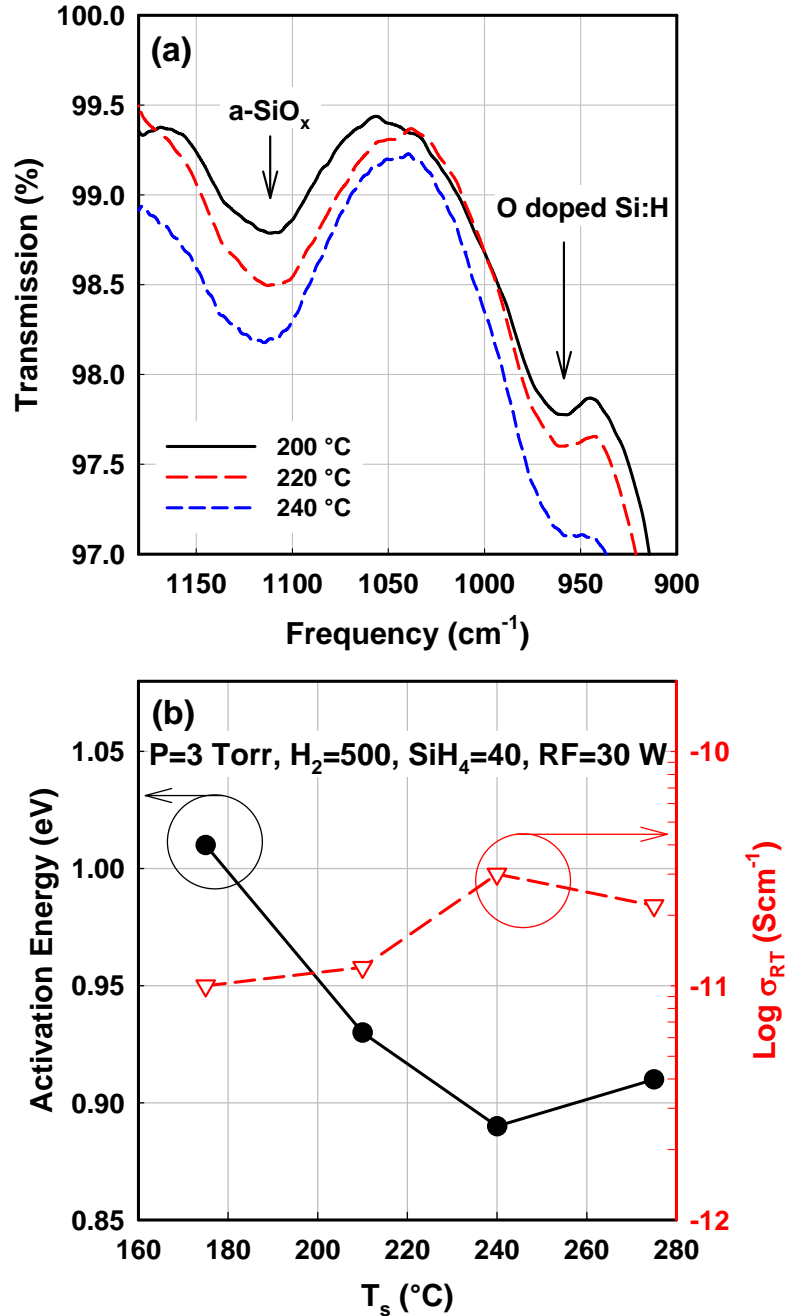


Figure 2.17 – (a) FTIR transmission spectra in Si-O-Si stretching mode region of  $T_s$  series and (b) Activation energy, room temperature conductivity of  $T_s$  series.

At high  $T_s$ , another problem should be considered from a practical point of view. Figure 2.17(a) shows FTIR transmission

spectra in Si-O-Si stretching mode region of the  $T_s$  series of Figure 2.15(b). Two peaks at  $960\text{ cm}^{-1}$  and  $1110\text{ cm}^{-1}$  provide a signature of oxygen-type a-Si:H and amorphous  $\text{SiO}_x$ , respectively [2.58]. It is widely known that oxygen is deleterious impurity acting as a deep-state donor, thus careful effort is needed to reduce the oxygen contamination [2.59]. Indeed, room temperature conductivity and activation energy of those films showed a moderate change and evidence of slight n-type doping, yet the properties are still in the range of intrinsic materials, as shown in 2.17(b). Oxygen may come from leaks due to imperfection of the vacuum system, or more likely, from out-gassing from the inner wall of the reactor. As a matter of fact, ARCAM is a monochamber reactor without loadlock. ARCAM is indeed designed to maintain chemical purity by high gas flow, achieving high process-gas-flow/out-gassing ratio [2.1]. Moreover, in pm-Si:H deposition condition, high pressure is obtained by reducing throttle valve diameter. In other words, pm-Si:H deposition condition in ARCAM consists of relatively high out-gassing in comparison to low pressure a-Si:H deposition. Therefore, in ARCAM, pm-Si:H deposition would be difficult to maintain chemical purity at high temperature. The oxygen contamination issue can be resolved by an addition of a small amount of silicon-tetra-fluoride ( $\text{SiF}_4$ ) [2.60]. Auxiliary results obtained in  $T_s$  series can be found in annex 2.4.

### **2.8 Powder formation and residence time**

This chapter deals with a deposition study of intrinsic pm-Si:H with various plasma conditions. The goal is still to develop high quality material deposited at high  $r_d$ . Plasma deposition is a sensitive process, and any change in plasma process parameters brings various effects. For example, Figure 2.18 shows a SIMS profile of the hydrogen and oxygen content of a RF power series of pm-Si:H deposited on FZ c-Si.

Increasing the RF power results in high  $r_d$ , and high  $r_d$  greatly reduces oxygen content in the films, compared to a-Si:H. In this case, impurities such as oxygen originate from out-gassing or leaks. During the deposition process, one may then consider a precursor gas flow and an additional impurity gas flow. At high  $r_d$ , relatively less supply of the impurity, with respect to  $\text{SiH}_x$ , is expected. However, at higher RF power, reduction of oxygen content becomes less significant, as  $r_d$  saturates at RF powers greater than 80 W (Figure 2.11). Therefore, one can notice that the impurity content can be controlled by the  $r_d$ , but not by the RF power.

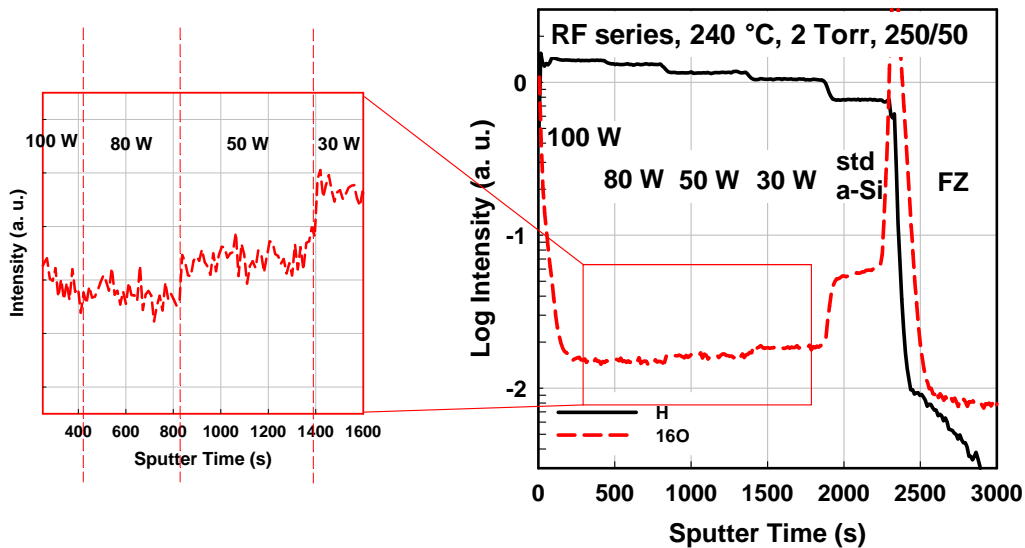


Figure 2.18 – SIMS profile of hydrogen and oxygen content of a RF power series of pm-Si:H deposited on FZ c-Si

Along the same lines, the residence time ( $\tau_r$ ) can be controlled by varying the gas flow while keeping the total pressure and gas flow ratio the same. From larger to low gas flow,  $\tau_r$  becomes longer. At longer residence time, higher impurity content can be expected. Figure 2.19(a) shows the SIMS profile of a total flow series. Figure 2.19(b) also demonstrates that increasing residence time increases the oxygen content but also the hydrogen content.

## 2.8 Powder formation and residence time

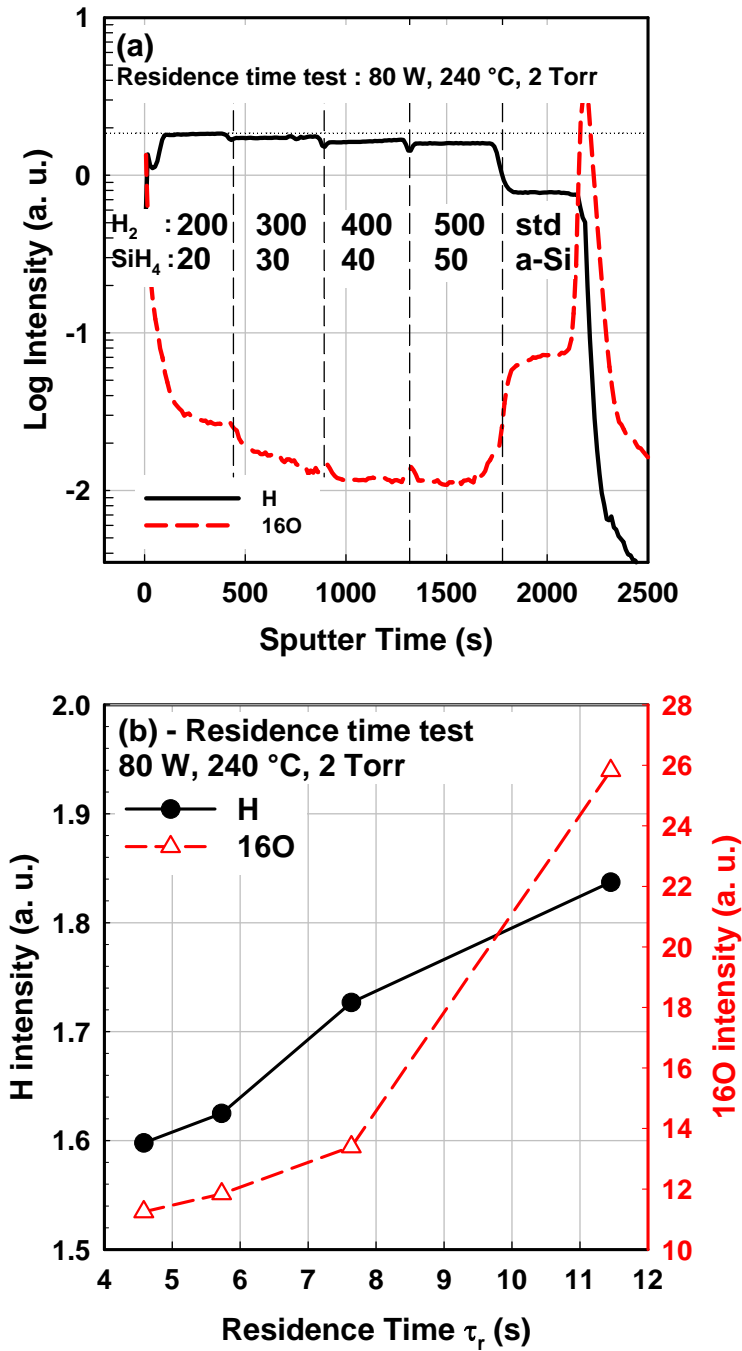


Figure 2.19 – (a) SIMS profile of residence time series. Total pressure and gas flow ratio is fixed, while only gas flow is changed. (b) O and H content from (a) as functions of calculated residence time.

$C_H$  is known to closely relate to optical bandgap ( $E_{opt}$ ) of material [2.61, 2.62]. Figure 2.20(a) shows  $E_{opt}$  versus  $r_d$  of pm-Si:H in various series, such as pressure and RF power. We observe a sharp

increase of  $E_{\text{opt}}$  when  $r_d$  saturates at extreme plasma conditions such as pressure  $> 3$  Torr or RF power  $> 50$  W. The sharp increase of  $E_{\text{opt}}$  is a consequence of the high  $C_H$ , as seen in Figure 2.20(c). Therefore, one can notice that extreme plasma conditions mentioned above do not contribute to a further increase in  $r_d$ , but rather lead to excessive hydrogen incorporation ( $C_H > 16$  at.%). Recalling that long  $\tau_r$  leads to high oxygen content, one is tempted to suggest that high  $E_{\text{opt}}$  originate from  $\text{SiO}_x$  alloy formation, as both oxygen and hydrogen content are linked to widening of  $E_{\text{opt}}$ . However, for device-quality intrinsic layers, the oxygen content is orders or magnitude below that necessary for any alloying effects. For further proof, in Figure 2.14-2.17, as temperature increases, the  $E_{\text{opt}}$  decreases while hydrogen content decreases and oxygen content increase. However, oxygen is an important doping impurity that degrades the material quality [2.63], especially as oxygen incorporation on crystalline silicon is more serious because of higher doping efficiency. Therefore, due to the mixed-phase nature of pm-Si:H, efforts to reduce oxygen content should be taken.

In overall, this chapter deals with pm-Si:H deposition under various plasma conditions, and the most critical issue should be increasing the  $r_d$  while maintaining the material quality. Under extreme process conditions e.g.  $P > 3$  Torr and RF power  $> 50$  W, the material shows notable features of change, such as the evolution of a low temperature exodiffusion peak, a higher  $C_H$ , and the rise of a MSM band. In other words, excessive hydrogen incorporation is a signal for the extreme process conditions of pm-Si:H which do not further contribute to  $r_d$ . Returning to the  $E_{\text{opt}}$  versus  $r_d$  plot in Figure 2.20(a), the consequence of extreme plasma conditions such as pressure  $> 3$  Torr or RF power  $> 50$  W is reflected as excessive hydrogen incorporation that widens  $E_{\text{opt}}$  of the material, without further contributing to deposition rate. Therefore, the  $E_{\text{opt}}$  versus  $r_d$  plot provides a simple diagnostic for this pm-Si:H deposition study on how

much  $r_d$  can be increased while maintaining the material quality. For example, the Tauc plot of Figure 2.20(b) shows that the  $E_{opt}$  of the pm-Si:H deposited at 30 W and 50 W are identical, while the  $E_{opt}$  of the pm-Si:H starts to increase at higher RF power. Figure 2.20 displays that  $r_d$  can be increased up to 16 Å/s while keeping  $E_{opt}$  of about 1.69 eV and  $C_H$  of 16 at.%.

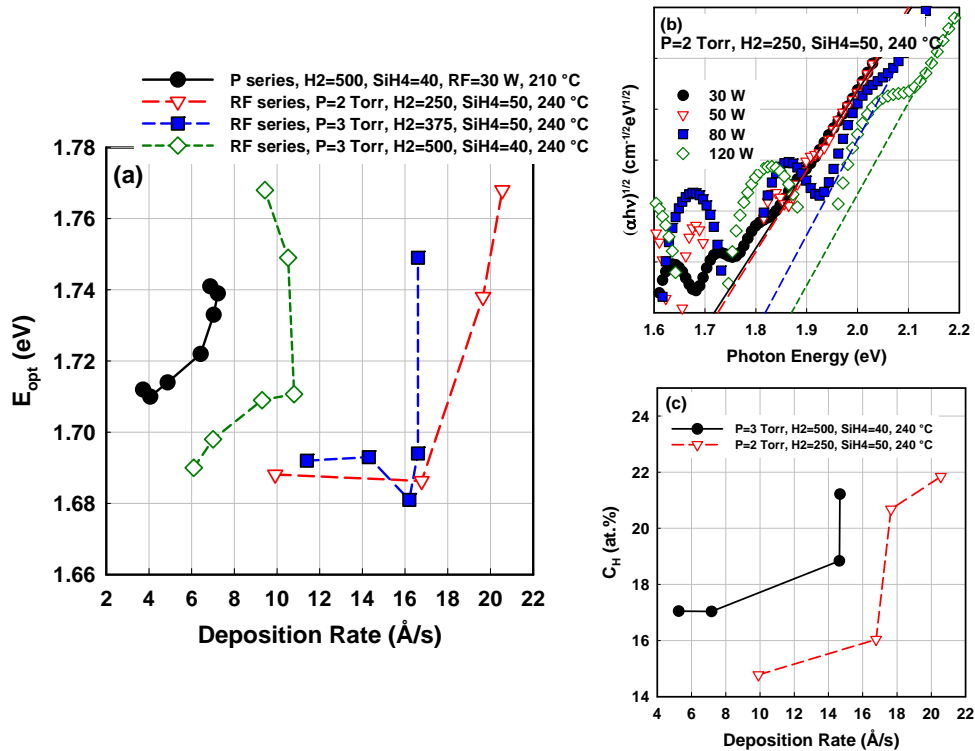


Figure 2.20 – (a) Optical bandgap,  $E_{opt}$ , versus  $r_d$  of different pressure, RF series of pm-Si:H. (b) Tauc plot of one of the RF series in (a). (c) Hydrogen content,  $C_H$ , versus  $r_d$ .

## 2.9 Summary

We have made an extensive test on the material properties of pm-Si:H under various plasma parameters. The main goal in this chapter is to deposit pm-Si:H at high  $r_d$  while maintaining material quality. A QMS study of a-Si:H and pm-Si:H deposition conditions reveals the existence of higher-order-silane species in pm-Si:H deposition, which

could be correlated with the contribution of nanoparticles. In the pressure and RF series, varying the precursor concentration, dissociation, and  $\tau_r$  values result in an increase in the  $r_d$ , but could also lead to poor quality material. The material deposited at extreme process conditions such as  $P > 3$  Torr or RF power  $> 50$  W shows the evidence of deterioration such as roughness, porosity and interconnected voids, and excessive  $C_H$ . Deposition at higher  $T_s$  helps to suppress hydrogen incorporation, but in practical view, impurity incorporation due to outgasing becomes significant, and furthermore, p-type a-SiC deteriorates at high  $T_s$ . Therefore, at high  $T_s$ , making solar cell device would be difficult. Regarding the nature of pm-Si:H deposition, control of  $\tau_r$  seems interesting, to avoid powder formation and to reduce impurity incorporation while maintaining  $r_d$  and any deposition contribution by nanoparticles.

As discussed above, there are many controllable process parameters. In addition, the cause-effect-consequence relationship between each process parameter and material property are inter-related, adding more complexity to the study. Therefore, Table 2.2 shows possible actions in controllable plasma parameters and the ensuing benefits and drawbacks. The solutions for the drawbacks are also considered. As mentioned above, deposition at high  $r_d$  while maintaining material quality is a key issue in pm-Si:H deposition, recalling that extreme process conditions such as too high pressure or RF power lead to poor material. There are indeed few fundamental solutions such as installing a load-lock on the reactor, reducing the volume of reactor, or having a multichamber cluster. As mentioned above, lowering of  $\tau_r$  appears to be more interesting in order to avoid powder formation and excessive hydrogen incorporation while maintaining  $r_d$ .  $\tau_r$  can be simply reduced by increasing total gas flow and opening throttle valve, without changing any other plasma parameters above.

Actions	Benefits	Drawbacks	Solution
SiH <sub>4</sub> flow ↑	Precursor ↑	Material changes	Fixed gas flow rate
Pressure ↑	Precursor ↑ Ion energy ↓	Powder ↑ Residence time ↑	Total gas flow ↑ Inter electrode gap ↓ Small volume reactor Multichamber cluster T <sub>s</sub> ↑
RF power ↑	Dissociation ↑ μ <sub>H</sub> ↑	Powder ↑ Ion energy ↑	Gas flow ↑ Pressure ↑ T <sub>s</sub> ↑ Novel plasma sources Multichamber cluster
T <sub>s</sub> ↑	Powder ↓ C <sub>H</sub> ↓ μ <sub>H</sub> ↑	Outgasing ↑ Poor p a-SiC	Loadlock Multichamber cluster Use of SiF <sub>4</sub> Novel doped layers

Table 2.2 – Controllable plasma parameters and their benefits, drawbacks and solutions. Note that most of the case, the drawbacks are powder formation, and solutions are indeed trade-off of each other cause-and-effects.

### References

- 2.1 Oerlikon's annual report in 2011.  
([http://annualreport.oerlikon.com/uploads/bricks/download/asset\\_en/466/OC\\_Oerlikon\\_Annual\\_Report\\_2011.pdf](http://annualreport.oerlikon.com/uploads/bricks/download/asset_en/466/OC_Oerlikon_Annual_Report_2011.pdf))
- 2.2 M. A. Green, Photovoltaic Technical Conference 2012, Aix-en-Provence (2012).
- 2.3 P. Roca i Cabarrocas, J. B. Chevrier, J. Huc, A. Lloret, J. Y. Parey, and J. P. M. Schmitt, *J. Vac. Sci. Technol. A* 9, 2331 (1991).
- 2.4 H. Tasaki, W. Y. Kim, M. Hallerdt, M. Konagai, and K. Takahashi, *J. Appl. Phys.* 63, 550 (1988).
- 2.5 B. Rech, C. Beneking, and H. Wagner, *Sol. Energ. Mater. Sol. Cells* 41-42, 475 (1996).
- 2.6 H. Stiebig, F. Siebke, W. Beyer, C. Beneking, B. Rech, and H. Wagner, *Sol. Energ. Mater. Sol. Cells* 48, 351 (1997).
- 2.7 J. P. M. Schmitt, *J. Non-Cryst. Solids* 59-60, 649 (1983).
- 2.8 A. Matsuda, M. Takai, T. Nishimoto, and M. Kondo, *Sol. Energ. Mater. Sol. Cells* 78, 3 (2003).
- 2.9 M. J. Kushner, *J. Appl. Phys.* 63, 2532 (1988).
- 2.10 J. Perrin, *J. Non-Cryst. Solids* 137-138, 639 (1991).
- 2.11 J. Robertson, *J. Appl. Phys.* 87, 2608 (2000).
- 2.12 C. C. Tsai, J. C. Knights, G. Chang, and B. Wacker, *J. Appl. Phys.* 59, 2998 (1986).
- 2.13 R. A. Street, *Phys. Rev. B* 43, 2454 (1991).
- 2.14 T. Novikova, B. Kalache, P. Bulkin, K. Hassouni, W. Morscheidt, and P. Roca i Cabarrocas, *J. Appl. Phys.* 93, 3198 (2003).
- 2.15 H. Kawasaki, H. Ohkura, T. Fukuzawa, M. Shiratani, T. Watanabe, Y. Yamamoto, S. Suranuma, M. Hori, and T. Goto, *Jpn. J. Appl. Phys.* 36, 4985 (1997).
- 2.16 G. Bano, P. Horvath, K. Rozsa, and A. Gallagher, *J. Appl. Phys.* 98, 013304 (2005).
- 2.17 T. Nagai, A. H. M. Smets, and M. Kondo, *Jpn. J. Appl. Phys.* 47, 7032 (2008).
- 2.18 J. Dutta, H. Hofmann, R. Houriet, H. Hofmeister, and Ch. Hollenstein, *Colloids & Surfaces* 127, 263 (1997).
- 2.19 P. Roca i Cabarrocas, P. Gay, and A. Hadjadj, *J. Vac. Sci. Technol. A* 14, 655 (1996).
- 2.20 P. Roca i Cabarrocas, S. Hamma, S. N. Sharma, G. Viera, E.

- Bertran, and J. Costa, *J. Non-Cryst. Solids* 227-230, 871 (1998).
- 2.21 P. Roca i Cabarrocas, *Phys. Stat. Sol. (c)* 1, 1115 (2004).
- 2.22 G. Oversluizen and W. H. M. Lodders, *J. Appl. Phys.* 83, 8002 (1998).
- 2.23 P. Roca i Cabarrocas, Th. Nguyen-Tran, Y. Djeridane, A. Abramov, E. Johnson and G. Patriarche, *J. Phys. D: Appl. Phys.* 40, 2258 (2007).
- 2.24 T. Ifuku, M. Otobe, A. Itoh, and S. Oda, *Jpn. J. Appl. Phys.* 36, 4031 (1997).
- 2.25 A. Fontcuberta i Morral, P. Roca i Cabarrocas, *Thin Solid Films* 383, 161 (2001).
- 2.26 A. Grill *Cold Plasma Materials Fabrication: From Fundamentals to Applications*, Wiley-IEEE Press, 1994, ISBN: 978-0-7803-4714-4 Page. 94
- 2.27 Th. Nguyen-Tran, P. Roca i Cabarrocas, and G. Patriarche, *Appl. Phys. Lett.* 91, 111501 (2007).
- 2.28 P. Roca i Cabarrocas, N. Chaabane, A. V. Kharchenko, and S. Tchakarov, *Plasma Phys. Control. Fusion* 46, B235–B243, (2004).
- 2.29 A. Matsuda, *J. Non-Cryst. Solids* 59–60 767 (1983).
- 2.30 T. Matsui, M. Kondo, and A. Matsuda, *Jpn. J. Appl. Phys.* 42, L901 (2003).
- 2.31 S. Tchakarov, D. Das, O. Saadane, A. V. Kharchenko, V. Suendo, F. Kail, and P. Roca i Cabarrocas, *J. Non-Cryst. Solids* 338–340, 668 (2004).
- 2.32 A. Gordijn, M. Vanecek, W. J. Goedheer, J. K. Rath, and R. E. I. Schropp, *Jpn. J. Appl. Phys.* 45, 6166 (2006).
- 2.33 A. Matsuda, *J. Non-Cryst. Solids* 59–60, 767 (1983).
- 2.34 J. L. Andujar, E. Bertran, A. Canillas, C. Roch, and J. L. Morenza, *J. Vac. Sci. Technol. A* 9, 2216 (1991).
- 2.35 R. C. Ross and J. Jaklik, *J. Appl. Phys.* 55, 3785 (1984).
- 2.36 K. Tanaka and A. Matsuda, *Mater. Sci. Rep.* 2, 139 (1987).
- 2.37 S. Röhlecke, R. Tews, A. Kottwitz, and K. Schade, *Surf. Coat. Technol.* 74-75, 259 (1995).
- 2.38 W. Beyer, W. Hilgers, P. Prunici, D. Lennartz, *J. Non-Cryst. Solids* , Article in Press, <http://dx.doi.org/10.1016/j.jnoncrysol.2011.09.030>
- 2.39 A. H. M. Smets, W. M. M. Kessels, and M. C. M. van de Sanden, *Appl. Phys. Lett.* 82, 1547 (2003).
- 2.40 D. K. Biegelsen, R. A. Street, C. C. Tsai, and J. C. Knights , *Phys.*

- Rev. B 20, 4839 (1979).
- 2.41 A. H. Mahan, W. Beyer, B. L. Williamson, J. Yang, and S. Guha, *Philos. Mag. Lett.* 80, 647 (2000).
- 2.42 E. Bertran, J. Costa, G. Sardin, J. Campmany, J. L. Andujar, and A. Canillas, *Plasma Sources Sci. Technol.* 3, 348 (1994).
- 2.43 K. Tanaka and A. Matsuda, *Mat. Sci. Rep.* 2, 139 (1987).
- 2.44 J. C. Knights, *Jpn. J. Appl. Phys.* 18, Supplement 18-1, 101 (1979).
- 2.45 E. V. Johnson, P.A. Delattre, and J.P. Booth, *Appl. Phys. Lett.* 100, 133504 (2012).
- 2.46 E. Bhattacharya and A. H. Mahan, *Appl. Phys. Lett.* 52, 1587 (1988).
- 2.47 S. Guha, J. Yang, S. J. Jones, Y. Chen, and D. L. Williamson, *Appl. Phys. Lett.* 61, 1444 (1992).
- 2.48 G. Lucovsky, R. J. Nemanich, and J. C. Knights, *Phys. Rev. B* 19, 2064 (1979).
- 2.49 A. A. Langford, M. L. Fleet, B. P. Nelson, W. A. Lanford, and N. Maley, *Phys. Rev. B* 45, 13367 (1992).
- 2.50 P. Roca i Cabarrocas, A. Fontcuberta i Morral, and Y. Poissant, *Thin Solid Films* 403, 39 (2002).
- 2.51 A. von Keudell and J. R. Abelson, *Phys. Rev. B* 59, 5791 (1999).
- 2.52 J. L. Dorier, Ch. Hollenstein, A. A. Howling, and U. Kroll, *J. Vac. Sci. Technol. A* 10, 1048 (1992).
- 2.53 A. A. Fridman, L. Boufendi, T. Hbid, B. V. Potapkin, and A. Bouchoule, *J. Appl. Phys.* 79, 1303 (1996).
- 2.54 U. V. Bhandarkar, M. T. Swihart, S. L. Girshick and U. R. Kortshagen, *J. Phys. D: Appl. Phys.* 33 2731 (2000).
- 2.55 Y. M. Soro, A. Abramov, M. E. Gueunier-Farret, E. V. Johnson, C. Longeaud, P. Roca i Cabarrocas, and J. P. Kleider, *Thin Solid Films* 516, 6888 (2008).
- 2.56 G. Parascandolo, G. Bugnon, A. Feltrin, and C. Ballif, *Prog. Photovolt: Res. Appl.* 18, 257 (2010).
- 2.57 W. Beyer, *J. Non-Cryst. Solids* 338–340, 232 (2004).
- 2.58 P. G. Pai, S. S. Chao, Y. Takagi, and G. Lucovsky, *J. Vac. Sci. Technol., A* 4, 689 (1986).
- 2.59 P. Torres, J. Meier, R. Flückiger, U. Kroll, J. A. Anna Selvan, H. Keppner, A. Shah, S. D. Littlewood, I. E. Kelly, and P. Giannoulès, *Appl. Phys. Lett.* 69, 1373 (1996).
- 2.60 A. Abramov and P. Roca i Cabarrocas, *Phys. Stat. Sol. (c)* 3-4, 529 (2010).

- 2.61 Y. Hishikawa, S. Tsuda, K. Wakisaka, and Y. Kuwano, *J. Appl. Phys.* 73, 4227 (1993).
- 2.62 W. Futako, S. Takeoka, C. M. Fortmann, and I. Shimizu *J. Appl. Phys.* 84, 1333 (1998).
- 2.63 J. Woerdenweber, T. Merdzhanova, H. Stiebig, W. Beyer, and A. Gordijn, *Appl. Phys. Lett.* 96, 103505 (2010).



# Chapter 3

## Hydrogenated Polymorphous Silicon Solar Cells

3.1 Introduction.....	98
3.2 Standard PIN solar cells.....	98
3.3 Effect of light-trapping .....	106
3.4 Intrinsic layer optimization.....	107
3.5 HR pm-Si:H PIN solar cells.....	113
3.6 Stability issues of PIN solar cells.....	119
3.7 Summary .....	123

### 3.1 Introduction

This chapter deals with pm-Si:H solar cells made of intrinsic material prepared under various deposition conditions. In the previous chapter we have studied the growth of pm-Si:H at various process conditions. In this chapter, we present experimental studies on the performance of pm-Si:H solar cells using various intrinsic layers. Controlling  $\tau_r$  leads to fabricate solar cells with high  $FF$ , which is attributed to the low defect density material, and the application of ITO/Ag reflector enhanced  $J_{sc}$  thus allows high efficiency PIN solar cells showing initial  $\eta_{\text{initial}}$  of 9.22 %. Application of HR pm-Si:H layers was also studied. HR pm-Si:H PIN solar cells show potential to further cost reduction, but also showed deterioration of device performance. The improvement in material quality of HR pm-Si:H is needed.

### 3.2 Standard PIN solar cells

In a-Si:H solar cells, the diffusion length of the charge carriers is shorter than that in crystalline silicon. For example, device quality intrinsic a-Si:H shows an as-deposited ambipolar diffusion length around 200 nm [3.1], and doped layers have even lower diffusion length of the minority carriers because of the high defect density associated with the doping in a-Si:H. A solar cell structure in crystalline silicon is based on the transport of the minority carriers by diffusion in the base material, but it is inefficient for thin film silicon solar cells. A PN junction based on a-Si:H would show very low efficiency due to the very short diffusion length, and the photogenerated carriers would recombine before being separated by the electric field in the depletion region of the PN junction. Therefore, thin film silicon solar cells should be designed differently compared to the standard PIN junction of a crystalline silicon cell.

A schematic structure of a PIN solar cell is shown in Figure 3.1. The PIN device consists of three fundamental components: a p-type a-SiC:H, an intrinsic layer, and an n-type a-Si:H, which form a PIN junction. This structure is often called a single junction solar cell. The PIN devices in this study were deposited in the ARCAM reactor. Standard a-Si:H and pm-Si:H materials are used in the intrinsic layers. The structure of PIN solar cell consists of a textured Asahi SnO<sub>2</sub> substrate/p-type a-SiC/SiC buffer/intrinsic layer/n-type a-Si:H/Top contact. Various back-contacts such as Al, Ag, and ITO/Ag can be used. The area of the cells was 0.126 cm<sup>2</sup>. The thickness of p and n-type layers were about 150 Å, and the intrinsic thickness can vary from 1500 to 7000 Å. Figure 3.1 shows an SEM image of cross-section of a pm-Si:H PIN solar cell deposited on textured SnO<sub>2</sub> substrate.

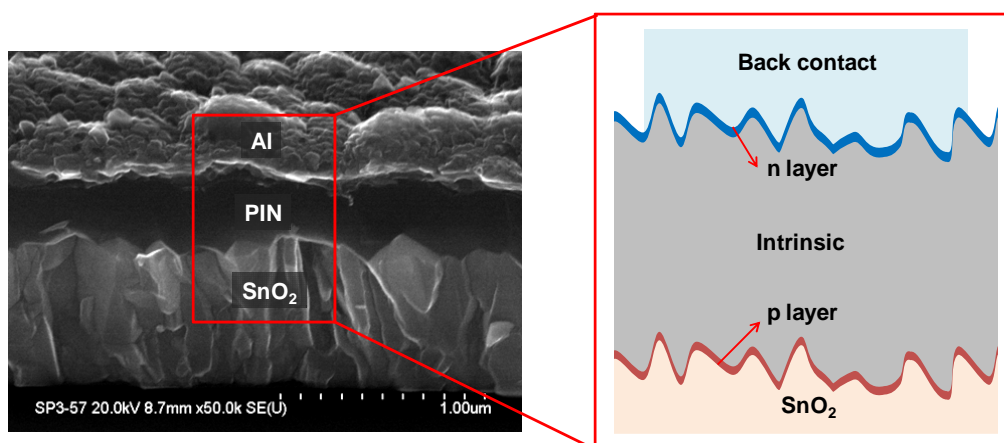


Figure 3.1 –SEM image of the cross-section of a pm-Si:H PIN solar cell deposited on textured SnO<sub>2</sub> substrate and its schematic drawing. In SEM image, silicon layers appear dark due to the low conductivity.

Boron doped a-SiC:H has become a standard p-type layer in a-Si:H solar cells [3.2]. Since boron incorporation reduces the bandgap of a-SiC:H, it should be carefully considered that an optimal p-type layer is a result of a trade-off between conductivity and absorption. In this experiment, our standard p-type a-SiC:H layer was obtained from the following flow rates for the different gases injected in the reactor: H<sub>2</sub>:

100 sccm, SiH<sub>4</sub>: 25 sccm, CH<sub>4</sub>: 100 sccm and trimethyl-boron (TMB): 20 sccm, and deposited at a pressure of 120 mTorr and RF power of 1W. After the deposition of p-type a-SiC:H layers, a thin buffer layer is deposited. It is widely known that the design of the p/i interface region significantly influences the efficiency of solar cells, and a thin interlayer (buffer) improves solar cell performance [3.3, 3.4]. The buffer layer prevents diffusion of boron from the p-type a-SiC:H into intrinsic layer and back diffusion of the photogenerated electrons from the intrinsic into p-type layer. The thin buffer layer is often coupled with a lightly doped p-type a-SiC:H to make smooth gradient of distribution of the electric field. Therefore, usually p/i interface region consists of multilayers including heavily doped p / lightly doped p / intrinsic a-SiC:H. Intrinsic a-SiC:H film was applied in highly efficient solar cells as a thin buffer layer in the following condition: H<sub>2</sub>: 100 sccm, SiH<sub>4</sub>: 40 sccm, CH<sub>4</sub>: 80 sccm.

In the intrinsic layer, the electron-hole pairs are generated and collected, and the strength and profile of the internal electric field across the intrinsic layer determines the collection of the photogenerated charge carriers. The electric field profile in the intrinsic layer strongly depends on the defect density and the distribution in the intrinsic layer and at the interfaces with the doped layers. Therefore, the material quality of the intrinsic layer is a crucial part of the solar cell performance, and intrinsic pm-Si:H film should be deposited in carefully controlled plasma conditions. In this chapter, work is described where plasma parameters of pm-Si:H were varied to optimize the solar cells, and two series of pm-Si:H are tested. Standard intrinsic pm-Si:H was deposited under pressure of 2 Torr, RF power of 5 W, T<sub>s</sub> of 175 °C. Inter-electrode distance was 22 mm. Relative and total gas flow rates of SiH<sub>4</sub> and H<sub>2</sub> were varied. High deposition rate (HR) intrinsic pm-Si:H PIN solar cells were also studied under various plasma conditions. For HR pm-Si:H, the pressure was varied from 2

Torr to 3.5 Torr, the RF power varied from 30 W to 80 W, and the substrate temperature ( $T_s$ ) was varied from 210 °C to 240 °C. Narrower inter-electrode distance of 12 mm was used in HR pm-Si:H, and gas flow rate was varied. Application of such deposition parameters leads to pm-Si:H films such as very stable films at low deposition rate ( $r_d$ ) of 1.5 Å/s to films with  $r_d$  as high as 10 Å/s while still maintaining device quality [3.5]. The best quality film is obtained at the lowest  $r_d$  of 1.5 Å/s, and another good quality material with higher  $r_d$  up to 10 Å/s was also possible. The  $r_d$  was further increased up to 20 Å/s with higher RF power, but the material quality tends to degrade at high  $r_d$ . Standard a-Si:H was deposited dissociating undiluted silane at pressure of 45 mTorr and low RF power of 1 W leading to a deposition rate of  $\sim 0.7$  Å/s

On the top of intrinsic layer, a n-type a-Si:H layer was deposited from a mixture of 100 sccm of hydrogen, 50 sccm of silane and 2 sccm of phosphine under a pressure of 110 mTorr and RF power of 1 W. Since n-type a-Si:H layer is located at the back end of the PIN solar cells and most of high energy photons are absorbed in the intrinsic layer, the transparency of n-type layer is less important than that of the p-type layer. However, still there is some parasitic absorption in n-type layer, which leads to a decrease in  $J_{sc}$ , so wide bandgap n-type layer should be an important topic. Table 3.1 summarizes material properties of doped layers and standard PIN solar cell components. After the deposition of the PIN layer stack, back-contact should be deposited. Various materials such as Al, Ag, and ITO/Ag can be used. Evaporated Al is the simplest back-contact, providing high conductivity and moderate reflectivity. Sputtered ITO and evaporated Ag are often coupled in order to enhance  $J_{sc}$ . After the fabrication, the solar cells were annealed at 160 °C for two hours for Al and ITO/Ag case. In case of Ag contact, annealing was done at 150 °C for 30 minutes in order to prevent Ag diffusion.

Sample	H <sub>2</sub>	SiH <sub>4</sub>	CH <sub>4</sub>	TMB	PH <sub>3</sub>	Pressure (mTorr)	RF* (W)	T <sub>s</sub> (°C)	d <sub>f</sub> (mm)	r <sub>d</sub> (Å/s)	E <sub>opt</sub> (eV)	A	E <sub>0</sub>	C	Rough (Å)	σ <sub>RT</sub> (Scm <sup>-1</sup> )	E <sub>a</sub> (eV)
n-type a-Si:H	100	50			2	110	1	175	28	0.64	1.76	210	3.6	2.2	12.9	> 10 <sup>-3</sup>	< 0.2
Intrinsic a-Si:H		50				45	1	175	28	0.7	1.67	211	3.57	2.28	10.5	~ 10 <sup>-11</sup>	~ 0.9
Intrinsic pm-Si:H	500	50				2000	5	175	22	1.5	1.70	226	3.63	2.14	16.7	~ 10 <sup>-11</sup>	~ 0.9
p-type a-SiC:H	100	25	100	20		120	1	175	28	0.95	2.01	186	3.8	3	12.9	> 10 <sup>-7</sup>	< 0.5

Table 3.1 – Deposition condition and physical properties of the standard PIN solar cells components.

\* Area of plasma electrodes in ARCAM is 171.95 cm<sup>2</sup>.

The physical properties of PIN solar cells and the material quality of the two groups of materials listed above can be tested by the dark  $J(V)$  characteristics. Figure 3.2 shows the dark  $J(V)$  characteristics of a-Si:H and pm-Si:H PIN solar cells, and Table 3.1 shows dark diode parameters extracted in Figure 3.2. In Figure 3.2, both a-Si:H and pm-Si:H produce good diodes with clear rectifying characteristic, the on/off ratio reaching up to  $10^6$ . In Table 3.2, extracted dark parameters are in the range of good a-Si:H PIN diodes presented in literature [3.6]. Low ideality factor, low  $J_0$ , and high on/off ratio with clear rectifying characteristic indicate that both materials are of device quality and that the doped layers work effectively. Dark  $J(V)$  curve of pm-Si:H PIN solar cell shows small shift to higher voltage and a lower current density compared to that of a-Si:H, and it is also reflected in dark parameters. In Table 3.1, the pm-Si:H PIN solar cell shows lower  $J_0$  because of the shift in the dark  $J(V)$  curve due to wider bandgap. It is interesting that the ideality factor of pm-Si:H PIN solar cell is a bit higher than that of a-Si:H PIN solar cell. It can be also explained by that the bandgap of pm-Si:H is slightly wider than that of a-Si:H.

$J(V)$  curves of PIN solar cells can be also measured under illumination. Figure 3.3 shows initial characteristics of typical a-Si:H and pm-Si:H PIN solar cells. Intrinsic layer thickness ( $d_i$ ) was about 3000 Å for both solar cells, and Al back-contact was used. Table 3.3 shows solar cell parameters of PIN solar cells shown in Figure 3.3. Note that multiple (usually six) individual solar cells on  $2.5 \times 2.5$  cm<sup>2</sup> substrate are measured and the solar cell parameters are averaged. Figure 3.3 and Table 3.3 show that both a-Si:H and pm-Si:H indeed result in good solar cells at initial state. High fill factor ( $FF$ ) of both cells indicates that both materials have low defect density at initial states. In  $V_{oc}$  and  $J_{sc}$ , there is slight difference, namely pm-Si:H PIN solar cell shows a slightly lower  $J_{sc}$  and high  $V_{oc}$  compared to that of a-

Si:H PIN solar cell. External quantum efficiency (EQE) in Figure 3.3(b) also shows that absorption edge of pm-Si:H PIN solar cell is slightly shifted to shorter wavelength region, thus pm-Si:H PIN solar cell shows a bit lower  $J_{sc}$ . It is related to the bandgap difference between the two materials. Due to the higher bandgap, pm-Si:H PIN solar cells show higher  $V_{oc}$  than a-Si:H PIN solar cells, which is attractive in view of multi-junction solar cells [3.7].

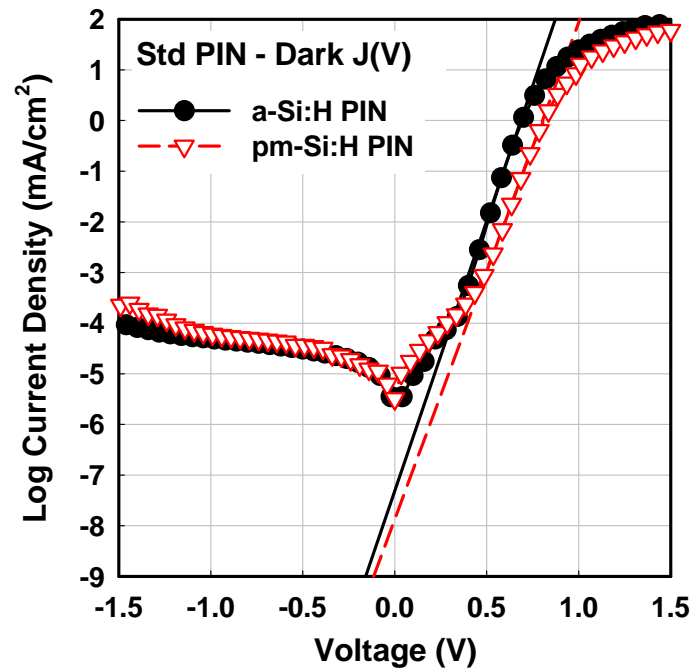


Figure 3.2 – Initial dark  $J(V)$  characteristics of a-Si:H and pm-Si:H PIN solar cells. Ideality factor and  $J_0$  can be extracted from the extrapolation of forward bias region. Note that intrinsic layer thickness was about 3000 Å.

Sample	$n$	$J_0$ (mA/cm <sup>2</sup> )
a-Si:H a1102252	1.66	$4.65 \times 10^{-8}$
pm-Si:H a1104114	1.75	$1.14 \times 10^{-8}$

Table 3.2 – Ideality factor  $n$  and  $J_0$  of a-Si:H and pm-Si:H PIN solar cells in Figure 3.2. Dark diode parameters are extracted from the extrapolation of forward bias region.

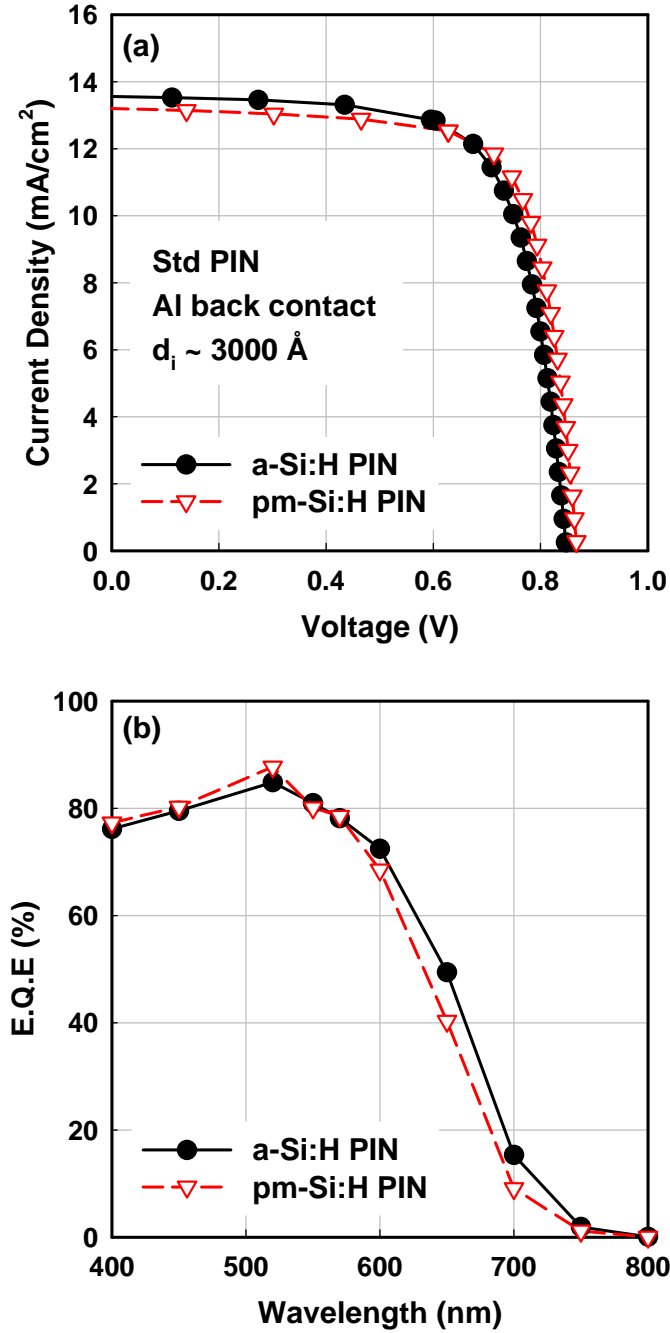


Figure 3.3 – Initial characteristics of a-Si:H and pm-Si:H PIN solar cells. (a) J(V) curve and (b) external quantum efficiency. Note that intrinsic layer thickness was about 3000 Å, and Al back-contact was used.

Sample	FF	$R_{sc}$ ( $\Omega\text{cm}^2$ )	$R_{oc}$ ( $\Omega\text{cm}^2$ )	$J_{sc}$ ( $\text{mA}/\text{cm}^2$ )	$V_{oc}$ (V)	$\eta$ (%)
a-Si:H	72.56	4786	6.44	13.56	0.842	8.28
pm-Si:H	73.67	2982	5.86	12.95	0.867	8.28

Table 3.3 – Solar cell parameters of PIN solar cells shown in Figure 3.3.

### 3.3 Effect of light-trapping

One of the most effective approaches to enhance the solar cell efficiency is to increase  $J_{sc}$ . In PIN solar cells,  $J_{sc}$  mostly depends on the absorption in the intrinsic layer, thus application of thicker intrinsic layer could be a simple way. However, thick intrinsic layer weakens the internal electric field across the intrinsic layer, increases recombination, and thus degrades the collection of photo-generated-carriers, thus introducing a decrease in  $FF$ . Furthermore, this increased sensitivity to recombination accelerates light-induced degradation in thick intrinsic layers. Therefore, it is important to use special device design of “optically thick” while maintaining “electrically thin” features [3.8], also known as light trapping. In brief, studies on intrinsic layer thickness and its effects on PIN solar cells can bring important information on device physics. A brief detail on intrinsic layer thickness on PIN solar cells can be found in annex 3.1 and chapter 5.

At present, the most important research in the thin film solar cells is the development and implementation of efficient light trapping. Efficient light trapping mostly relies on light scattering at rough interfaces and employment of highly reflective back contacts, and refractive index matching (or mis-matching) between each component. The light scattering at rough interfaces spreads the photons in random directions and introduces internal-reflection at the back and front contacts, thus resulting in a longer optical path, thus making an “optically thick” device structure. For the light-trapping, transparent conductive oxide (TCO) and innovative doped layers (such as doped  $\mu\text{-SiO}_x$ ) play an important role, through their surface texture and refractive index matching. Indeed, recent progress on the efficiency of a-Si:H and  $\mu\text{-Si:H}$  solar cells are results of an improvement in TCO [3.9] or innovative doped layers [3.10].

An example of the effect of highly reflective back contact is demonstrated in Figure 3.4, which shows initial  $J(V)$  curves and EQE of a pm-Si:H PIN solar cell with different back reflector of Al and ITO/Ag. Table 3.4 shows solar cell parameters extracted from Figure 3.4. Increase in  $J_{sc}$  is a significant change with ITO/Ag back reflector, and it is also seen in EQE curve, increase in  $J_{sc}$  mostly comes from enhanced response in red region. However, there is also a trade off factors that the  $FF$  and  $R_{sc}$  are smaller for the ITO/Ag contact. One can suspect that while Al and  $\text{SnO}_2$  form  $\text{Al}_2\text{O}_3$  at any small pinholes which can remove the shunt path, the ITO/Ag contact does not remove the shunt path through any such mechanism. It is also seen that  $R_{oc}$  slightly increases. Ohmic contact at n-type a-Si:H/ITO/Ag should be improved. In 2012, more recent trends in the device design are based on the development and implementation of innovative doped layers such as doped  $\mu\text{c-SiO}_x$  having high conductivity and low refractive index. In this thesis, results on pm-Si:H solar cells using doped  $\mu\text{c-SiO}_x$  will be presented in chapter 5.

### 3.4 Intrinsic layer optimization

In chapter 2, we have demonstrated that minimizing residence time,  $\tau_r$  is a critical key factor to improve the material quality. As seen in Figure 2.19, reducing  $\tau_r$  lead a good quality material with low hydrogen content  $C_H$ . One of the most convenient indicators of material property change is the optical bandgap,  $E_{opt}$ , because  $E_{opt}$  is sensitive to  $C_H$ .

A series of pm-Si:H PIN solar cells were fabricated, using different intrinsic layer deposition conditions, having different  $\tau_r$  and gas flow ratio. Three pm-Si:H PIN solar cells are having identical substrates (Textured  $\text{SnO}_2:\text{F}$  and corning glass), both p and n-type layers, and Al back contacts.

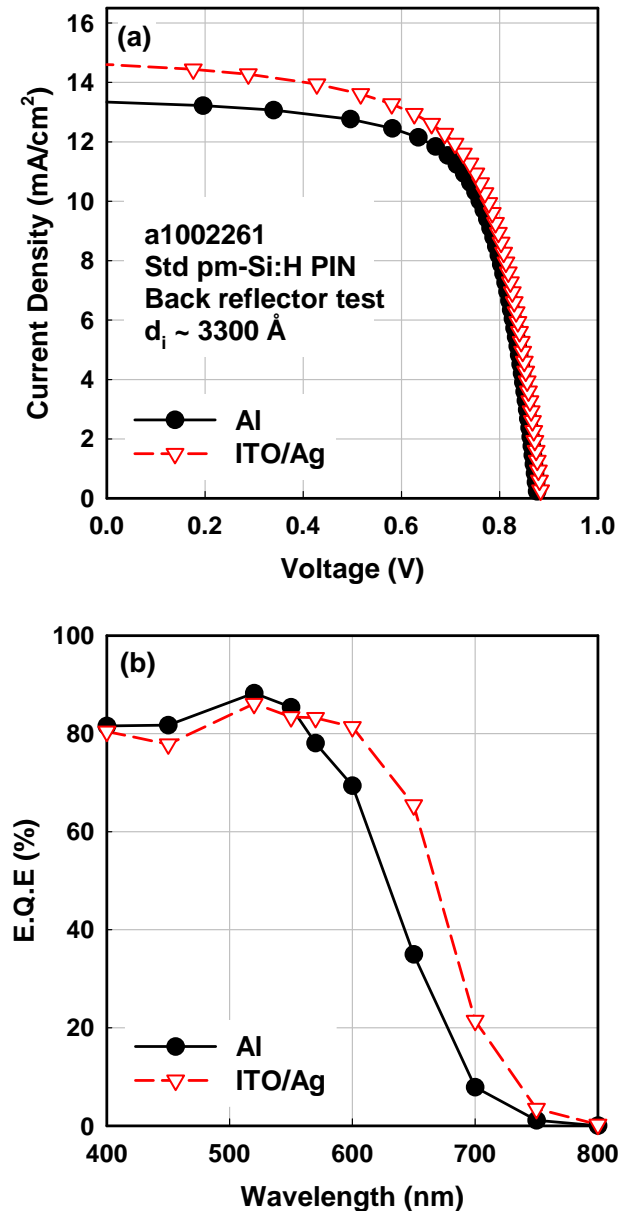


Figure 3.4 – Initial characteristics of a pm-Si:H PIN solar cell with different back reflector of Al and ITO/Ag. (a) J(V) curve and (b) external quantum efficiency. Note that intrinsic layer thickness was about 3300 Å.

Back reflector	FF	$R_{sc}$ ( $\Omega\text{cm}^2$ )	$R_{oc}$ ( $\Omega\text{cm}^2$ )	$J_{sc}$ (mA/cm <sup>2</sup> )	$V_{oc}$ (V)	$\eta$ (%)
Al BR	70.51	4052	6.14	13.59	0.871	8.34
ITO/Ag BR	68.24	2775	6.81	14.87	0.885	9.01

Table 3.4 – Solar cell parameters of PIN solar cells shown in Figure 3.4.

### 3.4 Intrinsic layer optimization

For the intrinsic layer deposition, only the gas flow and the total flow were varied while total pressure, RF power, and  $T_s$  were fixed to 2 Torr, 5 W, and 175 °C, respectively. After deposition, sample thickness and material parameters are obtained from SE modeling on PIN layer stack co-deposited on Corning glass. Table 3.5 shows the brief sample description.. From a1104092 to a1104112, hydrogen flow was kept same and silane flow was increased by 40 %. As a result,  $r_d$  increased and  $E_{opt}$  decreased. Increased  $r_d$  can be explained by higher silane partial pressure (larger flow). Effect of changing gas flow ratio also changes hydrogen content ( $C_H$ ) [3.11].

Sample	H <sub>2</sub>	SiH <sub>4</sub>	E <sub>opt</sub> (eV)	d <sub>i</sub> (Å)	r <sub>d</sub> (Å/s)
<b>a1104092</b>	<b>200</b>	<b>12</b>	<b>1.74</b>	<b>2700</b>	<b>1.2</b>
<b>a1104112</b>	<b>200</b>	<b>20</b>	<b>1.71</b>	<b>3000</b>	<b>1.5</b>
<b>a1104114</b>	<b>500</b>	<b>50</b>	<b>1.70</b>	<b>3000</b>	<b>1.5</b>

Table 3.5 – Gas flow and SE modeling parameters from pm-Si:H PIN solar cells deposited in three different intrinsic layer conditions. Note that the three pm-Si:H PIN solar cells are having identical substrates (Textured SnO<sub>2</sub>:F and corning glass), both p and n-type layers, and Al back contacts. For the intrinsic layer deposition condition, only gas flow and total flow were varied while total pressure, RF power, and  $T_s$  were fixed at 2 Torr, 5 W, and 175 °C, respectively.

Meanwhile, from a1104112 to a1104114, increasing total gas flow while keeping same total pressure (2 Torr) and same gas flow ratio leads to a large reduction of  $\tau_r$ . Figure 3.5 shows initial J(V) curves of a pm-Si:H PIN solar cells deposited under conditions described above. Table 3.6 shows extracted solar cell parameters.

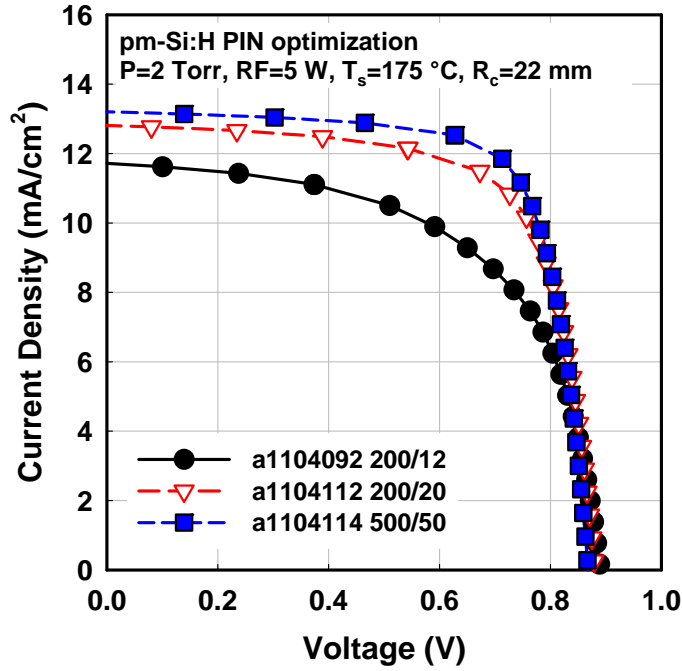


Figure 3.5 – Initial characteristics of a pm-Si:H PIN solar cells deposited under various gas flow. Note that intrinsic layer thickness was about 3000 Å, Al back contact are used.

Sample (Gas flow)	FF	$R_{sc}$ ( $\Omega\text{cm}^2$ )	$R_{oc}$ ( $\Omega\text{cm}^2$ )	$J_{sc}$ ( $\text{mA}/\text{cm}^2$ )	$V_{oc}$ (V)	$\eta$ (%)	$C_o$ (a.u.)
a1104092 (200/12)	57.89	2103	11.11	11.19	0.887	5.75	7.85
a1104112 (200/20)	69.82	2742	6.82	12.6	0.881	7.75	5.67
a1104114 (500/50)	73.67	2982	5.86	12.95	0.867	8.28	4.03

Table 3.6 – Solar cell parameters of PIN solar cells shown in Figure 3.5. Oxygen content deduced from Figure 3.6 is also marked. Note that multiple individual solar cells on  $2.5 \times 2.5$   $\text{cm}^2$  substrate are measured and the solar cell parameters are averaged. Al back-contact was used.

In Figure 3.5 and Table 3.6, it is well demonstrated that  $J(V)$  curve improves with greater gas flow, having higher  $FF$  that suggests low defect density in intrinsic layer. An interesting result is that  $V_{oc}$  also decreases at large gas flow. As mentioned above, low  $C_H$  results low  $E_{opt}$ . Since  $V_{oc}$  is largely affected by bandgap of the material [3.13], decrease in  $V_{oc}$  comes from narrower bandgap of the material. It is

again cross-validated by SIMS result. Figure 3.6 shows a SIMS profile of hydrogen and oxygen content of intrinsic pm-Si:H layer stack deposited on FZ c-Si. Intrinsic pm-Si:H films are deposited using different gas flow condition presented in Table 3.5. The result in Figure 3.6 is coherent with the result presented in Table 3.6. Increasing SiH<sub>4</sub> flow from 12 to 20 sccm (at fixed H<sub>2</sub> flow of 200) resulted in a decrease in both hydrogen and oxygen content, which is a consequence of different gas flow ratio and higher  $r_d$ . This is consistent with the improvement in solar cell parameters, as well as decrease in both  $E_{opt}$  and  $V_{oc}$ . Furthermore, at fixed gas flow ratio of H<sub>2</sub>/SiH<sub>4</sub> = 10, increase in total gas flow from 200/20 to 500/50 causes low  $\tau_r$ . In this case, decrease in oxygen incorporation in the intrinsic layer is more significant, and the reduced oxygen content results in even better solar cell parameters, e.g. high  $FF$ . The result of optimized pm-Si:H PIN with low defect density material, with light tapping from ITO/Ag back-contact is shown in Figure 3.7.

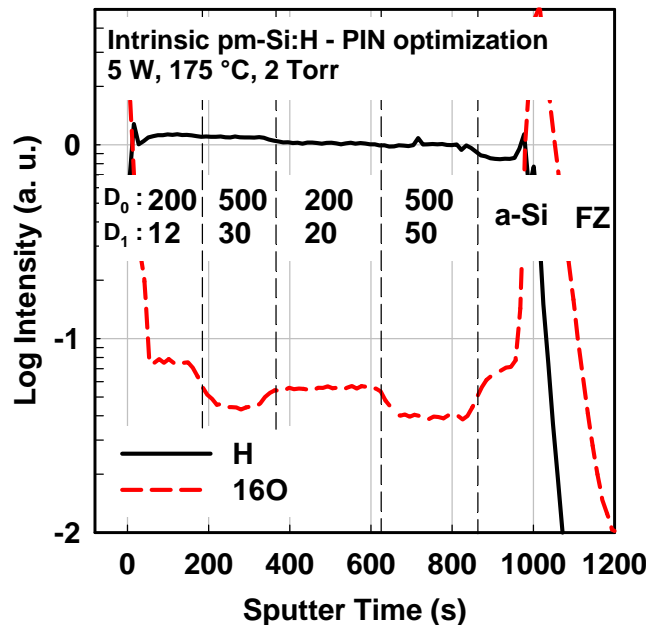


Figure 3.6 – SIMS profile of hydrogen and oxygen content for different gas flow in intrinsic pm-Si:H deposition condition. Note that entire layer stack is deposited on FZ c-Si wafer, and a-Si:H was also deposited as a reference.

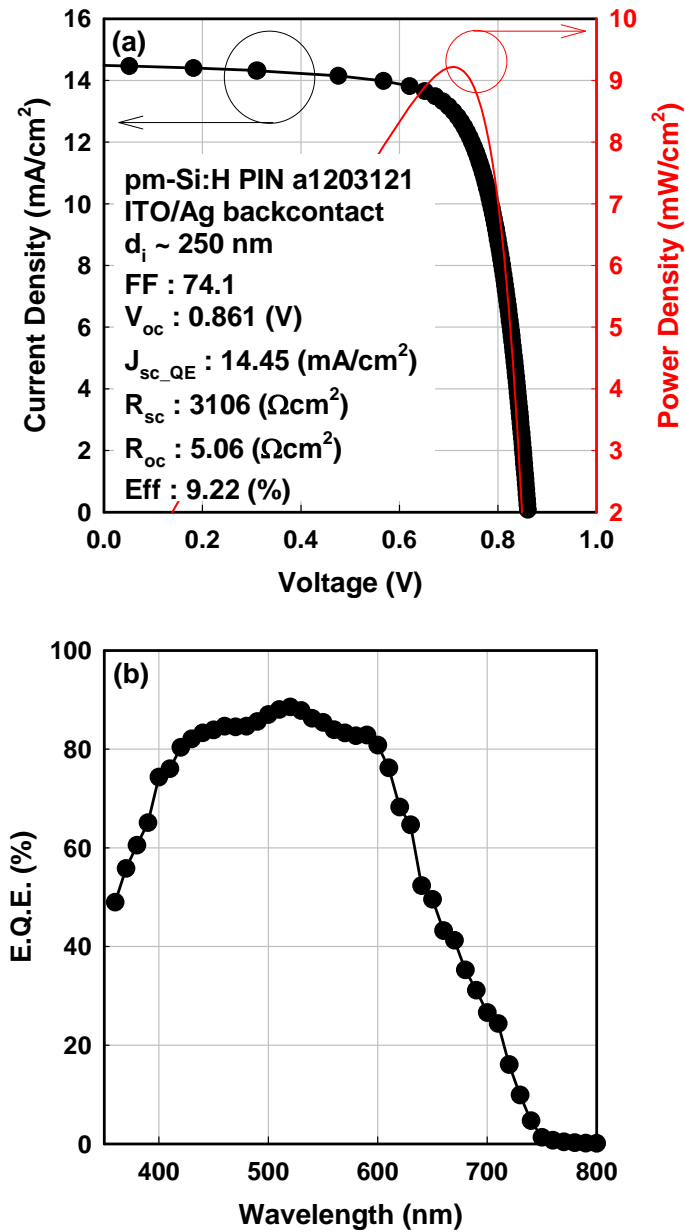


Figure 3.7 – Initial characteristics of an optimized pm-Si:H PIN solar cell (a) J(V) curve and (b) external quantum efficiency. Intrinsic layer thickness was about 2500 Å, and ITO/Ag was used as back reflector. Solar cell parameters are indicated in (a).

Figure 3.7 shows initial J(V) curve and EQE of the optimized pm-Si:H PIN solar cell. Thanks to the improved light trapping efficiency due to the ITO/Ag back reflector, red response of EQE shown in Figure 3.7(b) is high in spite of only 2500 Å of intrinsic layer thickness. Initial FF of 74.1 suggests that the intrinsic layer has a low defect density, and  $J_{sc}$

of 14.45 mA/cm<sup>2</sup> pushes the initial efficiency up to 9.2 %. It should be mentioned that the optimized pm-Si:H PIN solar cell shows low  $V_{oc}$  because of low bandgap of intrinsic layer, but  $V_{oc}$  can be enhanced by novel device design. Improvement in  $V_{oc}$  by development of new device design will be presented in chapter 5.

### 3.5 HR pm-Si:H PIN solar cells

The  $r_d$  of the intrinsic layer for standard pm-Si:H PIN solar cells is about 1.5 Å/s. Deposition of 2500 Å intrinsic layer takes about 30 minutes, and an accelerated  $r_d$  would be industrially relevant from the point of productivity and cost reduction. Therefore, now we turn to the study on pm-Si:H PIN solar cells using high  $r_d$  (HR) intrinsic layer. For HR pm-Si:H, in order to avoid the powder formation, the intrinsic layers are deposited at a higher temperature of 210 °C, and the plasma chamber has narrower inter-electrode distance of 12 mm, as previously reported [3.14]. In HR pm-Si:H, the intrinsic layer was optimized in same way as for std pm-Si:H, i.e., by reducing  $\tau_r$ . In addition, to test the results obtained for the low  $r_d$  pm-Si:H, for HR pm-Si:H, SiH<sub>4</sub> flow is fixed and H<sub>2</sub> flow is varied.

Table 3.7 summarizes the process conditions and SE modeling parameters from HR pm-Si:H PIN solar cells. HR pm-Si:H PIN solar cells are all deposited on identical substrates (textured SnO<sub>2</sub>:F) with the same p- and n-type layers, and Ag back contacts. For the intrinsic layer deposition condition, only gas flow and total flow were varied while total pressure, RF power, and T<sub>s</sub> were fixed at 3 Torr, 30 W, and 210 °C, respectively. After deposition, the sample thickness and material parameters were obtained from SE modeling on PIN layer stack co-deposited on Corning glass.

Sample	H <sub>2</sub>	SiH <sub>4</sub>	E <sub>opt</sub> (eV)	d <sub>i</sub> (Å)	r <sub>d</sub> (Å/s)
a910291	338	50	1.69	2500	10.3
a910292	375	50	1.69	2500	10.25
a910293	412	50	1.69	2400	10.05
a910302	450	50	1.68	2400	9.92
a910303	500	50	1.65	2400	9.18

Table 3.7 – Gas flow and SE modeling parameters from HR pm-Si:H PIN solar cells deposited in five different intrinsic layer conditions. Note that the five HR pm-Si:H PIN solar cells are having identical substrates (Textured SnO<sub>2</sub>:F and corning glass), both p and n-type layers, and Ag back contacts. For the intrinsic layer deposition condition, only gas flow were varied while total pressure, RF power, and T<sub>s</sub> were fixed to 3 Torr, 30 W, and 210 °C, respectively.

Note that the p-type a-SiC was first deposited at 175 °C and the intrinsic and n-type layers were deposited at 210 °C. The process could be further optimized by better device design or use of multichamber reactor.

Table 3.8 shows solar cell parameters of HR pm-Si:H solar cells. The trend in HR pm-Si:H is in agreement with std pm-Si:H series, namely, the lower  $\tau_r$ , the better the material quality. Moreover, narrowing of E<sub>opt</sub> at larger total gas flow is also seen in HR pm-Si:H series. The behavior of E<sub>opt</sub> also results in a decrease in V<sub>oc</sub> at larger gas flow. It should be pointed out that even though the intrinsic layers are thin, and Ag back-contact provide insufficient light trapping, overall J<sub>sc</sub> in HR pm-Si:H PIN solar cells are low.

Sample	FF	R <sub>sc</sub> (Ωcm <sup>2</sup> )	R <sub>oc</sub> (Ωcm <sup>2</sup> )	J <sub>sc</sub> (mA/cm <sup>2</sup> )	V <sub>oc</sub> (V)	η (%)
a910291	65.74	2936	8.22	12.98	0.855	7.30
a910292	68.84	3387	7.78	12.34	0.854	7.23
a910293	68.22	2699	7.56	12.3	0.851	7.14
a910302	69.51	3077	7.85	12.11	0.847	7.13
a910303	69.9	2695	7.87	11.83	0.847	7.00

Table 3.8 – Solar cell parameters of HR pm-Si:H PIN solar cells shown in Figure 3.7. Note that multiple individual solar cells on 2.5×2.5 cm<sup>2</sup> substrate are measured and the solar cell parameters are averaged. Ag back-contacts are used.

Figure 3.8 shows the EQE curves of HR pm-Si:H PIN solar cells deposited at 210 °C and a single std pm-Si:H PIN cell deposited at 175 °C for comparison. The HR cells use the conditions of Table 3.7 and have a Ag back-reflector, while the LR cell is one with ITO/Ag previously shown in Figure 3.6. The EQE curve of HR pm-Si:H solar cells show low response in the entire region compared to that of std pm-Si:H. One can rule out the effect of different back-contact because light-trapping is more efficient in red-IR response, but in Figure 3.8, EQE curve of HR pm-Si:H solar cells show low response even in blue-green region.

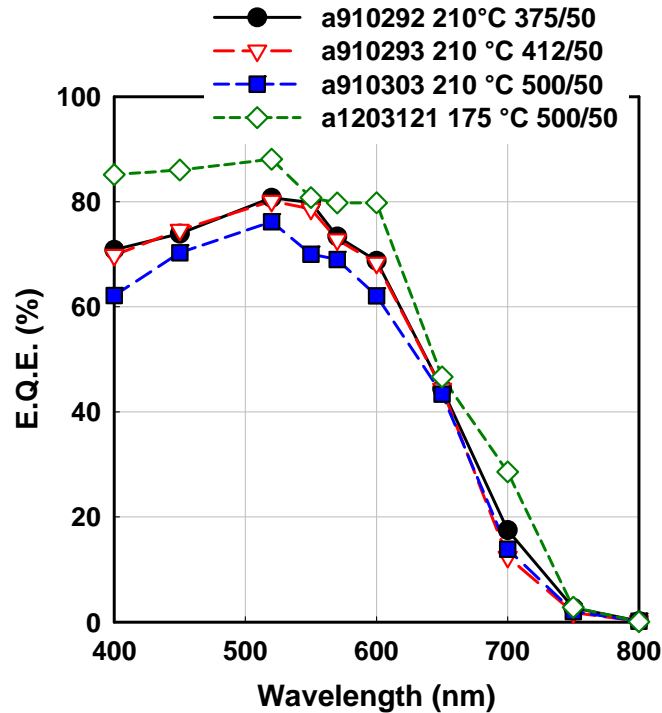


Figure 3.8 – EQE of various pm-Si:H PIN solar cells. pm-Si:H PIN solar cells deposited at 210 °C are indeed HR pm-Si:H solar cells with Ag back-reflector that shown in Table 3.7. pm-Si:H PIN solar cell deposited at 175 °C is one with ITO/Ag shown in Table 3.6.

Moreover, the deterioration of EQE becomes more serious for the PIN deposited under larger  $H_2$  flow. It suggests that at high  $T_s$  (210 °C), high RF (30 W), and under large  $H_2$  flow, deposition of intrinsic HR pm-Si:H introduced reduction of  $SnO_2:F$  by the H in the plasma, and

resulted in a gray-filter effect. This effect is facilitated at high deposition temperature [3.15]. The gray filter effect becomes more significant at larger  $H_2$  flow because reduction of  $SnO_2:F$  is induced by H plasma. ZnO substrate or thin ZnO coated Asahi substrate could be a solution. In the optimization of both low  $r_d$  pm-Si:H and HR pm-Si:H, there is a consistent trend that good quality material - namely low defect density material - comes from low  $\tau_r$  in process condition. By suppressing powder formation, low  $\tau_r$  results in low  $E_{opt}$  at the same time as low impurity concentration. The general relationship between  $E_{opt}$  and the initial  $FF$  of pm-Si:H is represented in Figure 3.9.

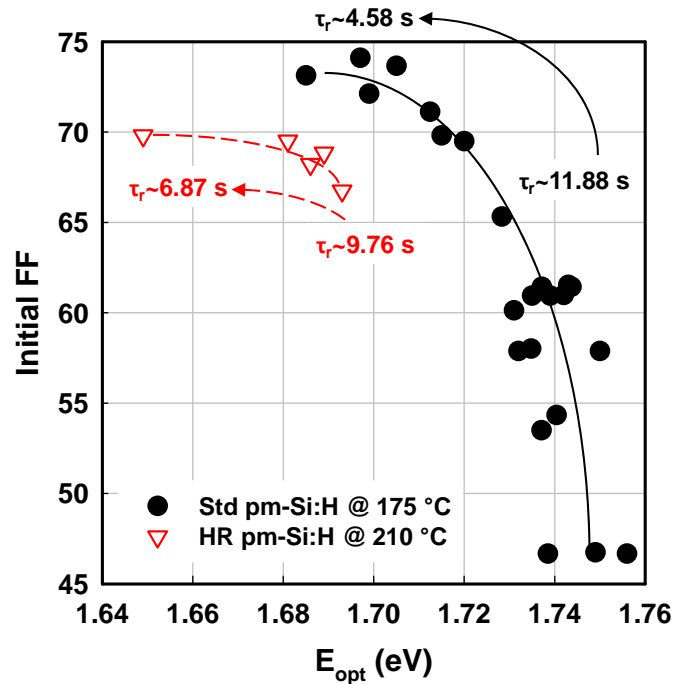


Figure 3.9 – Initial fill factor of pm-Si:H PIN solar cells versus optical bandgap ( $E_{opt}$ ) of various pm-Si:H PIN solar cells. Note that the  $E_{opt}$  is also a consequence of  $\tau_r$ , so  $\tau_r$  is also marked on the plot. There is a general trend in  $\tau_r$ - $E_{opt}$ - $FF$ , in which pm-Si:H having high FF come from low  $\tau_r$ .  $FF$ - $E_{opt}$  relation of HR pm-Si:H shows a little shift from std pm-Si:H series probably due to high  $T_s$  (210 °C).

In Figure 3.9, the initial fill factor of pm-Si:H PIN solar cells versus optical bandgap ( $E_{opt}$ ) is plotted for various pm-Si:H PIN solar cells having different gas flow and  $\tau_r$  of intrinsic layer deposition. As  $E_{opt}$

can be linked under certain conditions to  $\tau_r$ , this value is also marked on the plot. There is a general trend in  $\tau_r$  -  $E_{opt}$  -  $FF$  of PIN solar cells: pm-Si:H deposited at long  $\tau_r$  and high  $E_{opt}$  (in the range between 1.72-1.76 eV) results in a low initial  $FF$ , which is also randomly scattered at low values. The pm-Si:H deposition condition at low  $\tau_r$  leads to low impurity (O) concentration, as well as lower excess hydrogen content, leading to higher  $FF$ . One may notice that the deposition at long  $\tau_r$  leads not only to lower  $FF$ , but also to a higher degree of scattering in the material quality. It suggests that the powder formation becomes uncontrollable in long  $\tau_r$  condition.

It is also interesting that the  $FF$  -  $E_{opt}$  relation of HR pm-Si:H shows little shift from the std pm-Si:H series. Recalling the  $T_s$  series result in chapter 2, the high  $T_s$  of 210 °C used for HR pm-Si:H series is expected to result in a shift of  $E_{opt}$ . However, it should also be pointed out that in std pm-Si:H PIN optimization, decrease in  $\tau_r$  was realized by increasing  $SiH_4$  flow and increasing total flow. On the other hand, in HR pm-Si:H PIN optimization, decrease in  $\tau_r$  was realized by increasing  $H_2$  flow and increasing total flow. However, the same effect in  $E_{opt}$  and  $FF$  is observed, despite opposite direction of movement in gas flow ratio. If we only consider the effect of gas flow ratio of  $SiH_4/H_2$  and the resulting structural re-construction from different degree of hydrogen dilution, it is difficult to explain why both std and HR pm-Si:H PIN solar cells have high  $FF$ . Therefore, one can conclude that  $\tau_r$  strongly determines the material quality, and thus, in order to have good pm-Si:H PIN solar cell, the intrinsic pm-Si:H layer should be deposited under the condition at the lowest  $\tau_r$ .

As a high  $r_d$  is very attractive from the point of view of industry, we further tried to maximize the  $r_d$ . Another pm-Si:H PIN solar cell was deposited with intrinsic layer deposited at 19.6 Å/s, using high RF power of 80 W and higher silane concentration ratio. At

the same time, the pressure was lowered to 2 Torr and  $T_s$  was increased to 240 °C in order to reduce  $\tau_r$  and suppress powder formation. Table 3.9 summarizes the difference in process conditions.

Sample	H <sub>2</sub>	SiH <sub>4</sub>	P (Torr)	T <sub>s</sub> (°C)	RF (W)	r <sub>d</sub> (Å/s)	d <sub>electrode</sub> (mm)
pm-Si:H 1.5 Å/s a1104114	500	50	2	175	5	1.5	22
pm-Si:H 10 Å/s a910303	500	50	3	210	30	9.18	12
pm-Si:H 20 Å/s a1103225	250	50	2	240	80	19.6	12

Table 3.9 – Process conditions of pm-Si:H PIN solar cells. From 10 to 20 Å/s condition, silane concentration ratio, RF power was increased. At the same time, pressure was lowered and  $T_s$  was increased in order to suppress powder formation.

Figure 3.10 shows initial J(V) curves of two HR pm-Si:H PIN solar cells deposited at 10 Å/s and 20 Å/s. J(V) curve of pm-Si:H PIN solar cell deposited at 20 Å/s shows notable features of deterioration in material quality. Compared to that of 10 Å/s PIN solar cell, 20 Å/s PIN solar cell shows modest slope at  $P_{max}$  region, low  $R_{sc}$ , and high  $R_{oc}$ , which result in a low  $FF$ , due to higher recombination and poor transport properties. Relatively flat reverse bias up to -1 V suggests that the physical origin of the low  $FF$  is poor material quality, rather than shunted diode. Indeed, it was already implied in previous chapter that a high  $r_d$  of pm-Si:H deteriorates the material quality. Further improvement is needed in HR pm-Si:H PIN solar cells. Table 3.10 shows solar cell parameters of HR pm-Si:H PIN solar cells extracted from Figure 3.10.

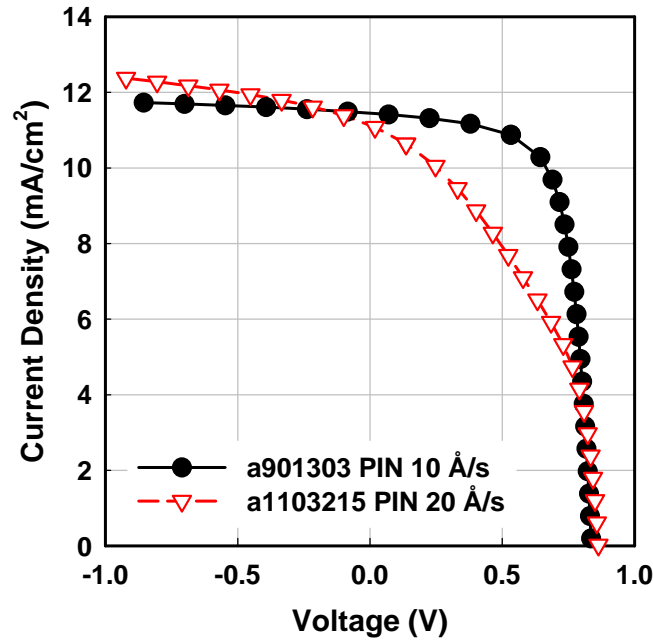


Figure 3.10 – Initial characteristics of HR pm-Si:H PIN solar cells deposited at 10 Å/s and 20 Å/s. The PIN at 20 Å/s was annealed at 160 °C for two hours, while the PIN at 10 Å/s was annealed at 150 °C for 30 minutes in order to avoid Ag diffusion.

Sample, BR	FF	R <sub>sc</sub> (Ωcm <sup>2</sup> )	R <sub>oc</sub> (Ωcm <sup>2</sup> )	J <sub>sc</sub> (mA/cm <sup>2</sup> )	V <sub>oc</sub> (V)	η (%)
pm-Si:H 10 Å/s a910303, Ag	69.9	2695	7.87	11.83	0.847	7.00
pm-Si:H 20 Å/s a1103225, Al	46.71	402	17.81	11.15	0.866	4.51

Table 3.10 – Solar cell parameters of HR pm-Si:H PIN solar cells in Figure 3.10. Note that multiple individual solar cells on 2.5×2.5 cm<sup>2</sup> substrate are measured and the solar cell parameters are averaged. Ag back-contact is used in 10 Å/s PIN, and Al back-contact is used in 20 Å/s PIN .

### 3.6 Stability issue of PIN solar cells

A light-induced degradation study was done for representative PIN solar cells. Sets of successive J(V) measurements were performed to observe changes of solar cell parameters. Between each J(V) measurement, the cells were light-soaked by light from a non-filtered Oriol-Apex Xe lamp. The cells were light soaked and their J(V) curves were measured under an illumination of 100 mW/cm<sup>2</sup>, which is

equivalent to one sun. Few initial  $J(V)$  measurements were set to be measured more often than later in order to carefully observe initial behavior. The representative PIN solar cells are a standard a-Si:H PIN, a 1.5 Å/s pm-Si:H PIN, a 10 Å/s pm-Si:H PIN, and a 20 Å/s pm-Si:H PIN. Their intrinsic layer thickness is 3000 Å for a-Si:H and 1.5 Å/s pm-Si:H PIN, and 2400 Å and 2500 Å for HR pm-Si:H PIN solar cells. Evaporated Al was used as back reflector except 10 Å/s pm-Si:H PIN (Ag), resulting in lower  $J_{sc}$ . Figure 3.11 shows the result of the light-soaking test.

In Figure 3.11(a), an interesting behavior for a-Si:H and 1.5 Å/s pm-Si:H PIN solar cells can be observed. The initial efficiency of the two PIN solar cells is similar, but the stabilized efficiency becomes different, as the 1.5 Å/s pm-Si:H PIN solar cell shows less degradation than the a-Si:H PIN solar cell. Moreover, the initial efficiency of 10 Å/s pm-Si:H PIN solar cell was much lower than that of a-Si:H PIN solar cell, but after light-soaking, the stabilized efficiency of 10 Å/s pm-Si:H PIN solar cell became comparable to that of a-Si:H PIN solar cell. The 20 Å/s pm-Si:H PIN solar cell barely degraded from initial to stabilized efficiency, but the efficiency is too low to merit a discussion of the kinetics. The kinetics of  $FF$  shown in Figure 3.11(b) is closely related to that of efficiency. As well, one can notice that the major source of the light-induced degradation is the degradation of  $FF$  that is attributed to the deterioration of transport and recombination properties of the intrinsic layers.  $V_{oc}$  indeed showed the lowest degradation among the solar cell parameters under LS. Moreover, 1.5 Å/s and 10 Å/s pm-Si:H PIN solar cells show increase in  $V_{oc}$  during light-soaking, with the 1.5 Å/s PIN solar cells showing more pronounced behavior. The  $V_{oc}$  increase of pm-Si:H PIN solar cells is consistent and reproducible. On the contrary a-Si:H PIN solar cells deposited in ARCAM show a consistent  $V_{oc}$  decrease.

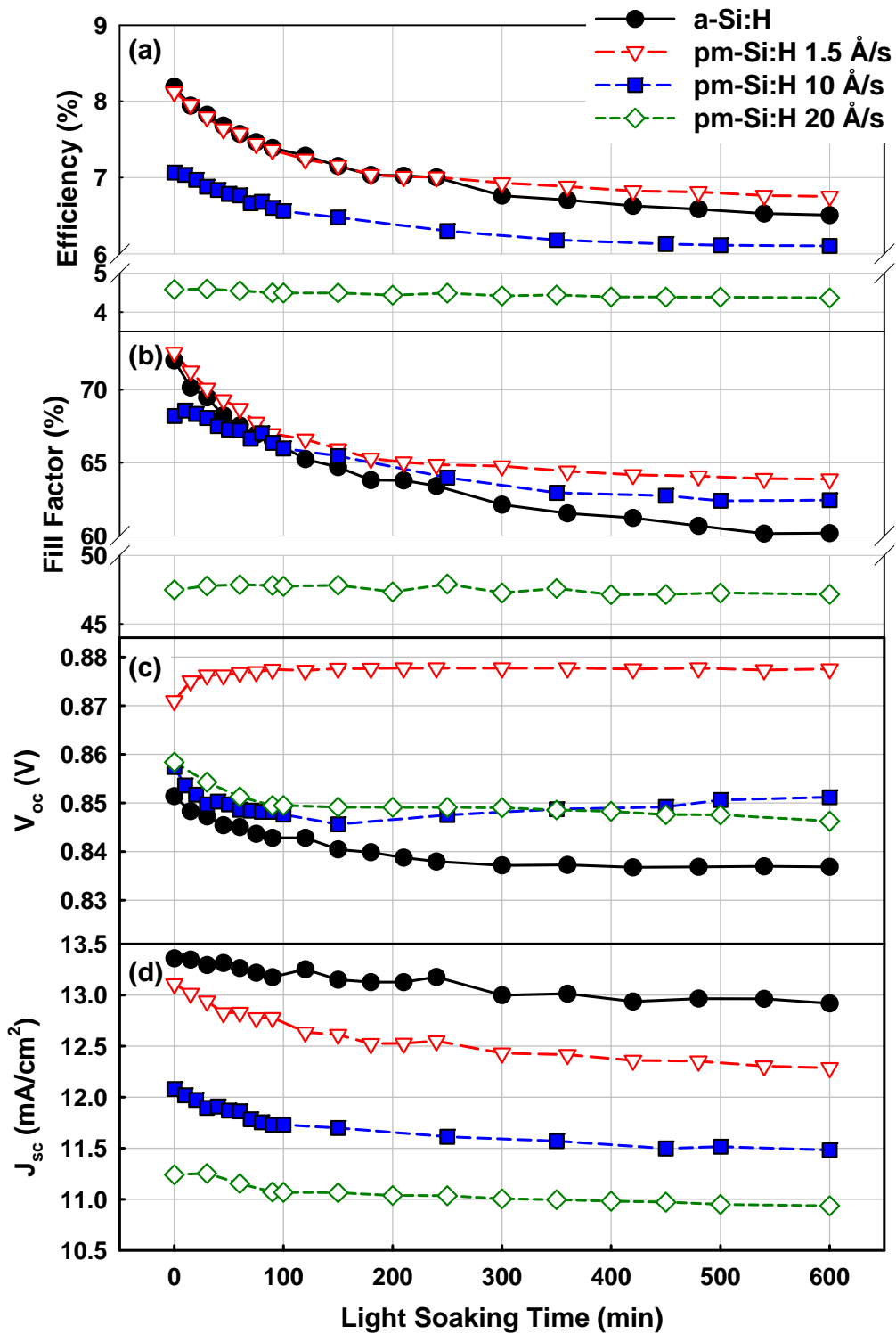


Figure 3.11 – Evolution of solar cell parameters of PIN solar cells using different intrinsic layers, (a)  $\eta$ , (b)  $FF$ , (c)  $V_{oc}$ , and (d)  $J_{sc}$  during LS under an illumination of 1 sun. The PIN solar cells were light-soaked and measured the  $J(V)$  curve by non-filtered Oriel-Apex Xe lamp.

A detailed discussion on  $V_{oc}$  increase will be held in the next chapter. In Figure 3.11(d),  $J_{sc}$  of the pm-Si:H PIN solar cell shows a faster initial drop followed by a phase of more moderate degradation at longer light-soaking times, while the a-Si:H solar cell demonstrates a monotonic degradation and no clear distinction into such phases. The faster initial decrease of  $J_{sc}$  is a major contribution to the initial efficiency degradation of pm-Si:H solar cells in contrast to that of a-Si:H. Due to the initial drop of  $J_{sc}$ , degradation kinetics of pm-Si:H PIN solar cells differ in character from the classic stretched exponential behavior observed in a-Si:H. Extracted solar cell parameters from Figure 3.11 are presented in Table 3.11. Magnitudes of degradation,  $\Delta\eta$  and intrinsic layer thickness,  $d_i$  are also marked. As mentioned above, smaller light-induced degradation of HR pm-Si:H PIN solar cells compared to a-Si:H is indeed due to the low initial efficiency.

Sample		FF	$J_{sc}$ (mA/cm <sup>2</sup> )	$V_{oc}$ (V)	$\eta$ (%)	$\Delta\eta$ (%)	$d_i$ (Å)
a-Si:H a1004083	Initial	72.01	13.37	0.851	8.19	-20.64	3000
	LS 10 hrs	60.19	12.92	0.837	6.5		
pm-Si:H 1.5 Å/s a1104264	Initial	72.57	13.1	0.871	8.12	-16.88	3000
	LS 10 hrs	63.89	12.28	0.878	6.75		
pm-Si:H 10 Å/s a910303	Initial	68.21	12.08	0.857	7.06	-13.6	2400
	LS 10 hrs	62.44	11.48	0.851	6.10		
pm-Si:H 20 Å/s a1103215	Initial	47.48	11.24	0.858	4.58	-4.81	2500
	LS 10 hrs	47.16	10.93	0.846	4.36		

Table 3.11 – Solar cell parameters extracted from light-soaking test in Figure 3.11. Degradation,  $\Delta\eta$  and intrinsic layer thickness,  $d_i$  are also marked. Note that low light-induced degradation of HR pm-Si:H PIN solar cells compared to a-Si:H and 1.5 Å/s pm-Si:H PIN solar cells are indeed due to the low initial efficiency. The stabilized efficiency is a consequence of both initial efficiency and  $\Delta\eta$ .

### 3.7 Summary

In this chapter we have presented pm-Si:H PIN solar cells made of intrinsic materials prepared under various deposition conditions. Minimizing  $\tau_r$  leads to depositing low defect density material, and the application of an ITO/Ag reflector enhanced  $J_{sc}$ , resulting in PINs showing  $\eta_{initial}$  of 9.22 %. Application of HR pm-Si:H layers was also studied and HR pm-Si:H PIN solar cells using 10 Å/s pm-Si:H still show a reasonable  $\eta_{initial}$  of 7 %. Further increase in the  $r_d$  up to 20 Å/s was not successful. Further improvement of material quality is needed.

## References

- 3.1 S. Okur, M. Güneş, O. Göktaş, F. Finger, and R. Carius, *J. Mater. Sci. Mater. Electronics* 15, 187 (2004).
- 3.2 Y. Tawada, H. Okamoto, and Y. Hamakawa, *Appl. Phys. Lett.* 39, 237 (1981).
- 3.3 B. Rech, C. Beneking, and H. Wagner, *Sol. Energ. Mater. Sol. Cells* 41-42, 475 (1996).
- 3.4 B. von Roedern, *Mat. Res. Soc. Symp. Proc.* 668, H6.9 (2001).
- 3.5 Y. M. Soro, A. Abramov, M. E. Gueunier-Farret, E. V. Johnson, C. Longeaud, P. Roca i Cabarrocas, J. P. Kleider, *J. Non Cryst. Solids* 354, 2092 (2008).
- 3.6 R. A. Street, *Hydrogenated Amorphous silicon*. Cambridge University Press; 1991; citing pp. 371-372.
- 3.7 A. Shah, M. Vanecek, J. Meier, F. Meillaud, J. Guillet, D. Fischer, C. Droz, X. Niquille, S. Fay, E. Vallat-Sauvain, V. Terrazzoni-Daudrix, and J. Bailat, *J. Non Cryst. Solids* 338–340, 639 (2004).
- 3.8 M. Vanecek, A. Poruba, Z. Remes, J. Holovsky, A. Purkrt, O. Babchenko, K. Hruska, J. Meier, and U. Kroll, *Proc. 24th European PVSEC, Hamburg 2009*, pp. 2286-2289.
- 3.9 S. Benagli, D. Borrello, E. Vallat-Sauvain, J. Meier, U. Kroll, J. Hötzel, J. Bailat, J. Steinhauser, M. Marmelo, G. Monteduro, and L. Castens, *Proc. 24th European PVSEC, Hamburg 2009*, pp. 21-25.
- 3.10 B. Yan, G. Yue, L. Sivec, J. Yang, S. Guha, and C-S. Jiang, *Appl. Phys. Lett.* 99, 113512 (2011).
- 3.11 U. Kroll, J. Meier, A. Shah, S. Mikhailov and J. Weber, *J. Appl. Phys.* 80, 4971 (1996).
- 3.12 W. Futako, S. Takeoka, C. M. Fortmann, and I. Shimizu *J. Appl. Phys.* 84, 1333 (1998).
- 3.13 E. V. Johnson, M. Nath, P. Roca i Cabarrocas, A. Abramov, and P. Chatterjee, *J. Non Cryst. Solids* 354, 2455 (2008).
- 3.14 Y. M. Soro, A. Abramov, M. E. Gueunier-Farret, E. V. Johnson, C. Longeaud, P. Roca i Cabarrocas, and J.P. Kleider, *Thin Solid Films* 516, 6888 (2008).
- 3.15 H. Stiebig, F. Siebke, W. Beyer, C. Beneking, B. Rech, and H. Wagner, *Sol. Energ. Mater. Sol. Cells* 48, 351 (1997).

# Chapter **4**

## **Light-Induced Degradation and Solar Cell Stability**

4.1 Introduction.....	126
4.2 PIN solar cell device stability – initial behavior .....	126
4.3 Light-induced structural changes .....	144
4.4 Light-induced hydrogen motion .....	160
4.5 Hypothesis on light-induced changes .....	171
4.6 Long-term stability and new device structure .....	174
4.7 Summary .....	181

### 4.1 Introduction

This chapter is devoted to the stability issue of pm-Si:H PIN solar cells compared to that of a-Si:H solar cells.. The pm-Si:H solar cells show an irreversible degradation at the first hours of light-soaking, while having higher stabilized efficiency with respect to a-Si:H cells. Such irreversible degradation of pm-Si:H solar cells cannot be explained by Staebler-Wronski Effect (SWE) models proposed so far. We correlate the particular behavior of pm-Si:H solar cells to changes in hydrogen incorporation and structural properties in their layers. Numerous techniques are used to study the light-induced changes from microscopic to macroscopic scales (up to tens of microns). Our results lead us to view the kinetics from a different angle: that stimulated hydrogen motion - which occurs in a-Si:H under extreme conditions - takes place in pm-Si:H under conditions close to the device operation, and it introduces structural changes including diffusion of molecular hydrogen, hydrogen accumulation at p-layer/substrate interface and localized delamination of the interface. Based on these results we propose that light-induced degradation of PIN solar cells has to be addressed not only from a material perspective, but also from a device point of view. In particular we bring experimental evidence that localized delamination at the interface between the p-layer and SnO<sub>2</sub> substrate by light-induced hydrogen motion causes the rapid drop of short circuit current density.

### 4.2 PIN solar cell device stability – initial behavior

The PIN solar cells were deposited at 175 °C by the radio-frequency (RF, 13.56 MHz) glow discharge (PECVD) method in the ARCAM reactor [4.1]. Standard a-Si:H was obtained by the dissociation of pure silane and under a pressure of 50 mTorr and a RF power of 1 W.

Intrinsic pm-Si:H layers were deposited at a pressure of 2 Torr and RF power density was varied from 30 to 60 mW/cm<sup>2</sup>. The solar cells had the PIN structure: glass/textured SnO<sub>2</sub>:F/p-type hydrogenated amorphous silicon carbon (a-SiC:H)/a-SiC:H buffer/intrinsic layer/n-type a-Si:H/Al contact. NIP solar cells were also fabricated to test our hypothesis on the metastability. More details on NIP solar cell structure will be given in forthcoming chapter. The area of the cells was 0.126 cm<sup>2</sup>. The thickness of p and n-type layers were about 150 Å, and the intrinsic layer thickness varied from 3000 to 6500 Å.

For the light-induced degradation studies, sets of current-density-voltage ( $J(V)$ ) measurements at various stages of the light-soaking were performed. The  $J(V)$  measurements during the early stages of light-soaking were taken more frequently than later, in order to accurately monitor the dynamics during this critical phase. Between each  $J(V)$  measurement, the cells were light-soaked in the open-circuit condition using an Oriel-Apex Xe lamp. The cells were both light-soaked and had their  $J(V)$  curves measured under an illumination of 100 mW/cm<sup>2</sup> (equivalent to one sun). In some cases, to accelerate light-induced degradation, the solar cells are light-soaked and  $J(V)$  curves measured under an intense illumination of 200 mW/cm<sup>2</sup> (equivalent to two suns). During light-soaking, the PIN solar cells were fan cooled to limit illumination induced heating. The temperature of the PIN solar cells, measured by a PT100 thermometer during light-soaking (LS), stayed under 50 °C. Figure 4.1 shows the evolution of a-Si:H and pm-Si:H PIN solar cell parameters, such as the power conversion efficiency ( $\eta$ ), fill factor ( $FF$ ), open-circuit voltage ( $V_{oc}$ ), and short-circuit current density ( $J_{sc}$ ) as functions of LS time. Note that here, the PIN solar cells are light-soaked and measured  $J(V)$  curves under two suns. One can find a notable difference in the light-induced degradation behavior of the pm-Si:H and the a-Si:H PIN solar cells.

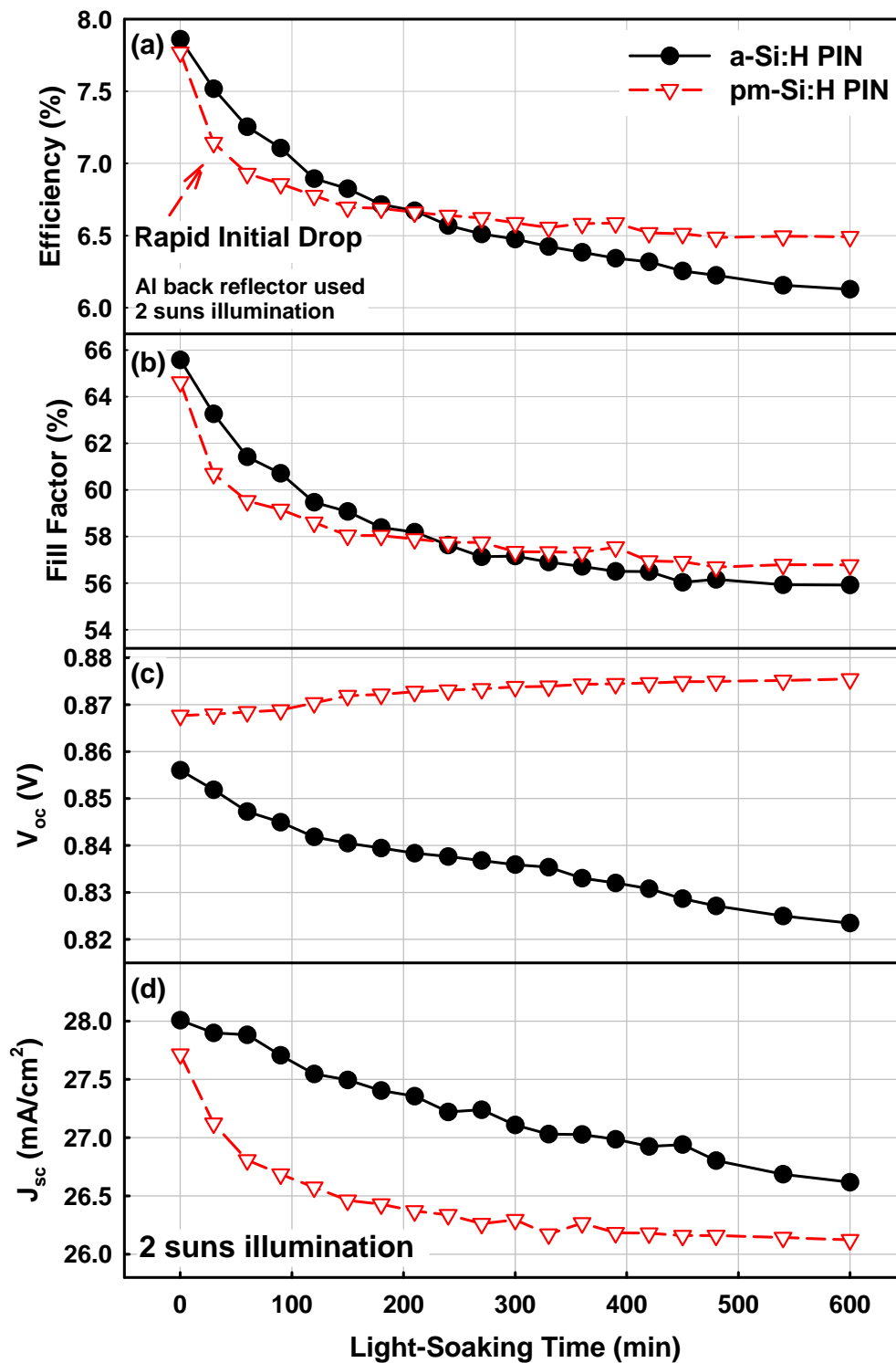


Figure 4.1 – Evolution of a-Si:H and pm-Si:H PIN solar cell parameters. (a) power conversion efficiency (b) fill factor (c)  $V_{oc}$  and (d)  $J_{sc}$  during light-soaking under an illumination of 200 mW/cm².

The  $\eta$  in Figure 4.1(a) shows that the pm-Si:H PIN solar cell is more stable than the a-Si:H. However, the pm-Si:H PIN solar cell shows a rapid  $\eta$  drop at the early stages (about first two hours) of light-soaking. Strong proportionality between the  $FF$  and the  $\eta$  implies that the  $FF$  provides a major contribution of the  $\eta$  degradation, and that most of the light-induced degradation takes place in the intrinsic layer. The difference in behavior between the two types of cells is also striking for  $V_{oc}$  (Figure 4.1c), which increases for the pm-Si:H cell, whereas it drops for the a-Si:H solar cell during light-soaking. This behavior cannot be explained by heating of the cells. Indeed if this were the case, then we should observe a decrease in  $V_{oc}$  and an increase in  $J_{sc}$ . Therefore, the increase of  $V_{oc}$  provides a strong indication that heating effects are negligible during light-soaking, in agreement with PT100 thermoresistor probe measurement indicating that the temperature of the PIN solar cells stayed under 50 °C during light-soaking. It is important to note that the data in Figure 4.1 were continuously recorded during the light-soaking, without turning off the lamp.

Various hypothesis have been proposed to explain the increase in  $V_{oc}$  during light-soaking- i) the activation of boron in the p-layer of the solar cells during light-soaking [4.2-4.8], ii) light-induced changes in the intrinsic mixed-phase material [4.9-4.11] and iii) decrease in valence band tail and state re-distribution at p/i interface [4.12]. Most of those studies deal with solar cells based on a-Si:H materials deposited by dissociating silane-hydrogen gas mixtures, while our standard a-Si:H was deposited by dissociating pure silane. Therefore, the physical origin of the  $V_{oc}$  kinetics of the a-Si:H solar cells in the literature can differ from that of our standard a-Si:H PIN solar cells. Besides, a common physical origin in the discussion of the  $V_{oc}$  increase is hydrogen motion, and it is rather related to the highly hydrogen diluted silane gas mixture used in pm-Si:H deposition. Another interesting point concerning the  $V_{oc}$  increase as addressed in the

literature is that none of those studies included comprehensive observation of the kinetics of  $J_{sc}$ . The  $J_{sc}$  of the pm-Si:H PIN solar cell (Figure 4.1d) shows a faster initial drop followed by a phase of more moderate degradation at longer LS times, while the a-Si:H solar cell demonstrates a monotonic degradation and no clear distinction into such “phases”. The faster initial decrease of  $J_{sc}$  is another contribution to the initial  $\eta$  degradation of pm-Si:H PIN solar cells, and it differs in character from the classic stretched exponential behavior observed in a-Si:H. It has also been reported that a-Si:H shows very fast creation of charged gap states during light-soaking [4.13], which could be related to the fast degradation kinetics of the pm-Si:H cell. However, midgap state defect creation should lead to a decrease in  $V_{oc}$  in addition to that of the overall efficiency. Therefore, we consider that fast defect creation is insufficient to explain the particular degradation of pm-Si:H solar cells and that other phenomena must be involved.

The initial degradation behavior of the pm-Si:H PIN solar cells is indeed irreversible. The a-Si:H and pm-Si:H PIN solar cells were both light-soaked and had their  $J(V)$  curves measured under an illumination of one sun. After 10 hours of LS, both a-Si:H and pm-Si:H based PIN solar cells were annealed at 160 °C for two hours. This LS-annealing cycle was repeated three times. During the LS, the PIN solar cells were fan cooled to reduce illumination-induced heating. The temperature of the PIN solar cells was also monitored to verify that the device temperature stayed at 40 °C. The main source of uncertainty in the solar cell parameters comes from the dependence of  $V_{oc}$  and  $J_{sc}$  on the measurement temperature. We have determined that a variation in the temperature of  $\pm 7.5$  °C results in a variation in  $J_{sc}$  and  $V_{oc}$  of  $\pm 1.5$  % and  $\pm 0.5$  %, respectively, and a negligible change in  $FF$ . Figure 4.2 shows the reversibility test result.

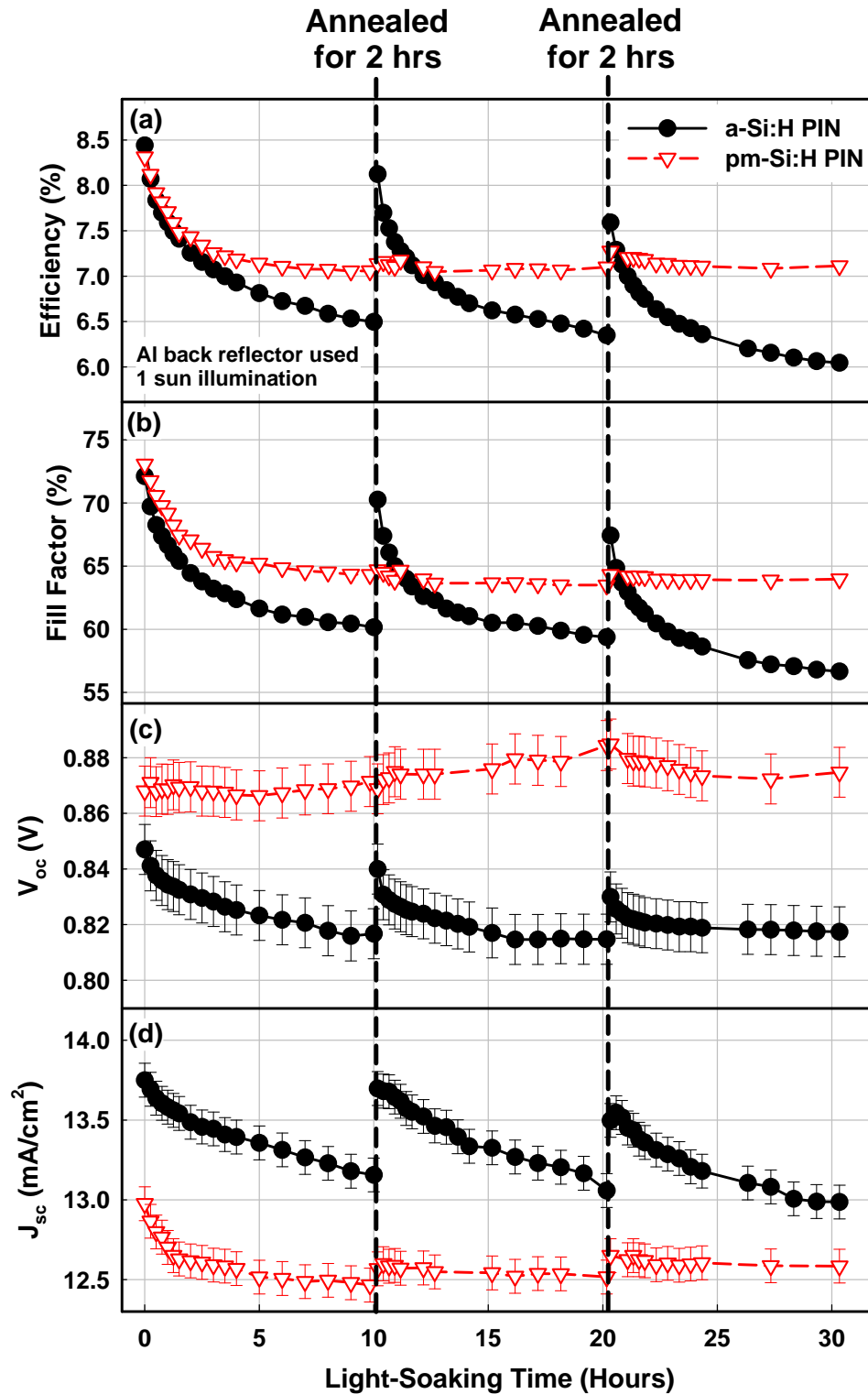


Figure 4.2 – Evolution of a-Si:H and pm-Si:H PIN solar cell parameters: (a)  $\eta$ , (b)  $FF$ , (c)  $V_{oc}$ , and (d)  $J_{sc}$  during LS under an illumination of 1 sun. Note that every 10 hours LS was interrupted and the solar cells were annealed at 160 °C for 2 hours in order to check for the reversibility of the light-soaking effect. Note that the error bars indicate temperature dependent ( $\pm 7.5$  °C) variation of solar cell parameters.

Figure 4.2 shows evolution of a-Si:H and pm-Si:H PIN solar cell parameters as functions of LS time, including two annealing steps (as described above). Figure 4.2a again shows that the  $\eta$  of the pm-Si:H PIN solar cells is more stable than that of the a-Si:H PIN solar cells. Most of the degradation in the  $\eta$  of the pm-Si:H PIN solar cells occurs in the first five hours of the LS while that of the a-Si:H PIN solar cell shows continuous degradation. Figure 4.2b shows the  $FF$  of a-Si:H and pm-Si:H PIN solar cells as functions of LS time. Strong proportionality between the  $FF$  and the  $\eta$  implies that the  $FF$  provides a major contribution to the  $\eta$  degradation, and that most of the light-induced degradation takes place in the intrinsic layer. However, there is an interesting feature in the  $FF$  behavior after the first LS cycle. After annealing, the  $FF$  of the pm-Si:H PIN solar cell remained at its degraded value, while the  $FF$  of the a-Si:H PIN solar cell recovered to 97 % of its initial value. Moreover, the pm-Si:H PIN solar cell shows an absence of further degradation in the  $FF$  with further LS, in contrast to the a-Si:H PIN solar cell, which degrades again in both the second and third LS cycles. To our knowledge, the irreversible degradation of the pm-Si:H PIN solar cells has never been reported before. Moreover, such irreversibility cannot be explained by the conventional SWE alone [4.14, 4.15], so a different physical origin must exist. Even though the irreversibility of pm-Si:H PINs is consistently demonstrated, we have examined our results with a critical eye because they fall out of the conventional paradigm of metastability in a-Si:H. Such irreversibility in the  $FF$  decay for the pm-Si:H PIN solar cells is coherent with evidence that the defect density in pm-Si:H films shows irreversible light-induced defect creation and increase in tail states after LS [4.16]. Furthermore, the fast initial degradation and rapid stabilization of the  $FF$  in pm-Si:H resembles the behavior of a-Si:H after a high temperature (above 350 °C) annealing treatment, which creates additional initial defects,

but suppresses further light-induced defect creation [4.17]. It should be mentioned that we have also tested annealing the PIN solar cells at higher temperatures, at 175 and 200 °C. However the higher temperature annealing deteriorated both a-Si:H and pm-Si:H solar cells.

The deviation between a-Si:H and pm-Si:H PIN solar cell behavior becomes even more striking when observing the  $V_{oc}$  (Figure 4.2c) and  $J_{sc}$  (Figure 4.2d) kinetics. Note that the error bars indicate temperature dependent ( $\pm 7.5$  °C) variation of parameters. The initial increase in the  $V_{oc}$  of PIN solar cells during LS has already been discussed above, especially for material deposited at the onset of the amorphous-to-crystalline transition [4.9-4.11, 4.18]. There are interesting features to discuss on the  $V_{oc}$  of the pm-Si:H PIN solar cells. First, the changes in  $V_{oc}$  are due to two opposing processes: an initial increase (explained above) and a slow decrease due to the SWE. Second, even if the  $V_{oc}$  of the pm-Si:H PIN solar cells shows a moderate initial increase during LS while that of the a-Si:H PIN solar cells shows a decrease, the changes are within the error range. Third, it is hard to imagine that  $V_{oc}$  will continue to increase. The magnitude of the initial increase in  $V_{oc}$  mainly depends on the gas flow ratio during intrinsic layer deposition [4.9, 4.11], and the variation of initial increase in  $V_{oc}$  is limited to about 150 mV [4.11]. The  $J_{sc}$  of the pm-Si:H PIN solar cell shows a rapid drop in the first two hours, followed by a phase of stability at longer LS times. An even more interesting feature of the  $J_{sc}$  kinetics of the pm-Si:H PIN solar cell is the absence of further degradation as well as the absence of annealing induced recovery during subsequent LS cycles. Such interesting behavior of the  $J_{sc}$  is confirmed by external quantum efficiency (EQE) measurements. Figure 4.3 shows EQE curves of both a-Si:H and pm-Si:H PIN solar cells in their as-deposited, light-soaked and annealed states.

In Figure 4.3a, it is shown that the a-Si:H PIN solar cell suffers from a uniform degradation over its entire EQE curve after LS. However, the pm-Si:H PIN solar cell (Figure. 4.3b) shows degradation only in the blue region, while the response at longer wavelength region has increased with LS. Such behavior in EQE - a decrease in the blue and an increase at longer wavelengths - has been previously reported [4.19, 4.20].

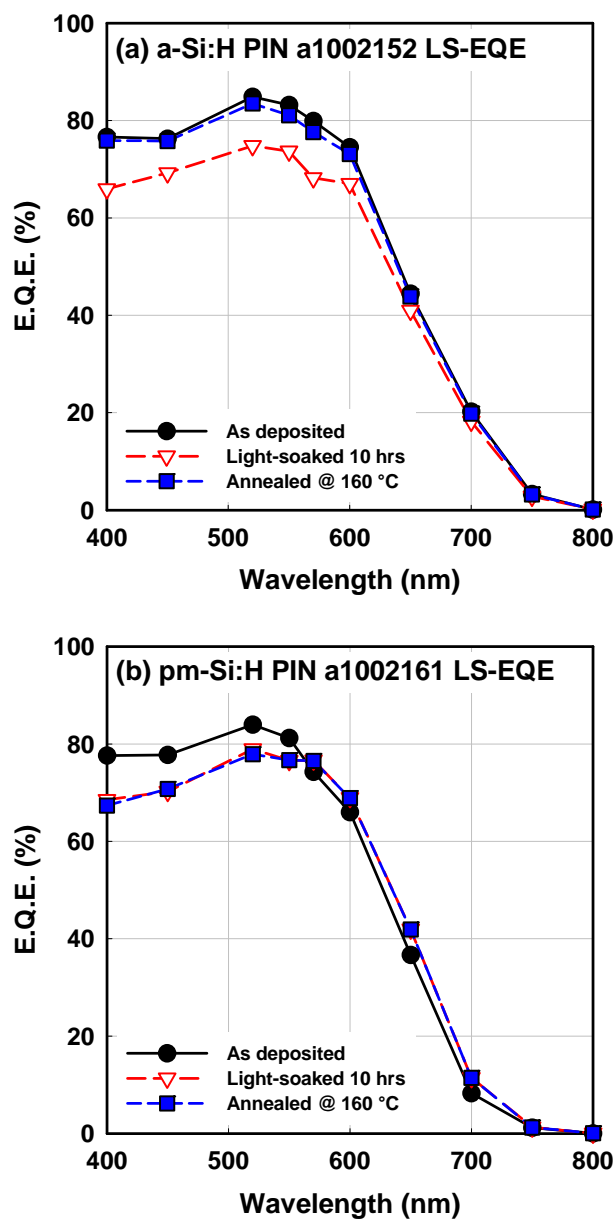


Figure 4.3 – EQE curves of both a-Si:H and pm-Si:H PIN solar cells in their as-deposited, light-soaked, and annealed states.

Numerical simulation studies examining such behavior in pm-Si:H PIN solar cells showed that an electric field re-distribution introduces the  $V_{oc}$  increase and the specific  $J_{sc}$  behavior during LS [4.19].

In some aspects, the light-induced degradation behavior of pm-Si:H PIN solar cells resembles that of a-Si:H PIN solar cells exposed to an intense illumination ( $\sim 50$  suns) at elevated temperatures ( $> 130$  °C) [4.20, 4.21]. Under such conditions, a-Si:H PIN solar cells also show irreversible degradation - namely significant degradation of EQE in the blue - a result attributed to the hydrogen diffusion and the delamination of p-layer/SnO<sub>2</sub> interface under extreme conditions [4.20]. Carlson and Rajan observed “blisters” after subjecting their a-Si:H solar cells to extreme conditions of LS, and they related them to interface delamination. We note that here also, the irreversibility comes from device scale structural changes. Interestingly, the discussions on the increase in  $V_{oc}$  also invoke structural changes, such as barrier formation at the p-layer/SnO<sub>2</sub> interface [4.9] and hydrogen evolution from the surface of nanocrystals [4.18]. Contrary to the a-Si:H PIN solar cells, the pm-Si:H PIN solar cells examined herein display irreversibility under conditions close to normal solar cell operation ( $\sim$  one sun,  $< 40$  °C).

Let us now focus on the initial degradation kinetics of pm-Si:H PIN solar cells, which is quite different from that of a-Si:H. The  $\eta$  degradation of a-Si:H and pm-Si:H PIN solar cells are modeled by Redfield-Bube Model (RB model) introduced in chapter 1. The model is in the stretched exponential form, and defined by the relation below;

$$N_D = N_s + (N_s - N_0) \exp \left[ - \left( \frac{t}{\tau} \right)^\beta \right]$$

Here  $N_D$  is the density of metastable defects,  $N_s$  is the saturated defect density, and  $N_0$  is the initial defect density.  $\tau$  defines an inflection

point of the defect creation, and  $\beta$  is a broadening term, which characterizes the “stretched” nature. Usually a-Si:H shows  $\beta$  ranges in  $0.6 < \beta < 0.8$ . Furthermore, solar cell efficiency degrades with logarithmic time scale, and the defect density in the meantime follows a power law in stretched exponential form as described above. The simplified following relationship can be proposed as below

$$\eta = -A \cdot \log N_D$$

where  $\eta$  is the cell efficiency and  $A$  is a constant depending on the structure of the solar cell such as intrinsic layer thickness [4.23]. Therefore, one can model  $\eta$  with the expression below

$$\eta = y_0 + A_1 \exp \left[ - \left( \frac{t}{\tau} \right)^\beta \right]$$

where  $y_0$  is estimated normalized stabilized efficiency and  $A_1$  is magnitude of degradation. Figure 4.4 shows normalized efficiency of a-Si:H and pm-Si:H PIN solar cells as functions of LS time and fit to the model. Table 4.1 shows the fitting parameters of the modeling. As seen in the results above, pm-Si:H PIN solar cell shows less light-induced degradation. More interesting features are contained in  $\tau$  and  $\beta$ . According to the modeling result, pm-Si:H PIN solar cell shows smaller  $\tau$ . As explained above,  $\tau$  determines an inflection point, that is, metastable defect creation process starts to saturate after  $\tau$ . pm-Si:H PIN solar cell shows about half of  $\tau$  comparing to that of a-Si:H, and it suggests the light-induced degradation process of pm-Si:H PIN solar cells is about twice faster than that of a-Si:H PIN solar cells. Similarly, higher  $\beta$  of pm-Si:H PIN solar cells is another notable feature.  $\beta$  characterizes the stretched nature of degradation kinetics, and the process is no more in “stretched” form when  $\beta$  approaches to 1. In case of pm-Si:H,  $\beta$  is far-above than empirical range of a-Si:H. Indeed, the fitting with  $\beta=1$ , the LS result of pm-Si:H PIN solar cell shows

reasonable agreement. In other words, the degradation process of pm-Si:H PIN solar cells is indeed in “barely stretched” form, and it is much faster than the degradation kinetics of a-Si:H PIN solar cell.

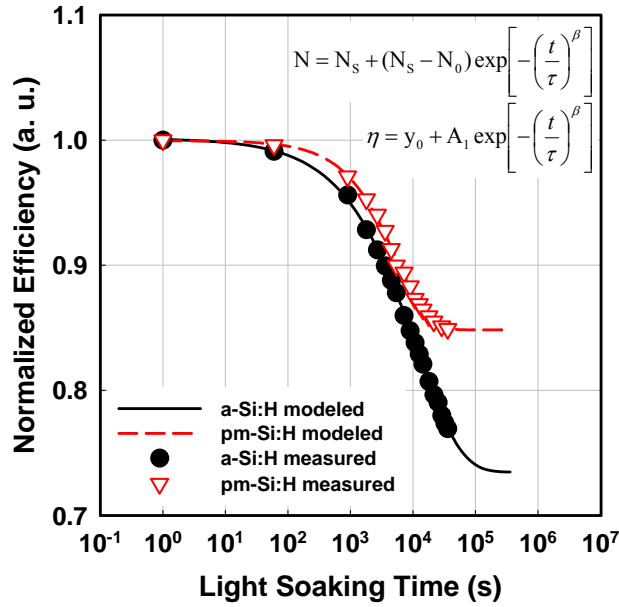


Figure 4.4 – Normalized efficiency of a-Si:H and pm-Si:H PIN solar cells as functions of LS time and fit to the model. Note that the LS result is from Figure 4.2.

	a-Si:H	pm-Si:H
$y_0$	<b>0.734</b>	<b>0.849</b>
$A_1$	<b>0.267</b>	<b>0.151</b>
$\tau$	<b>11719</b>	<b>5344</b>
$\beta$	<b>0.621</b>	<b>0.934</b>

Table 4.1 – Fitting parameters of modeling in Figure 4.4.  $y_0$  is estimated stabilized efficiency,  $A_1$  is magnitude of degradation,  $\tau$  decides an inflection point of the defect creation, and  $\beta$  is a broadening term, which characterize the “stretched” nature of the expression.

Before we proceed into structural studies, we would like to briefly mention that most of the degradation of pm-Si:H PIN solar cells is induced by high energy photons (400-500 nm). A set of a-Si:H and pm-Si:H PIN solar cells was prepared and light-soaked for 180 minutes under band-pass filtered 570 nm illumination. LS intensity of filtered light was about 40 mW/cm<sup>2</sup>, and J(V) curves are measured

under white light of  $100 \text{ mW/cm}^2$ . The intrinsic layer thickness of PIN solar cells is  $3000 \text{ \AA}$ . Figure 4.5 shows the evolution of a-Si:H and pm-Si:H PIN solar cell parameters under filtered  $570 \text{ nm}$  illumination. It is notable that the pm-Si:H PIN solar cell barely degrades. Indeed, it has been already published that even  $0.75 \text{ \mu m}$  thick pm-Si:H solar cell shows no significant degradation under red light illumination [4.2], and Figure 4.5 shows a nice reproducibility of our previous result. Another interesting feature is that under filtered  $570 \text{ nm}$  illumination,  $FF$  and  $J_{sc}$  of pm-Si:H show an absence of rapid initial degradation, while the  $V_{oc}$  of pm-Si:H shows a relatively large increase. Thus, most of the degradation of pm-Si:H PIN solar cell occurs at the front of the cell where high energy photons are absorbed, as shown in the EQE curve of Figure 4.3. Moreover, recalling that evolution of  $V_{oc}$  of pm-Si:H PIN solar cells is a consequence of two opposing processes leading to an initial increase and a slow decrease (Figure 4.2c), large increase of  $V_{oc}$  under filtered  $570 \text{ nm}$  illumination shows only an initial increase portion of  $V_{oc}$ . Of course,  $V_{oc}$  will eventually degrade at longer times.

What happens if the PIN solar cells are left in dark right after the LS? We have tested so-called “healing” experiment. The a-Si:H and pm-Si:H PIN solar cells were first light-soaked for 90 minutes, and left in the dark for another 90 minutes. Then, the cells were again light-soaked for another 90 minutes. In this case, the intrinsic layer thickness of PIN solar cells is  $5000 \text{ \AA}$ . PT100 thermo-resistor revealed that LS heats the PIN solar cells up to  $50 \text{ }^\circ\text{C}$ .

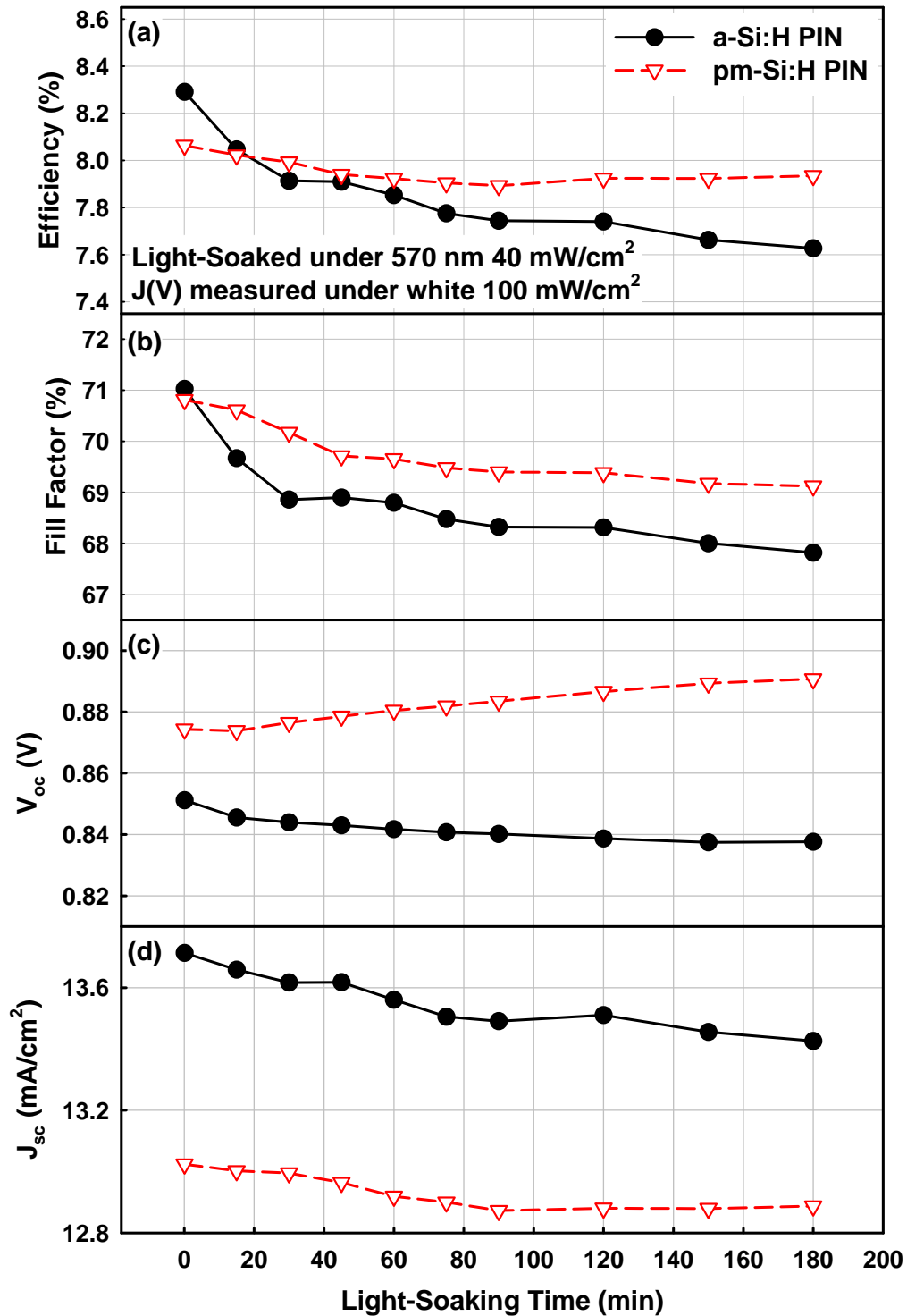


Figure 4.5 – Evolution of a-Si:H and pm-Si:H PIN solar cell parameters under yellow illumination: (a)  $\eta$ , (b)  $FF$ , (c)  $V_{oc}$ , and (d)  $J_{sc}$  during LS of band-pass filtered 570 nm illumination. Note that the LS intensity was about 40 mW/cm<sup>2</sup>, and J(V) curves are measured under white light of 100 mW/cm<sup>2</sup>. The intrinsic layer thickness of PIN solar cells is 3000 Å.

Figure 4.6 shows the result of the LS-healing-LS test. One can notice that for the pm-Si:H PIN solar cell, the initial rapid drop in  $FF$  and  $J_{sc}$  and increase in  $V_{oc}$  that were previously observed are well reproduced. After the PIN solar cells were light-soaked, they were left in the dark and the solar cell parameters were measured for one hour. The PIN solar cells are illuminated only when the  $J(V)$  curves are measured. During this period, the  $\eta$  of pm-Si:H PIN solar cell slightly recovered in the dark through a recovery in its  $FF$ , while the a-Si:H PIN solar cell kept its degraded cell parameters. In more detail, both PIN solar cells show increase of  $V_{oc}$  and decrease in  $J_{sc}$ , which is attributed to the effect of temperature. The temperature effect is also shown in the second LS cycle, in which both PIN solar cells show decrease in  $V_{oc}$  and increase in  $J_{sc}$ . The initial stage of the first LS cycle did not show the effect of heating, because the PIN solar cells had already been subjected to several  $J(V)$  measurements, in order to ensure electrical contact and setup. During the healing cycle,  $FF$  of the pm-Si:H cell slightly increased. Moreover, the  $J_{sc}$  of the pm-Si:H cell only slightly decreased compared to that of the a-Si:H cell. It is assumed that the  $J_{sc}$  of the a-Si:H cell decreased during the healing cycle due to the effect of temperature, and it is expected that pm-Si:H PIN solar cell should also experience the cool-down, as suggested by the large increase in its  $V_{oc}$  during the healing cycle. Together, these results suggests that the  $J_{sc}$  of the pm-Si:H cell experiences some decrease due to a cooling effect, but there is also an increasing portion of  $J_{sc}$ , so  $J_{sc}$  of pm-Si:H PIN solar cell had less decrease than that of a-Si:H PIN solar cell. In summary, the pm-Si:H PIN solar cell shows healing after LS because of a combined effect of  $FF$  increase and  $J_{sc}$  stability.

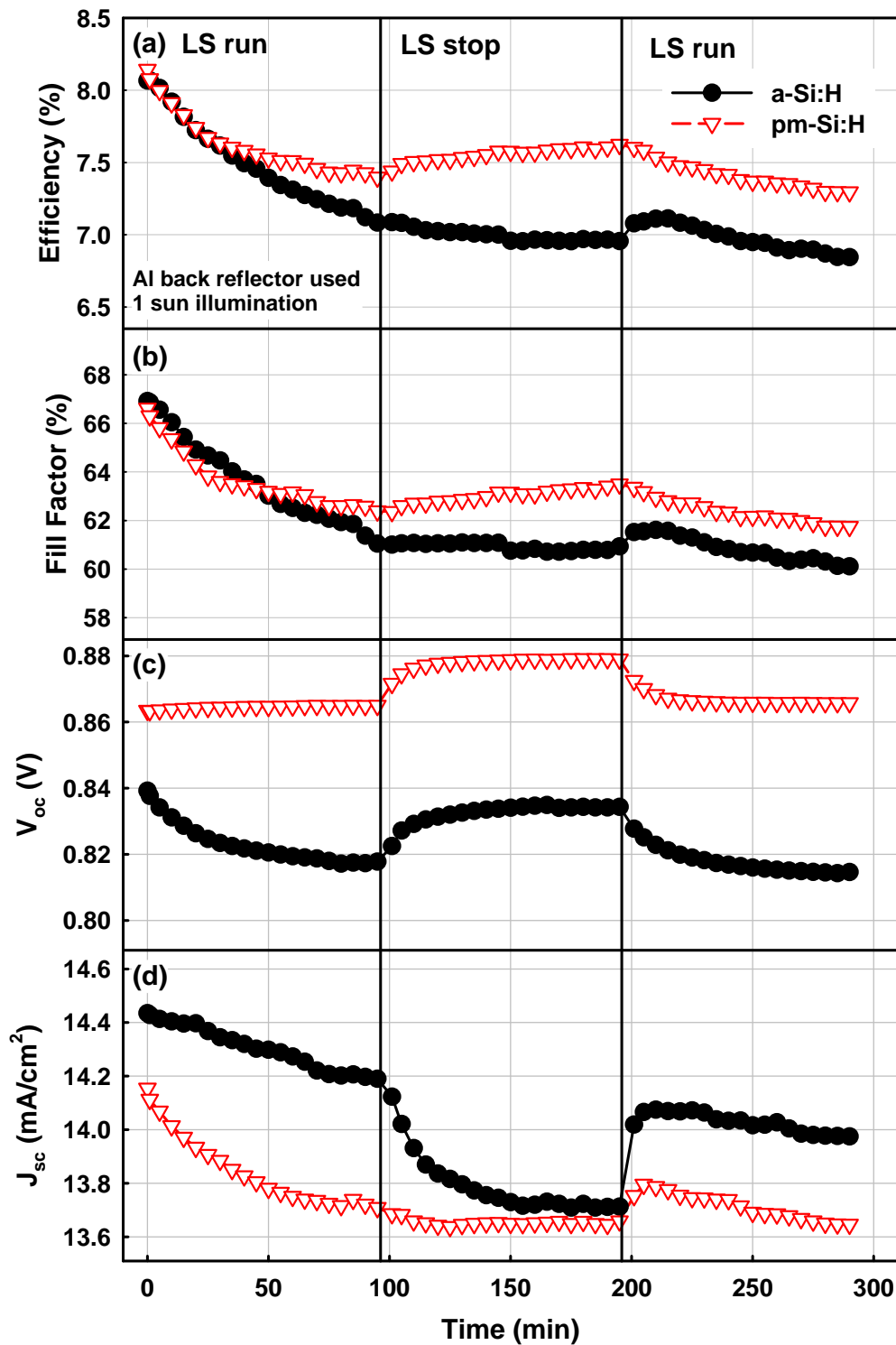


Figure 4.6 – Evolution of a-Si:H and pm-Si:H PIN solar cell parameters: (a)  $\eta$ , (b)  $FF$ , (c)  $V_{oc}$ , and (d)  $J_{sc}$  during LS under an illumination of 1 sun and healing. Note that after 90 minutes of LS, the PIN solar cells are left in the dark for another 90 mins. At last, the PIN solar cells were again light-soaked for another 90 minutes. The intrinsic layer thickness of PIN solar cells is 5000 Å.

Another interesting aspect comes out in the second LS cycle. In second LS cycle, degradation kinetics of pm-Si:H PIN solar cell change become more similar to those of a-Si:H. No more rapid decrease in  $FF$  and  $J_{sc}$  are observed in the second LS cycle, as well as  $V_{oc}$  shows initial decrease instead of increase. In addition, suppression of the characteristic initial behavior makes degradation kinetics of pm-Si:H PIN solar cell monotonous, like that of a-Si:H PIN solar cell.

Pioneering work in such healing behavior was carried out in Wronski's group [4.24-4.26], who studied room-temperature (RT) annealing of hydrogenated protocrystalline silicon (pc-Si:H) solar cell after LS. They presented phenomenological observation of dark J(V) parameters of pc-Si:H solar cells, and suggested various presoak-relaxation relationship. Yang and Chen suggested "Fast and slow defects" model [4.27, 4.28]. They light-soaked both diluted and undiluted a-Si:H PIN solar cell under 1 sun, after LS under 50 suns. As a result, the  $\eta$  of a-Si:H solar cells converge into 1 sun stabilized state. They suggested a model based on RB model [4.22] that having two different stretched exponential components with different  $\tau$ . Takeda et al. suggested a model with more practical view [4.29]. They fabricated a-Si:H samples having unusually high  $C_H$  between 22 - 36 at.%, and light-soaked at various intensities. They observed that ESR signal decreases under illumination of above 1000 mW/cm<sup>2</sup> while ESR signal increases under illumination of 700 mW/cm<sup>2</sup>. They suggested a model that hydrogen rich voids work as hydrogen reservoir and supply hydrogen into dangling bonds under illumination while normal isolated Si-H bonds create dangling bonds under illumination. Those two mechanisms compete against each other during LS. Meaudre and Meaudre have presented more detailed experiments whereupon they annealed a sample after illumination, and reported that the efficiency of annealing depends on the illumination intensity. At moderate illumination, annealing becomes efficient while under intense

illumination the annealing becomes less efficient. For the healing effect, many research groups have worked and suggested various mechanisms, but there are some similarities and common features. Materials showing healing effect are usually deposited from highly diluted hydrogen gas-mixture. Materials with high  $C_H$  also show significant effect of healing under moderate illumination. At last, LS creates defect states anyway under intense illumination around one sun.

One may suspect that both healing behavior and irreversible degradation of pm-Si:H PIN solar cells have a common physical origin: hydrogen. Highly heterogeneous materials like pm-Si:H contain surface of nanocrystals covered with hydrogen. The different light-induced degradation kinetics of pm-Si:H PIN solar cells must originate from the peculiar nanostructure of pm-Si:H material. An interesting aspect is that the irreversible changes in light-induced degradation kinetics of pm-Si:H PIN solar cells can be explained recalling the hydrogen evolution from internal surface [4.29]. The internal surfaces of nanovoids (or nanocrystal surface) are apparently hydrogenated with SiH and SiH<sub>2</sub> bonds [4.31-4.33], and hydrogen evolves during metastable defect creation [4.29, 4.34]. Hydrogen evolves and passivates newly created dangling bonds, but if the hydrogen in voids is depleted, the kinetics of the creation of dangling bonds would be similar to that of a-Si:H. Moreover, the evolution of hydrogen introduces various structural modifications, initiated by creation of bond-centered hydrogen [4.16, 4.35-4.37]. It has been suggested that the evolution of hydrogen from surface of nanocrystals originates from structural changes such as coalescence and agglomeration of the monovacancies into larger vacancies [4.37, 4.38] and that hydrogen is emitted as a consequence of reduced internal surface areas. Annealing at temperatures over 350 °C leads to similar effects [4.17]. Furthermore, one may imagine that such nanoscale structural changes

will consequently lead to large macroscopic changes.

### 4.3 Light-induced structural changes

To better exploit the light-induced macroscopic changes discussed above, a set of complementary techniques was used to characterize the changes in the structure of the PIN layer stacks during or after LS. a-Si:H and pm-Si:H PIN layer stacks were also deposited on Corning Eagle glass, flat TCO and highly resistive ( $>10^4 \Omega\text{cm}$ ) FZ c-Si substrates for more comprehensive studies.

Structural changes can affect the stress in thin film. Raman spectroscopy is a vibrational spectroscopic technique to characterize molecular vibrations. Raman peaks normally indicate the material's phonon modes. It is sensitive to strain, allowing it to be used to detect stress in a semiconductor material or device [4.39]. Structural changes during light-soaking were characterized through in-situ micro Raman scattering measurements. A He–Ne laser (632 nm) and a back-scattering collection configuration were used for the Raman measurements. For LS, a white light source with an intensity of  $80 \text{ mW/cm}^2$  was applied from the glass side. The test was done for both a-Si:H and pm-Si:H PIN layer stacks on Corning Eagle glass, and the study on the pm-Si:H PIN was done twice to check its reproducibility. During LS, Raman spectra were measured every five minutes, and for the second pm-Si:H PIN test, the measurement was done every two minutes.

Figure 4.7a and 4.7b show the evolution of the Raman spectra during LS of the a-Si:H and pm-Si:H PIN layer stacks on glass, for which the spectra have been normalized to the intensity of the TO mode. In Figure 4.7b, in contrast with a-Si:H PIN stack, the Raman spectra of the pm-Si:H PIN layer stack displays a peak shift during LS,

and this change was found to be reproducible in multiple pm-Si:H PIN layer stacks. To quantify these changes, TO peak position was determined through deconvolution of the measured spectra. Figure 4.7c shows the Raman spectrum of as-deposited pm-Si:H PIN stack and its deconvolution. The Raman spectra of both pm-Si:H and a-Si:H consist of a broad peak located at around  $480\text{ cm}^{-1}$ , which corresponds to the TO mode in the amorphous phase, and the LO and LA modes are additionally observed at lower wave numbers around  $330\text{ cm}^{-1}$  and  $440\text{ cm}^{-1}$ , respectively [4.40, 4.41]. The shift of the peak position can be treated as a measure of the average strain resulting from built-in stress. To minimize the influence of the weak vibrational modes, LA and LO, we performed a fit on each spectrum from  $250$  to  $550\text{ cm}^{-1}$  by three Gaussian curves and a straight base line [4.40].

Figure 4.8 shows the evolution of TO peak position during LS. One can recognize the notable feature that the TO peak of pm-Si:H PIN shifts towards lower wavenumbers during LS, whereas the two a-Si:H PINs show no significant change. Since the shift of the Raman peak towards lower wavenumbers could be due to local heating from laser excitation, the pm-Si:H PIN was allowed to cool in the dark for 20 minutes after LS. However, the peak position remained the same. Physically, a phonon is a quantized mode of vibration occurring in a rigid crystal lattice, such as the atomic lattice of a solid. The Raman spectra peak shift towards lower  $k$  can be regarded as a consequence of increasing the inter-atomic distance, that is, tensile stress. On the other hand, it should be noted that for all the samples, the TO band position in the as-deposited state is above  $480\text{ cm}^{-1}$  which can be related to compressive stress in the as-deposited films. However, while the peak position does not change for the a-Si:H PIN stack, it shifts to low wavenumbers for the pm-Si:H case during light-soaking. It can therefore be stated that the cells are under high compressive stress, as is usually the case for plasma deposited silicon thin films [4.42].

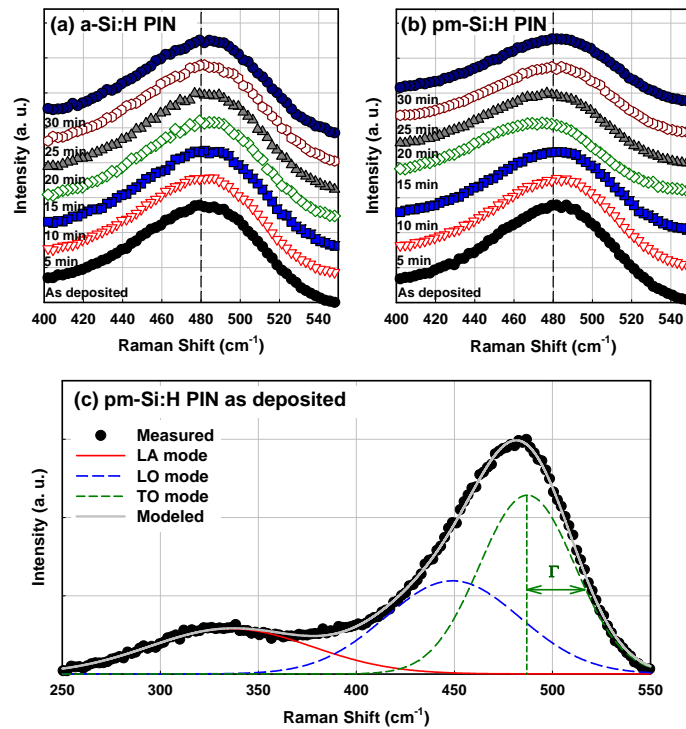


Figure 4.7 – Evolution of Raman spectra during LS of (a) a-Si:H and (b) pm-Si:H PIN solar cells, and (c) Raman spectrum of as-deposited pm-Si:H PIN solar cell and its deconvolution.

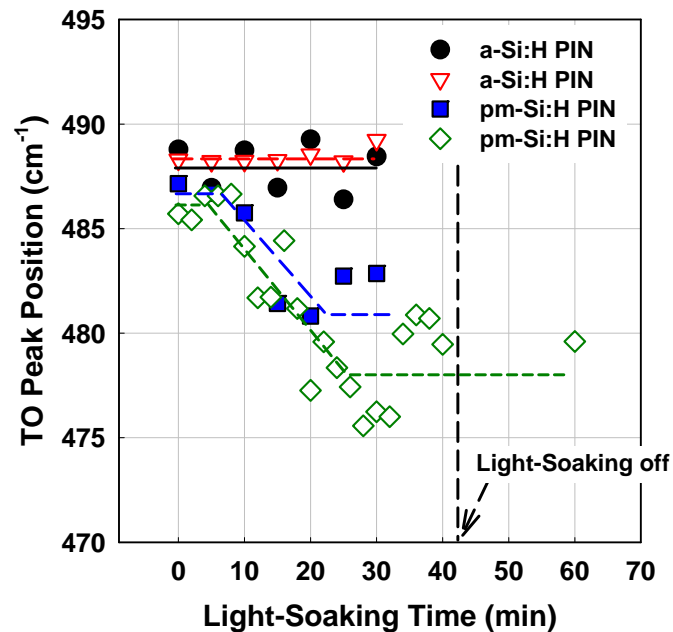


Figure 4.8 – Evolution of TO peak position during light-soaking. Note that on some samples we have checked that these material properties did not change after turning off the light.

In other words, the peak position evolution from higher  $k$  to lower  $k$  (towards  $480\text{ cm}^{-1}$ ) suggests a relaxation of compressive stress during LS for the pm-Si:H PIN layer stacks.

In-situ surface morphology characterization during LS was obtained from AFM measurements. Tapping mode was used to prevent the cantilever from dragging across the surface and resulting in surface damage, as well as providing higher resolution. Due to the design of AFM setup, PIN layer stacks were illuminated from the top (n-type layer side), with an intensity of  $150\text{ mW/cm}^2$ . The scan rate was chosen to be slow because the surface displays low roughness and small features. Scanning area size was varied from  $500\times 500\text{ nm}^2$  to  $2\times 2\text{ }\mu\text{m}^2$ . Sets of AFM images were analyzed by surface grain extraction, from which the surface grain size and distribution were obtained. Figure 4.9 show examples of AFM images taken in both the as-deposited and light-soaked states for both a-Si:H and pm-Si:H PIN stacks on glass. For both a-Si:H and pm-Si:H PIN layer stacks we observe a grain structure related to the surface roughness of the samples. Indeed, based on the Raman spectra shown in Figure 4.8, the grains are amorphous. The Watershed image processing segmentation algorithm was used to extract information about the surface grain area [4.43, 4.44] by splitting the images into surface grains, based on the topology of the image.

Figure 4.9e summarizes the surface grain size growth during LS analyzed from surface grain extraction. One can see that the surface grain area of pm-Si:H PIN layer stack increases during LS, and this expansion stops when LS is stopped, which is to say that the surface expands while illuminated, and the expansion remains even after LS stops.

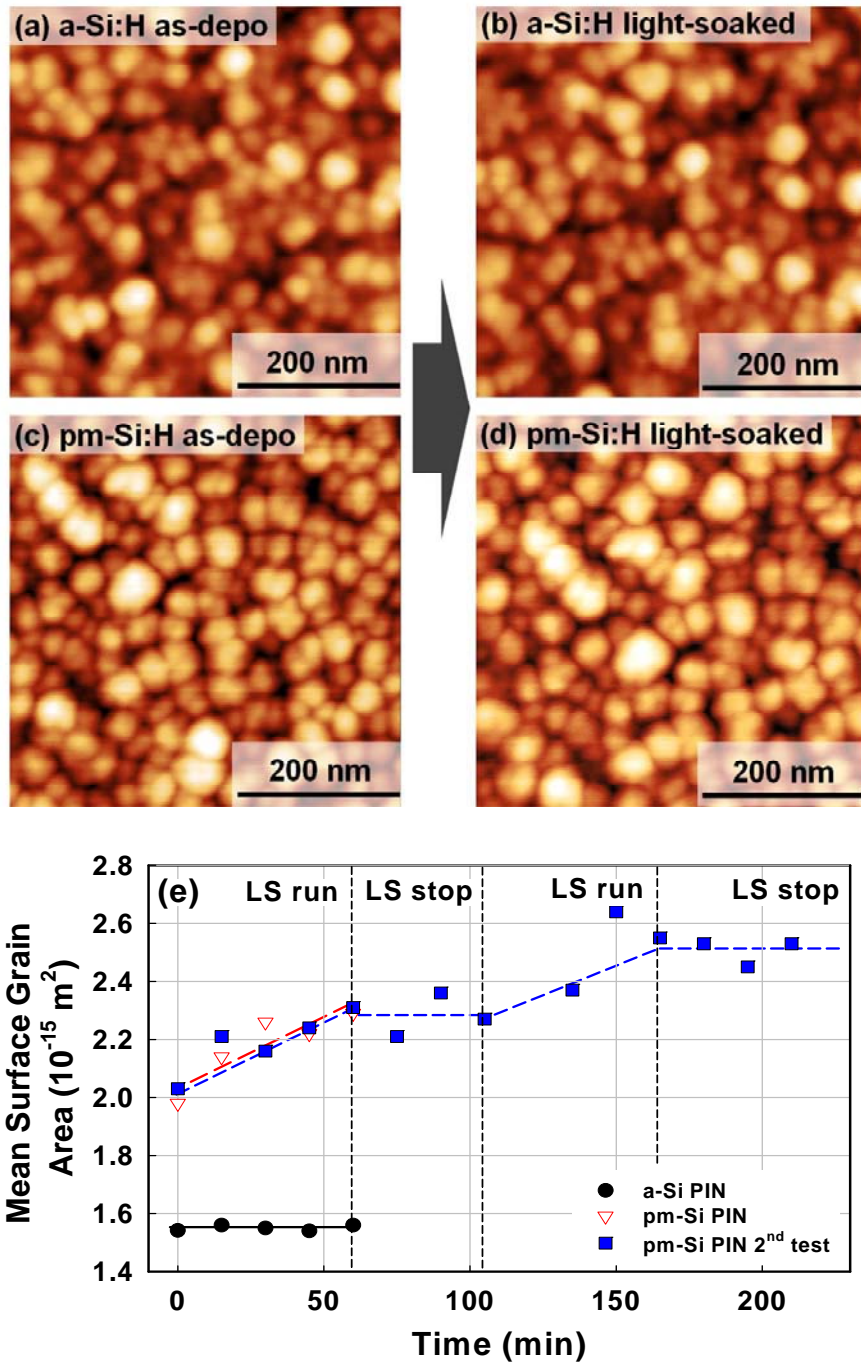


Figure 4.9 – AFM images of a-Si:H and pm-Si:H PIN layer stacks on Corning Eagle glass before (a, c) and after (b, d) LS, and (e) mean surface grain area evolution during LS, as extracted from AFM images. Note that no evolution is observed for the a-Si:H PIN layer stacks, and that the evolution for the pm-Si:H PIN layer stacks stops when the LS is turned off.

### 4.3 Light-induced structural changes

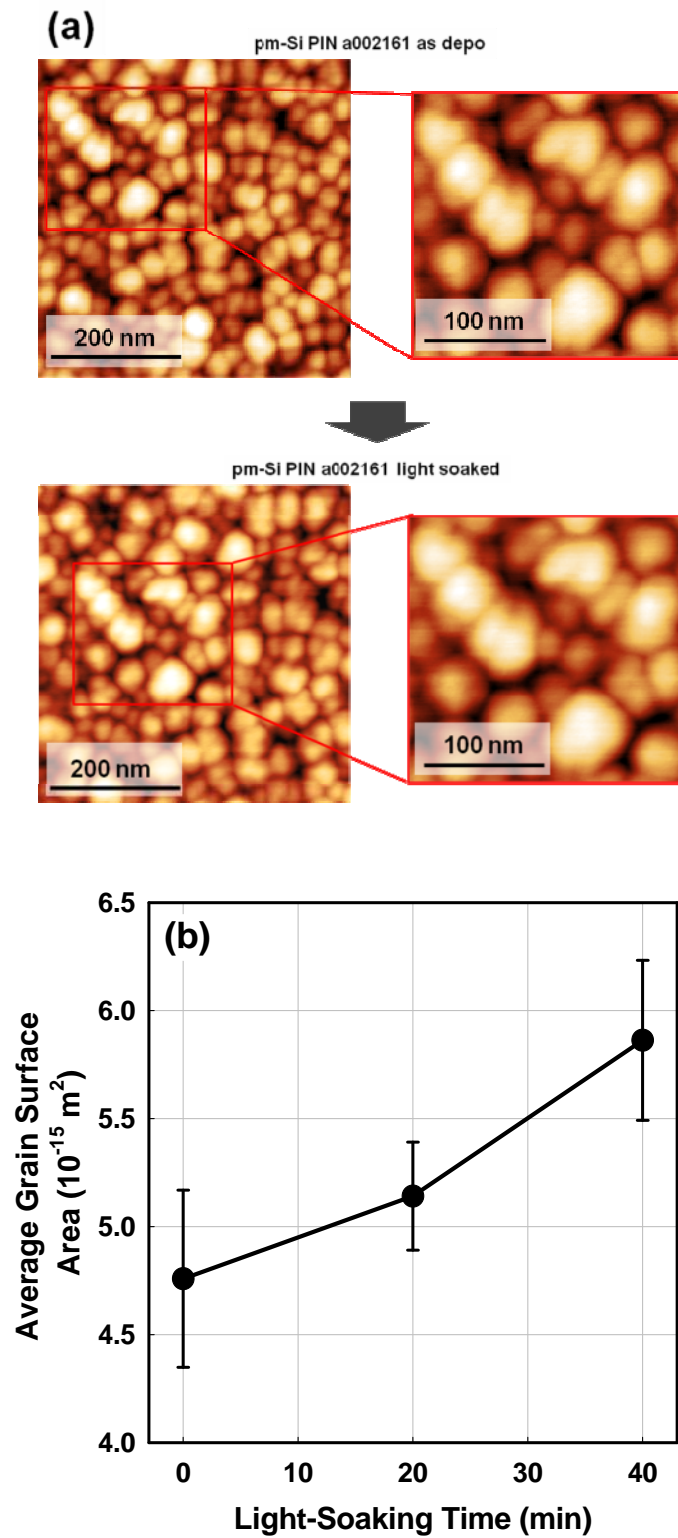


Figure 4.10 – (a) Demonstration of zone selection for AFM images to follow changes in area of individual grains, and (b) average surface area evolution of selected grains during LS of pm-Si:H PIN layer stacks.

For the a-Si:H PIN layer stacks, no significant changes were observed. As in the case of the Raman measurements, these results were reproduced in multiple trials. To eliminate the effect of image drift on the AFM scan during LS, individual grain sampling was performed on a selected set of grains. As shown in Figure. 4.10(a), a region was first cropped from the AFM images that remained within the field of measurement during the LS, and eight surface-grains from within that region were analyzed. The surface of each grain was extracted by the Watershed algorithm. Figure 4.10(a) shows an example from cropping a sample region, and Figure 4.10(b) shows the average area of the eight selected grains as a function of LS time. In spite of the small sampling number, the manual grain extraction shows the same trend as the statistical group behavior of surface grains in Figure 4.9(e). Therefore, one can conclude that the “swelling” behavior of the surface grains is not due to an image drift effect, but due to LS induced changes on the thin film topology.

Changes in film morphology during light-soaking were observed for the films deposited on glass. We turn now to effects of LS on the same PIN layer stacks deposited on transparent conductive oxide (TCO) substrates. Another set of pm-Si:H PIN layer stacks co-deposited on various substrates such as Corning Eagle glass, textured SnO<sub>2</sub>:F (Asahi-U), and flat ZnO:Al, was LS for longer periods (up to 100 hours under 100 mW/cm<sup>2</sup>) and the changes in their topology were characterized by scanning electron microscopy (SEM) and AFM. Figure 4.11 shows SEM and AFM images of the surface of pm-Si:H PIN solar cell on flat ZnO:Al, before and after LS for 16 hours. Images throughout the entire 1×1 square inch substrate were acquired on the as-deposited state and light-soaked. While the as-deposited sample shows no clear feature except surface roughness (Figure. 4.11(a),(b)), the light-soaked sample shows that the surface morphology is strongly modified (Figure. 4.11(c),(d)).

### 4.3 Light-induced structural changes

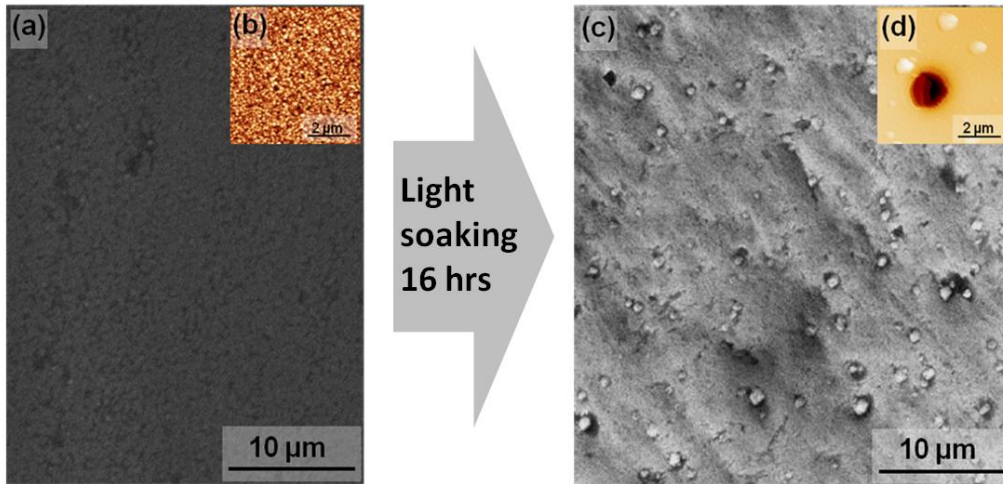


Figure 4.11 – SEM images of pm-Si:H PIN solar cell surface when deposited on flat ZnO:Al : (a) as-deposited, and (c) LS for 16 hours. (inset b, d) AFM image of surface shown in Figure.

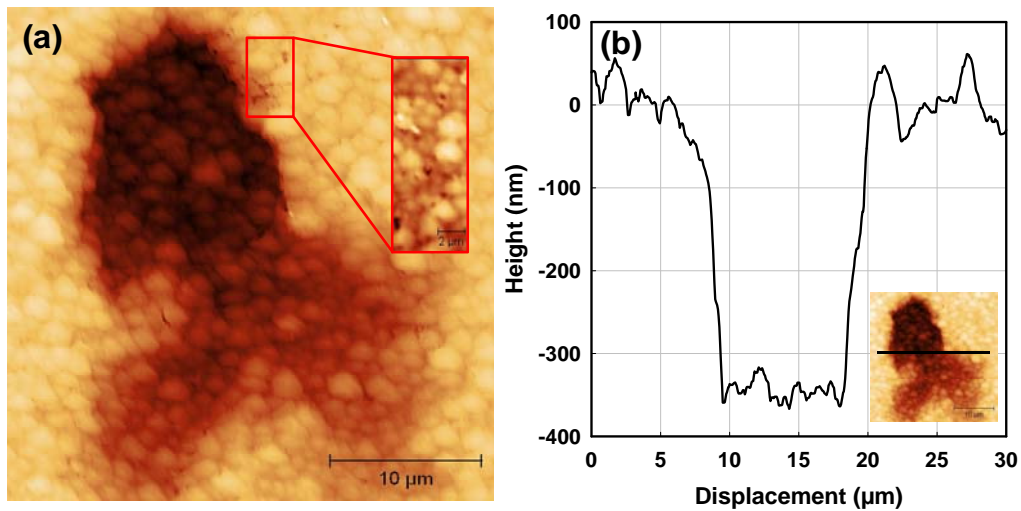


Figure 4.12 – An AFM image of a pm-Si:H PIN solar cell on textured Asahi substrate after 100 hours of LS and (b) cross-sectional profile measurement through center of hole showing a depth of film thickness.

A large number of bubbles is observed and the formation of holes takes place all over the surface. The depth of the holes and height of the bubbles are estimated from the cross-section of the AFM images. The depth of the holes varies from 30 to 400 nm, which means that some of the holes correspond to a complete peeling of the pm-Si:H PIN layers. The height of the bubbles reaches up to 1 μm. It is clear

that bubbles are not dust or particles because of their surface topology is similar to that of the rest of the surface, as well as the fact that they are not seen in the as-deposited state. In addition, not only circular shaped holes, but also many irregular shaped holes are found in SEM images. It implies that the macroscopic changes are similar to the buckling observed when films are annealed at high temperature [4.45-4.48].

Because the above results could be due to the use of flat ZnO:Al, we performed another light-soaking test on a pm-Si:H PIN layer stack deposited on a textured Asahi (SnO<sub>2</sub>:F) substrate, which is usually used for PIN solar cells. The pm-Si:H PIN solar cell was light-soaked for 100 hours, and again many irregularly shaped large holes were found. Figure 4.12 shows an AFM image of one of these holes. One can see that the size of the hole is larger ( $\sim 20 \mu\text{m}$ ) than the ones in Figure 4.11 ( $\sim \text{few } \mu\text{m}$ ), suggesting that the size of macroscopic defect grows with LS time. Another interesting aspect is also seen, wherein the groups of many small holes are found in the AFM image along with larger ones. The size distribution of the holes shows a high density of small ones ( $\sim \text{few } \mu\text{m}$ ), and few larger ones (as large as  $20 \mu\text{m}$ ). Considering the fact that small holes are locally grouped, the origin of the large hole might be related to the coalescence or agglomeration of small ones. Therefore, one can conjecture that the macroscopic structural change proceeds with LS, and the growth mechanism of the holes and bubbles is most probably the agglomeration. The depth of hole corresponds to the film thickness (about 400 nm), suggesting that the film has completely peeled off. Furthermore, many small sized holes ( $\sim \text{few } \mu\text{m}$ ) are also seen in Figure 4.12, similar to those observed on flat ZnO:Al (Figure 4.11(c),(d)). Developing the idea, assuming that the holes are a result of local stress relief, a region where small holes are grouped is most likely less rigid than nearby areas, and when those areas crack and peel-off

during LS, compressive stress is relaxed. Large cracked holes could be created through such stress release-crack cycle while more areas are cracked and peeled-off.

In order to examine the conjecture on the coalescence and the agglomeration of the vacancies into larger voids, a longer period of illumination is needed. Since studies on the SWE are time consuming, accelerated degradation tests, such as current-injection degradation (CID), are also widely used to study the mechanism [4.49, 4.50]. A set of a-Si:H and pm-Si:H PIN layer stacks were deposited on Cr evaporated on Corning Eagle glass. Sputtered ITO was used as a top contact and to define the cell area of 0.0314 cm<sup>2</sup>. The total thickness of PIN layer stack was about 2100 Å. The PIN layer stacks were connected to a DC power supply and constant current bias of 300 mA/cm<sup>2</sup> was injected to the PIN diodes. The current density of 300 mA/cm<sup>2</sup> can be regarded as equivalent to an illumination under 15 suns [4.49]. CID was done for 200 mins, which is equivalent to 500 hrs of LS under one sun illumination [4.23]. During the CID, a series of optical images were taken in real time with an Olympus BX61 optical microscope for both a-Si:H and pm-Si:H PIN layer stacks. The temperature of the PIN solar cells was monitored using a PT100 thermometer during the CID, verifying that the device temperature stayed at 80 °C.

Figure 4.13 shows optical images of a-Si:H and pm-Si:H PIN layer stacks at various stages of CID. In Figure 4.13a, a-Si:H PIN layer stack shows no significant changes under CID, while the pm-Si:H PIN layer stack in Figure 4.13(b) shows macroscopic changes.

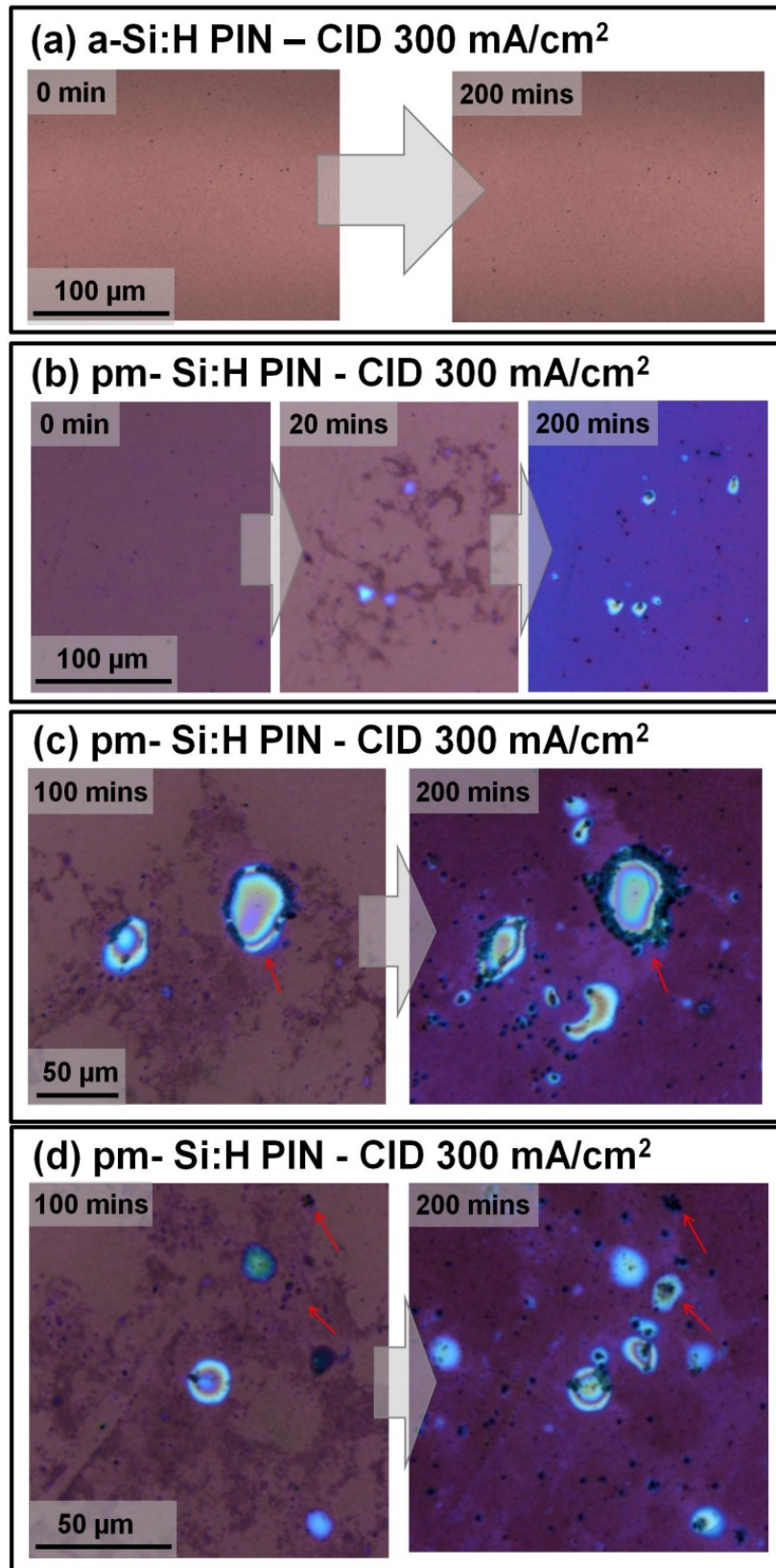


Figure 4.13 – Optical images of a-Si:H and pm-Si:H PIN layer stacks at various stages of current-injection degradation (CID). CID condition was done for 200 mins under 300 mA/cm<sup>2</sup>, and it is equivalent to the LS of 500 hrs under 1 sun illumination.

Bubbles and dark regions appear at 20 minutes. The bubbles keep growing and the dark regions also expand with CID. At 100 minutes, pinholes appear at the borders of bubbles, as shown in Figure 4.13(c), (d). They look like cracks extending out from the border of bubbles, and some of the bubbles have multiple opening holes. As CID continues, larger topological defects appear for both the bubbles and holes. An interesting point is that after CID for 200 minutes, the dark region disappears and the entire surface turns to dark-blue. No artificial modification on optical microscope was done and such chromatic changes are reproducible.

In order to have more detailed information on the bubbles, an AFM image was taken on one of the bubbles. Fig. 4.14 shows an AFM image of a bubble and its cross section profile, showing that the bubbles are up to 1.2  $\mu\text{m}$  high. Similarly to the LS test, the surface of the bubble and the rest of the surface show homogeneous morphology, which allows us to conclude that the bubbles are not an experimental artifact such as dust. The macroscopic defects (such as dark regions, bubbles and holes) first appear in small sizes, and then the dark regions expand and more bubbles and holes emerge, and finally the bubbles and holes merge into larger ones. The growth behavior of such macroscopic defects is depicted (as discussed above) as a result of the coalescence or the agglomeration of voids into larger ones at the interface [4.37, 4.38]. As hydrogen evolution occurs due to microscopic structural changes, this hydrogen may fill the bubbles that form. The holes appearing from the bubbles can be thought as a consequence of cracks extending out from the bubble, these holes can be explained as the cavity inside the bubble being unveiled after the destruction of the bubble.

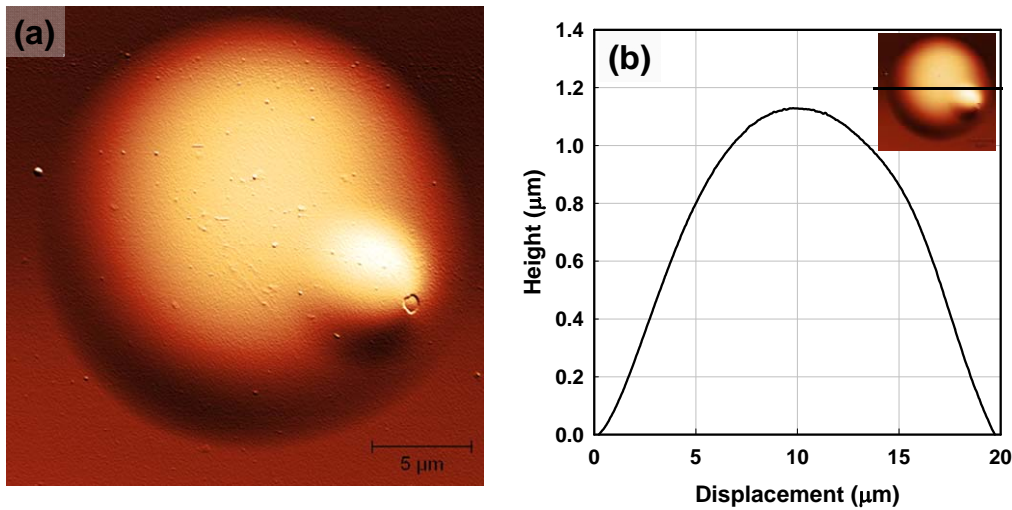


Figure 4.14 – An AFM image of a pm-Si:H PIN solar cell on Cr/glass substrate after CID and (b) cross-sectional profile measurement through center of bubble shown in Figure 4.13. CID condition was done for 200 mins under 300 mA/cm<sup>2</sup>, and it is equivalent to the LS of 500 hrs under 1 sun illumination.

One can recall that the entire surface turned to dark-blue after CID of 200 minutes. As mentioned above, no artificial modification was done. The reason could be that either the film or the interface between film/substrate became very porous after CID. The dark region could be a group of very small topological defects, both holes and bubbles, too small to be individually seen by optical microscope, but previously observed in SEM and AFM images in Figure 4.11, 4.12. This further supports the concept of the agglomerating growth behavior of the structural defects. Furthermore, there are still small holes and bubbles coming out after current-injection of 200 minutes, even after large scale topological changes. Assuming that the dark regions consist of with very small topological defects, the small holes and bubbles would be continuously created during CID. The strong contrast in refractive index of nanovoids would cause strong optical scattering, reflected in the change in color of film surface. Paul et al. [4.51] have discussed in detail the effects of voids of dimensions of 5 - 40 Å on the optical properties of amorphous germanium and have demonstrated

that large voids have the effect of reducing the refractive index. The change in refractive index after long term LS should be also detectable.

Spectroscopic ellipsometry (SE) is a useful tool to measure the optical properties of thin films. SE measurements were performed on a pm-Si:H PIN layer stack deposited on flat glass. The pm-Si:H PIN solar cell was light-soaked for 500 hours and SE spectra of as-deposited and light-soaked state were measured. The measured spectra were modeled using the Tauc-Lorentz dispersion model and the material parameters were obtained from the modeling [4.52, 4.53]. Figure 4.15 summarizes the SE modeling of pm-Si:H PIN layer stacks before and after LS of 500 hrs. Figure 4.15(a) shows the optical model used to analyze the experimental data. The imaginary part of the pseudo-dielectric function ( $\epsilon_2$ ) of the film measured by spectroscopic ellipsometry, as well as the material parameters deduced from modeling the pm-Si PIN stack on glass. SE spectrum of as-deposited pm-Si:H PIN layer stack can be modeled by a simple single layer with a surface roughness [4.54]. However, after LS of 500 hrs, SE spectrum cannot be modeled with the same optical model. The best fit was obtained when adding a bottom layer of 1000 Å with 50 % of void fraction. Indeed, in Figure 4.15b, the raw  $\epsilon_2$  spectra before/after LS are very different, in particular the peak intensity and optical bandgap ( $E_{\text{opt}}$ ) decreased a lot. Figure 4.15c shows that the refractive index of pm-Si:H PIN layer stack also decreased after LS.

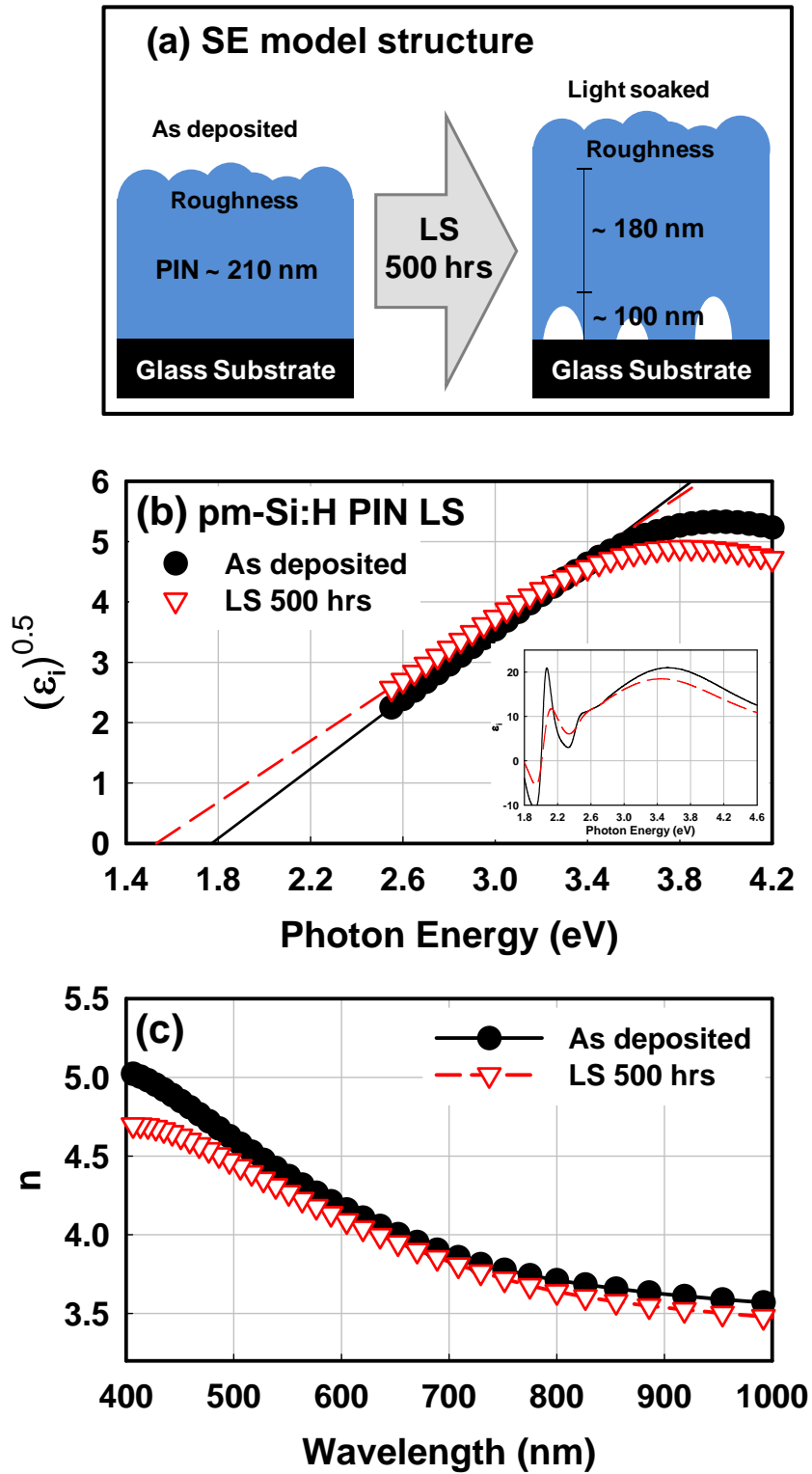


Figure 4.15 – Summary of SE modeling of pm-Si:H PIN layer stacks before and after LS of 500 hrs. (a) the structure of the optical model, (b) optical bandgap ( $E_{opt}$ ) and raw  $\epsilon_2$  spectra (inset), and (c) modeled refractive index before/after LS. The sample was light-soaked under Mercury lamp illumination and the intensity was about 0.7 sun.

Table 4.2 shows the fitting parameters of Tauc-Lorentz dispersion from Figure 4.15. Let us recall that  $E_{\text{opt}}$  is the optical bandgap, whereas A and C are fitting parameters related to the density and the disorder, respectively. Significant changes are observed in the material, in particular  $E_{\text{opt}}$ , A, and surface roughness. LS introduced a shift of the absorption edge (low energy part of  $\epsilon_2$ ) to lower energy. This shift is associated with the decrease of the  $E_{\text{opt}}$ . There are two possible reasons for the decrease in  $E_{\text{opt}}$ . It could suggest that Si-H bonds are breaking as a consequence of LS. The other reason can be changes in the inter-atomic distance. In-situ Raman and AFM revealed that light-soaking introduces stress-relaxation, which also implies that inter-atomic distance gets larger after light-soaking. Less splitting of orbital energy (band gap) is then expected from larger inter-nuclear distance of atoms. Such narrowing of  $E_{\text{opt}}$  seems to correlate with the evolution in the red response of EQE of pm-Si:H shown in Figure 4.3.

State	$E_{\text{opt}}$ (eV)	A	$E_0$	C	Roughness ( $\text{\AA}$ )
<b>As-deposited</b>	<b>1.69</b>	<b>207</b>	<b>3.88</b>	<b>2.35</b>	<b>44.2</b>
<b>LS 500 hrs</b>	<b>1.56</b>	<b>178</b>	<b>3.75</b>	<b>2.55</b>	<b>58.5</b>

Table 4.2 – Fitting parameters of Tauc-Lorentz dispersion model of Figure 4.15.  $E_{\text{opt}}$  is the optical bandgap,  $E_0$  is peak-to-peak transition energy, whereas A and C are fitting parameters related to the film density and the disorder.

LS introduced a strong decrease in the amplitude of  $\epsilon_2$ , which can be accounted for by an increase of the surface roughness and/or a decrease in the density parameter A. Decrease in the density parameter A suggests that the sample becomes porous. Such porosity could connect to the evolution of macroscopic structural changes such as bubbles and holes, shown in Figure 4.11-4.14.

#### 4.4 Light-induced hydrogen motion

We have examined the light-induced degradation kinetics of pm-Si:H PIN solar cells and associated macroscopic structural changes. An important feature in the evolution of solar cell parameters and macroscopic structural changes under LS is evolution in the hydrogen bonding. In order to study the characteristics of Si-H bond breaking and subsequent dangling bond recombination as a consequence of light-soaking, infrared absorption was measured for both a-Si:H and pm-Si:H solar cells. Infrared spectra in transmission mode were measured with a Nicolet 6700 Fourier transform infrared (FTIR) spectrometer on samples grown on <100> highly resistive ( $>10^4 \Omega\text{cm}$ ) FZ c-Si substrates. Its resolution was set to  $4 \text{ cm}^{-1}$ . The transmission spectra, resulting from the average over 32 scans, were normalized to the transmission of the c-Si substrates. As a complementary study for infrared absorption, hydrogen exodiffusion experiments were performed on both a-Si:H and pm-Si:H PIN stacks. During these experiments, the base vacuum was  $10^{-7}$  mbar and the heating rate was  $10 \text{ }^\circ\text{C}/\text{min}$ . The effused hydrogen was detected by a Quadruple Mass Spectrometer (QMS), and recorded in a continuous manner with the increase in temperature, to obtain the hydrogen exodiffusion spectrum. For this study, a pm-Si:H PIN solar cell was prepared on Corning Eagle glass substrate and then cut into three pieces: one as a control, a second one to be LS for one hour, and a third one to be LS for 20 hours.

Figure 4.16 shows the FTIR spectra in the stretching region of a-Si:H and pm-Si:H PIN stacks on FZ c-Si substrates extracted from infrared transmission. The stretching region of infrared absorption consists of two peaks centered at  $2000 \text{ cm}^{-1}$  and  $2090 \text{ cm}^{-1}$  [4.55]. The  $2000 \text{ cm}^{-1}$  mode is commonly associated with isolated Si-H groups in the bulk, related to the saturation of the dangling bonds during growth, while the  $2090 \text{ cm}^{-1}$  mode is attributed to clustered monohydrides

and/or dihydrides. Furthermore, there is a third peak, which is detected in pm-Si:H PIN samples, centered at around  $2030\text{ cm}^{-1}$ . The stretching mode at  $2030\text{ cm}^{-1}$  has been interpreted as clustered Si-H groups in the form of platelet-like configurations [4.56]. Therefore, this component could come from Si-H bonds at the amorphous-crystalline interface at nanocrystals surface in pm-Si:H. One can recognize that the stretching mode peak of pm-Si:H PIN layer stacks is shifted to the high wavenumbers compared to that of a-Si:H. This supports the existence of the  $2030\text{ cm}^{-1}$  band.

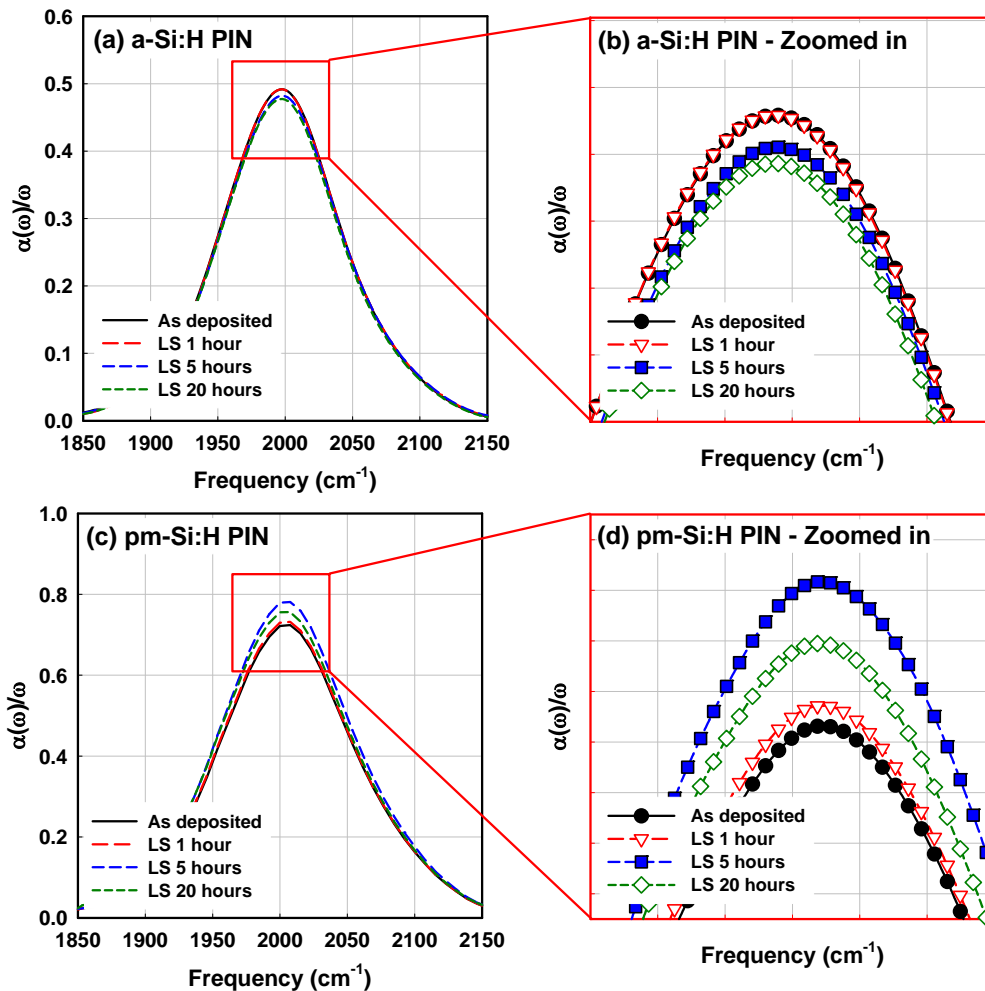


Figure 4.16 – Absorption coefficient spectra of FTIR stretching modes of (a) a-Si:H and (c) pm-Si:H PIN layer stacks on intrinsic FZ wafer and their zoom-in to the peak (b, d). The spectra are extracted from infrared transmission at four light-soaking (LS) states : as-deposited (black), after one hour of LS (red), after 5 hours (blue) and after 20 hours (green).

Evolution of FTIR stretching mode during LS is also quite distinct for those two materials. a-Si:H PIN shows a slow but steady reduction of its stretching modes absorption during LS. This result implies that Si-H bonds are broken under illumination, creating dangling bonds. However, in pm-Si:H PIN case, there is an increase in the stretching modes absorption at the early stages (up to five hours) of LS. The absorption starts to decrease after LS for 20 hours, but the absorption is still higher than in the as-deposited state. Similar experimental results are found in the literature [4.57-4.60]. Z. Yiping et al. observed a light induced increase of the Si-H stretching mode upon LS, and the authors argue that the increase cannot be due to an increase in the oscillator strength of those Si-H bonds [4.57]. They suggest that the primary effect of LS is an increase in the concentration of Si-H bonds that originate from H<sub>2</sub> molecules in the material. However, H. Fritzsche suggested another interpretation on the same reference. He proposed that LS introduced structural changes such as light-induced increase in strain or structural disorder, and the structural change increased the effective bond charge of Si-H bonds, so just sensitivity increased [4.58]. R. Darwich et al. reported indeed light-induced increase in bending mode ( $\sim 870\text{ cm}^{-1}$ ), and they suggested the formation of bond-centered hydrogen [4.59]. At last, S. Sheng et al. demonstrated irreversible light-induced increase in stretching mode that is non-monotonic [4.60]. They also suspected some structural changes, but could not propose further explanation.

In our case, first of all, the magnitude of the change is very small, However, multiple tests were done to confirm that the initial absorption increase was reproducible. Multiple infrared transmission spectra were taken to check the error range, which was found to be within  $\pm 0.1\%$  of the absolute value of transmission. Thus the error range is much lower than the change in transmission caused by light-soaking, which is more than  $\pm 0.5\%$ . Therefore, one can conclude that

there is very small change in the total amount of Si-H bonds, both in a-Si:H and pm-Si:H PIN layer stacks, with a reproducible consistency in their behavior. An initial increase is observed in the infrared absorption band of a pm-Si:H PIN layer stack, contrary to one containing a-Si:H, which shows a monotonous decrease.

Figure 4.17 shows the H<sub>2</sub> partial pressure detected during exodiffusion, normalized to the volume of the sample, as a function of temperature for a-Si:H and pm-Si:H PIN layer stacks on Corning glass. The exodiffusion spectrum of the as-deposited pm-Si:H PIN layer stack (Figure 4.17(b)) shows two distinct peaks at around 350 °C and 500 °C along with hydrogen spikes at low temperature around 250 °C. Otherwise, the exodiffusion spectra of a-Si:H PIN layer stacks show only one peak at 500 °C. The evolution peak at 300-400 °C is associated to molecular hydrogen release from internal surfaces of interconnected voids [4.61] or from silicon nanoparticle surface [4.62]. It is of note that materials deposited under CVD growth conditions only show an evolution peak at 500-600 °C [4.63]. Exodiffusion shoulder at 600 °C indicates hydrogen evolution from isolated voids during crystallization [4.64]. There is another possibility that the low temperature peak at 350 °C can also originate from the fact that we are analyzing a PIN stack instead of just an intrinsic layer. As a matter of fact, it has been shown that there is a different effusion behavior between p/i and n/i layer stacks. The p/i structure shows a low temperature effusion peak at 300 °C, while n/i structure shows a shift of the effusion peak to a higher temperature of 450 °C [4.65]. There are few possible reasons to have a low temperature peak in the structure with a p-layer at the bottom. Boron doped a-SiC:H layers are porous, and have a high diffusion coefficient of hydrogen [4.66], so atomic hydrogen could be incorporated in this layer when another layer is deposited on top of it. In this way, molecular hydrogen could already exist in p-layer or p-layer/substrate interface.

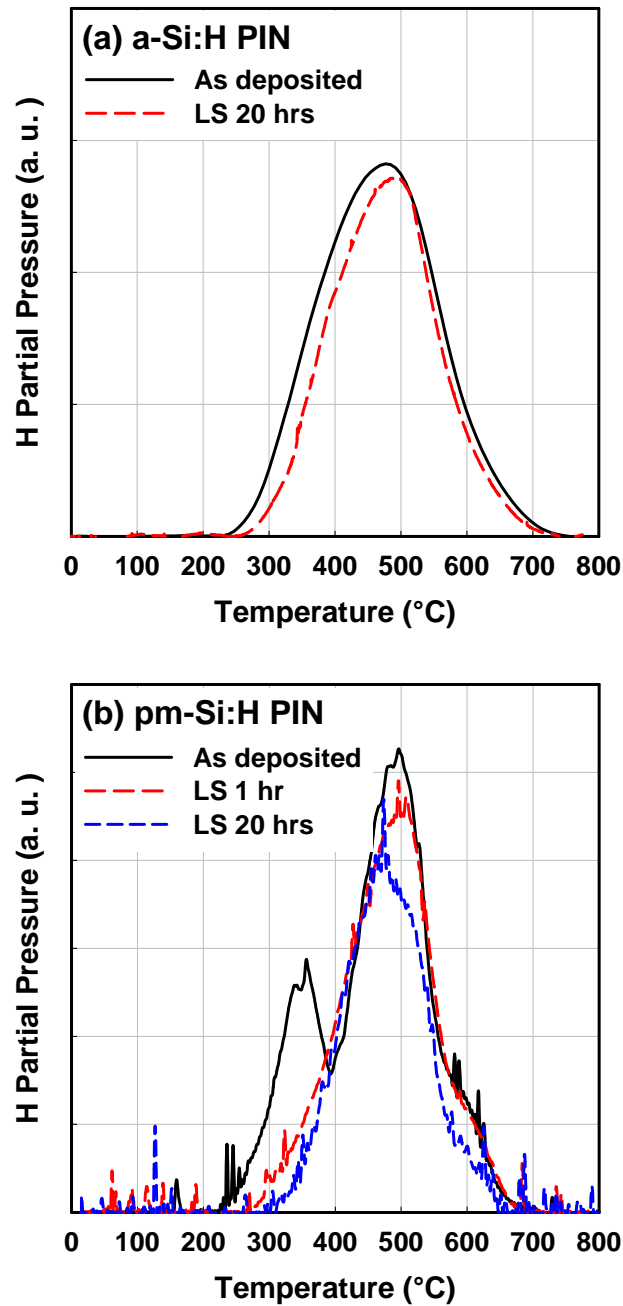


Figure 4.17 – Hydrogen exodiffusion spectra of co-deposited (a) a-Si:H and (b) pm-Si:H PIN layer stacks for different light-soaking (LS) states. Note that the pm-Si:H PIN layer stack shows abrupt disappearance of the peak around 350 °C even after 1 hour of LS, while there is only small change in a-Si:H PIN layer stack.

The most striking result in Figure 4.17 is obtained for the pm-Si:H PIN layer stack after LS for one hour, as the low-temperature peak at 350 °C disappears. This change is reproducible and is also

observed on the sample light-soaked for 20 hours. This result is surprising because not only is the change very abrupt, but also such change is much stronger than the one observed in the FTIR study (Figure 4.16). Recalling that only bonded hydrogen is detected by FTIR, this suggests that the origin of the peak at 350 °C is molecular hydrogen in the stack. Furthermore, the signal at 400 °C increased after LS, which can be linked to the initial increase of stretching modes absorbance in the previous section (Figure 4.16). This implies that a portion of molecular hydrogen associated with the 350 °C peak may have converted into bonded hydrogen. After LS for 20 hours, the signal at 400 °C is still higher than its initial value, even if the high temperature signal (~500 °C) shows a notable reduction. Last but not least, unusual sharp spikes are observed at low temperature (as low as 50 °C) for the light-soaked samples. The detection of these low temperature spikes in the light-soaked samples suggests that a portion of molecular hydrogen (350 °C peak) is also transformed to be mobile during the LS and accumulates at internal cavities or at the film/substrate interface. This hydrogen can easily escape during macroscopic cracking events and introduce sharp and rapid increases in hydrogen partial pressure at even lower temperature than 350 °C in the exodiffusion experiments [4.61].

In order to have more detailed information, the exodiffusion results were deconvoluted into five Gaussian peaks. The results of such analysis are summarized in Table 4.3. The exodiffusion spectrum of the as-deposited pm-Si:H PIN layer stack is characterized by five peaks at 320 °C, 353 °C, 469 °C, 516 °C and 591 °C. Note that the spikes were not taken into account in the deconvolution. Table 4.3 shows that the area of the peak at 469 °C increased after LS for one hour, while the two low temperature peaks (320, 353 °C) disappeared. This gives support to the fact there is not only diffusion of molecular hydrogen, but also reconstruction of Si-H bonding during light-soaking

[4.67].

As-Deposited		LS 1 hour		LS 20 hours	
Peak position (°C)	Area (a .u.)	Peak position (°C)	Area (a. u.)	Peak position (°C)	Area (a. u.)
320	2.43				
353	2.32				
469	9.06	464	12.1	457	9.44
516	2.99	507	2.59	509	1.98
590	2.23	596	1.18	584	1.35
<b>Total</b>	<b>19.03</b>		<b>15.87</b>		<b>12.77</b>

Table 4.3 – Peak positions and integrated areas extracted from exodiffusion results of Figure 4.17. Data are presented for co-deposited pm-Si:H cell layer stacks in the as-deposited state and after two light-soaking times ( 1 hour, and 20 hours).

With the experimental results presented in this chapter, we now aim to understand the light-induced degradation kinetics of the pm-Si:H PIN solar cells, such as rapid initial drop of  $FF$  and  $J_{sc}$ , increase in  $V_{oc}$ , irreversibility, and healing. In-situ Raman and AFM measurements reveal that LS relaxes compressive stress. LS on pm-Si:H PIN solar cells introduces the evolution of macroscopic structural changes, such as holes and bubbles, which grow by coalescence and agglomeration. The structural changes listed above are indeed because of stimulated hydrogen motion, as deduced from infrared absorption and exodiffusion.

One could argue that the results above are due to the illumination induced local heating. However, there are several points disputing this perspective. First, heating of the PIN solar cells by illumination was suppressed by fan cooling. As mentioned above, the temperature stayed under 50 °C even at 2 suns of illumination (well below the deposition temperature of 175 °C). Second, we have observed

increasing  $V_{oc}$  and decreasing  $J_{sc}$ . The opposite would be seen if pm-Si:H cells were heated. At last, Raman measurements show that the TO peak remained in same position even after cooling down for 20 minutes. Therefore, we conclude that the macroscopic changes presented here do not rely on heating, but on illumination.

Based on our experimental study, the collected results can be summarized as follows:

1. LS of pm-Si:H PIN solar cells introduces various unusual effects which are not observed in a-Si:H solar cells, such as a fast decrease in  $FF$  and  $J_{sc}$ , an increase of  $V_{oc}$ , irreversibility, and healing.
2. At the initial stages of LS, pm-Si:H PIN solar cells experience a relaxation of their compressive stress.
3. LS of pm-Si:H solar cells results in evolution of macroscopic structural changes, creating bubbles and holes, growing up to few hundred  $\mu\text{m}$  scale. This is observed by AFM, SEM, optical microscope, and SE measurements, all of which provide evidence of macroscopic changes of pm-Si:H PIN solar cells.
4. Infrared absorption and exodiffusion studies demonstrate that LS induces strong changes in the hydrogen distribution in the material. In particular, the disappearance of the exodiffusion peak at 350 °C, the increase in FTIR stretching modes, as well as the increase in the exodiffusion signal at 400 °C and the appearance of low temperature sharp spikes after light-soaking. These results suggest that molecular hydrogen in the pm-Si:H PIN layer stacks (350 °C peak in exodiffusion) effuses out during LS, and a portion of the effused hydrogen is converted into bonded hydrogen and into hydrogen filled cavities, in particular at the substrate/p-layer interface.

These results lead us to postulate that LS leads molecular hydrogen to effuse from pm-Si:H PIN solar cells, and a fraction of molecular hydrogen (made mobile during LS) forms cavities, probably around the silicon nanocrystals of the pm-Si:H material and at the substrate/p-layer interface. This causes the peel-off observed in microscope images. Therefore, the question is whether there is a connection between the macroscopic changes and the behavior of the solar cell parameters.

Indeed, there is a general consensus on light-soaking modifying hydrogen incorporation in a-Si:H. Light-induced, long-range H motion has been postulated as the key step in the Branz model of SWE defect formation [4.68, 4.69]. According to the Branz model, only a small subset of the Si-H bonds involved in the SWE contributes to metastable dangling bond formation, while most of the broken Si-H bonds are recycled by re-trapping mobile hydrogen. This process could be a reason for the molecular hydrogen diffusion during LS [4.68-4.70]. We therefore postulate that the large structural changes reported above are macroscopic manifestations of molecular hydrogen accumulation at the interface between the substrate and the pm-Si:H PIN stacks.

However, there is still a question remaining about the fast diffusion of hydrogen. As a matter of fact, it is reported that hydrogen diffusion in a-Si:H is more moderate than the result presented here [4.61, 4.69, 4.70]. Nevertheless, one can still find the difference in the hydrogen diffusivity between pm-Si:H and a-Si:H, recalling the abrupt disappearance of exodiffusion peak at 350 °C (Figure 4.17) while FTIR measurements show only small changes in Si-H bond concentration (Figure 4.16). Therefore, such fast hydrogen diffusion cannot originate from Si-H bond breaking, but from molecular hydrogen in the material. As mentioned above, molecular hydrogen could exist either in microvoids or at the p-layer/substrate interface or it could have been

created during LS by the coalescence of nanovoids. It has been reported that molecular hydrogen can diffuse faster in a highly inhomogeneous material such as pm-Si:H [4.71]. In addition, such diffusion would be even accelerated if the material experiences a volume expansion, providing larger space for hydrogen to diffuse. As a matter of fact, there has been a great deal of research on light-induced volume changes [4.72]. Various beam bending experiments have been performed using samples consisting of long and narrow pieces of thin glass or quartz substrates coated with a-Si:H [4.73-4.79]. These results reveal that light-induced volume expansion follows a stretched exponential behavior, usually showing saturation at  $dV/V \sim 10^{-3}$  [4.42]. This phenomenon has also been connected with hydrogen motion, as light-induced volume changes have been shown to depend on the hydrogen content of the film [4.42]. “On-the-edge” or mixed phase materials grown under high hydrogen dilution and having improved order result in solar cells with significantly reduced light-induced degradation. Interestingly enough, these materials show the fastest and largest photo-expansion amongst many different a-Si:H materials [4.15, 4.42]. Their large photo-induced volume change prompts comparison to the macroscopic evolution of our pm-Si:H solar cells. In other words, the volume expansion of the film is a product of the stress being relieved, and is particularly important at the p-layer/substrate interface.

Turning now to the light-induced degradation kinetics of a-Si:H and pm-Si:H PIN solar cells, one should also consider the different process conditions of a-Si:H and pm-Si:H materials (notably vastly different hydrogen dilution and ion-bombardment conditions) which could induce different modification of the p-type a-SiC:H layer of the solar cells. Indeed, the deposition conditions of the pm-Si:H layer could strongly modify the hydrogen content and bonding configurations in the p-layer, even if the p-type a-SiC:H layer was

deposited under the same conditions for both the a-Si:H and pm-Si:H PIN solar cells. As atomic hydrogen has a high diffusivity in boron doped a-SiC:H [4.66], it is even more likely that deposition conditions involving high hydrogen dilution will modify the p-type a-SiC:H layer and weaken the interface between the substrate and the p-type layer. The fact that we study PIN stacks and not just intrinsic layers may also be the reason for the exodiffusion peak at 350 °C as it has been reported elsewhere [4.46]. Therefore, we suggest that pm-Si:H deposition conditions may lead to a fragile p-layer/substrate interface, which can be further damaged during LS. This is supported by the low temperature sharp spikes in the exodiffusion results. Indeed, those sharp spikes are evidence of molecular hydrogen escaping from cavities at relatively low temperature. The hydrogen evolving from these cavities must have been accumulated during LS.

The initial increase in FTIR stretching mode of pm-Si:H PIN during LS can be explained in the framework of Branz model, where mobile hydrogen is emitted by photo-carrier recombination, creating dangling bonds. When mobile hydrogen diffuses through the silicon network it can be captured by a dangling bond and recycled into another Si-H bond [4.80]. In this cycle, re-trapped hydrogen is assumed to originate from Si-H bond breaking. However, if a large amount of mobile hydrogen exists in the material (for instance molecular hydrogen), then the number of hydrogen atoms captured by dangling bonds can be larger than the number of hydrogen atoms produced by Si-H bond-breaking. The presence of molecular hydrogen in pm-Si:H PIN solar cells, suggested by the exodiffusion spectra (Figure 4.17) may cause the fast hydrogen diffusion and initial increase in Si-H bonding (Figure 4.16, 4.17) during LS. Indeed, our result on hydrogen diffusion after LS of pm-Si:H PIN solar cells is found to be much faster [4.81] and indeed takes place at much lower temperature than that of a-Si:H in literature.

Therefore, the initial increase in FTIR stretching mode can be explained by creation of bond-centered hydrogen [4.59], mediated by molecular hydrogen [4.16]. In this mechanism, atomic hydrogen comes to passivate a newly created dangling bond left by another atomic hydrogen parted from bond centered position, and two hydrogen atoms form a molecular hydrogen or interstitial hydrogen [4.16]. This mechanism of bond centered hydrogen creation and annihilation at the very beginning of the LS process indicates that bond centered hydrogen could play the role as an intermediate precursor [4.59], initiating structural changes [4.82]. It may seem difficult for molecular hydrogen to spontaneously dissociate into atomic hydrogen. Indeed, molecular hydrogen in free space is more stable than Si-H bond. However, the energy level of molecular hydrogen in silicon is much less stable than in free space [4.83, 4.84]. Moreover, the existence of not only molecular hydrogen, but also metastable diatomic species in silicon has been reported [4.85]. Diatomic species are denoted as  $H_2^*$  while molecular hydrogen is denoted as  $H_2$ . They are metastable and are at higher energy level (unstable) compared to  $H_2$ .  $H_2^*$  has asymmetric charge distribution between two hydrogen atoms. Recent works have reported on strain-induced dissociation of molecular hydrogen, in particular at the vicinity of strained Si-Si bonds [4.86, 4.87]. This is interesting in light of the results we have seen in Raman study that LS of pm-Si:H PIN solar cells is accompanied by a large amount of stress relaxation.

### **4.5 Hypothesis on light-induced changes**

The structural studies presented above can be summarized in proposing the macroscopic defect creation scenario shown in Figure 4.18. In the as-deposited state (Figure 4.18(a)), the pm-Si:H PIN solar cells have already weak film/substrate interface due to the process

conditions of the pm-Si:H intrinsic layer. Then, light-soaking (Figure 4.18(b)) introduces volume changes, stress relaxation, and coalescence of nanovoids at the interface. Molecular hydrogen in the material becomes mobile and isotropically diffuses to the film free surface as well as to the interface with the substrate where it can accumulate and form hydrogen cavities (Figure 4.18(c)). This delamination continues to release built-in “compressive” stress of the film, and the stress relaxation will eventually result in the formation of mechanical defects such as bubbles and holes (Figure 4.18(d)), as well as the accumulation of hydrogen at the interface. Based on the above scenario we propose that the unusual evolution of pm-Si:H solar cell parameters, particularly rapid decrease in  $FF$  and  $J_{sc}$  is related to the diffusion of molecular hydrogen, resulting in a reduction of active solar cell area due to delamination.

It should be mentioned that a-Si:H also shows large macroscopic structural changes such as redistribution of Si-H bonding configuration [4.17], increase in band-tail states attributed to the change in microstructure [4.88], relief of internal stress [4.89, 4.90], nanovoid formation [4.91], and internal diffusion of hydrogen [4.92] but all at temperatures above 350 °C. As well as irreversible solar cell degradation is observed when material is light-soaked under 50 suns at 130 °C [4.20, 4.21]. However, in pm-Si:H, the structural changes listed above manifest under one sun illumination at temperatures as low as 40 °C. When a-Si:H is annealed at 350 °C [4.47, 4.48] and these extreme conditions lead to enhanced hydrogen motion at the origin of the reported macroscopic structural changes in both films and a-Si:H solar cells. Interestingly, our results on pm-Si:H PIN solar cells show that such irreversible changes can take in this material under standard LS conditions.

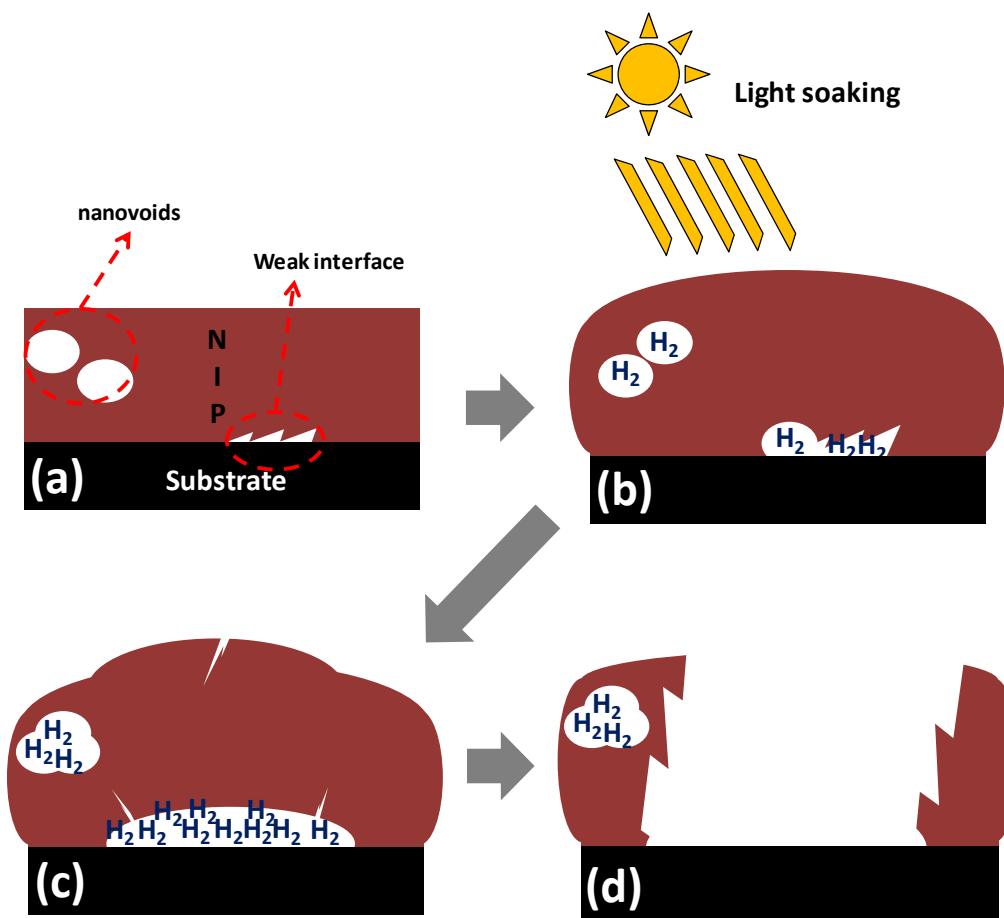


Figure 4.18 – Schematic representation of proposed mechanism for structural defect formation through localized delamination. In the as-deposited state (a), a weak film/substrate interface is due to the pm-Si:H deposition conditions. Light-soaking (b) introduces volume changes, stress relaxation, and nanovoids agglomerate into larger ones. Molecular hydrogen in the material becomes mobile and diffuses to the interface where it forms hydrogen cavities (c). The delamination continues to release built-in “compressive” stress, and the stress relaxation eventually results in the formation of macroscopic defects such as bubbles and holes (d), as well as the accumulation of hydrogen at the interface.

We attribute this to the peculiar nanostructure of pm-Si:H which provides a good environment for hydrogen diffusion [4.67, 4.71], and to the presence of weakly bonded hydrogen in the material. Therefore, one can conclude that the reported degradation kinetics of pm-Si:H PIN solar cells is a particular case of a-Si:H solar cells, which also show hydrogen induced structural changes under extreme conditions.

## 4.6 Long-term stability and new device structure

Now we turn to the kinetics of light-induced degradation after a long period of time. A set of PIN and NIP solar cells were prepared and were subjected to LS for 800 hours. The intrinsic layers of PIN solar cells were deposited at various RF powers, and some pairs of PIN cells varied only in intrinsic layer thickness. A state-of-art a-Si:H PIN mini-module from external group is also studied as a reference. NIP solar cells are also fabricated, and our NIP solar cells utilize p-type  $\mu\text{-SiO}_x$  while our PIN solar cells are optimized with p-type a-SiC:H. All the solar cells are illuminated and light-soaked through p-type layer side. Table 4.4 summarizes the process conditions and intrinsic thickness of selected solar cells.

Sample	Description	RF power (W)	$r_d$ (Å/s)	$d_i$ (Å)
State-of-art reference	a-Si:H PIN			3000
a1102253	a-Si:H PIN	1	1	3000
a1104264	pm-Si:H PIN	5	1.5	3000
a1104282	pm-Si:H PIN	5	1.5	3500
a1104181	pm-Si:H PIN	10	5	3000
a1104182	pm-Si:H PIN	10	5	6500
a1112121	a-Si:H NIP	1	1	3000

Table 4.4 – Process conditions of various PIN and NIP solar cells. The intrinsic layers of PIN solar cells were deposited at various RF power, and some PIN solar cells had same material properties with different intrinsic layer thickness.

For the long term LS, the PIN and NIP solar cells are light-soaked under a Mercury-vapor lamp (Hg lamp) of an intensity of 100 mW/cm<sup>2</sup>. Hg lamp was chosen due to the advantages of a long bulb lifetime and a high intensity, in spite of the spectrum mismatch to the AM1.5 standard. Emission line spectrum of Hg lamp mainly consists of UV-blue light [4.93], as well as intense emission lines in the visible

[4.94]. The lamp intensity was calibrated with a commercial c-Si reference solar cell. During LS, the PIN and NIP solar cells are fan cooled and the solar cell temperature was monitored by a PT100 thermometer, ensuring that the solar cell temperature stayed under 50 °C. J(V) measurements of the solar cells are measured under an intensity of 100 mW/cm<sup>2</sup> with AM1.5 spectrum. For each J(V) measurement, six individual solar cells on 2.5×2.5 cm<sup>2</sup> substrates are measured and the solar cell parameters are averaged. The maximum and minimum values are reflected by error bars.

Figure 4.19 shows the evolution of solar cell parameters of selected PIN and NIP solar cells during LS under Hg lamp illumination. There is notable difference in light-induced degradation kinetics compared to earlier results on short period LS. In particular, one can find out that pm-Si:H PIN solar cells show disappointing stability, degrading down from about 9 % to 3 % in worst case. Such disappointing long-term stability of pm-Si:H PIN solar cells can be attributed to the spectrum of LS illumination. We have seen that pm-Si:H PIN solar cells are especially stable under yellow-red illumination, but are much more sensitive to degradation done with UV-blue light (Figure 4.3). Since the emission spectrum of Hg lamp mainly consists of UV-blue light, it makes sense that pm-Si:H PIN solar cells show such accelerated degradation under Hg lamp. Moreover, one can find many interesting aspects in light-induced degradation kinetics of pm-Si:H PIN solar cells under Hg illumination. First, the stable efficiency of pm-Si:H PIN solar cells does not depend on the intrinsic layer thickness, but depends on the RF power used in the deposition of intrinsic layers. This is another distinguishing characteristic of light-induced degradation kinetics of pm-Si:H PIN solar cells. Light-induced degradation of a-Si:H sample should depend on the intrinsic layer thickness.

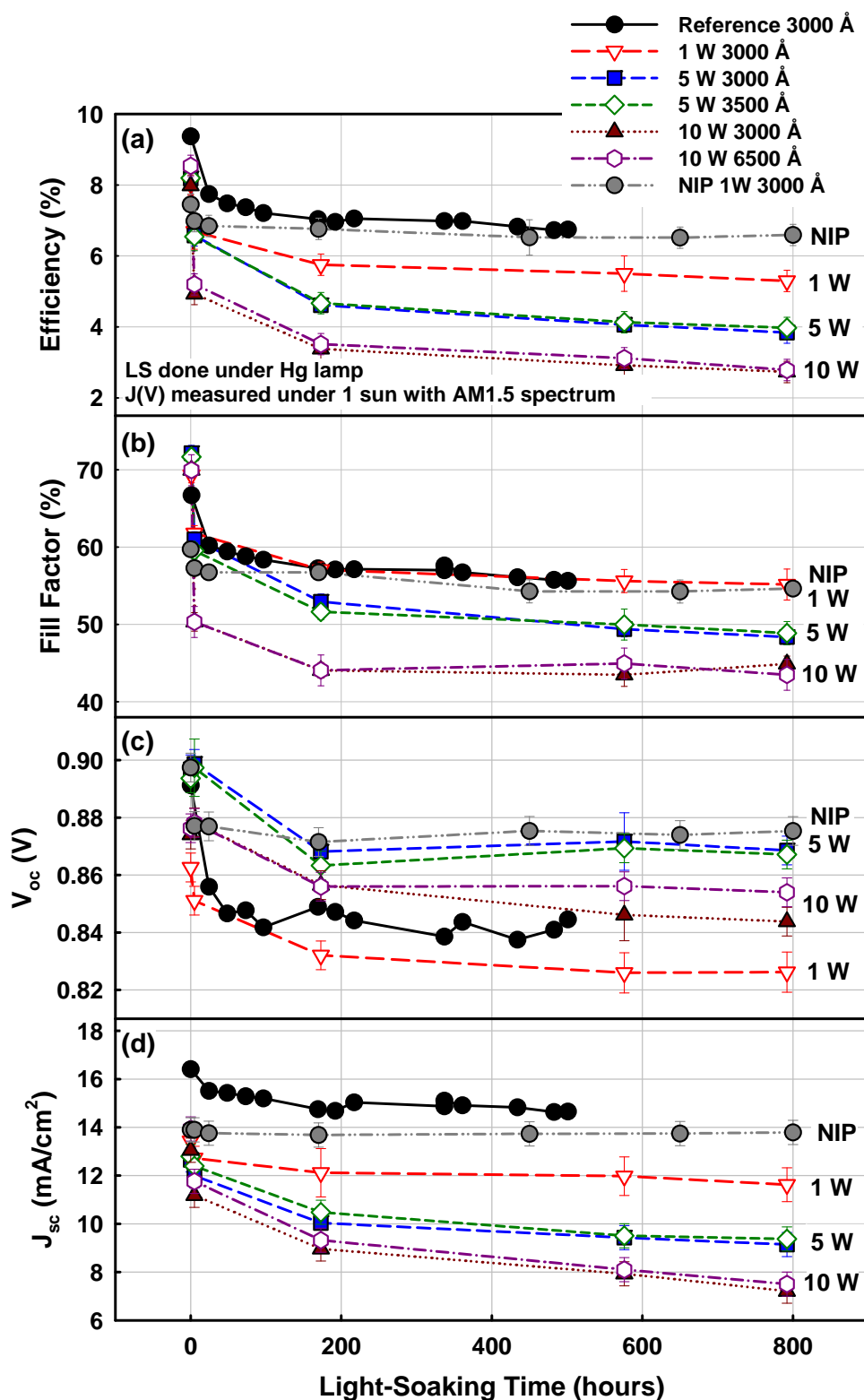


Figure 4.19 – Evolution of solar cell parameters of selected PIN and NIP solar cells summarized in Table 4.4: (a)  $\eta$ , (b)  $FF$ , (c)  $V_{oc}$ , and (d)  $J_{sc}$  during LS under an Hg lamp illumination. Note that multiple individual solar cells on  $2.5 \times 2.5$  cm<sup>2</sup> substrate are measured and the solar cell parameters are averaged. The maximum and minimum values are reflected in error bars. Al is used as back-reflector in PIN solar cells except the state-of-art reference sample, and ITO is used in NIP.

Usually, the magnitude of the light-induced degradation of a-Si:H solar cells varies with intrinsic layer thickness [4.95, 4.96], thus motivating the many efforts on enabling thin intrinsic layers with efficient light trapping [4.95, 4.97]. Again, another evidence of the additional physical origin in the light-induced degradation kinetics of pm-Si:H PIN solar cells is seen in their independence on the intrinsic layer thickness. In Figure 4.19(b),  $FF$  of PIN and NIP solar cells show that the stabilized  $FF$  is mostly determined by the RF power used in the deposition of intrinsic layers. Note that even the state-of-art reference sample shows stabilized  $FF$  of about 55. It suggests that the LS condition in this test is obviously harsher than standard condition. Looking the pm-Si:H PIN solar cells deposited at 10 W, their initial  $FF$  approaches to 70, which is indeed good  $FF$  attributing good transport and recombination properties, but after LS, the  $FF$  drops to 45. This large degradation is also found in  $J_{sc}$ , Figure 4.19(d). The  $J_{sc}$  of PIN solar cells also vary with RF power used for intrinsic layer deposition. In addition, the  $J_{sc}$  of the pm-Si:H PIN solar cells deposited at 10 W show continued degradation even after LS for 800 hrs. It is interesting that  $J_{sc}$  of the state-of-art reference sample is very high, while the degradation behavior is similar. This can be explained by an efficient light trapping technique in the state-of-art reference sample. Looking now at the  $V_{oc}$ , pm-Si:H PIN solar cells show no net increase in  $V_{oc}$ , even though there is a slight increase at the initial stage (~10 hrs) of LS. Otherwise, the  $V_{oc}$  is the most stable parameter during LS, remaining unchanged after initial degradation within about 5 %. It is impressive that the NIP solar cell shows high  $V_{oc}$  through the use of p-type  $\mu\text{-SiO}_x$ . More detail on the doped  $\mu\text{-SiO}_x$  will be given in the next chapter.

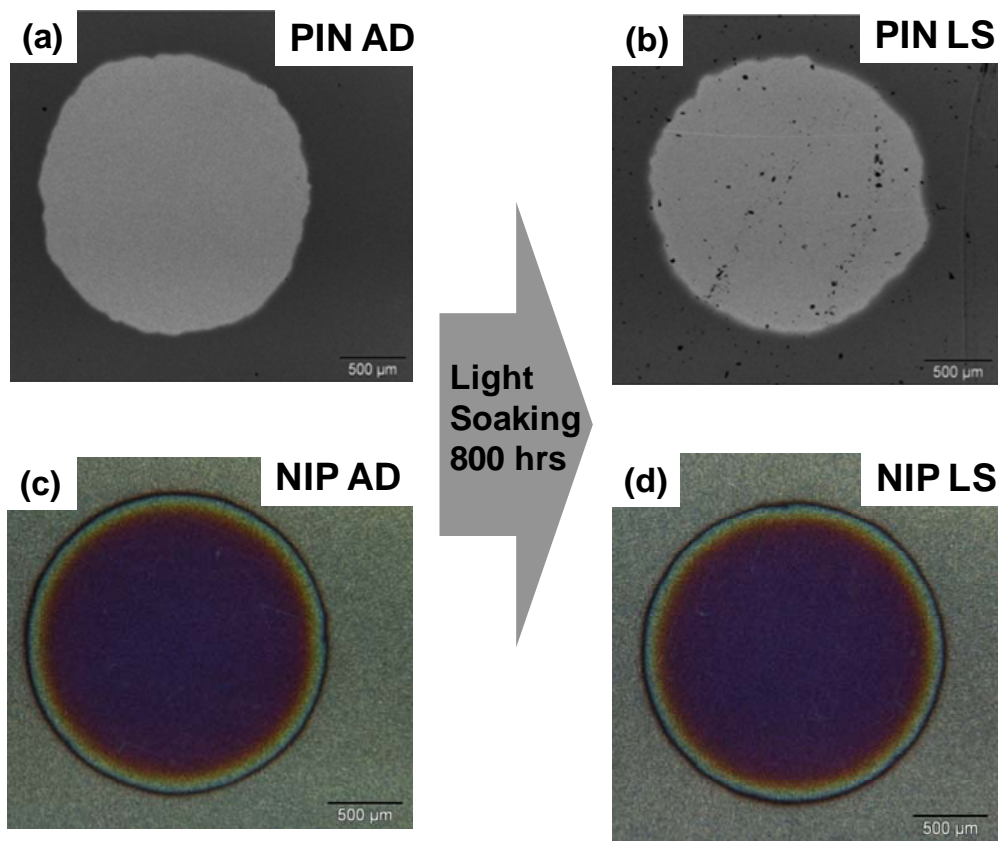


Figure 4.20 – Optical images of pm-Si:H PIN and NIP solar cells as deposited (a, c) and light-soaked (b, d). One can observe that there are large macroscopic changes in the pm-Si:H PIN solar cell, resulting in a loss of the actual solar cell area, while NIP solar cell shows no visible changes.

In general, the results presented in Figure 4.19 are indeed a magnified version of the LS result presented earlier in this chapter. Therefore, one should also observe the macroscopic structural changes of pm-Si:H PIN solar cells after LS. Figure 4.20 shows a set of optical images of pm-Si:H PIN and NIP solar cells. As expected, there are large macroscopic changes in the pm-Si:H PIN solar cells, leading to a loss of actual solar cell area. In addition, the loss of actual solar cell area results in additional loss in  $J_{sc}$ . As a matter of fact, we have observed a clear trend between  $J_{sc}$  degradation and the area loss. Figure 4.21 shows the  $J_{sc}$  loss as a function of the area loss, in the PIN solar cell case represented in Figures 4.19 and 4.20. A large set of stability results at various stages of LS shows the progressive growth

of macroscopic defects that have accumulated into a significant area loss. Simultaneously, the loss of  $J_{sc}$  shows clear proportionality to the area loss. It suggests that the additional degradation of  $J_{sc}$  is because of the decreased real collection area.

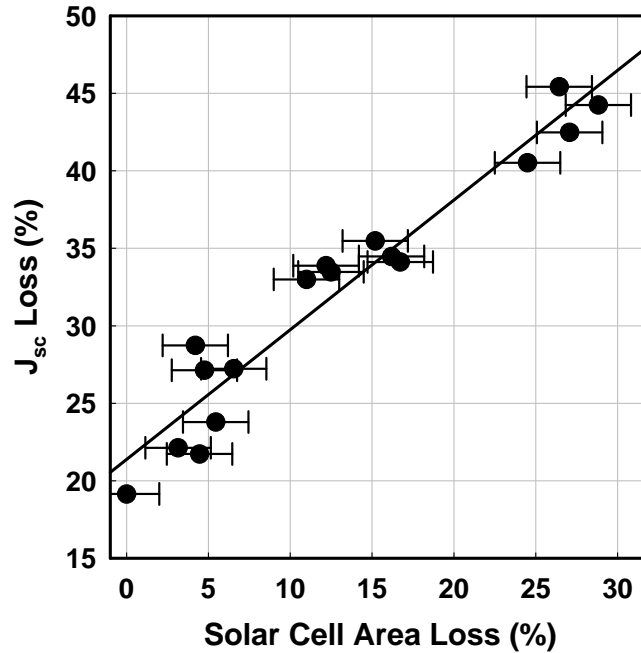


Figure 4.21 – The  $J_{sc}$  loss as a function of the area loss, in the PIN case represented in Figure 4.19 and 4.20. The loss of  $J_{sc}$  shows clear proportionality to the area loss.

Meanwhile, returning to Figures 4.19 and 4.20, one may point out another aspect concerning the NIP structure. In the set of optical images, the NIP solar cell shows no area loss, implying that NIP structure might not suffer from the light-induced macroscopic structural changes of PIN solar cells. The light-induced degradation kinetics of NIP solar cell presented in Figure 4.19 are consistent with the lack of structural changes observed in Figure 4.20. In Figure 4.19, in spite of the reasonable initial parameters, the NIP solar cell shows the smallest degradation, so that the stabilized efficiency of NIP solar cell remained the best among the sample group. Furthermore, the smallest  $\eta$  degradation of NIP solar cell is related to surprisingly

stable  $FF$  and  $J_{sc}$ . As discussed, the characteristic light-induced degradation kinetics of pm-Si:H PIN solar cells, such as a rapid decrease in  $FF$  and  $J_{sc}$ , originate from the macroscopic structural changes, and no such changes are observed in these stable cells. Recalling previous sections, one of the most striking results on light-induced structural changes is the exodiffusion data. Figure 4.22 shows the exodiffusion spectra of pm-Si:H NIP layer stacks in the as-deposited state and for two different light-soaking (LS) times. Compared to the exodiffusion spectra of pm-Si:H PIN layer stacks (Figure 4.17), the exodiffusion spectra of NIP structures show large differences. As mentioned, the exodiffusion spectrum of as-deposited pm-Si:H PIN layer stack shows two clear peaks at 350 °C and 500 °C, which differs from NIP structure, which shows a broad, non-Gaussian peak centered at around 490 °C and an additional high temperature peak at 650 °C. Let us recall that the exodiffusion signal at 350 °C indicates interconnected voids [4.61] while the one over 600 °C corresponds to the isolated ones [4.64]. We suggest that the NIP structure consists of less interconnected voids, but instead contains more isolated ones, probably at the interface between the substrates.

Taking a look into the evolution of exodiffusion spectra during LS, the difference is even larger. In the PIN case, there is a disappearance of the 350 °C peak after only one hour of LS. At the same time, the NIP structure shows the entire spectrum reduced, rather similar to the behavior of a-Si:H PIN layer stacks. From the evolution of exodiffusion spectra, NIP structure shows only moderate change at low temperature region ( $\sim$  350 °C), while PIN structure shows highly pronounced and abrupt disappearance of the 350 °C exodiffusion peak. Such moderate change for NIPs could correlate to the absence of structural changes i.e. the delamination at TCO/p-layer interface, which is supported by the stable solar cell parameters in  $J_{sc}$  and  $FF$  under LS.

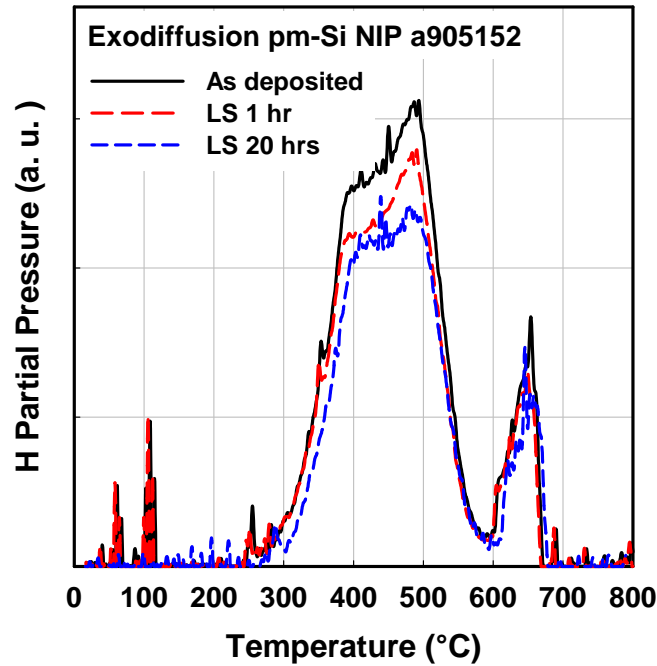


Figure 4.22 – Hydrogen exodiffusion results of pm-Si:H NIP solar cells for three states : as-deposited (black), after one hour of LS (red), and after 20 hours (blue). Note that the NIP structure shows no significant change in exodiffusion signal as well as no delamination.

## 4.7 Summary

We have performed a detailed and extensive study on light-induced changes in a-Si:H and pm-Si:H PIN and NIP solar cells deposited on various substrates and characterized these changes by a wide range of techniques. The experimental results support the hypothesis that LS results in the formation of cavities at the interface between the substrate and the p-layer which are progressively filled by molecular hydrogen during LS. This process weakens this interface and causes mechanical defects such as delamination. This is an often forgotten aspect degradation occurring in parallel to the SWE. Indeed our results show that besides the creation of electronic defects, macroscopic defects related to the delamination of the SnO<sub>2</sub>/p-layer interface and H<sub>2</sub> diffusion should be considered as the source for this effect. This is particularly true in the case of pm-Si:H PIN solar cells,

for which a fast initial drop in  $J_{sc}$  has been explained by the delamination of the interface at the  $\text{SnO}_2/\text{p-layer}$  interface. As a consequence, the pm-Si:H PIN solar cells suffer greatly from irreversible light-induced electrical and macroscopic changes. In particular, pm-Si:H PIN solar cells demonstrate rapid initial degradation, which cannot be explained by conventional paradigms on SWE. We correlated the effects to changes in hydrogen incorporation and structural properties in the PIN solar cells. In addition, with the goal of suppressing the rapid initial degradation, we have demonstrated that the NIP structure does not show large structural changes i.e. interface delamination. Therefore, a highly stable solar cell could be obtained from the NIP structure. However, the solar cell parameters of NIP solar cell presented in Figure 4.19 are not yet satisfying compared to the state-of-art solar cells in literature [4.95]. Therefore, optimization of NIP solar cell is needed. Hence, the next chapter will be dedicated to the optimization of NIP solar cell parameters and the cross-verification of the high stability of NIP structures.

---

**References**

- 4.1 P. Roca i Cabarrocas, J. B. Chevrier, J. Huc, A. Lloret, J. Y. Parey, and J. P. M. Schmitt, *J. Vac. Sci. Technol. A* **9**, 2331 (1991).
- 4.2 P. Roca i Cabarrocas, P. St'ahel, S. Hamma, and Y. Poissant, *Proc. 2nd World Conference on Photovoltaic Solar Energy Conversion*, p. 355 (1998).
- 4.3 J. Jang and S. Y. Lee, *Appl. Phys. Lett.* **52**, 1401 (1988).
- 4.4 L. Yang and L. Chen, *Mater. Res. Soc. Symp. Proc.* **336**, 669 (1994).
- 4.5 P. Siamchai and M. Konagai, *Appl. Phys. Lett.* **67**, 3468 (1995).
- 4.6 M. Isomura, H. Yamamoto, M. Kondo, and A. Matsuda, *Proceedings of the Second World Conference and Exhibition on Photovoltaic Solar Energy Conversion, 6–10 July 1998 (European Commission, Vienna, 1998)*, p. 925.
- 4.7 C. Longeaud, J. P. Kleider, M. Gauthier, R. Brüggemann, Y. Poissant, and P. Roca i Cabarrocas, *Mater. Res. Soc. Symp. Proc.* **557**, 501 (1999).
- 4.8 P. St'ahel, P. Roca i Cabarrocas, P. Sladek, and M. L. Theye, *MRS Symp. Proc.* **507**, 649 (1998).
- 4.9 M. Isomura, M. Kondo, and A. Matsuda, *Jpn. J. Appl. Phys.* **39**, 3339 (2000).
- 4.10 K. Lord, B. Yan, J. Yang, and S. Guha, *Appl. Phys. Lett.* **79**, 3800 (2001).
- 4.11 J. Yang, K. Lord, B. Yan, A. Banerjee, and S. Guha, *Mater. Res. Soc. Symp. Proc.* **715**, A26.1.1 (2002).
- 4.12 E. V. Johnson, F. Dadouche, M. E. Gueunier-Farret, J. P. Kleider, and P. Roca i Cabarrocas, *Phys. Stat. Sol. (a)*, **207**, 691 (2010).
- 4.13 V. Nadazdy and M. Zeman, *Phys. Rev. B.* **69**, 165213 (2004).
- 4.14 D. L. Staebler and C. R. Wronski, *Appl. Phys. Lett.* **31**, 292 (1977).
- 4.15 H. Fritzsche, *Annu. Rev. Mater. Res.* **31**, 47 (2001).
- 4.16 C. Longeaud, D. Roy, and O. Saadane, *Phys. Rev. B.* **65**, 85206 (2002).
- 4.17 D. C. Bobela, H. M. Branz, and P. Stradins, *Appl. Phys. Lett.* **98**, 201908 (2011).
- 4.18 S. Guha, J. Yang, A. Banerjee, B. Yan, and K. Lord, *Sol. Energ. Mater. Solar Cells.* **78**, 329 (2003).
- 4.19 Y. Poissant, P. Chatterjee, P. Roca i Cabarrocas, *J. Appl. Phys.* **94**, 7305 (2003).

- 4.20 D. E. Carlson and K. Rajan, *Appl. Phys. Lett.* 69, 1447 (1996).
- 4.21 D. E. Carlson and K. Rajan, *Appl. Phys. Lett.* 68, 28 (1996).
- 4.22 D. Redfield and R. H. Bube, *Appl. Phys. Lett.* 54, 1037 (1989).
- 4.23 L. Yang, L. Chen, and A. Catalano, *Appl. Phys. Lett.* 59, 840 (1991).
- 4.24 J. Deng, J. M. Pearce, V. Vlahos, R. W. Collins, and C. R. Wronski, *Mater. Res. Soc. Symp. Proc.* 808, A8.8.1 (2004).
- 4.25 M. L. Albert, J. Deng, X. Niu, J. M. Pearce, R. W. Collins, and C. R. Wronski, *Mater. Res. Soc. Symp. Proc.* 862, A13.2.1 (2005).
- 4.26 J. M. Pearce, J. Deng, M. L. Albert, C. R. Wronski, R. W. Collins, *Photovoltaic Specialists Conference, Conference Record of the 31st IEEE* p.1536 (2005).
- 4.27 L. Yang and L. Chen, *Appl. Phys. Lett.* 63, 400 (1993).
- 4.28 L. Yang and L. Chen, *Mater. Res. Soc. Symp. Proc.* 336, 669 (1994).
- 4.29 K. Takeda, H. Hikita, Y. Kimura, H. Yokomichi, M. Yamaguchi, and K. Morigaki, *Jpn. J. Appl. Phys.* 36, 991 (1997).
- 4.30 R. Meaudre and M. Meaudre, *Phys. Rev. B* 45, 12134 (1992).
- 4.31 J. A. Reimer, R. W. Vaughan, and J. C. Knights, *Phys. Rev. B* 24, 3360 (1981).
- 4.32 Y. Katayama, T. Shimada, K. Usami, E. Maruyama, *J. Phys. (Paris)* 42, C4-787 (1981).
- 4.33 A. H. M. Smets and M. C. M. van de Sanden, *Phys. Rev. B* 76, 073202 (2007).
- 4.34 D. E. Carlson *Appl. Phys. A* 41, 305 (1986).
- 4.35 R. Darwich, P. Roca i Cabarrocas, S. Vallon, R. Ossikovski, P. Morin, and K. Zellamam, *Phil. Mag. B* 72, 363 (1995).
- 4.36 C. Godet and P. Roca i Cabarrocas, *J. Appl. Phys.* 80, 97 (1996).
- 4.37 S. B. Zhang and H. M. Branz, *Phys. Rev. Lett.* 87, 105503 (2003).
- 4.38 A. H. M. Smets, *MRS 2012 Spring Meeting, Oral Presentation A4.3* (San Francisco, 2012)
- 4.39 D. K. Schroder, *Semiconductor material and device characterization.* Wiley-IEEE Press; 3rd edition. 2006; citing pp.608-611.
- 4.40 Y. Wang, O. Matsuda, T. Serikawa, and K. Murase, *J. Phys. IV France* 10, Pr7-259 (2000).
- 4.41 J. M. Owens, D. Han, B. Yan, J. Yang, K. Lord and S. Guha, *Mat. Res. Soc. Symp. Proc.* 762 A4.5.1 (2003).
- 4.42 E. Stratakis, E. Spanakis, P. Tzanetakis, H. Fritzsche, S. Guha, and J. Yang, *Appl. Phys. Lett.* 80, 1734 (2002).

- 
- 4.43 L. Vincent and P. Soille, *IEEE Transactions on Pattern Analysis and Machine Intelligence* 13, 583 (1991).
- 4.44 S. Beucher and F. Meyer, the watershed transformation In *Mathematical Morphology in Image Processing*, edited by E. R. Dougherty, (Marcel Dekker, New York, 1992) pp. 433-481.
- 4.45 S. Lebib and P. Roca i Cabarrocas, *Eur. Phys. J. Appl. Phys.* 26, 17 (2004).
- 4.46 N. Pham, Y. Djeridane, A. Abramov, A. Hadjadj, and P. Roca i Cabarrocas, *Mat. Sci. Eng. B* 159-160, 27 (2009).
- 4.47 H. R. Shanks, C. J. Fang, L. Ley, M. Cardona, F. J. Demond, and S. Kalbitzer, *Phys. Stat. Sol. (b)* 100, 43 (1980).
- 4.48 H. R. Shanks and L. Ley, *J. Appl. Phys.* 52, 811 (1981).
- 4.49 R. A. Street, *Appl. Phys. Lett.* 59, 1084 (1991).
- 4.50 A. Dasgupta, N. Palit, S. Ray, *Sol. Energ. Mater. Sol. Cells* 55, 395 (1998).
- 4.51 W. Paul, G.A.N. Connell and R.J. Temkin, *Advan. Phys.* 22, 529 (1973).
- 4.52 G. E. Jellison, Jr. and F. A. Modine, *Appl. Phys. Lett.* 69, 371 (1996).
- 4.53 G. E. Jellison, Jr., F. A. Modine, P. Doshi, and A. Rohatgi, *Thin Solid Films* 313, 193 (1998).
- 4.54 A. Fontcuberta i Morral, P. Roca i Cabarrocas, and C. Clerc, *Phys. Rev. B* 69, 125307 (2004).
- 4.55 M. H. Brodsky, M. Cardona, and J. J. Cuomo, *Phys. Rev. B* 16, 3556 (1977).
- 4.56 S. Lebib and P. Roca i Cabarrocas, *Eur. Phys. J. Appl. Phys.* 26, 17 (2004).
- 4.57 Z. Yiping, Z. Dianlin, K. Guanglin, P. Guangqin, and L. Xianbo *Phys. Rev. Lett.* 74, 558 (1995).
- 4.58 H. Fritzsche, *Solid State Commun.* 94, 953 (1995).
- 4.59 R. Darwich, P. Roca i Cabarrocas, S. Vallon, R. Ossikovski, P. Morin, and K. Zellamam, *Phil. Mag. B* 72, 363 (1995).
- 4.60 S. Sheng, G. Kong, and X. Liao, *Solid State Commun.* 116, 519 (2000).
- 4.61 A. H. Mahan, W. Beyer, B. L. Williamson, J. Yang, and S. Guha, *Philos. Mag. Lett.* 80, 647 (2000).
- 4.62 E. Bertran, J. Costa, G. Sardin, J. Campmany, J. L. Andujar, and A. Canillas, *Plasma Sources Sci. Technol.* 3, 348 (1994).
- 4.63 D. K. Biegelsen, R. A. Street, C. C. Tsai, and J. C. Knights , *Phys.*

- Rev. B 20, 4839 (1979).
- 4.64 H. Stiebig, F. Siebke, W. Beyer, C. Beneking, B. Rech, and H. Wagner, *Sol. Energ. Mater. Sol. Cells* 48, 351 (1997).
- 4.65 N. Pham, Y. Djeridane, A. Abramov, A. Hadjadj, and P. Roca i Cabarrocas, *Mat. Sci. Eng. B* 159-160, 27 (2009).
- 4.66 F. Kail, A. Hadjadj, and P. Roca i Cabarrocas, *Thin Solid Films* 487, 126 (2005).
- 4.67 F. Kail, S. Fellah, A. Abramov, A. Hadjadj, and P. Roca i Cabarrocas, *J. Non-Cryst. Solid.* 352, 1083(2006).
- 4.68 H. M. Branz, *Phys. Rev. B* 59, 5498 (1999).
- 4.69 H. M. Cheong, S.H. Lee, B. Nelson, A. Mascharenas, and S. K. Deb. *Appl. Phys. Lett.* 77, 2686 (2000).
- 4.70 H. M. Branz, S. Asher, H. Gleskova, and S. Wagner. *Phys. Rev. B* 59, 5513 (1999).
- 4.71 F. Kail, J. Farjas, P. Roura, and P. Roca i Cabarrocas, *Phys. Rev. B* 80, 073202 (2009).
- 4.72 P. Tzanetakis, *Sol. Energ. Mater. Solar Cells.* 78, 369 (2003).
- 4.73 T. Hatano, Y. Nakae, H. Mori, K. Ohkado, N. Yoshida, S. Nonomura, M. Itoh, A. Masuda, and H. Matsumura. *Thin Solid Films* 395, 84 (2001).
- 4.74 S. Nonomura, N. Yoshida, T. Gotoh, T. Sakamoto, M. Kondo, A. Matsuda, and S. Nitta. *J. Non-Cryst. Solids.* 266–269, 474 (2000).
- 4.75 T. Sakamoto, N. Yoshida, H. Harada, T. Kishida, S. Nonomura, T. Gotoh, M. Kondo, A. Matsuda, T. Itoh, and S. Nitta. *J. Non-Cryst. Solids.* 266–269, 481 (2000).
- 4.76 K. Shimizu, T. Tabuchi, K. Hattori, H. Kida, and H. Okamoto. *Mater. Res. Soc. Symp. Proc.* 507, 735 (1998).
- 4.77 T. Gotoh, S. Nonomura, M. Nishio, N. Masui, S. Nitta, M. Kondo, and A. Matsuda. *J. Non-Cryst. Solids.* 227–230, 263 (1998).
- 4.78 T. Gotoh, S. Nonomura, M. Nishio, S. Nitta, M. Kondo, and A. Matsuda. *Appl. Phys. Lett.* 72,2978 (1998).
- 4.79 N. Yoshida, Y. Shobajima, H. Kamiguchi, T. Ida, T. Hatano, H. Mori, Y. Nakae, M. Itoh, A. Masuda, H. Matsamura, and S. Nonomura. *J. Non-Cryst. Solids.* 299–302, 516 (2002).
- 4.80 H. M. Branz, *Sol. Energ. Mater. Solar Cells* 78, 425 (2003).
- 4.81 P.V. Santos, N. M. Johnson, and R. A. Street, *Phys. Rev. Lett.* 67, 2686 (1991).
- 4.82 S. Sriraman, S. Agarwal, E. S. Aydil, and D. Maroudas, *Nature*

- (London) 418, 62 (2002).
- 4.83 W. B. Jackson, *Curr. Opin. Solid. State. Mater. Sci.* 1, 562 (1996).
- 4.84 C. G. Van de Walle, *Phys. Rev. B* 49, 4579 (1994).
- 4.85 K. J. Chang and D. J. Chadi, *Phys. Rev. Lett.* 62, 937 (1989).
- 4.86 S. K. Estreicher, J. L. Hastings, and P. A. Fedders, *Phys. Rev. B* 57, R12663 (1988).
- 4.87 S. K. Estreicher, J. L. Hastings, and P. A. Fedders, *Appl. Phys. Lett.* 70, 432 (1997).
- 4.88 J. Serra, J. Andreu, G. Sardin, C. Roch, J.M. Asensi, J. Bertomeu and J. Esteve, *Physica B* 170, 269 (1991).
- 4.89 E. Spanakis, E. Stratakis, P. Tzanetakis, and Q. Wang, *J. Appl. Phys.* 89, 4294 (2001).
- 4.90 D. Han, NREL Technical Report, SR-520-24741 (1998).
- 4.91 S. Acco, D. L. Williamson, W. G. J. H. M. van Sark, W. C. Sinke, W. F. van der Weg, A. Polman, and S. Roorda, *Phys. Rev. B* 58 12853 (1998).
- 4.92 J. A. Reimer, R. W. Vaughan, and J. C. Knights, *Solid State Commun.* 37, 161 (1981).
- 4.93 [http://en.wikipedia.org/wiki/Mercury-vapor\\_lamp](http://en.wikipedia.org/wiki/Mercury-vapor_lamp)
- 4.94 <http://assets.newport.com/web900w-EN/images/1121.gif>
- 4.95 S. Benagli, D. Borrello, E. Vallat-Sauvain, J. Meier, U. Kroll, J. Hötzel, J. Bailat, J. Steinhauser, M. Marmelo, G. Monteduro, and L. Castens, *Proc. 24th European PVSEC, Hamburg 2009*, pp. 21-25.
- 4.96 F. Dadouche, O. Béthoux, M. E. Gueunier-Farret, E. V. Johnson, P. Roca i Cabarrocas, C. Marchand, and J. P. Kleider, *Eur. Phys. J. Photovolt.* 2, 20301 (2011).
- 4.97 M. Vanecek, O. Babchenko, A. Purkrt, J. Holovsky, N. Neykova, A. Poruba, Z. Remes, J. Meier, and U. Kroll, *Appl. Phys. Lett.* 98, 163503 (2011).



# Chapter 5

## Prospective – Towards High Stabilized Efficiency

5.1 Introduction.....	190
5.2 p-type $\mu\text{c-SiO}_x$ .....	190
5.3 pm-Si:H NIP solar cells using p-type $\mu\text{c-SiO}_x$ .....	200
5.4 Stable pm-Si:H NIP solar cells.....	210
5.5 Summary .....	212

## 5.1 Introduction

This chapter deals with the optimization of pm-Si:H NIP solar cells. NIP solar cells are made in the “substrate” configuration, and are illuminated through the top, p-type layer. As for a-Si:H and pm-Si:H solar cells should be always illuminated through the p-type layer side due to lower mobility of holes in comparison to electrons. Since most of the photo-generated carriers are generated near the p/i interface, on average, holes have shorter distance for the collection. NIP structure uses thin TCO such as 100 nm thick ITO as a front contact, on top of the p-type layer. Highly conductive and transparent p-type layer is needed. The main challenge in the optimization of the NIP solar cells is to develop a novel p-type layer. While p-type  $\mu\text{c-Si:H}$  layer with the high conductivity ( $\sigma$ ) and low absorption coefficient ( $\alpha$ ) in the visible range has been explored by some authors [5.1], nowadays p-type  $\mu\text{c-SiO}_x$  layers have attracted much interest [5.2, 5.3]. One of the merits of doped  $\mu\text{c-SiO}_x$  layers is their “tunable refractive index”, achieved by varying the  $\text{SiH}_4/\text{CO}_2$  gas precursor ratio during deposition. Such high flexibility in the optical properties of doped  $\mu\text{c-SiO}_x$  layers enables their application as both the front window layer [5.2] and as the intermediate reflector in tandem junctions [5.3, 5.4]. Recently a record efficiency of 16.3% has been demonstrated in triple junction solar cells incorporating doped  $\mu\text{c-SiO}_x$  layers [5.4]. In this chapter, optimization of high efficiency pm-Si:H NIP solar cells using p-type  $\mu\text{c-SiO}_x$  layers will be presented.

## 5.2 p-type $\mu\text{c-SiO}_x$

Doped  $\mu\text{c-SiO}_x$  can be deposited by adding  $\text{CO}_2$  gas during  $\mu\text{c-Si}$  deposition. While n-type  $\mu\text{c-SiO}_x$  are readily achieved (see annex

5.1), p-type  $\mu\text{-SiO}_x$  is more difficult to achieve due to the amorphization effect of  $\text{B}(\text{CH}_3)_3$  (TMB). In this chapter, optimization of p-type  $\mu\text{-SiO}_x$  and its application to solar cells is studied. Table 5.1 summarizes the deposition conditions of p-type  $\mu\text{-SiO}_x$ . The p-type  $\mu\text{-SiO}_x$  layers are deposited at 175 °C from a gas mixture of  $\text{SiH}_4$ ,  $\text{H}_2$ , and  $\text{CO}_2$ , and p- and n-type doping is achieved by adding TMB and  $\text{PH}_3$ , respectively. The effect of  $\text{CO}_2$  addition was studied by varying the  $\text{CO}_2$  flow.

Sample	$\text{H}_2$	$\text{SiH}_4$	TMB	$\text{CO}_2$	Pressure	RF power	$T_s$
p-type	500	9	1.5	Varied (optimum : 2)	2 Torr	14 W	175 °C

Table 5.1 – Summary of the deposition conditions of p-type  $\mu\text{-SiO}_x$ .

The addition of  $\text{CO}_2$  during the deposition results into a transition from  $\mu\text{-Si:H}$  to amorphous growth. Figure 5.1 shows Raman scattering spectra of p-type  $\mu\text{-SiO}_x$  layers deposited with different  $\text{CO}_2$  flow rates. A He–Ne laser (632 nm) and a back-scattering collection configuration were used for the micro Raman measurements. In the Raman spectra, at low  $\text{CO}_2$  flow, a crystalline silicon (c-Si) peak is detected at 520  $\text{cm}^{-1}$ . It is also observed that c-Si peak shifts to lower wave-numbers with higher  $\text{CO}_2$  flow. The c-Si peak shift may indicate smaller grain size at larger  $\text{CO}_2$  flow. Broad peaks centered at  $\sim 470 \text{ cm}^{-1}$  indicate an amorphous phase such as a-Si and  $\text{SiO}_2$ , but the peaks of a-Si ( $\sim 480 \text{ cm}^{-1}$ ) and  $\text{SiO}_2$  ( $\sim 460 \text{ cm}^{-1}$ ) are almost indistinguishable. One could claim that the Raman spectrum of the sample with 3 sccm of  $\text{CO}_2$  flow still shows c-Si peak at around 520  $\text{cm}^{-1}$ . However, it is difficult to determine the c-Si peak because of the broad amorphous peak. Furthermore, even if the c-Si phase exists, the crystalline

volume fraction would be low thus would not contribute to the electrical conductivity.

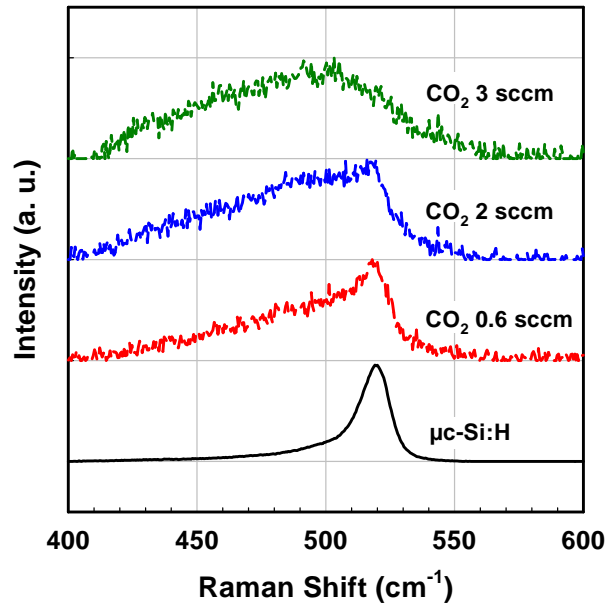


Figure 5.1 – Raman spectra of p-type  $\mu\text{c-SiO}_x$  layers deposited with different  $\text{CO}_2$  flow. A transition from crystalline ( $520\text{ cm}^{-1}$ ) to amorphous ( $480\text{ cm}^{-1}$ ) when varying  $\text{CO}_2$  flow is notably seen.

The phase shift from crystalline to amorphous is also shown in spectroscopic ellipsometry (SE) measurements and modeling. The measured spectra were modeled using the Bruggeman effective medium approximation (BEMA). This approach, based on the assumption of the linearity of the optical response of mixed phase materials, gives a unique opportunity to define the films' structure as expressed in terms of the volume fraction of its constituents. The modeling steps consist of rebuilding the measured pseudo-dielectric function from a combination of the optical responses of a mixture of known dielectric function materials [5.5, 5.6]. This approach has been shown to be very well adapted to modeling complex multilayer structures consisting of amorphous and nanocrystalline silicon materials [5.7]. Figure 5.2

shows the SE spectra of various p-type materials. SE spectrum of c-Si shows two peaks at 3.4 and 4.2 eV, representing the first two direct transition energies in the dispersion relation. SE spectrum of the material consisting of smaller crystallite size, such as  $\mu\text{-Si:H}$ , shows a broadening of these peaks. p-type a-SiC shows a broad single peak centered at around 3.75 eV in the SE spectrum, while p-type  $\mu\text{-Si:H}$  shows a broad peak with a plateau between 3.4 and 4.2 eV due to the broadening of these two peaks. Addition of  $\text{CO}_2$  to the gas mixture produces a decrease in the peak intensity of  $\epsilon_i$ , indicating that the material is less dense or the surface is rougher.

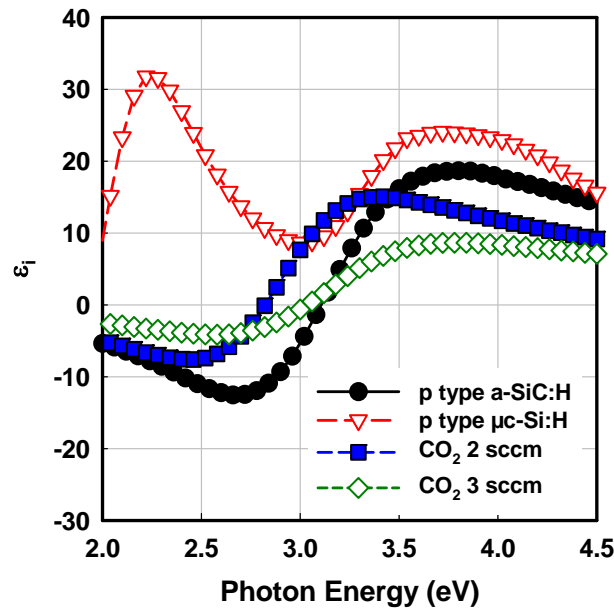


Figure 5.2 – SE spectra of various p-type layers. p-type  $\mu\text{-SiO}_x$  deposited with two different  $\text{CO}_2$  flows, 2 and 3 sccm are also shown.

The reduction of the amplitude of the interference fringes at low photon energy region of material deposited at high  $\text{CO}_2$  flow indicates that the refractive index of the material decreases and becomes closer to that of the glass substrate, implying more  $\text{SiO}_2$  fraction. It should be mentioned that in the SE spectra, the interference fringes might be confused as an absorption edge. This

is due to the thickness of the samples ( $\sim 150 \text{ \AA}$ ), and that is why there is sharp increase in  $\epsilon_i$  at the photon energy of 2.5~3 eV.

BEMA modeling of the SE spectra provides more detailed information on the material properties. The measured spectra were modeled by a medium based on the relative fractions of  $\text{SiO}_2$ ,  $\mu\text{-Si}$ , and a-Si. Figure 5.3(a) shows evolution of  $\text{SiO}_2$ ,  $\mu\text{-Si}$ , and a-Si volume fraction of p-type  $\mu\text{-SiO}_x$  as functions of  $\text{CO}_2$  flow. Evolution of  $\mu\text{-Si}$  and a-Si fraction show same trend, while  $\text{SiO}_2$  fraction increases with  $\text{CO}_2$  flow. It suggests that the  $\text{SiO}_2$  fraction originates from  $\text{CO}_2$  flow, and the  $\text{SiO}_2$  fraction and silicon ( $\mu\text{-Si}$ , a-Si) fractions are in trade off. Such highly heterogeneous mixed phase nature of  $\mu\text{-SiO}_x$  is necessary for the material to perform its multifunctional role. In other words,  $\text{SiO}_2$  fraction modifies the optical properties and contributes to the transparency of the material, while  $\mu\text{-Si}$  maintains the electrical conductivity. Therefore, it is needed to find the optimum trade-off between transparency and conductivity.

Another interesting aspect is the necessity of a crystallized  $\mu\text{-Si}$  bottom layer in SE optical model, as shown in Figure 5.3(b). Figure 5.3(c) shows that the thickness of this bottom layer is linked with the  $\mu\text{-Si}$  fraction in the “top” layer. It is suspected that during growth, there would be a phase transition from  $\mu\text{-Si:H}$  to  $\mu\text{-SiO}_x$ . It can be due to that highly reactive and electronegative oxygen atoms have longer residence time compared to the other gases such as  $\text{H}_2$  and  $\text{SiH}_4$  [5.8]. The film would initially grow as  $\mu\text{-Si:H}$  at the initial stage and then slowly evolve into  $\mu\text{-SiO}_x$ . Further studies based on TEM and the analysis of a film thickness series should provide a clearer view on the growth mechanism of doped  $\mu\text{-SiO}_x$ .

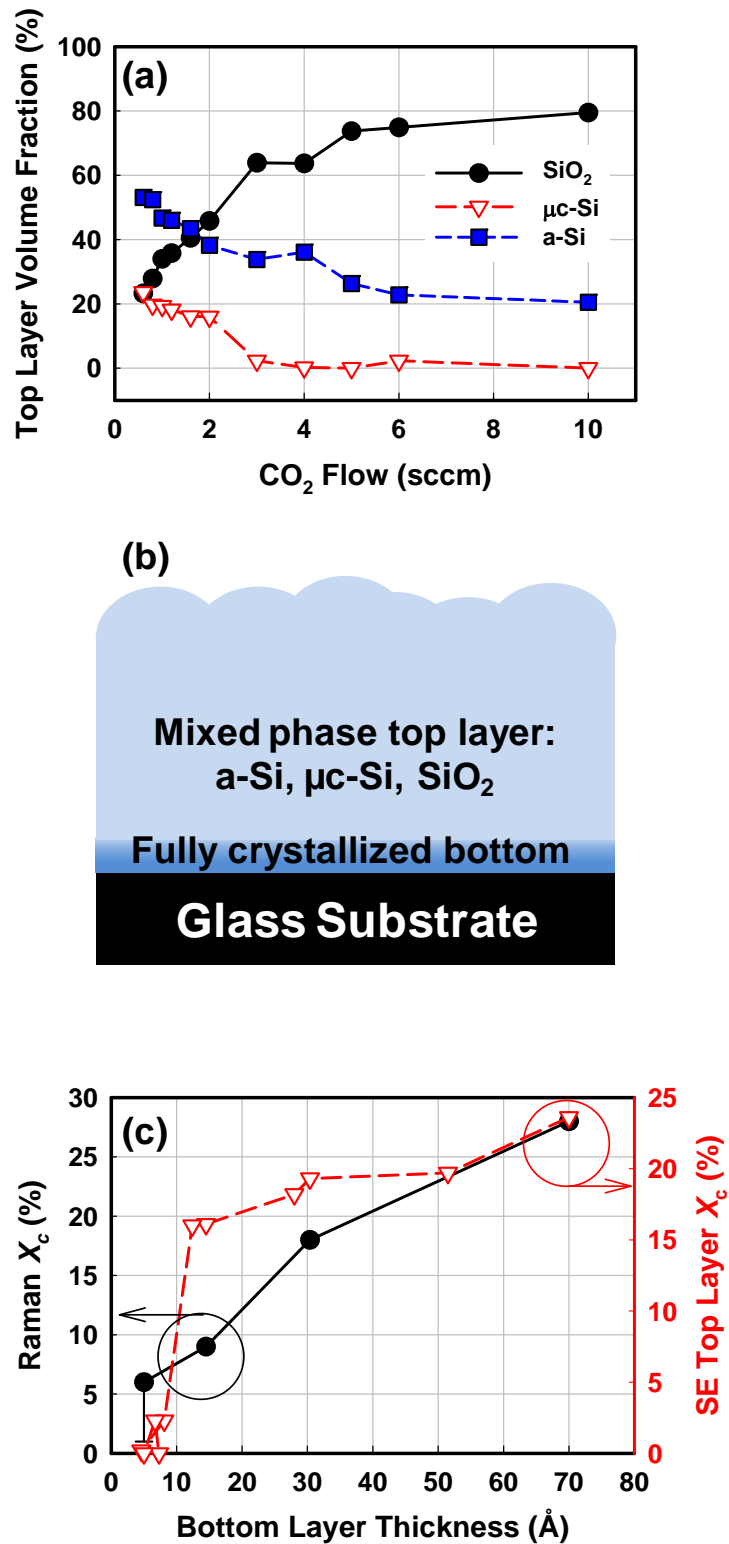


Figure 5.3 – (a) Evolution of  $\text{SiO}_2$ ,  $\mu\text{c-Si}$ , and a-Si volume fractions of p-type  $\mu\text{-SiO}_x$  as functions of  $\text{CO}_2$  flow deduced from BEMA method, (b) structure of optical model, and (c) Raman crystalline fraction  $X_c$  and SE top layer crystalline fraction  $X_c$  versus thickness of fully crystallized bottom layer.

Over parts of the spectrum,  $\varepsilon_i$  is closely related to the absorption coefficient of the material. The  $\text{SiO}_2$  fraction increases with the  $\text{CO}_2$  flow, while the  $\mu\text{-Si}$  fraction decreases. As a consequence, the absorption coefficient ( $\alpha$ ) of the film decreases with increasing  $\text{CO}_2$  flow rate. A set of p-type layers was deposited on Corning glass substrate and their transmission spectra were measured. The absorption coefficient ( $\alpha$ ) was calculated from the transmission spectra, neglecting any reflection losses. Under the assumption of a parabolic distribution of electronic states, a simple analysis of transmission measurement can be performed [5.9]. Optical absorption occur by transition of electrons and holes between electronic states such as conduction and valence bands, tail states, and gap states. Tauc gap ( $E_{\text{Tauc}}$ ) is generally used for determining  $E_{\text{opt}}$  of a-Si:H. However, it is risky to represent the  $E_{\text{Tauc}}$  of a two phase material such as  $\mu\text{-Si:H}$ . It should be noted that an indirect bandgap material does not have a single distinct absorption onset, which corresponds to a more gradually sloping curve in the Tauc plot. Therefore, here we present  $E_{04}$ , a photon energy where  $\alpha=10^4 \text{ cm}^{-1}$ . Figure 5.4 shows  $\alpha$  for various p-type layers versus photon energy.

In Figure 5.4, p-type  $\mu\text{-Si:H}$  shows higher  $\alpha$  compared to that of p-type a-SiC:H, so from an optical point of view,  $\mu\text{-Si:H}$  is less preferable than a-SiC:H as window layer if one neglects the effect of reflection losses. However, addition of  $\text{CO}_2$  during the growth of p-type  $\mu\text{-Si:H}$  changes the composition of the material, as shown in Figure 5.3, and decreases  $\alpha$ , as is also shown in Figure 5.5. Figure 5.5 shows  $E_{04}$  from transmission measurement and  $\text{SiO}_2$  fraction deduced from SE modeling of p-type  $\mu\text{-SiO}_x$  as functions of  $\text{CO}_2$  flow. Notably,  $E_{04}$  and  $\text{SiO}_2$  fraction shows strong correlation. Electrically,  $\text{SiO}_2$  is an insulator with electrical conductivity of  $10^{-15} \text{ Scm}^{-1}$ . Even though p-type  $\mu\text{-SiO}_x$  shows wide bandgap thanks to

the  $\text{SiO}_2$  fraction, it is easy to imagine that too much  $\text{SiO}_2$  fraction would deteriorate the electrical properties of the material.

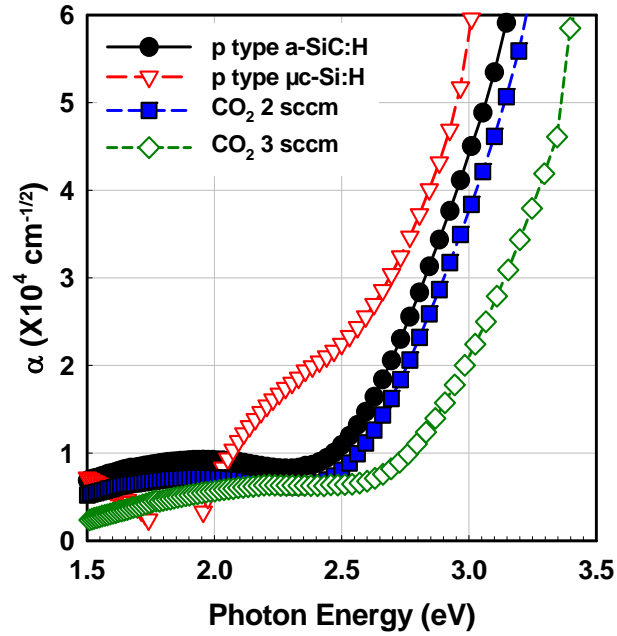


Figure 5.4 – Absorption coefficient of various p-type layers. p-type  $\mu\text{-SiO}_x$  deposited with two different  $\text{CO}_2$  flow, 2 and 3 sccm are also shown.  $E_{04}$  can be extracted at the energy where  $\alpha=10^4$ .

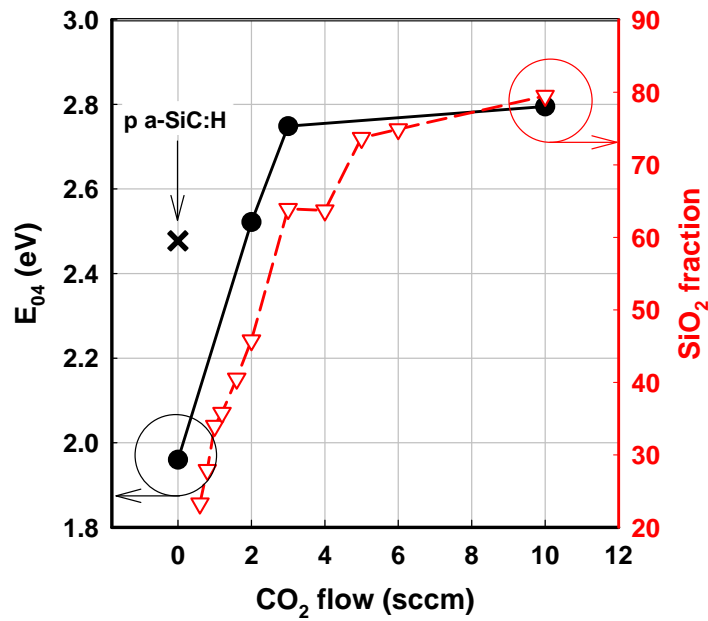


Figure 5.5 –  $E_{04}$  from transmission measurement and  $\text{SiO}_2$  fraction deduced from SE modeling as functions of  $\text{CO}_2$  flow. Note that  $E_{04}$  and  $\text{SiO}_2$  fraction show strong correlation.

Returning back to Figure 5.3, the p-type  $\mu\text{-SiO}_x$  consists of about 20 % of  $\mu\text{-Si}$  fraction up to 2 sccm of  $\text{CO}_2$  flow, and the  $\mu\text{-Si}$  fraction sharply drops to zero at larger  $\text{CO}_2$  flow. One can imagine an impact on conductivity of the material because the conductivity of the doped  $\mu\text{-SiO}_x$  layer relies on the nanocrystalline fraction [5.8]. Meanwhile, p-type  $\mu\text{-SiO}_x$  layers show high a-Si fraction, from 20 to 55 %. It suggests that the a-Si fraction in p-type  $\mu\text{-SiO}_x$  only gives negative effects due to its high (parasitic) absorption coefficient and low conductivity. Therefore, further work on the removal of a-Si fraction and its replacement by  $\mu\text{-Si}$  would improve both transparency and conductivity.

The electrical properties of various p-type materials have been investigated through the temperature-dependence of their dark conductivity ( $\sigma(T)$ ) using evaporated Al coplanar electrodes. 5 mm wide Al coplanar electrodes were separated by 1 mm gap. The current was measured under voltage bias while the samples are heated / cooled. At every 5 °C of the cycle, current was measured after 5 minutes of stabilization. The measurement sequence is then repeated for another temperature (+ 5 °C). In this manner, a series of points are obtained to generate an Arrhenius plot. The samples were heated up to 160 °C than cooled down to 50 °C, and the conductivity of both heating-cooling cycles was recorded. Activation energy ( $E_a$ ) of the material can be determined from the slope obtained during the cooling cycle. The cooling rate was slow enough (0.016 °C/s) in order to avoid the quenching the defect states [5.10]. Figure 5.6 shows the Arrhenius plots of various p-type layers. The  $\sigma(T)$  reveals that p-type  $\mu\text{-Si:H}$  has a higher conductivity ( $\sigma$ ) compared to the p-type a-SiC:H. On the contrary to the optical properties, p-type  $\mu\text{-Si:H}$  layer is electrically a much more preferable doped layer. As seen in Figure 5.3, addition of  $\text{CO}_2$  introduces changes in material composition, resulting in a large

fraction of a-Si and  $\text{SiO}_2$ .

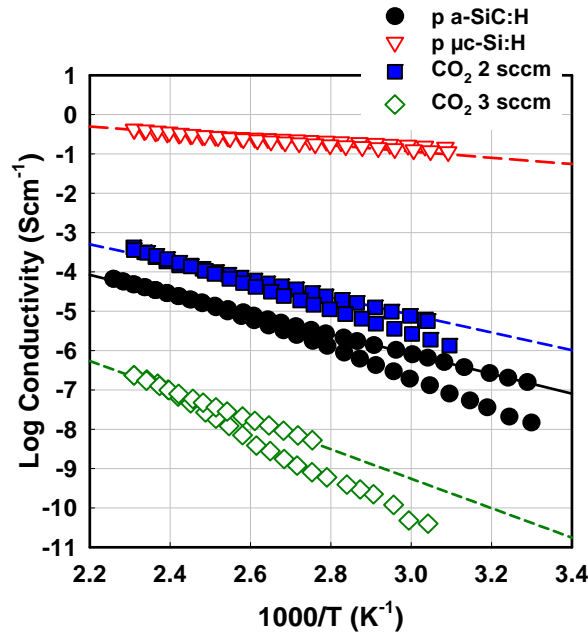


Figure 5.6 – Arrhenius plots of various p-type layers. p-type  $\mu\text{-SiO}_x$  deposited with two different  $\text{CO}_2$  flows, 2 and 3 sccm are also shown. Activation energy ( $E_a$ ) can be extracted from the slopes of the plots.

Electrically, both a-Si and  $\text{SiO}_2$  degrade the electrical properties of the material. Addition of 2 sccm of  $\text{CO}_2$  results in a decrease of the room-temperature conductivity ( $\sigma_{\text{RT}}$ ) from  $10^{-1}$  to  $10^{-6}$ , a factor of  $10^5$ . Further increase of  $\text{CO}_2$  flow continues to decrease the conductivity, and the material becomes too resistive to be used as a p-layer in solar cells. Therefore, considering the electrical properties, the p  $\mu\text{-SiO}_x$  material should be deposited with  $\text{CO}_2$  flow of less than 2 sccm, in spite of enhanced optical properties (Figure 5.5). Similarly, the  $\mu\text{-Si}$  fraction dominates electrical properties of the material. Figure 5.7 shows a relationship between  $E_a$ ,  $\sigma_{\text{RT}}$  from  $\sigma(T)$  measurement and  $\mu\text{-Si}$  fraction ( $X_c$ ) deduced from SE modeling. The strong correlation between the electrical properties and  $X_c$  suggests the further possibility of the crystallization of residual a-Si fraction. Recalling the SE modeling

result of Figure 5.3, the p-type  $\mu\text{-SiO}_x$  consists of 20 % of  $\mu\text{-Si}$ . Continuous optimization of the deposition condition would bring even more transparent and conductive window layers. Based on these results we will use 2 sccm of  $\text{CO}_2$  for the p-layers of solar cells, as shown in the Table 5.1.

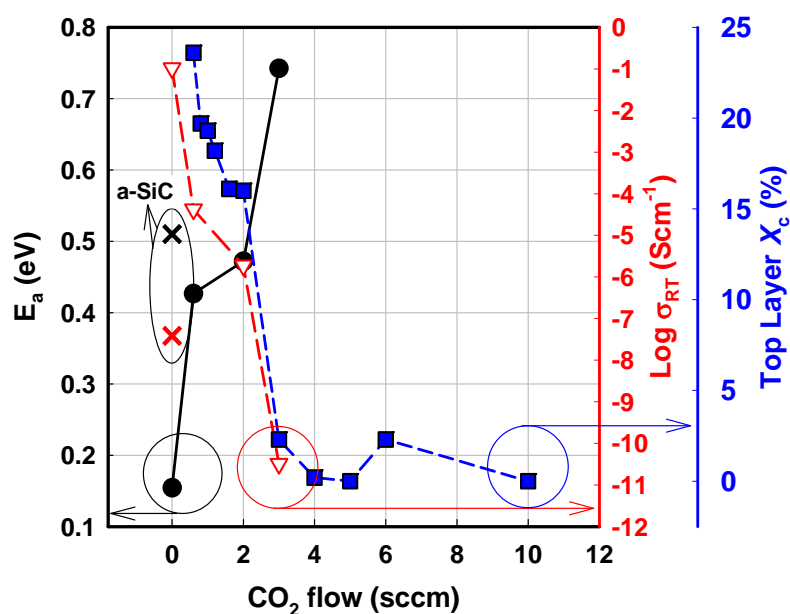


Figure 5.7 –  $E_a$  and  $\sigma_{RT}$  from  $\sigma(T)$  measurement and  $\mu\text{-Si}$  fraction ( $X_c$ ) deduced from SE modeling as functions of  $\text{CO}_2$  flow. Note that  $E_a$ ,  $\sigma_{RT}$  and  $\mu\text{-Si}$  fraction show strong correlation.

### 5.3 $\mu\text{-Si:H}$ NIP solar cells using p-type $\mu\text{-SiO}_x$

In the previous chapter, it was observed that a NIP solar cell showed superior stability under light-soaking (LS) compared to PIN structure. The comprehensive material study revealed that the reason why NIP is more stable than PIN is the suppression of the hydrogen accumulation at the substrate/cell interface and the subsequent interface delamination. However, previous trials of NIP solar cells showed low initial efficiency due to the incomplete optimization of device structure. In this chapter, we have studied various material properties of p-type  $\mu\text{-SiO}_x$  as functions of  $\text{CO}_2$

gas flow rate, and we have fabricated a p-type  $\mu\text{-SiO}_x$  layer, which is both more conductive and more transparent than our standard p-type a-SiC:H. The next step should be, of course, the introduction of the optimized p-type  $\mu\text{-SiO}_x$  layers in the NIP devices.

The NIP cells have the following structure: textured Asahi ( $\text{SnO}_2$ ) substrate/n-type a-Si:H/intrinsic pm-Si:H/p-type  $\mu\text{-SiO}_x$ /p-type  $\mu\text{-Si:H}$ /sputtered indium-tin-oxide (ITO). The NIP solar cells in this study were deposited in ARCAM. The intrinsic pm-Si:H was the one previously optimized in chapter 3. The p-type layer had to be  $\mu\text{-SiO}_x/\mu\text{-Si:H}$  bi-layer in order to have good ohmic contact with ITO front contact. The NIP solar cells are deposited on textured Asahi substrate as a back reflector. Use of better optimized substrate and back reflector is necessary further work. Figure 5.8 shows an initial  $J(V)$  and EQE curves of a pm-Si:H NIP solar cell using p-type  $\mu\text{-SiO}_x$ . A great enhancement in  $V_{oc}$  is the most impressive feature. About 100 mV of improvement compared to std pm-Si:H PIN solar cells has been achieved, and a shift of  $V_{max}$  compared to Figure 3.7 also shows that the high  $V_{oc}$  is a consequence of application of such heterojunction structure. The NIP solar cell show a  $FF$  of 65.2, which needs to be further optimized. There are three reasons for the limited  $FF$ . At first, the pm-Si:H NIP solar cells using  $\mu\text{-SiO}_x$  is indeed the first trial in this laboratory, and p/i interface is not yet fully optimized. The importance of the p/i interface is widely known in particular for the transport properties of solar cells [5.11, 5.12]. Gradual interface or novel buffer layer at p/i interface could further improve the  $FF$  [5.12]. Second, the limitation of  $FF$  in NIP solar cells seems to come from the low  $R_{sc}$ . The physical origin of this low  $R_{sc}$  could be the recombination, or the physical shunt in diode. In the thin film solar cells, shunted diode is made by the pinhole, non-conformal coverage of textured substrate, or imperfection of substrate cleaning. It is

also supported by the fact that solar cells with thicker intrinsic layer showed less shunted diodes. A third reason is the conductive p-type  $\mu\text{c-Si:H}$  layer at the interface with the ITO. This layer will act like a poor TCO layer, and collection through this layer will increase the  $J_{sc}$  measured in a solar simulator (but with a poor  $FF$ ) but not the  $J_{sc}$  calculated from EQE. In Figure 5.8(b), EQE curve of NIP solar cell showed disappointing response, in spite of excellent optical properties of p-type  $\mu\text{c-SiO}_x$ . Poor EQE could be due to the thick p-type layer (about 280 Å) which absorbs too much light, or to insufficient light trapping due to no metallic back reflector.

In order to further optimize the NIP solar cell efficiency, various series of pm-Si:H NIP solar cells were fabricated. At first, effect of the intrinsic layer thickness was tested. A series of pm-Si:H NIP solar cells having different intrinsic layers were fabricated. pm-Si:H NIP solar cells were also light-soaked under Mercury (Hg) lamp illumination of an intensity of 1 sun for 500 hours. One can notice that the LS condition is done under strong UV component compared to standard AM1.5 condition because of high UV/blue emission of Hg lamp, as one can find the spectrum of the lamp in the reference [5.13]. However, the solar cell  $J(V)$  curves are measured under AM1.5 spectrum.

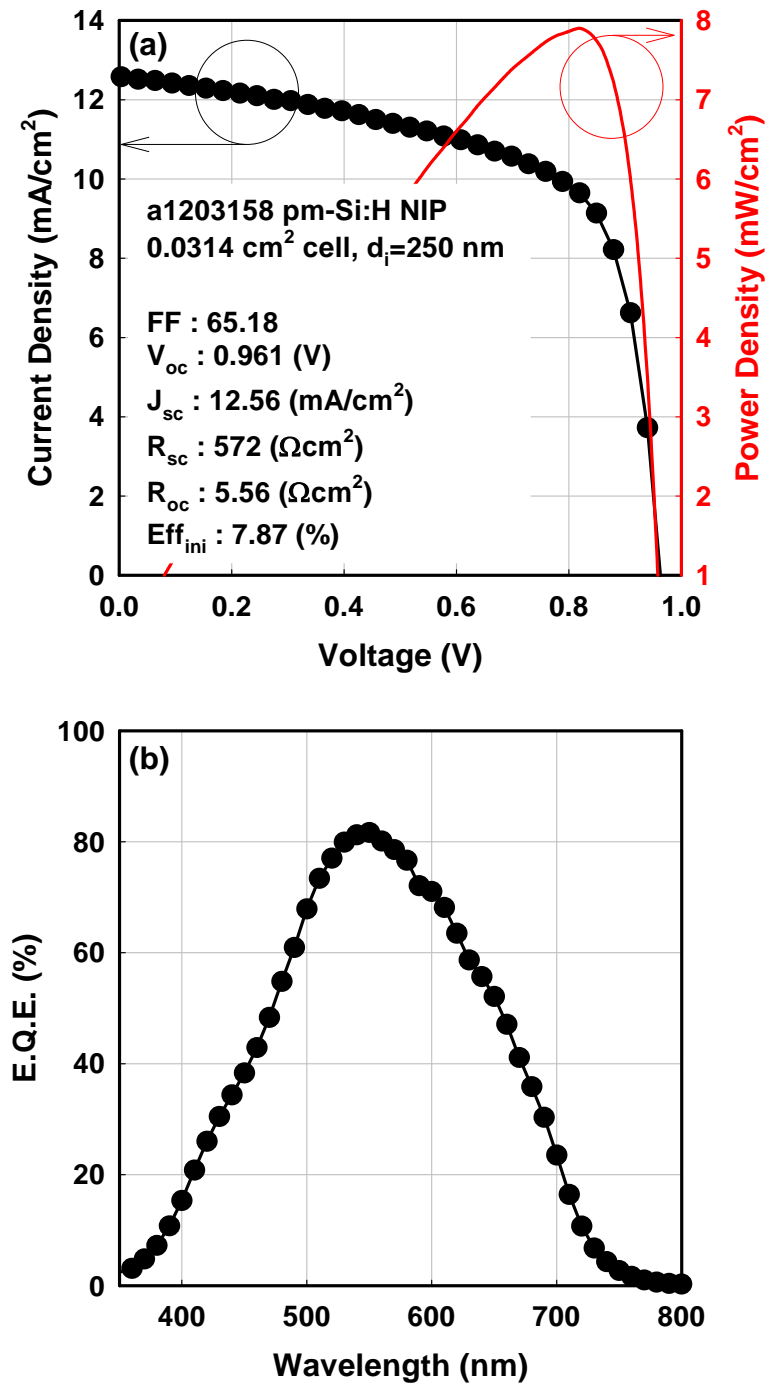


Figure 5.8 – Initial characteristics of a pm-Si:H NIP solar cell using p-type  $\mu\text{-SiO}_x$  (a) J(V) curve and (b) external quantum efficiency. The intrinsic layer thickness was about 2500 Å, and NIP solar cell is deposited on textured Asahi. Thickness of p  $\mu\text{-SiO}_x/\mu\text{-Si:H}$  bi-layer is 280 Å.

Figure 5.9 shows the evolution of pm-Si:H NIP solar cell parameters as functions of intrinsic layer thickness. Initial and stabilized solar cell parameters are shown together. In the thickness series, a NIP solar cell with 1500 Å thick intrinsic layer was almost entirely shunted, so the solar cell parameters of LS state could not be measured. The conversion efficiency ( $\eta$ ) of the thickness series shows the usual trend, namely that the initial efficiency ( $\eta_{\text{initial}}$ ) increases with the intrinsic layer thickness, but the stabilized efficiency ( $\eta_{\text{stable}}$ ) decreases with the intrinsic layer thickness. In other words, thicker intrinsic layer makes NIP solar cell less stable under LS in spite of the high  $\eta_{\text{initial}}$ . This is a widely known effect, and emphasizes the importance of the light-trapping. Another interesting aspect of the intrinsic layer thickness dependence of the stability is that NIP solar cells no longer suffer from hydrogen accumulation at interface and interface delamination. Looking into more detail, most of the degradation comes from the  $FF$  attributed to the fact that the solar cell efficiency is dominated by the degradation of intrinsic layer.  $V_{oc}$  stays stable after LS, showing the degradation of about 3 %. Degradation of  $J_{sc}$  is much less than that observed in PIN solar cells. This may be interpreted as evidence that the interface delamination no longer impacts the degradation kinetics. In the intrinsic thickness series, the stability of NIP solar cells depend on the intrinsic layer thickness, so one can notice that the intrinsic layer of the NIP solar cell should not be very thick in spite of high  $\eta_{\text{initial}}$ , as expected.

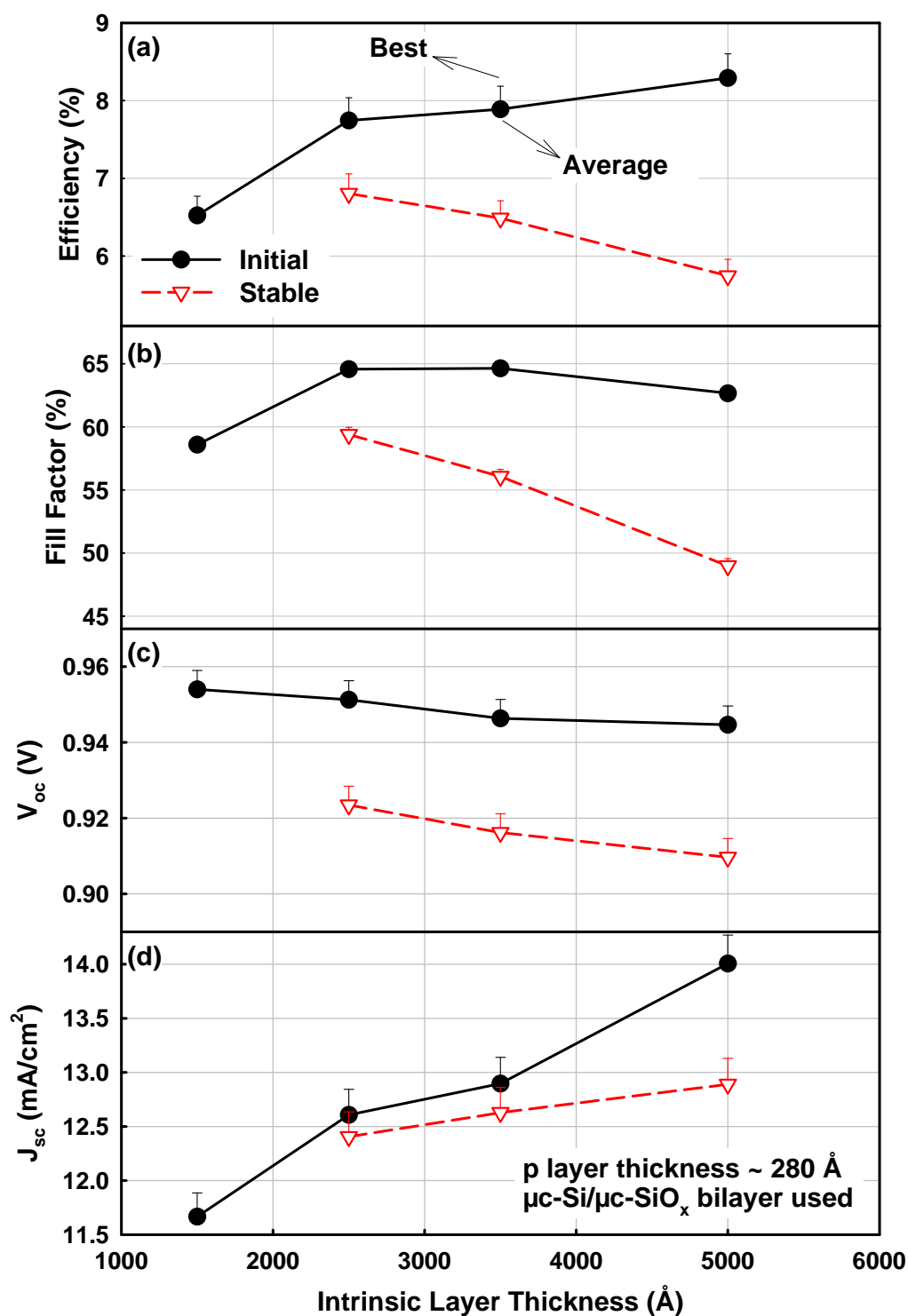


Figure 5.9 – Evolution of pm-Si:H NIP solar cell parameters as functions of intrinsic layer thickness: (a)  $\eta$ , (b)  $FF$ , (c)  $V_{oc}$ , and (d)  $J_{sc}$ . Note that initial and stabilized solar cell parameters are shown together. For the stabilization, the NIP solar cells are light-soaked under 1 sun of Hg lamp for 500 h, and  $J(V)$  curves are measured under 100 mW/cm<sup>2</sup> of simulated AM1.5 spectrum. Thickness of p  $\mu\text{-SiO}_x/\mu\text{-Si:H}$  bi-layer is 280 Å.

As mentioned above, in Figure 5.8, the p-type layer might have been too thick ( $\mu\text{c-SiO}_x/\mu\text{c-Si:H}$ , 280 Å), so another series with thinner p-type  $\mu\text{c-SiO}_x$  was tested. A series of pm-Si:H NIP solar cells having different p-type  $\mu\text{c-SiO}_x$  layer are fabricated. Same as in case of Figure 5.9, pm-Si:H NIP solar cells were light-soaked under Hg lamp illumination of an intensity of 1 sun for 500 hours. Figure 5.10 shows evolution of pm-Si:H NIP solar cell parameters as functions of p-type  $\mu\text{c-SiO}_x$  layer thickness. Notable improvement of  $\eta$  is demonstrated with thinner p-type layer. The improvement mainly relies on the increase in  $J_{sc}$ . Figure 5.11 shows an evolution of EQE curves of pm-Si:H NIP solar cells with different p-type  $\mu\text{c-SiO}_x$  layer thickness. Interestingly, the reduction of the p-type layer thickness enhances both short and long wavelength regions. Usually a thick p-type a-SiC:H layer only reduces the blue response, so the parasitic absorption in the long wavelength region suggests that there is another mechanism involved. This could be the parasitic absorption in p-type  $\mu\text{c-SiO}_x$  due to its  $\mu\text{c-Si}$  phase. Another interesting result is that the stabilized  $FF$  increases with p-layer thickness. This can be attributed to multiple reasons. Firstly, pm-Si:H is more stable under yellow/red illumination, and a thick p-type layer absorbs a large portion of blue light, working as a filter. Such a combined filtering effect looks interesting to make highly stable solar cells, but with the tradeoff of a large loss of blue response with thick p-type layer. Therefore, more efficient light-trapping is required to extract any net benefit from the filtering effect.

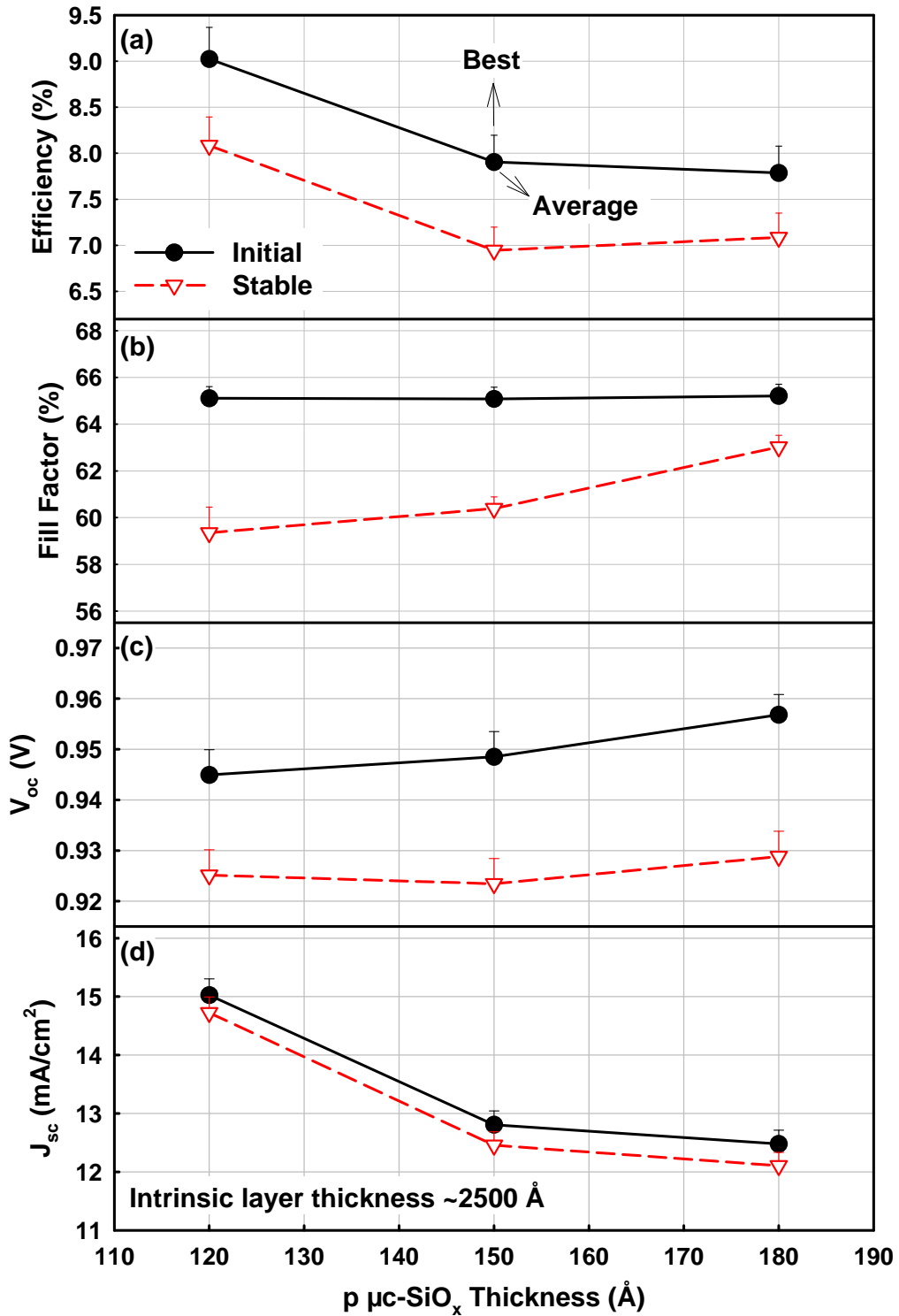


Figure 5.10 – Evolution of pm-Si:H NIP solar cell parameters as functions of p-type  $\mu\text{-SiO}_x$  layer thickness: (a)  $\eta$ , (b)  $FF$ , (c)  $V_{oc}$ , and (d)  $J_{sc}$ . Note that initial and stabilized solar cell parameters are shown together. For the stabilization, the NIP solar cells are light-soaked under 1 sun of Hg lamp, and  $J(V)$  curves are measured under 100 mW/cm<sup>2</sup> of AM1.5 spectrum. Thickness of p  $\mu\text{-Si:H}$  layer is 100 Å.

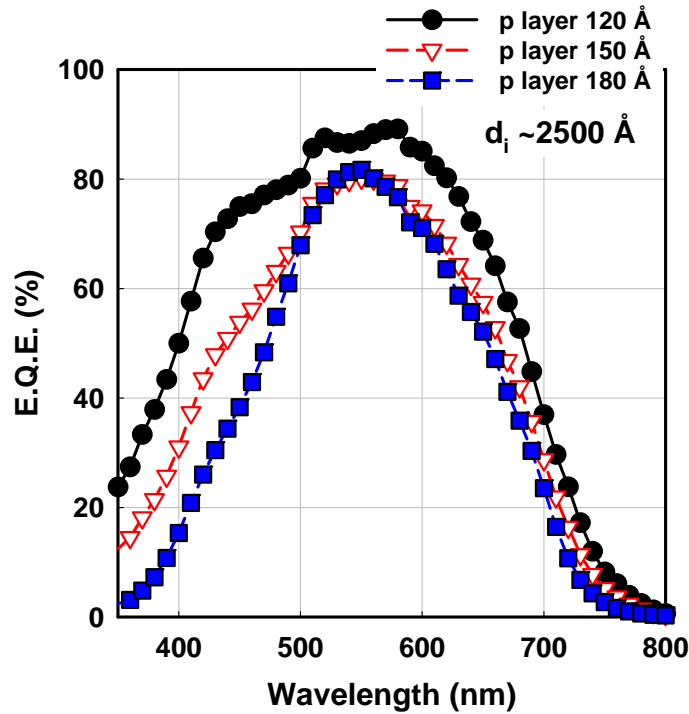


Figure 5.11 – Evolution of EQE curves of pm-Si:H NIP solar cells with different p-type  $\mu\text{c-SiO}_x$  layer thickness. Thickness of p  $\mu\text{c-Si:H}$  layer is 100 Å. Interestingly, the decrease of the p-type layer thickness enhances both short and long wavelength regions.

We have demonstrated device optimization of pm-Si:H NIP solar cells using p-type  $\mu\text{c-SiO}_x$  layers. Whereas a PIN structure facilitates the hydrogen accumulation at interface and the interface delamination during LS, use of NIP structure suppresses such interface delamination. In order to optimize NIP structure, it is necessary to use transparent and conductive window layer, so we have developed and optimized both p-type  $\mu\text{c-SiO}_x$  and NIP solar cells using the  $\mu\text{c-SiO}_x$ . An optimized pm-Si:H NIP solar cell is presented in Figure 5.12. Table 5.2 summarizes the solar cell parameters of the result in Figure 5.12. Even after 500 hours of LS, the pm-Si:H NIP solar cell shows only a small degradation of about 10 %. The stabilized  $\eta$  is found to be 8.4 %, with the excellent  $V_{oc}$  and  $FF$ .

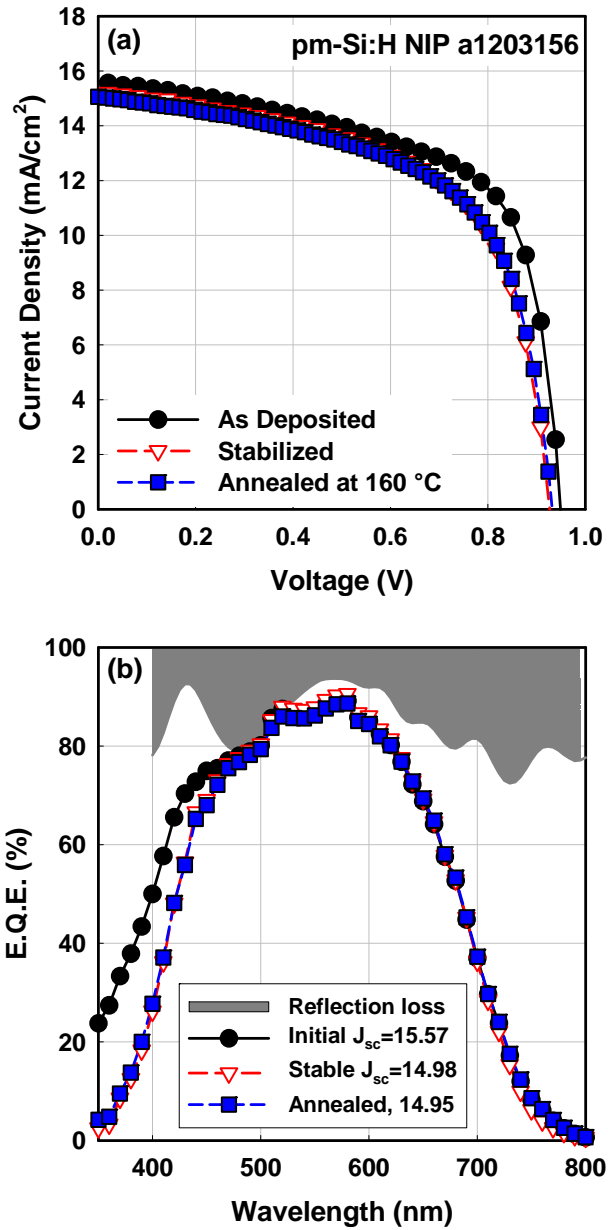


Figure 5.12 – Initial, stabilized and annealed (at  $160\text{ }^\circ\text{C}$  for 2 hrs) characteristics of an optimized pm-Si:H NIP solar cell (a)  $J(V)$  and (b) EQE curves. Intrinsic layer thickness was about  $2500\text{ \AA}$ .

Sample	State	FF	$J_{sc}$ ( $\text{mA}/\text{cm}^2$ )	$V_{oc}$ (V)	$\eta$ (%)
a1203156	As depo	64.56	15.57	0.950	9.38
	Stable	59.98	14.98	0.927	8.43
	Annealed $160\text{ }^\circ\text{C}$ 2 hrs	60.38	14.95	0.932	8.41

Table 5.2 – Solar cell parameters of an optimized pm-Si:H NIP solar cell from Figure 5.12.

The stabilized  $FF$  of about 60 is indeed lower than that of the state-of-art a-Si:H solar cell [5.14] and may be due to the different LS conditions and the presence of the thin p-type  $\mu\text{-Si:H}$  bottom layer. The NIP solar cells in this work are light-soaked under Hg lamp illumination, which spectrum consists of much more high energy photons than standard AM1.5 spectrum. EQE curve in Figure 5.12(b) also shows that most of the degradation in the pm-Si:H NIP solar cell is in the high energy photon region. Furthermore, recalling that the state-of-art reference sample shows stabilized  $FF$  of 55 under same LS spectrum (Figure 4.19), the stabilized  $FF$  of 60 is actually a high value. EQE curve of the pm-Si:H NIP solar cell shows that there is still needed for further improvement. Our record pm-Si:H NIP solar cells are fabricated on commercially available textured Asahi substrates, thus further studies on novel substrates for light trapping should bring NIP solar cells with even higher stabilized efficiency.

#### 5.4 Stable pm-Si:H NIP solar cells

As discussed in previous chapters, there are notable characteristics in the light-induced degradation kinetics of pm-Si:H PIN solar cells. At first, pm-Si:H PIN solar cells show poor stability, degrading down from about 9 % to 3 % in worst case. Second, the stable efficiency of pm-Si:H PIN solar cells does not depend on the intrinsic layer thickness, but depends on the RF power used in the deposition of intrinsic layers. The RF power dependency is attributed to the  $C_H$ , as shown in Figure 2.12. The most important contribution to the light-induced degradation in both a-Si:H and pm-Si:H comes from the change in  $FF$ , but pm-Si:H shows secondary effects, notably a rapid initial drop in  $FF$  and  $J_{sc}$ .

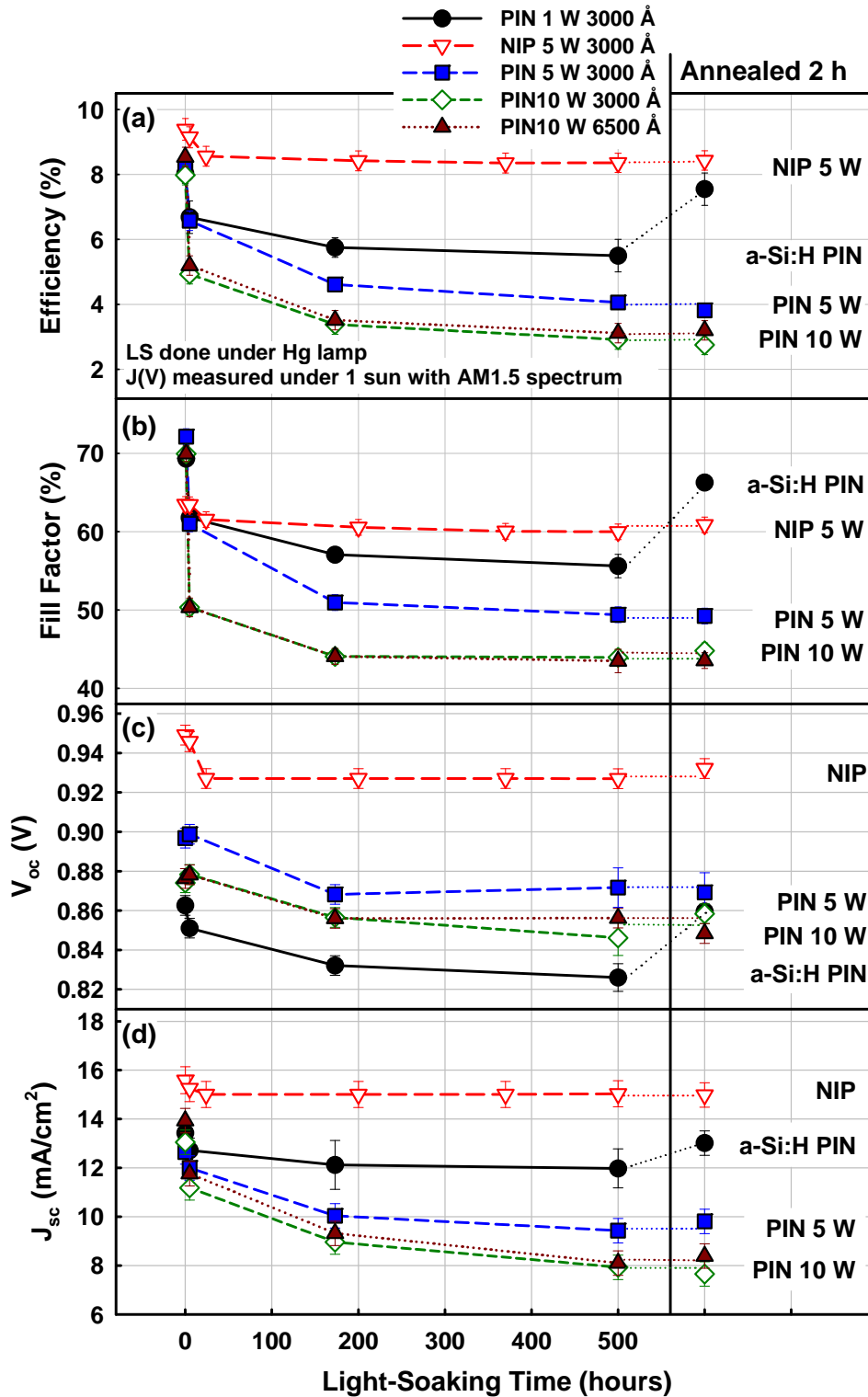


Figure 5.13 – Evolution of solar cell parameters of selected PIN and NIP solar cells (a)  $\eta$ , (b)  $FF$ , (c)  $V_{oc}$ , and (d)  $J_{sc}$  during LS under an Hg lamp illumination. Note that various individual solar cells (up to six) on the  $2.5 \times 2.5 \text{ cm}^2$  substrates were measured and the solar cell parameters are averaged. The maximum and minimum values are reflected in error bars. Al is used as back-reflector in PIN solar cells, and ITO is used in NIP. After the LS, the cells are annealed (at  $160 \text{ }^\circ\text{C}$  for 2 hrs) and checked for reversibility of the light-induced degradation.

Such rapid initial degradation is irreversible, and cannot be explained by the SWE. As we have extensively discussed in chapter 4, the physical origin of rapid drop of  $J_{sc}$  is the hydrogen accumulation at p/i interface and the delamination of pm-Si:H PIN solar cells, while this does not happen in NIP solar cells. Figure 5.13 summarizes the evolution of solar cell parameters of selected PIN and NIP solar cells during LS under Hg lamp illumination. After the LS, the cells were annealed and checked the reversibility of the light-induced degradation. One can see that only a-Si:H PIN solar cell recovers to the initial state after annealing. The pm-Si:H NIP solar cell shows the irreversible light-induced degradation, as seen in the PIN case (Figure 4.2) and in the materials [5.15]. Such small irreversible degradation may originate from structural changes and hydrogen motion in pm-Si:H, even though the hydrogen accumulation at interface and the interface delamination were significantly suppressed by the NIP structure. Therefore, the light-induced degradation kinetics of pm-Si:H NIP solar cells relies mostly on the stability of intrinsic layer, while in the case of pm-Si:H PIN solar cells degradation is mostly governed by interface delamination.

### 5.5 Summary

In this chapter we have presented preliminary results on the optimization of pm-Si:H NIP solar cells. In the previous chapters, we have demonstrated that our pm-Si:H PIN solar cells can reach a high initial efficiency, but suffer from unusual light-induced degradation, namely the interface delamination during light-soaking. Interestingly the use of NIP structure greatly suppresses the irreversible effects due to delamination. This lead us to pm-Si:H NIP solar cells showing a high stabilized efficiency of 8.43 %,

showing 10 % of light-induced degradation after light-soaking for 500 hours. While these results constitute a big step towards high stabilized efficiency pm-Si:H solar cells,, there are still some opportunities to further optimize their efficiency. In particular the development of proper buffer layer at p/i interface could reduce recombination and yield a higher  $FF$ . Moreover, EQE curves show that even higher  $J_{sc}$  could be achieved by applying light-trapping and anti-reflection solutions to our NIP solar cells.

## References

- 5.1 Y. Uchida, T. Ichimura, M. Ueno and H. Haruki, *Jap. J. Appl. Phys.*, 21, L586–L588 (1982).
- 5.2 P. Cuony, M. Marending, D. T. L. Alexander, M. Boccard, G. Bugnon, M. Despeisse, and C. Ballif, *Appl. Phys. Lett.* 97, 213502 (2010).
- 5.3 M. Despeisse, G. Bugnon, A. Feltrin, M. Stueckelberger, P. Cuony, F. Meillaud, A. Billet, and C. Ballif, *Appl. Phys. Lett.* 96, 073507 (2010).
- 5.4 B. Yan, G. Yue, L. Sivec, J. Yang, S. Guha, and C-S. Jiang, *Appl. Phys. Lett.* 99, 113512 (2011).
- 5.5 A. Abramov, Y. Djeridane, R. Vanderhaghen and P. Roca i Cabarrocas, *J. Non cryst. Solids* 352, 964 (2006).
- 5.6 S. Z. Feng, R. J. Zhang, Y. X. Zheng, J. Li, P. H. Mao, X. F. Li and L. Y. Chen, *J. Korean Phys. Soc.* 51, 1593 (2007).
- 5.7 P. Roca i Cabarrocas, S. Hamma, A. Hadjadj, J. Bertomeu and J. Andreu, *Appl. Phys. Lett.* 69, 529 (1996).
- 5.8 P. Cuony, D. T. L. Alexander, L. Löfgren, M. Krumrey, M. Marending, M. Despeisse, and C. Ballif, *Mater. Res. Soc. Symp. Proc.* 1321 A12-02 (2011).
- 5.9 J. Tauc, R. Grigorovici and A. Vancu, *Phys. Stat. Sol.* 15, 627 (1966).
- 5.10 R. A. Street, J. Kakalios, and T. M. Hayes, *Phys. Rev. B* 34, 3030 (1986).
- 5.11 B. Rech, C. Beneking, and H. Wagner, *Sol. Energ. Mater. Sol. Cells* 41-42, 475 (1996).
- 5.12 H. Stiebig, F. Siebke, W. Beyer, C. Beneking, B. Rech, and H. Wagner, *Sol. Energ. Mater. Sol. Cells* 48, 351 (1997).
- 5.13 <http://assets.newport.com/web900w-EN/images/1121.gif>
- 5.14 S. Benagli, D. Borrello, E. Vallat-Sauvain, J. Meier, U. Kroll, J. Hötzel, J. Bailat, J. Steinhauser, M. Marmelo, G. Monteduro, and L. Castens, *Proc. 24th European PVSEC, Hamburg 2009*, pp. 21-25.
- 5.15 C. Longeaud, D. Roy, and O. Saadane, *Phys. Rev. B*, 65, 85206 (2002).

## Conclusion and perspectives

The aim of this thesis was to develop pm-Si:H solar cells at high deposition rate ( $r_d$ ) and with high stabilized efficiency ( $\eta_{\text{stable}}$ ). This work further explores the optimization of pm-Si:H thin films addressed in the thesis of Anna Fontcuberta i Morral (2001), as well as the optimization of PIN solar cells studied in the thesis of Yves Poissant (2001) and Svetoslav Tchakarov (2004). Growth mechanism studies of pm-Si:H have been carried out at LPICM over the past 10 years. In this work we have compared QMS molecular mass measurements under a-Si:H and pm-Si:H deposition conditions. The QMS results reveal the presence of higher order silane species such as  $\text{Si}_2\text{H}_x$  and  $\text{Si}_3\text{H}_x$  during pm-Si:H deposition, supporting the original hypothesis about the contribution of nanoparticles to pm-Si:H growth. High deposition rate pm-Si:H was explored through various parametric studies e.g. gas flow rate, pressure, and RF power. During these parametric sweeps, we have observed a sharp increase in the optical bandgap ( $E_{\text{opt}}$ ) of the films when  $r_d$  saturates at extreme plasma conditions such as pressure  $> 3$  Torr or RF power  $> 50$  W. The sharp increase of  $E_{\text{opt}}$  is related to the excessive hydrogen content ( $C_{\text{H}}$ ) of the films. Therefore, extreme plasma conditions as mentioned above do not further contribute to  $r_d$  but lead to excessive hydrogen incorporation ( $C_{\text{H}} > 16$  at.%). Interestingly, we have found that a short residence time  $\tau_r$  reduces  $C_{\text{H}}$  as well as decreasing impurity content. Our results have demonstrated that  $r_d$  can be increased up to  $16 \text{ \AA/s}$  while keeping  $E_{\text{opt}} < 1.7 \text{ eV}$  and  $C_{\text{H}}$  of 16 at.%.

Based on the above results, pm-Si:H PIN solar cells were optimized. Various series of pm-Si:H PIN solar cells were fabricated with different intrinsic layer deposition conditions such as gas flow ratio and  $\tau_r$ . Once again, pm-Si:H PIN solar cells with the best  $FF$  were obtained using the intrinsic layer with the lowest  $E_{\text{opt}}$ , and the

intrinsic layer with low  $E_{\text{opt}}$  was obtained by low  $\tau_r$ . The  $FF$  of the PIN solar cells is controlled by the defect density of the intrinsic layers. We could fabricate pm-Si:H PIN solar cells with  $\eta_{\text{initial}}$  of 9.22 % and  $FF$  of 74.1 using optimized intrinsic layers at 1.5 Å/s. Moreover, the optimization of pm-Si:H PIN solar cells using high deposition rate (HR) intrinsic layers were fabricated. HR pm-Si:H PIN solar cell deposited at 10 Å/s showed  $\eta_{\text{initial}}$  of about 7 %, while pm-Si:H PIN solar cell deposited at 20 Å/s displays poor solar cell parameters and needs further improvements.

Metastability in a-Si:H thin film and solar cells is a 35 year-old topic, first reported by Staebler and Wronski. We have discovered that pm-Si:H PIN solar cells demonstrate unusual light-induced effects, namely i) a rapid and irreversible initial degradation and ii) large macroscopic structural changes including the interface delamination at TCO/p-layer. This is indeed a new finding because it cannot be explained by the metastability models that explain the Staebler-Wronski effect, which focus on the electronic defects in intrinsic layers. We have made comprehensive studies on the light-induced degradation kinetics of pm-Si:H PIN solar cells. As a result, we have shown a correlation between macroscopic structural changes (e.g. interface delamination) in the device and the electrical characteristics of solar cells.

An interesting result was that the pm-Si:H solar cell device stability largely depends on the illumination spectrum. External quantum efficiency (EQE) measurements show that most of the light-induced degradation of pm-Si:H solar cells takes place in the UV-blue region. Moreover pm-Si:H solar cells show pronounced degradation under Hg lamp illumination, which consists of more UV-blue than standard AM1.5 spectrum. On the contrary, pm-Si:H PIN solar cells remained stable under 570 nm (yellow-orange) illumination.

Furthermore, we have found that the delamination problem can be suppressed by changing the deposition sequence, from PIN, superstrate configuration to NIP, substrate configuration. In case of NIP structures, hydrogen does not accumulate at the TCO/p layer interface, thus preventing delamination. In order to optimize NIP structure, we developed highly conductive and transparent p-type  $\mu\text{c-SiO}_x$  layers. The application and optimization of the NIP structure, namely by using p-type  $\mu\text{c-SiO}_x$  window layers, has enabled us to fabricate pm-Si:H NIP solar cells showing a high  $\eta_{\text{initial}}$  of 9.38 % that shows a small (10 %) light-induced degradation after light-soaking for 500 hours, thus also showing a high  $\eta_{\text{stable}}$  of 8.43 %.

As future work, increasing the efficiency of single junction pm-Si:H solar cells is certainly to be considered. At first, EQE curves of optimized pm-Si:H NIP solar cells show losses in the UV-blue range of the spectrum. Enhancement on the UV-blue response could be done by reduction of parasitic absorption in the p-layer or by the use of anti-reflective coatings. pm-Si:H NIP solar cells also showed initial  $FF$  of about 65. Further enhancement could be done by removing shunt paths, more conductive ITO front contact, optimization of p/i interface, and application of highly conductive n-type  $\mu\text{c-SiO}_x$ . In particular, the material properties of n-type  $\mu\text{c-SiO}_x$  are interesting compared to our standard n-type a-Si:H. Our optimized n-type  $\mu\text{c-SiO}_x$  shows  $\sigma_{\text{RT}} \sim 10^{-1} \text{ Scm}^{-1}$  and  $E_{04} \sim 2.2 \text{ eV}$ . Finally, most of the solar cells studied in this thesis were deposited on the commercially available textured  $\text{SnO}_2\text{:F}$  (Asahi) substrate. Application of state-of-art TCO technologies such as APCVD ZnO would bring more efficient light-trapping.

One could further test HR pm-Si:H PIN solar cells. In this thesis, we have shown that intrinsic pm-Si:H layer deposited at  $16 \text{ \AA/s}$  could be a good material for solar cells, while intrinsic pm-Si:H layer deposited at  $20 \text{ \AA/s}$  showed poor material properties (high  $E_{\text{opt}}$ , high  $C_{\text{H}}$ ,

poor solar cell parameters...). Fabrication of HR pm-Si:H PIN solar cells using 16 Å/s process condition could be an interesting further work. Meanwhile, HR pm-Si:H NIP solar cells have not yet been tested. As the NIP structure shows superior device stability compared to that of PIN structure, the fabrication of HR pm-Si:H NIP solar cells would be also an interesting topic.

The spectral dependence of the light-induced degradation of pm-Si:H solar cells is another important topic which deserves further studies. Indeed, we have shown that pm-Si:H solar cells show most of the light-induced degradation in UV-blue region, while they remain stable under longer wavelength illumination (~570 nm). Moreover, we have found that a thick p-type layer in pm-Si:H NIP solar cells may contribute to an interesting “filter” effect, leading to higher stabilized  $FF$ . However, the physical origin of such spectral dependence of the solar cell stability is still an open question. Further studies on the spectral dependency would bring clearer view in the pm-Si:H solar cell device stability.

The high  $E_{opt}$  (~ 1.7 eV) of pm-Si:H solar cells along with their stable efficiency makes them an ideal “top-cell” for “micromorph” tandem or triple junction solar cells. It will be an interesting work to test if PINPIN tandem structure also suffers from the interface delamination. Otherwise NIPNIP structure could be used. Highly conductive n-type  $\mu\text{-SiO}_x$  would act an important role as an intermediate reflector and a tunnel junction.

Finally, the results presented in this thesis were done in the ARCAM reactor. Regarding its flexibility and simplicity, ARCAM is an excellent reactor for studies. However, this 25 year-old equipment also has practical limitations, particularly with respect to the impurity levels that can be achieved compared to state-of-the-art equipment. In particular, ARCAM does not have a load-lock port which increases the

time required to pump down and also makes it difficult to maintain chemical purity at high temperature or under high pressure. The multi-chamber cluster tool available at the Total-LPICM joint research team as of September 2012 will certainly help to further increase the stabilized efficiency of pm-Si:H solar cells.



# Annex

Annex 2.1 Gas flow series .....	222
Annex 2.2 Pressure series .....	225
Annex 2.3 RF power series.....	227
Annex 2.4 $T_s$ series .....	230
Annex 3.1 Intrinsic layer thickness series .....	232
Annex 5.1 n-type $\mu\text{-SiO}_x$ .....	234

## Annex 2.1 Gas flow series

Annex 2.1 provides auxiliary results of the gas flow series presented in chapter 2. Only  $\text{SiH}_4$  flow was varied while the other process parameters were fixed e.g. pressure = 3.5 Torr,  $T_s = 210^\circ\text{C}$ , RF = 30 W, and  $\text{H}_2 = 500$ . The films are deposited on flat corning glass. SE measurement and modeling result are provided. Typical value of a-Si:H is also marked as  $\times$ . This annex is to demonstrate the trend of the material properties during the parametric studies.

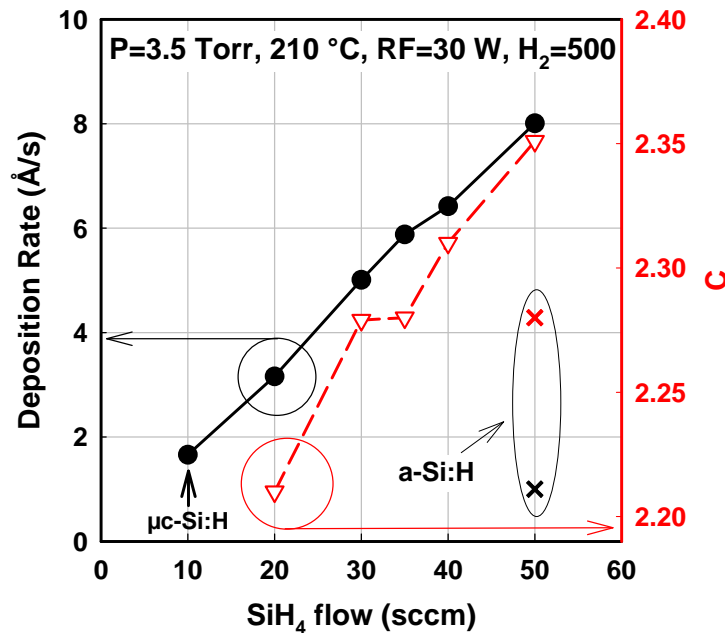


Figure A.1 –  $r_d$  and the disorder parameter C as functions of gas flow ratio. Note that  $\text{H}_2$  and was fixed to 500, and only  $\text{SiH}_4$  was varied.

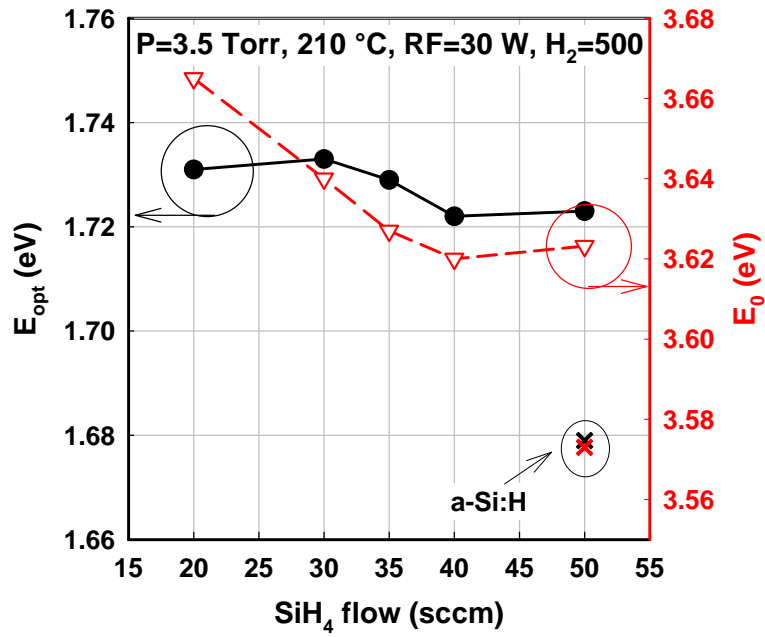


Figure A.2 – Optical bandgap and peak-to-peak transition energy  $E_0$  as functions of gas flow ratio. Note that  $H_2$  flow was fixed to 500, and only  $SiH_4$  was varied.

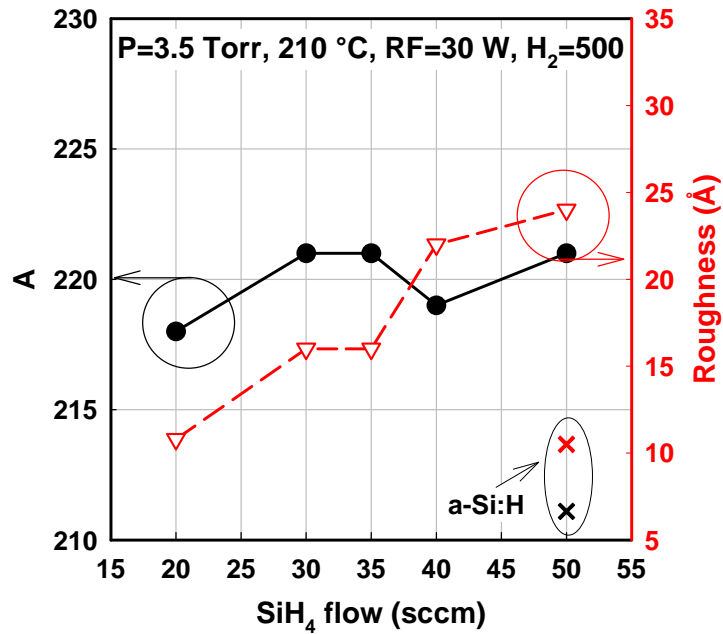


Figure A.3 – Density parameter  $A$  and surface roughness thickness as functions of gas flow ratio. Note that  $H_2$  flow was fixed to 500, and only  $SiH_4$  was varied.

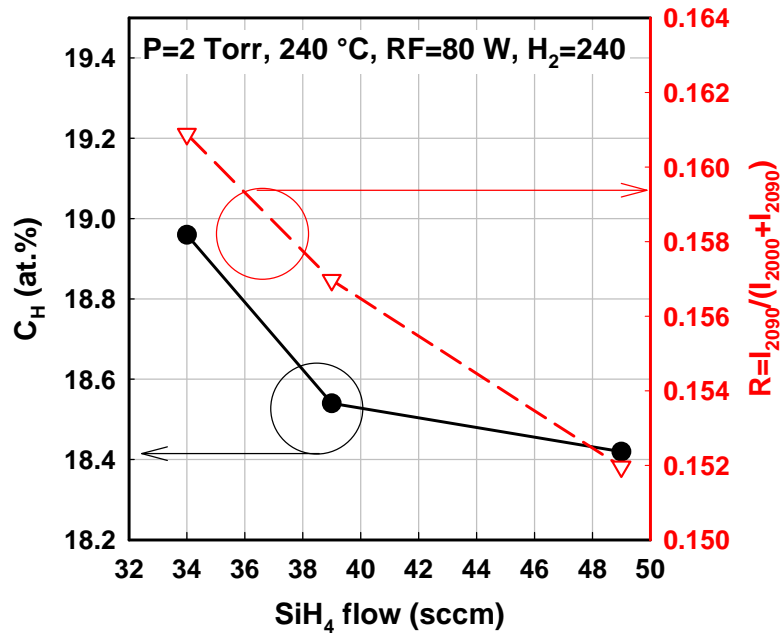


Figure A.4 – Hydrogen content and microstructure parameter  $R$  as functions of gas flow ratio. Note that  $H_2$  flow was fixed, and only  $\text{SiH}_4$  was varied.

## Annex 2.2 Pressure series

Annex 2.2 provides auxiliary results of the pressure series presented in chapter 2. Only total pressure was varied while the other process parameters were fixed e.g.  $T_s = 210\text{ }^\circ\text{C}$ ,  $\text{RF} = 30\text{ W}$ ,  $\text{H}_2 = 500$ , and  $\text{SiH}_4 = 40$ . The films are deposited on flat corning glass. SE measurement and modeling result are provided. Typical value of a-Si:H is also marked as  $\times$ . This annex is to demonstrate the trend of the material properties during the parametric studies.

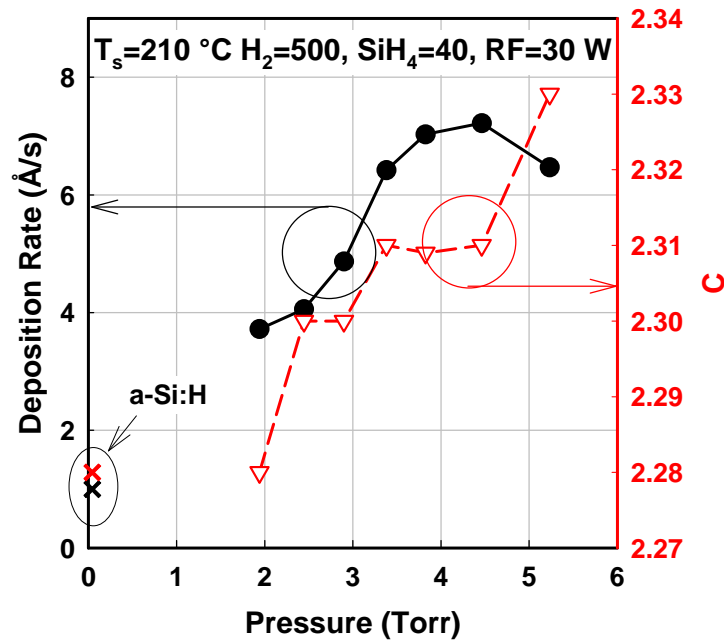


Figure A.5 –  $r_d$  and the disorder parameter C as functions of total pressure.

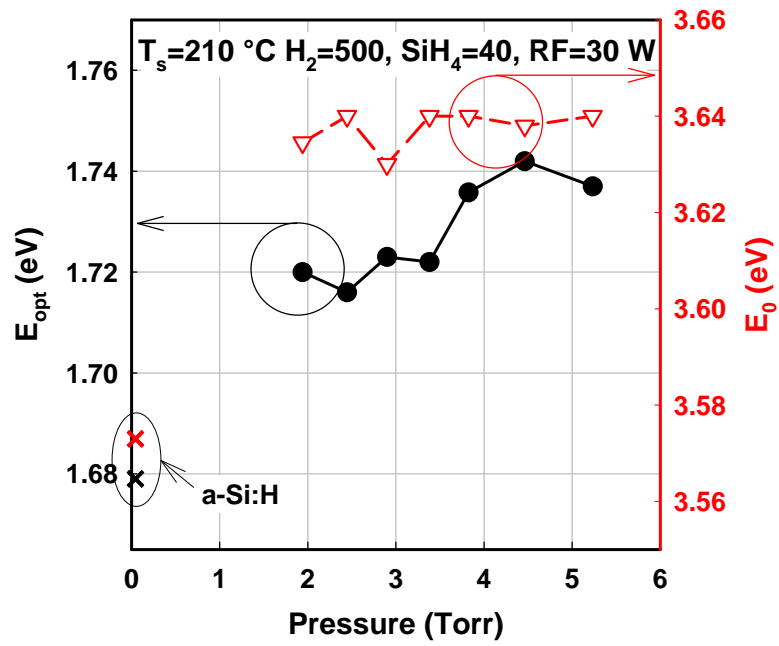


Figure A.6 – Optical bandgap and peak-to-peak transition energy  $E_0$  as functions of total pressure.

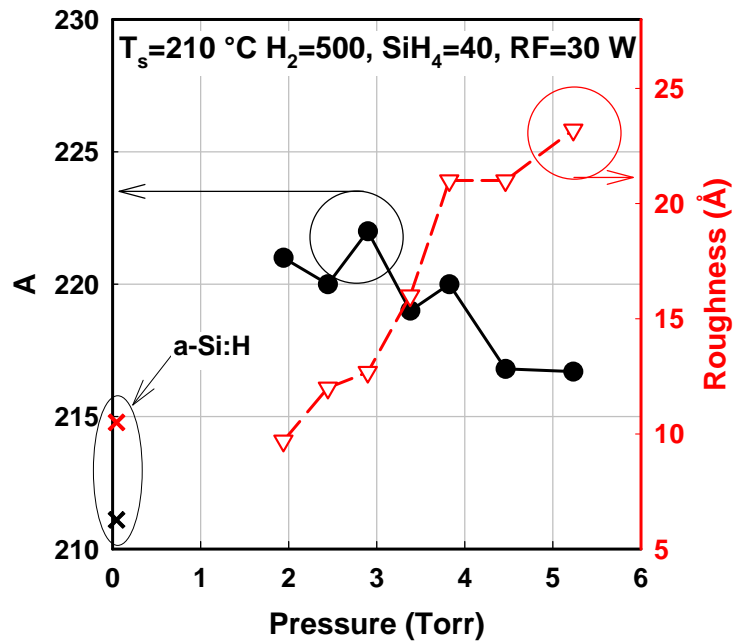


Figure A.7 – Density parameter  $A$  and surface roughness thickness as functions of total pressure.

### Annex 2.3 RF power series

Annex 2.3 provides auxiliary results of the RF power series presented in chapter 2. Only RF power was varied while the other process parameters were fixed e.g.  $T_s = 240$  °C, Pressure = 3 Torr,  $H_2 = 338$ , and  $SiH_4 = 50$ . The films are deposited on flat corning glass. SE measurement and modeling result are provided. Typical value of a-Si:H is also marked as  $\times$ . This annex is to demonstrate the trend of the material properties during the parametric studies.

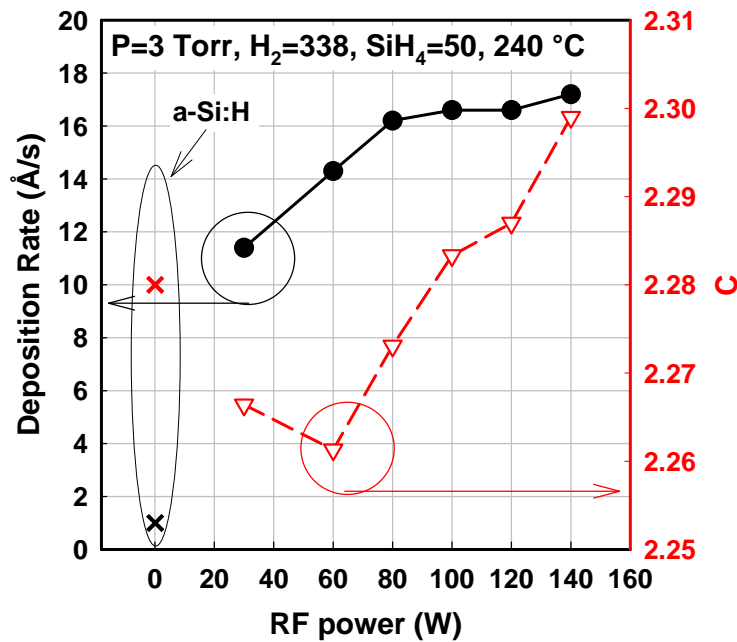
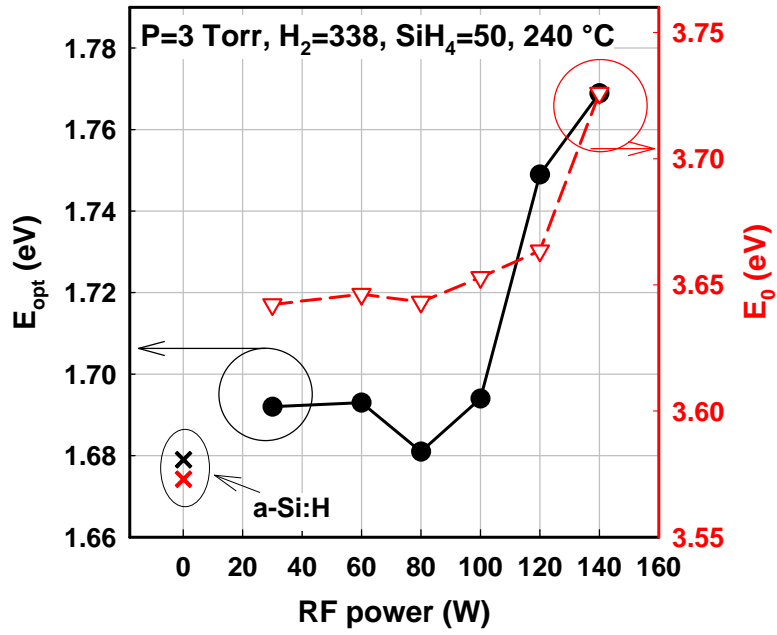
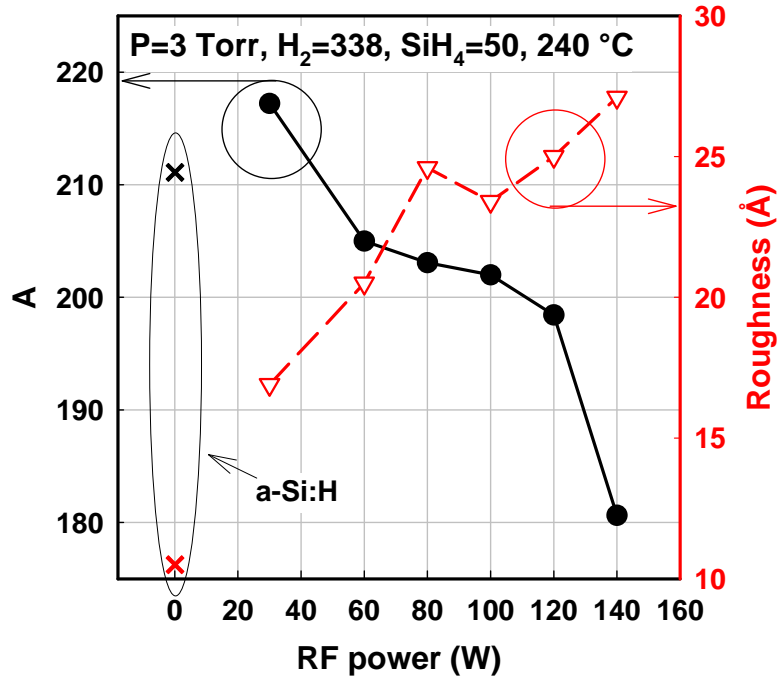


Figure A.8 –  $r_d$  and the disorder parameter C as functions of RF power.

Figure A.9 – Optical bandgap and peak-to-peak transition energy  $E_0$  as functions of RF power.Figure A.10 – Density parameter  $A$  and surface roughness thickness as functions of RF power.

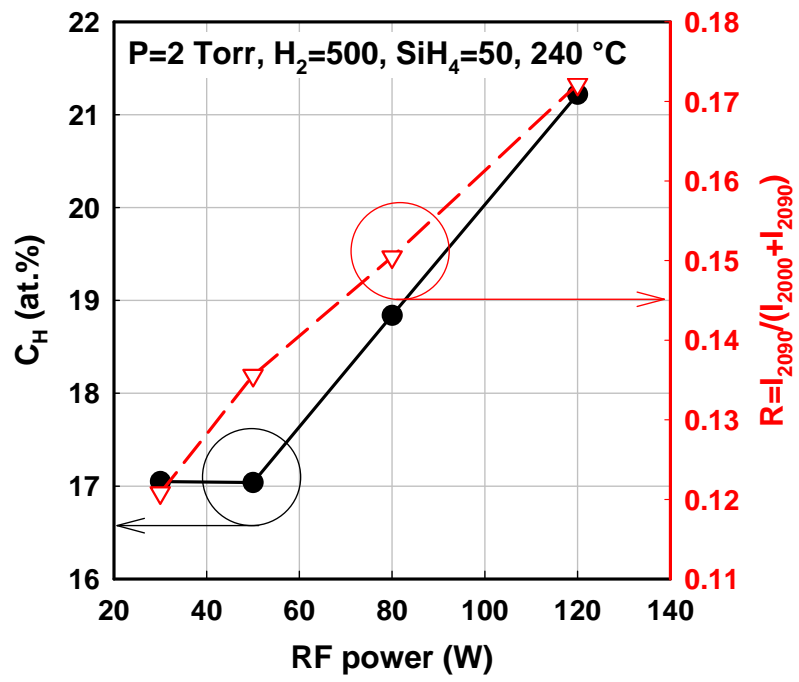


Figure A.11 – Hydrogen content and microstructure parameter R as functions of RF power.

## Annex 2.4 $T_s$ series

Annex 2.4 provides auxiliary results of the  $T_s$  series presented in chapter 2. Only  $T_s$  was varied while the other process parameters were fixed e.g. Pressure = 3 Torr, RF power = 30 W,  $H_2 = 500$ , and  $SiH_4 = 40$ . The films are deposited on flat corning glass. SE measurement and modeling result are provided. Typical value of a-Si:H is also marked as  $\times$ . This annex is to demonstrate the trend of the material properties during the parametric studies.

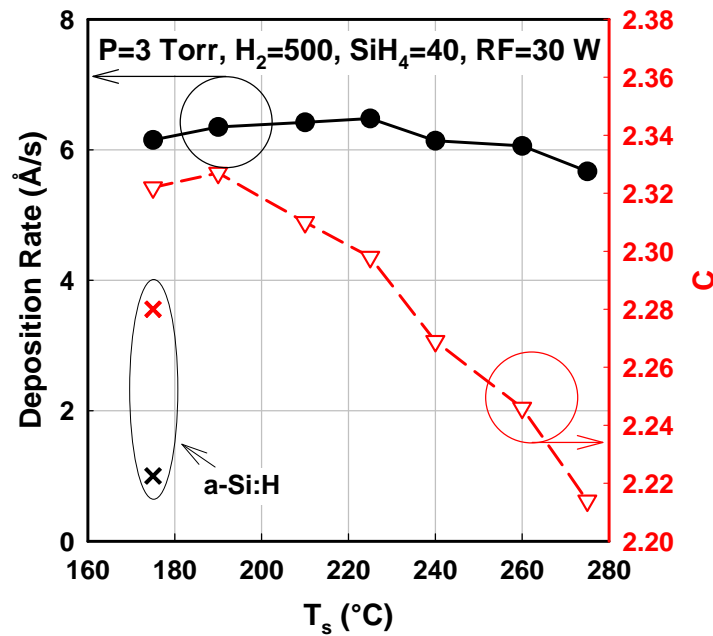


Figure A.12 –  $r_d$  and the disorder parameter  $C$  as functions of  $T_s$ .

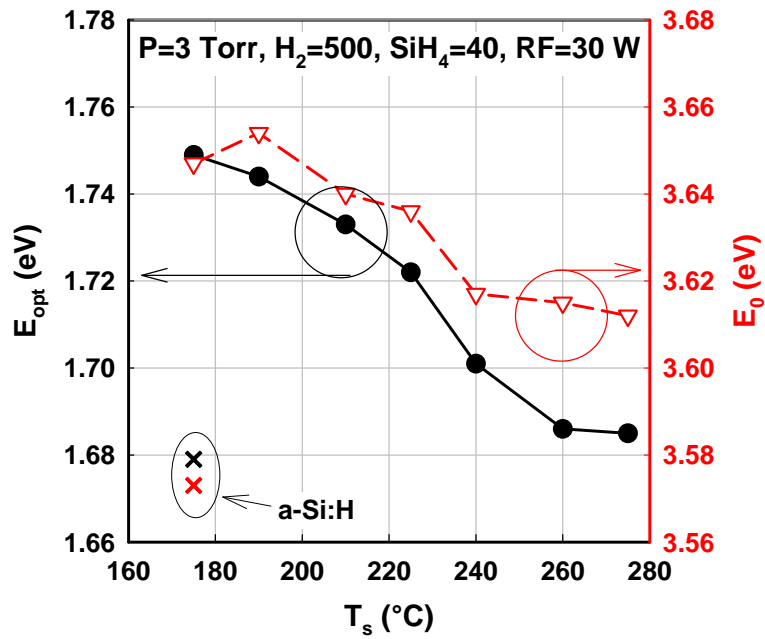


Figure A.13 – Optical bandgap and peak-to-peak transition energy  $E_0$  as functions of  $T_s$ .

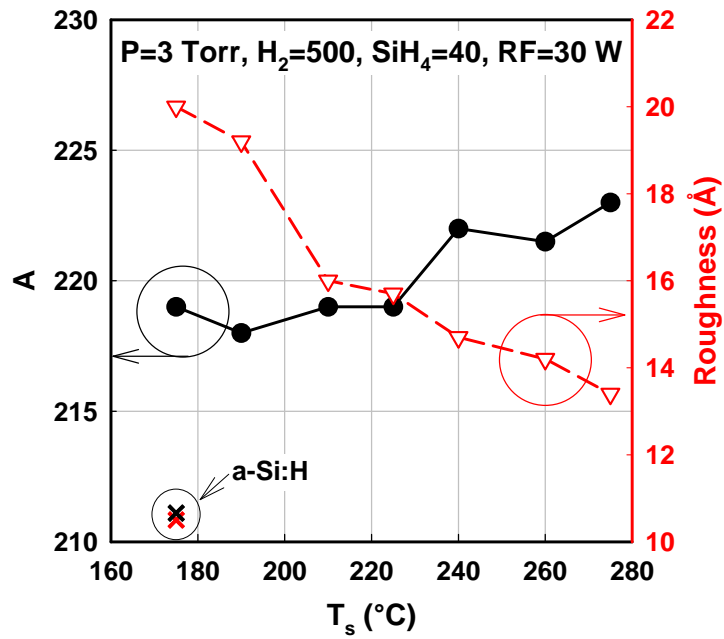


Figure A.14 – Density parameter  $A$  and surface roughness thickness as functions of  $T_s$ .

### Annex 3.1 Intrinsic layer thickness series

Annex 3.1 demonstrates the evolution of the solar cell parameters as functions of intrinsic layer thickness ( $d_i$ ). Multiple sets of PIN solar cells are fabricated with different  $d_i$ . The two major impacts of  $d_i$  are absorption and the electric field. Thicker  $d_i$  attributes to increase in absorber layer thickness, thus results in increase of  $J_{sc}$ . In particular, longer wavelength region, where the material have lower absorption coefficient. Figure A.15 shows EQE curves of a-Si:H PIN solar cells with different  $d_i$ . However, at the same time, thick  $d_i$  results weak electric field across the junction and longer carrier drift path, and it is reflected into higher recombination.

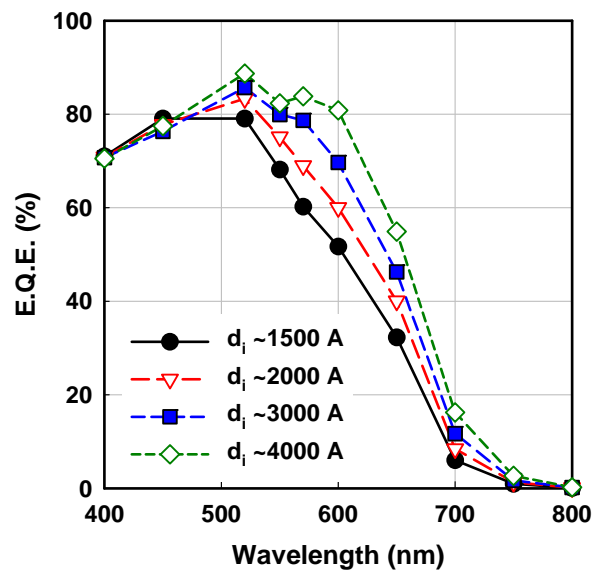


Figure A.15 – EQE curves of a-Si:H PIN solar cells having different intrinsic layer thickness.

It is more significant in the case of defective intrinsic layer case, one can notice that FF of bad pm-Si:H PIN rapidly decrease with  $d_i$  in Figure A.16. Even if good PIN solar cells show no significant change in the initial parameters, thick intrinsic layer would result in heavy light-induced degradation. Therefore, importance of the light-trapping is once again stressed.

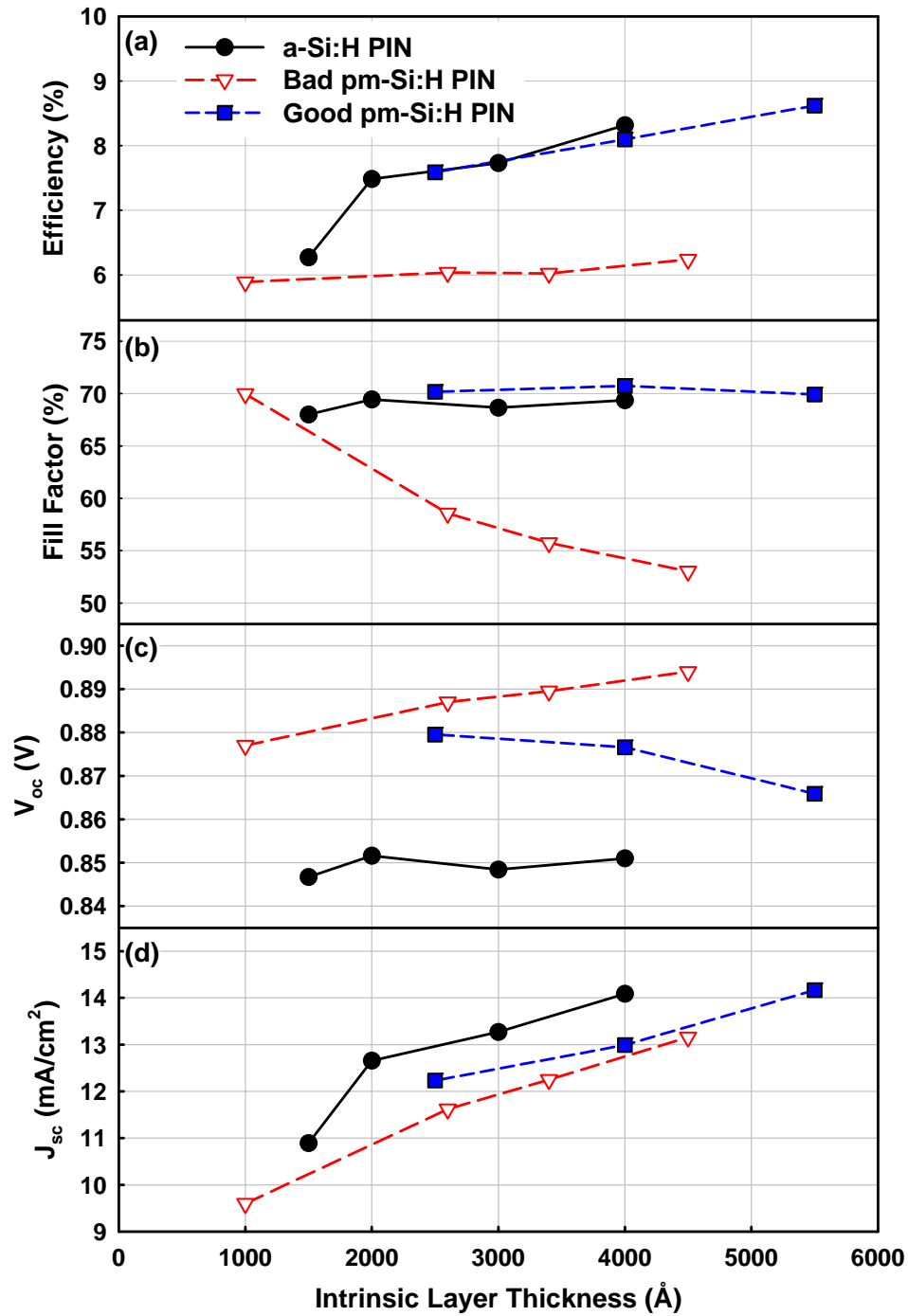


Figure A.16 – Evolution of solar cell parameters of selected PIN solar cells (a)  $\eta$ , (b)  $FF$ , (c)  $V_{oc}$ , and (d)  $J_{sc}$  as functions of  $d_i$ .

### Annex 5.1 n-type $\mu\text{c-SiO}_x$

Annex 5.1 provides material properties of n-type  $\mu\text{c-SiO}_x$  layers. Similarly in the p-type  $\mu\text{c-SiO}_x$ , the n-type  $\mu\text{c-SiO}_x$  layers are deposited at 175 °C from a gas mixture of  $\text{SiH}_4$ ,  $\text{H}_2$ , and  $\text{CO}_2$ . n-type doping is achieved by adding  $\text{PH}_3$ . Effect of  $\text{CO}_2$  addition was studied by varying the  $\text{CO}_2$  flow. It is shown that  $\text{CO}_2$  flow reduces  $\mu\text{c-Si}$  fraction and increase  $\text{SiO}_2$  fraction in the material. Therefore, increase in  $\text{CO}_2$  flow deteriorates electrical properties and enhances the optical properties.

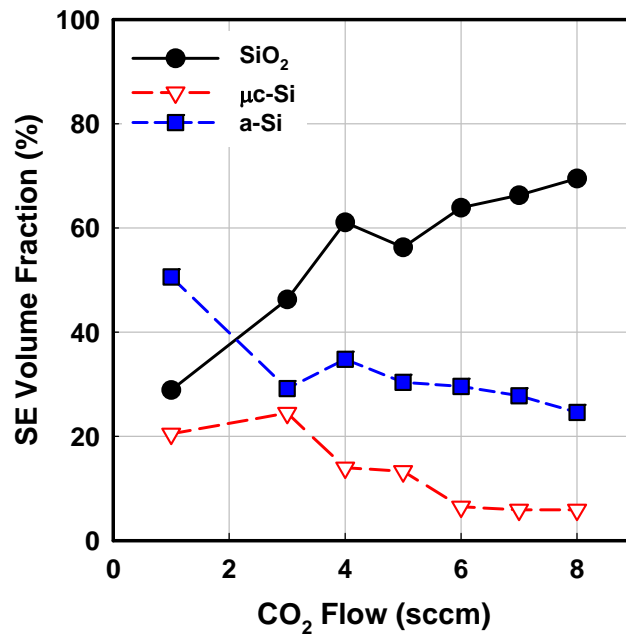


Figure A.17 – Evolution of  $\text{SiO}_2$ ,  $\mu\text{c-Si}$ , and a-Si volume fraction of n-type  $\mu\text{c-SiO}_x$  as functions of  $\text{CO}_2$  flow deduced from BEMA method.

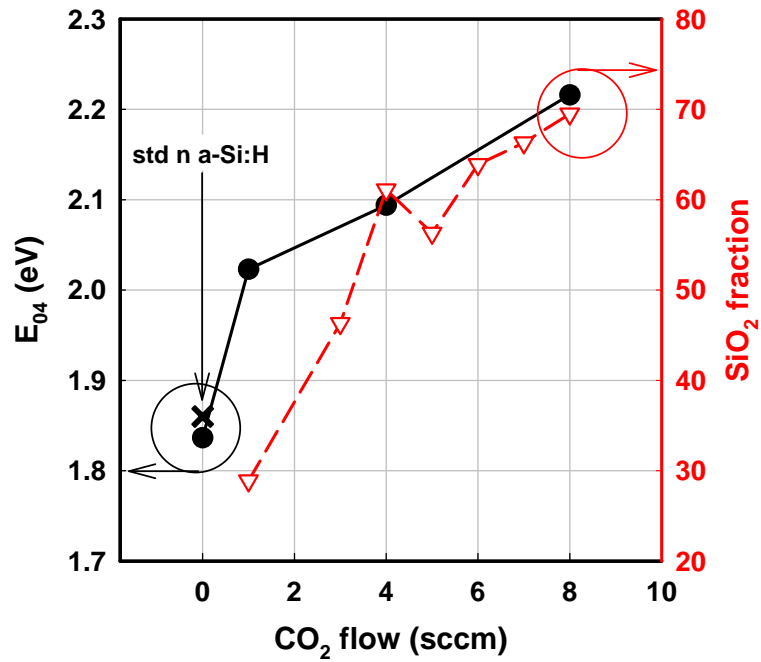


Figure A.18 –  $E_{04}$  from transmission measurement and  $\text{SiO}_2$  fraction of n-type  $\mu\text{-SiO}_x$  deduced from SE modeling as functions of  $\text{CO}_2$  flow. Note that  $E_{04}$  and  $\text{SiO}_2$  fraction show strong correlation

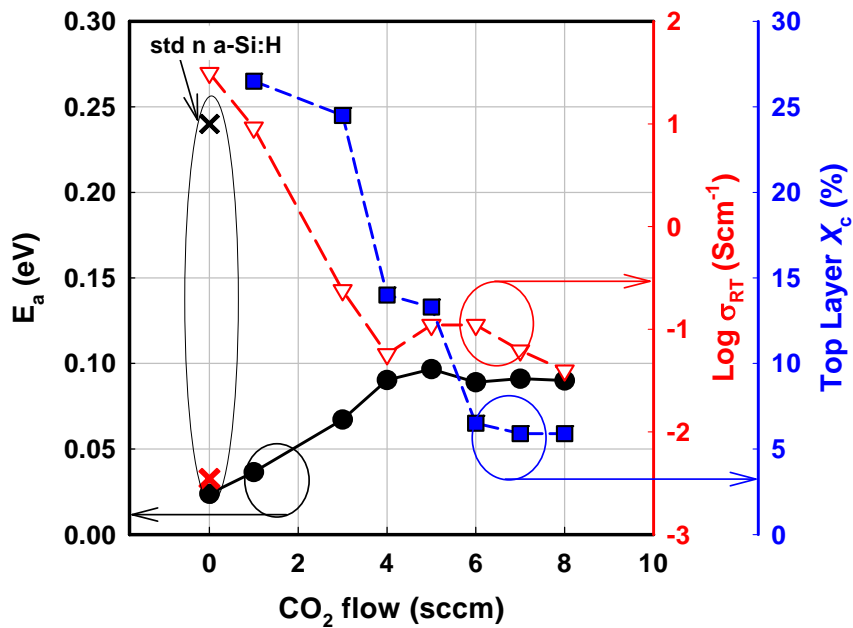


Figure A.19 –  $E_a$  and  $\sigma_{RT}$  from  $\sigma(T)$  measurement and  $\mu\text{-Si}$  fraction ( $X_c$ ) of n-type  $\mu\text{-SiO}_x$  deduced from SE modeling as functions of  $\text{CO}_2$  flow. Note that  $E_a$ ,  $\sigma_{RT}$  and  $\mu\text{-Si}$  fraction show strong correlation.



# List of publications

1. **Ka-Hyun Kim**, Samir Kasouit, Erik V. Johnson, and Pere Roca i Cabarrocas (Working title) *Hydrogenated polymorphous silicon for next generation thin film solar cells* Sol. Energ. Mat. Sol. Cells To be submitted (2012).
2. **Ka-Hyun Kim**, Samir Kasouit, Erik V. Johnson, and Pere Roca i Cabarrocas *Substrate versus superstrate configuration for stable solar cells* Appl. Phys. Lett. To be submitted (2012).
3. D. Senouci, R. Baghdad, A. Belfedal, L. Chahed, X. Portier, S. Charvet, **K.H. Kim**, P. Roca i Cabarrocas, K. Zellama, *Hydrogen related crystallization in intrinsic hydrogenated amorphous silicon films prepared by reactive radiofrequency magnetron sputtering at low temperature* Thin Solid Films, In Press (2012). <http://dx.doi.org/10.1016/j.tsf.2012.08.014>
4. **Ka-Hyun Kim**, Bicher Haj Ibrahim, Erik V. Johnson, Antonello De Martino, and Pere Roca i Cabarrocas, *Real-time-transmission Mueller polarimetry on hydrogenated polymorphous silicon under current-injection* J. Phys. D: Appl. Phys. Submitted (2012).
5. **Ka-Hyun Kim**, Erik V. Johnson, and Pere Roca i Cabarrocas *Irreversible light-induced degradation and stabilization of hydrogenated polymorphous silicon solar cells* Sol. Energ. Mat. Sol. Cells 105, 208 (2012). <http://dx.doi.org/10.1016/j.solmat.2012.06.026>
6. **Ka-Hyun Kim**, Erik V. Johnson, Alexei Abramov and Pere Roca i Cabarrocas *Light induced electrical and topological changes in hydrogenated polymorphous silicon solar cells* Eur. Phys. J. Photovolt. 3, 30301 (2012). <http://dx.doi.org/10.1051/epjpv/2012005>
7. **Ka-Hyun Kim**, Erik V. Johnson, Samir Kasouit and Pere Roca i Cabarrocas *Light Induced Changes in PIN Solar Cells: Beyond the Staebler-Wronski Effect* Mater. Res. Soc. Symp. Proc. (2012). <http://dx.doi.org/10.1557/opl.2012.861>
8. Pere. Roca i Cabarrocas, **Ka-Hyun Kim**, Romain Cariou, Martin Labrune, Erik V. Johnson, Mario Moreno, Alfonso Torres Rios, Sergey Abolmasov, and Samir Kasouit *Low Temperature Plasma Synthesis of Nanocrystals and their application to the Growth of Crystalline Silicon and Germanium Thin Films* Mater. Res. Soc. Symp. Proc. (2012). <http://dx.doi.org/10.1557/opl.2012.1094>
9. Junzhuan Wang, Linwei Yu, Sergey Abolmasov, **Ka-Hyun Kim**, and Pere Roca i Cabarrocas *Strong visible and near-infrared electroluminescence and formation process in Si-rich polymorphous silicon carbon* J. Appl. Phys. 111,

053108 (2012). <http://dx.doi.org/10.1063/1.3691904>

10. Jinyoun Cho, Benedict O'Donnell, Linwei Yu, **Ka-Hyun Kim**, Irène Ngo, Pere Roca i Cabarrocas, *Sn-catalyzed silicon nanowire solar cells with 4.9% efficiency grown on glass* Prog. Photovolt. Res. Appl. (2012). <http://dx.doi.org/10.1002/pip.1245>
11. Madhumita Nath, Sanghamitra Chakraborty, **Ka-Hyun Kim**, Erik V. Johnson, Pere Roca i Cabarrocas and Parsathi Chatterjee, *Performance of amorphous and microcrystalline silicon pin solar cells under variable light intensity* Phys. Stat. Sol. C 7/3-4 1105 (2010). <http://dx.doi.org/10.1002/pssc.200982726>
12. Yassine Djeridane, Pere Roca i Cabarrocas, **Ka-Hyun Kim**, Se Hwan Kim, Jung Ho Bae, Jun Young Jeong and Jin Jang *Fabrication and characterization of ion doped p-type nanocrystalline silicon thin film transistors* J. Kor. Phys. Soc. 54, 437 (2009). <http://dx.doi.org/10.3938/jkps.54.437>
13. Christophe Avis, Se Hwan Kim, **Ka-Hyun Kim**, Jin Jang, Sung Jun Hong, Youn Duck Nam and Ji Ho Hur *B-Ion Doping Effect in ZnO Thin-Film* J. Kor. Phys. Soc. 54, 535 (2009). <http://dx.doi.org/10.3938/jkps.54.535>
14. Erik V. Johnson, **Ka-Hyun Kim** and Pere Roca i Cabarrocas *In-situ Observation of High deposition rate (9Å/s) Hydrogenated Polymorphous Silicon Cell Degradation Through Variable Illumination Method Measurements* Mater. Res. Soc. Symp. Proc. A7.9. (2009). <http://dx.doi.org/10.1557/PROC-1153-A07-09>



## Abstract

This thesis is dedicated to hydrogenated polymorphous silicon (pm-Si:H) and solar cells based on this material. pm-Si:H is a nanostructured thin film deposited by conventional PECVD method. The effects of various deposition parameters (gas flow ratio, pressure, RF power,  $T_s$ ) on material properties were investigated in order to optimize its quality. The strategy was to combine a wide range of diagnostics (spectroscopic ellipsometry, hydrogen exodiffusion, SIMS, FTIR, AFM, etc.). Due to the contribution of plasma synthesized silicon nanoparticles, the process condition of pm-Si:H shows the difference in contrary to a-Si:H deposition through ionized radicals.

Studies on pm-Si:H deposition process allows to fabricate pm-Si:H PIN solar cells with a high initial efficiency of 9.22 % and fill factor of 74.1, but also demonstrate unusual light-induced effects, namely i) a rapid initial degradation, ii) an irreversible degradation, and iii) large macroscopic structural changes. Comprehensive investigation on the light-induced degradation kinetics of pm-Si:H PIN layer stacks reveals a pronounced hydrogen accumulation and delamination at the substrate/p-type layer interface under light-soaking, leading to macroscopic structural changes, e.g., peel-off and solar cell area loss.

We have found that a PIN structure leads to facilitated delamination during light-soaking, which we attribute to hydrogen accumulation at the substrate/p-layer interface, while use of a NIP structure prevents the hydrogen accumulation and delamination. This lead us to fabricate pm-Si:H NIP solar cells showing a high stabilized efficiency of 8.43 %, that shows a small (10 %) light-induced degradation after light-soaking for 500 hours.

**Keywords:** amorphous silicon, polymorphous silicon, nanocrystalline silicon, solar cell, hydrogen, PECVD

## Résumé

Cette thèse est consacrée au silicium polymorphe hydrogéné (pm-Si:H). Elle porte tout d'abord sur une étude du pm-Si :H puis sur une étude des cellules photovoltaïques fabriquées à partir de ce matériau. Le pm-Si:H est formé de couches minces nanostructurées et peut être déposé par PECVD conventionnelle. Les effets des différents paramètres de dépôt (mélanges gazeux, pression, puissance RF, température du substrat) sur les propriétés du matériau ont été étudiés pour optimiser sa qualité. La caractérisation des couches a été un enjeu primordial. Pour cela, nous avons choisi de combiner une palette très large de méthodes de caractérisation (ellipsométrie spectroscopique, exodiffusion d'hydrogène, SIMS, FTIR, AFM, etc...). A cause de la contribution des nanoparticules de silicium dans le plasma, la nature du dépôt du pm-Si:H montre la différence contrairement au a-Si:H pour lequel le dépôt se fait par le biais de radicaux ionisés.

L'étude des conditions du procédé nous a conduit à fabriquer des cellules solaires d'un rendement initial de 9.22 % avec un facteur de forme élevé (74.1), mais aussi de démontrer des effets de vieillissement inhabituels, tels que i) une dégradation initiale rapide, ii) une dégradation irréversible, et iii) de grands changements structuraux macroscopiques. Nous avons découvert que le principal problème se situe entre le substrat et la couche mince de silicium. L'hydrogène moléculaire diffuse et s'accumule à l'interface entre le substrat et la couche mince, ce qui introduit un délaminage local qui a pour conséquence une dégradation initiale rapide des performances des cellules.

Nous avons trouvé que sous éclairage une structure PIN facilite l'accumulation d'hydrogène et le délaminage à l'interface entre le substrat et la couche dopée p. Cependant, l'utilisation d'une structure NIP empêche l'accumulation d'hydrogène et le délaminage. Cela nous a permis de fabriquer des cellules solaires pm-Si:H de structure NIP d'un rendement stable de 8.43 %, mais aussi de démontrer une dégradation minimale (10 %) après un vieillissement de 500 heures.

**Mots-clés:** silicium amorphe, silicium polymorphe, silicium nanocristallin, cellule photovoltaïque, hydrogène, PECVD